

RADIOTHERAPY BEAMLINE DESIGN FOR LASER-DRIVEN PROTON BEAMS

Umar Masood

Wissenschaftlich-Technische Berichte
HZDR-104

Umar Masood

RADIOTHERAPY BEAMLINE DESIGN FOR LASER-DRIVEN PROTON BEAMS

HZDR

Druckausgabe: ISSN 2191-8708

Elektronische Ausgabe: ISSN 2191-8716

Die elektronische Ausgabe erscheint unter Creative Commons License (CC BY 4.0):

<https://www.hzdr.de/publications/Publ-29631>

[urn:nbn:de:bsz:d120-qucosa2-352302](https://nbn-resolving.org/urn:nbn:de:bsz:d120-qucosa2-352302)

DOI: [10.5281/zenodo.3386378](https://doi.org/10.5281/zenodo.3386378) (Dissertation)

Die vorliegende Arbeit wurde sowohl als Dissertation an der Medizinischen Fakultät Carl Gustav Carus der Technischen Universität Dresden sowie als Wissenschaftlich-Technischer Bericht des Helmholtz-Zentrum Dresden – Rossendorf mit der Berichtsnummer **HZDR-104** veröffentlicht.

2019

Herausgegeben vom

Helmholtz-Zentrum Dresden – Rossendorf

Bautzner Landstraße 400

01328 Dresden

Germany

Radiotherapy Beamline Design for Laser-driven Proton Beams

D i s s e r t a t i o n s s c h r i f t

zur Erlangung des akademischen Grades
Doktor der Medizintechnologie
Doctor rerum medicinalium (Dr. rer. medic.)

vorgelegt

der Medizinischen Fakultät Carl Gustav Carus
der Technischen Universität Dresden

von

M. Sc. Umar Masood
aus Lahore, Pakistan

Dresden 2018

1. Gutachter: Prof. Dr. Wolfgang Enghardt

2. Gutachter: Prof. Dr. Peter Michel

Tag der mündlichen Prüfung: 28. Juni 2019

gez.: Prof. Dr. Esther Troost
Vorsitzende der Promotionskommission

Contents

1	Introduction	1
2	Background	5
2.1	Conventional proton therapy	5
2.2	Advances in PT machines	9
2.3	Alternative approaches for PT machines	11
2.4	Laser-driven proton acceleration	12
2.4.1	Target normal sheath acceleration	16
2.4.2	Radiation pressure acceleration	17
2.4.3	LAP beam status and properties	17
2.5	Dose delivery systems	19
2.5.1	Conventional dose delivery systems	19
2.5.2	Advanced dose models for LAP beams	22
2.6	Previously published beamline solutions	25
2.7	Challenges and prospects	29
3	Beam optics	33
3.1	Transverse beam optics	33
3.1.1	Quadrupoles	36
3.1.2	Sector magnets	37
3.1.3	Solenoid	39
3.1.4	Drift space	41
3.2	Beam Dynamics	41
3.3	Pulsed magnets	44
3.3.1	Pulsed solenoid	46
3.3.2	Pulsed sector magnet	48
3.3.3	Pulsed quadrupole	49
3.3.4	Limits for gantry design studies	53
4	Preliminary Gantry Solution	55
4.1	Motivation	55
4.2	Materials and Methods	55
4.2.1	Broad energy assorted depth dose deposition model	55
4.2.2	Principal requirements from the gantry	59
4.2.3	One-step beam capture and collimation	60
4.2.4	Energy selection system	62
4.2.5	Achromatic beam transport	63
4.2.6	Simulated LAP sources	65

4.2.7	Gantry model simulations	67
4.2.8	Beam tracking simulations	68
4.3	Results	70
4.3.1	Solution for the gantry model	70
4.3.2	One-step beam capture and collimation	73
4.3.3	Energy selection system	74
4.3.4	Beam tracking through the whole gantry	77
4.3.5	Dose delivery	79
4.4	Features and limitations of the gantry solution	79
5	Advanced Clinical Gantry Design with Novel Nozzle	83
5.1	Objective	83
5.2	Materials and Methods	83
5.2.1	Clinical requirements from the gantry	83
5.2.2	Two-step beam capturing and collimation	85
5.2.3	Energy selection system	86
5.2.4	Achromatic beam transport	87
5.2.5	Advanced nozzle system – ELPIS	89
5.2.6	Gantry model and beam tracking simulations	93
5.2.7	Clinical applicability of the gantry design via 3D dose verification	93
5.2.8	Integrated intensity modulation scheme	96
5.2.9	LAP beam fluctuations	97
5.3	Results	100
5.3.1	Solution for the gantry model	100
5.3.2	Two-step beam capturing and collimation	100
5.3.3	Energy selection system	102
5.3.4	Achromatic beam delivery via the ELPIS system	103
5.3.5	3D dose verification	111
5.3.6	Integrated intensity modulation scheme	112
5.3.7	LAP beam fluctuations	114
5.4	Realization of the gantry: First tests of a pulsed beamline section	115
5.4.1	Experimental setup	116
5.4.2	Experimental methods and results	118
5.5	Highlight features of the advanced gantry design	120
6	Discussion	123
7	Summary	135
	Bibliography	141

Abbreviations

1D One dimensional

3D Three dimensional

6D Six dimensional

BEAD Broad Energy Assorted depth dose Deposition

BMBF German Federal Ministry of Education and Research

CERR Computational Environment for Radiotherapy Research

CT Computer Tomography

CTV Clinical Target Volume

DRACO DResden laser ACceleration sOurce

DVH Dose-Volume Histogram

ELI Extreme Light Infrastructure

ELIMED MEDical application at ELI-Beamlines

ELPIS broad-Energetic Large acceptance beam delivery via magnetic field shaPing In-
tegrated with short-throw Scanning

ESS Energy Selection System

FFAG Fixed Field Alternating Gradient

FWHM Full Width at Half Maximum

GPT General Particle Tracer

GSI Helmholtzzentrum für Schwerionenforschung, Darmstadt, Germany

HPC High Performance Computing facility at HZDR

HZDR Helmholtz-Zentrum Dresden-Rossendorf, Dresden, Germany

IMPT Intensity Modulated Proton Therapy

IMRT Intensity Modulated Radiation Therapy

ISESS Integrated Shot-to-shot Energy Selection System

LAP Laser-Accelerated Protons

LAP-CERR Laser-Accelerated Proton - Computational Environment for Radiotherapy Research

MC Monte-Carlo

OAR Organs At Risk

onCOOPTics Joint project of the center of innovation competence OncoRay, Dresden and Ultra-Optics, Jena

OncoRay National Center for Radiation Research in Oncology, Dresden, Germany

PT Proton Therapy

PTV Planning Target Volume

RBE Relative Biological Effectiveness

RCF Radiochromic film

RPA Radiation Pressure Acceleration

TNSA Target Normal Sheath Acceleration

TPS Treatment Planning System

UPTD University Proton Therapy Dresden, Germany

USA United States of America

Chapter 1

Introduction

Radiation therapy plays a crucial role in cancer treatment, along with surgery and chemo-therapy. The most commonly available state-of-the-art external beam radiation therapy is delivered using compact linear accelerators, which provide electron and photon beams to deliver radiation doses to tumour volumes. However, due to the inverse depth dose profile, proton beams can provide superior dose conformity and better healthy tissue sparing compared to the state-of-the-art photon or electron beams. Proton therapy (PT) systems utilize electromagnetic accelerators, like synchrotrons or cyclotrons, to accelerate proton beams to the energies relevant for therapy applications, i.e. 70–250 MeV. These beams are then transported via magnetic beamlines to the treatment room and then preferably to a magnetic gantry system which can rotate around the patient so to deliver these beams from different angles. Because of the heavier mass of protons, they require large accelerators with massive and large transport beamlines and gantry systems. Furthermore, heavy support structures are required to rotate these gantries which are then housed in enormous radiation protected buildings. This all adds up to the enormous size, complexity and cost of PT facilities requiring huge capital investments of about 25–100 million Euros (depending on the number of gantries). The number of PT facilities has rapidly increased recently, but still, due to the large size and costs, PT is limited to only about 65 operational centres worldwide.

Extensive efforts are going on to reduce the footprint of PT facilities as well as the costs by exploring both new acceleration schemes and new gantry designs. One of these approaches is to utilize high-power laser systems for proton acceleration. In laser acceleration, a highly focused ultra-intense laser pulse interacts with a thin solid-density target and accelerates an intense ion bunch within an acceleration length in the range of μm . The recent advancements in high-power laser technology have made laser-driven PT an attractive alternative to the conventional PT facilities for their potential for compact facilities. The Laser-accelerated protons (LAP) have been observed in experiments with maximum energies of about 90 MeV via laser power of a few hundred terawatt (TW), i.e. 10^{14} W. These are not yet sufficient for radiation therapy purposes, however, scaling models show higher energies are reachable with increased laser power and/or with new laser target geometries. The development of the next generation petawatt (PW), i.e. 10^{15} W, laser systems promises to reach therapeutic energies for LAP.

The LAP bunches exhibit very different beam properties than beams from conventional accelerators, i.e. they are ultra-intense proton bunches of pulse duration in the order of ns to ps, with up to 10^{12} protons per bunch and with up to 10^4 times better beam emittance. However, LAP bunches have broad energy spread of up to 100%, i.e. the energy spectrum ranges from 0 to maximum cut-off energy. In addition, LAP bunches have large divergence angles (up to about 10°) and can be delivered with only low repetition rate of up to 10 Hz (limited by the high-power laser systems). On the other hand, conventional beams are mono-energetic (i.e. with an energy spread of less than 1%), quasi-continuous and well-collimated (i.e. divergence less than 0.2° at maximum energy). These particular properties make it challenging to adapt LAP beams directly for medical applications with existing PT equipment and dose delivery approaches which were developed for conventional beams. LAP beams require new optimized transport beamline solutions to control and utilize these specific beam parameters for efficient and precise dose delivery to match high clinical standards.

The unique LAP beam properties also render challenges for therapy applications in many related areas of expertise. For the purpose of research and development of a laser-driven PT machine, the onCOOPtics project (Hochintensitätslaser für die Radioonkologie) was launched in 2007 supported by the German Federal Ministry of Education and Research (BMBF). The onCOOPtics project has three main partners; OncoRay and Helmholtz-Zentrum Dresden-Rossendorf (HZDR) in Dresden, Germany and Ultra-optics in Jena, Germany. This cooperation brought together the laser physicists from HZDR and Ultra-optics, and medical physicists, biologists and clinicians from OncoRay for the development of laser-driven PT. The onCOOPtics project has been committed to the integrated multi-disciplinary research and development in all related fields, such as, the development of stable and reliable high-power laser systems and laser-targets, the beam monitoring and dosimetry equipment for intense pulsed broad-energetic beams, the *in vitro* and *in vivo* characterization for radio-biological effects for ultra-high dose rates from LAP beams, the transport systems along with the development of pulsed magnets and beam controls for radiotherapy applications.

Thesis layout: The aim of this work, as a part of the onCOOPtics project, was to study and develop a transport beamline and beam control systems optimized for LAP beams, focused on the expected therapeutic proton energies from the future high-power laser systems. The fundamental requirement from these beamline systems is to deliver a beam (hence dose) via a rotatable gantry system which can be implemented in the clinical environment for patient treatment. This gantry system must be compact and provide efficient solutions to replace conventional big and massive gantry systems. First, in chapter 2 the reader is introduced to the existing PT facilities, along with the conventional approaches to accelerate protons, transport systems and importantly to the state-of-the-art dose delivery systems which are being used for the tumour conformal irradiation schemes. Furthermore, the particle acceleration via high-power laser systems and the unique LAP beam parameters are also introduced. Also, already published concepts for laser-driven PT solutions are presented and discussed. This chapter presents the background, challenges and the foundations for the need and development of a new

gantry system. Also, this provides the basis for the development and comparison of new techniques for laser-driven solutions.

In chapter 3, the basic theory of beam optics and dynamics is introduced, along with the characteristic influence of different magnetic elements on the charged particle beams. This provides the basic tools to manipulate different beam parameters for the development and optimization of beamline, beam controls and dose delivery systems. To make a beamline compact, relatively new air-core pulsed high-field magnets are also introduced in this chapter. These are utilized for the gantry design studies and practical realization. The construction, current status, limits and prospects of individual pulsed magnets are discussed. The design of a new pulsed quadrupole is discussed in detail as it was designed and developed as a part of this thesis work.

In chapter 4, a first approximation beamline design is presented with integrated multiple functionalities to accommodate several requirements, such as capture controls, energy selection and beam transport of broad energy bandwidths. This preliminary design showed the possibility to utilize pulsed beams with varied energy widths via compact pulsed magnet system which can fulfill the basic clinical needs, via a new 1D dose model developed for broad-energetic beams. Furthermore, it provided key parameters for parallel development of pulsed magnets and showed the possibility to control the LAP beam for dose delivery options, and encouraged further research and development as no insurmountable obstacles were found.

Therefore, in chapter 5, the gantry design is taken to an advanced level so that it can compete with the state-of-the-art PT facilities. This advanced gantry is further integrated with a novel active beam shaping and scanning system which is able to deliver advanced 3D dose options to the patient with high precision to meet state-of-the-art clinical standards. The feasibility of LAP beams filtered and transported via this advanced gantry for clinical applications was investigated via treatment planning studies on real cancer patient data. Furthermore, two proof-of-principle experiments are discussed which were performed to establish the use of pulsed magnets for radiotherapy beamline designs.

In the chapter 6, a discussion is presented with the current status of high-power laser systems, the future challenges and prospects of laser-driven PT development. The work presented in this thesis is brought together in the framework of the whole community and other related fields, and the laser-driven PT is discussed generally as its prospects to be a competing technology to the state-of-the-art commercially available conventional PT systems.

Finally, in chapter 7 a brief summary and conclusion of the thesis is presented.

Chapter 2

Background

In this chapter the background, techniques and equipment being utilized in the state-of-the-art proton therapy (PT) systems are introduced. The huge size and costs of PT facilities limit the patient access to the advantages of PT. New approaches are being explored to eliminate these limitations and help widespread adoption of PT. One of these approaches is the acceleration of proton beams via high-power lasers. A brief introduction to the physics behind laser particle acceleration is presented in this chapter. These laser-accelerated protons (LAP) have very different beam properties, compared with the beams attained via conventional electromagnetic circular accelerators in the existing PT machines, which will be referred to as conventional beams and conventional PT systems. Thus, LAP beams require new solutions to transport and manipulate these beams for PT applications. The challenges faced by the laser-driven PT are summarized and discussed. A few authors have presented beamline solutions to adapt LAP beams for PT applications along with new dose delivery options, these are also discussed to present the complete picture. The main purpose of this thesis work is to design a new beamline solution to overcome these challenges and evident drawbacks of the previously published beamline concepts.

2.1 Conventional proton therapy

Soon after the discovery of ionizing radiation in 1895, photons were utilized for medical diagnostic applications and also in the treatment of cancer as early as 1896 (Paganetti, 2012). The early radiation treatments of cancer patients were entirely based on intuition and experimentation. However, the treatment protocols and photon treatment machines have become highly sophisticated since then. For example, the development of sophisticated mega-voltage linear accelerators, LINACs, which are most commonly used for patient treatment. LINACs accelerate electrons and these electrons are then used to generate bremsstrahlung photon beams, and both electron and photon beams are available via these machines. LINACs in these machines are mounted on a compact light-weight rotatable structure, a so-called gantry, with ~ 2 m in diameter and ~ 2 m in length. These machines can provide state-of-the-art dose schemes like intensity modulated radiation therapy (IMRT), and a 3D computerized treatment planning system (TPS) ensures more

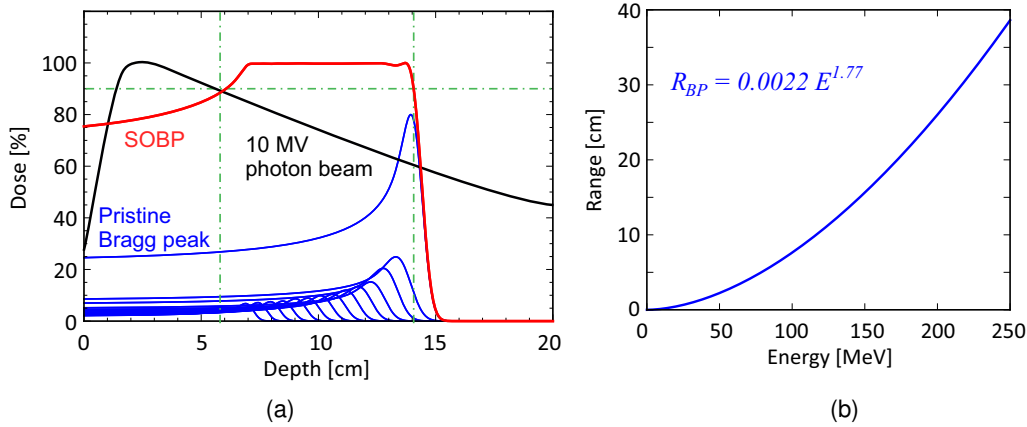


Figure 2.1: (a): Depth dose distribution of a 10 MV photon beam (black line), pristine Bragg peaks (blue lines) from mono-energetic proton beams and a spread out Bragg peak (SOBP) with sharp distal fall-off (red line). The SOBP is generated by superimposing individual weighted pristine Bragg peaks from energy and intensity modulated proton beams. The penetration depth (or range) of a pristine Bragg peak is measured as the depth of the distal plateau behind the peak at 90% dose value, and the SOBP width is given as the distance between the proximal and distal edge marked by 90% of the dose values, shown by the green lines. The state-of-the-art machines can achieve variation in dose of $\pm 2\%$ in the flat-top SOBP region. (b): Range of mono-energetic protons in water as a function of their energy E , as $R_{BP} = \alpha_R E^{p_R}$ (where α_R and p_R are the fit parameters to the experimental data and have values of 0.0022 and 1.77 respectively, for the therapeutic proton energies). Figure (a) is adapted from (Levin et al., 2005) and figure (b) is adapted from (Bortfeld, 1997).

confined doses to the tumour volume and thus, increased tumour control rate. In current cancer care practices, more than 50% of all cancer patients receive radiation therapy during the course of their treatment.

However, photons have a characteristic depth dose profile, i.e. they deposit maximum dose close to the skin (entrance) of the patient and then dose deposition exponentially decreases with increasing depth, see figure 2.1(a). Thus, a high dose is deposited in the normal tissue before and behind a tumour deep in the human body. In 1946, Wilson (Wilson, 1946) presented an alternative idea to use the depth dose advantages of ions, such as protons, in radiation therapy which could provide numerous advantages compared to the photon beam therapy because of their characteristic inverse depth dose profile, i.e. Bragg peak (see figure 2.1(a)). These advantages include superior dose conformity around tumour volumes, better sparing of surrounding healthy tissues and organs at risk (Lomax et al., 1999; Cozzi et al., 2001; Paganetti et al., 2012) and may reduce lifetime attributable risks of radiation treatment (Moteabbed et al., 2014). Additionally, protons have a slightly increased relative biological effectiveness (RBE) which comes from increased density of ionization along a proton track. This increased RBE in the Bragg peak region, although may require a specialized model, results in higher cell damage for the similar doses deposited by photons and provide additional therapeutic benefits (Schardt et al., 2010; Durante and Loeffler, 2010; Paganetti, 2014). It is estimated that 10 – 20% of all radiotherapy patients can benefit from PT (Baron et al., 2004; Mayer et al., 2004).

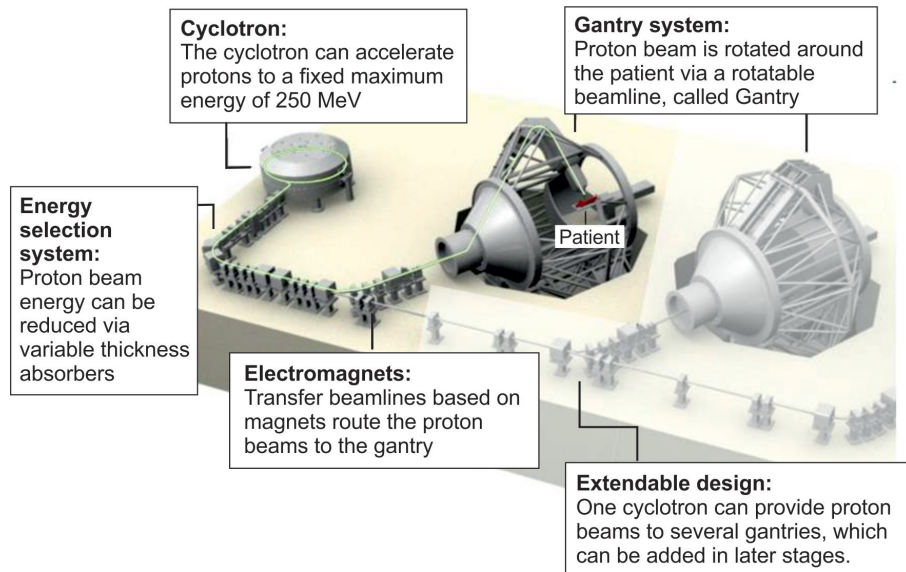


Figure 2.2: Schematic layout of a conventional PT facility. Protons are accelerated via a cyclotron up to a fixed energy of about 250 MeV, which can be degraded per demand through an external energy selection system (ESS). The mono-energetic pencil beam (green line) of the selected energy is then transported, via magnetic transferlines, to the gantry (also see the figure 2.3). This figure is adapted from (Nguyen, 2008).

To irradiate deep seated tumours, the proton beams are required to be accelerated to high energies relevant for therapeutic applications. The penetration depth, or *range*, of a mono-energetic proton beam can be determined by the range-energy relation, see figure 2.1(b) and also for details please see the reference (Bortfeld, 1997). The accelerated proton beams with therapeutic energies of 70 – 250 MeV are needed so to irradiate tumours at about 4 cm to 38 cm (water equivalent) depths, which would easily cover the required clinical ranges in patients. This is the first and critical requirement for clinical proton beams. To achieve this, conventional circular particle accelerators are being utilized, namely synchrotrons and cyclotrons, of those fixed energy cyclotrons are the preferred choice in commercially available PT systems, see figures 2.2 and 2.3 for typical PT facility and gantry layout. More than 85% of all ion beam therapy facilities in the world are based on proton beams only and more than 70% of these proton beams are based on cyclotron type machines (Particle Therapy Co-Operative Group, 2016).

The modern cyclotrons in PT facilities have a height of about 2 m and a diameter of about 5 m (weighing about 200 tons) for normal conducting type and about 3 m (weighing less than 100 tons) for recently introduced superconducting type cyclotrons (Schippers, 2012). The desired output beam parameters are listed in table 2.1. The main characteristic feature is that these cyclotrons deliver pencil beams of fixed maximum energy, with some control over the initial source intensity. The output beam is then degraded by an energy selection system (ESS) downstream (i.e. after) the cyclotron as per requirement, i.e. energy to reach the necessary depths in the patient for tumour irradiation. This degra-

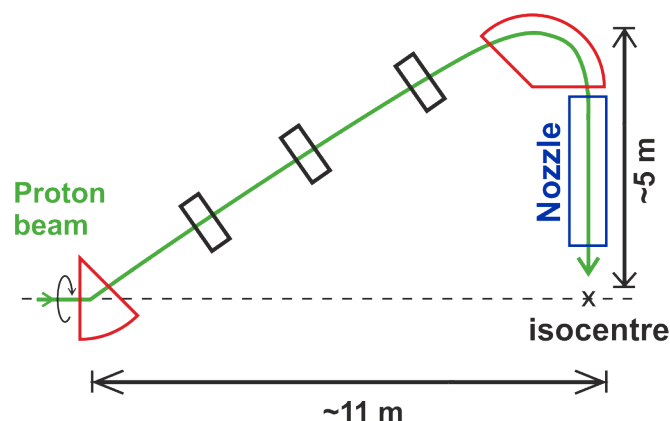


Figure 2.3: Simplified illustration of a PT gantry. The PT gantry can rotate the beam around the isocentre via dipole sector magnets (shown in red) while beam properties are maintained via magnetic quadrupoles (black rectangles). It is indispensable to shape or scan the mono-energetic pencil beam for patient irradiation for 3D tumour conformal dose delivery. This beam shaping and/or scanning is done via beam delivery equipment, commonly known as nozzle, which is installed usually behind the last bend in the commercially available proton gantries.

dation of the beam energy is achieved via passing through physical degraders¹, which do have a small degrading effect on the the beam quality and intensity (Meer and Psoroulas, 2015; Owen et al., 2016). Nevertheless, the degradation of energy is then followed by a dipole (sector) magnet and series of collimators which ensure only the desired energy protons follow the designed beamline path. This constitute the ESS. This mono-energetic proton beam of a selected energy is then transported via magnetic beamlines to the treatment room, preferably, to a gantry, i.e. rotatable beamline system. A state-of-the-art proton gantry is capable of rotating the beam 360° around an isocentre in the treatment room to irradiate the tumour volume from different directions, and the last part of the gantry is usually an equipment called nozzle. The nozzle can further manipulate the beam parameters, such as it can either change the size and shape of the pencil beam or deflect the small sized pencil beams to spots for entire tumour coverage. Nozzels are used for specialized dose delivery schemes, discussed further in the section 2.5. It is important to note here that therapeutic proton beams are rigid to bend and with the conventional iron-core magnets (with maximum magnetic field strength of up to 2 T) the isocentric proton gantries are massive (> 100 tons) and large (up to ~ 10 m in diameter and ~ 11 m in length), e.g. see Smith et al. (Smith et al., 2009). Also, heavy support structures are required to rotate these massive gantries which are housed in enormous radiation protected buildings. All of which adds up to the complexity and cost of PT facilities. As a result a huge capital investment of about 25 – 100 million Euros (depending on the number of gantries) is needed to build one PT facility.

¹materials with high Z (atomic number) are used to scatter the beam, e.g. Lead (Pb), whereas, lower Z materials are more efficient to absorb energy with minimum beam distortion, e.g. beryllium (Be) or graphite, for details please see the reference (Gottschalk, 2012).

2.2 Advances in PT machines

Huge efforts are going on in research and development to increase the cost effectiveness of the PT facilities via already available conventional techniques. This can be done by improving the acceleration and beam parameters and/or by reducing the footprint of the facility and associated infrastructure. Below a brief introduction and discussion is presented for different approaches.

Synchrotrons: As mentioned in the previous section, synchrotrons are currently in operation and were, in fact, used in the first clinical systems. They were popular in the early era of the ion beam therapy development. Synchrotron is a much bigger accelerator compared with cyclotron, with about 6 – 13 m diameter. However, its main advantage is the ability to accelerate wide range of ion species and it still is the main choice for heavy ion therapy systems. Also, synchrotrons can accelerate ions to all desired energies, thus, unlike cyclotron based systems, an external ESS is not required and the beam quality and intensity is independent of the chosen energy. In a synchrotron system, ion species are pre-accelerated to a few MeV via radio frequency quadrupole and/or drift tube linacs and then injected into the main synchrotron accelerator. The synchrotron has one accelerating structure, i.e. radio-frequency cavity, and ions revolve in a ring between several accelerating steps, with revolution frequency of about 1 – 8 MHz. The ring is a magnetic beamline which keeps the accelerating ions in a closed loop. The magnets require ramping after every accelerating step. The acceleration phase usually takes about 0.5 s, and the beam is extracted via slow extraction scheme which is necessary for accurate dose application via beam scanning techniques. This could take between 0.5 to 5 s depending upon the tumour size and amount of different energies required for tomour coverage (Schippers, 2012).

The slower acceleration and extraction process, along with its size and complicated pre-accelerated beam loading, reloading and dumping of the excessive particles make it a less robust and highly complex machine. The argument to use a synchrotron though is that a single facility can provide not only protons but also heavier ions, making it more cost effective with multiple gantry systems. But, due to the larger size and complexity, they lost their popularity for proton only facilities. However, synchrotrons are making a comeback with recent developments in scale reduction (for small ring synchrotron of about 5 m diameter) and proposed rapid-cycling synchrotrons with adjustable proton intensities by single turn extraction scheme, along with the idea to ramp down the machine to extract lower energy protons to implement spread out Bragg peak (SOBP), without dumping the beam and reloading it, please see for details references (Schippers, 2012). These modern synchrotrons, for proton beams only, would eliminate the need of external passive ESS which could ease the radiation protection constraints for the building and also they can efficiently provide better beam quality. However, the heavy transfer beamlines and associated gantries would remain the same. The cyclotron PT systems have been commercially established and are still cheaper and robust in operation, which makes them hard to compete with.

FFAG systems: In the fixed field alternating gradient (FFAG) accelerator concept, an

Table 2.1: Typical specifications of a clinical PT system.

Parameters	Specifications
Beam current	in the order of nA
Beam frequency	in the order of 100 MHz
Peak dose rate	about 10^3 Gy/s
Average dose rate	1 – 30 Gy/min
Energy width	0.1 – 1%
Divergence	0.1° – 2°
Dose accuracy	± 2 – 5%
Range of penetration	2 – 30 cm (in tissue)
Maximum field size	25×25 cm ²
Precision in range setting	0.1 cm
Sharpness of distal dose fall-off	0.1 cm

Note: The beam frequency is arising from the initial proton source and acceleration mechanism inside the cyclotron. Beam can be considered continuous for transport and other modulations downstream. The range settings are achieved by energy degradation via ESS (please note here that this range setting specification is only the ability of ESS to resolve and select different energies after energy degradation, and not from the statistical processes, like energy or range straggling). The dose rate values changes for the dose delivery schemes being applied, i.e. passive scattering and active pencil beam scanning. The values are taken from the references (Eickhoff et al., 2011; Schippers, 2012; Karsch et al., 2017).

azimuthal varying field (isochronous) cyclotron is split into separate sector magnets of alternating sign with radio-frequency electric field (Schippers, 2012). A non-scaling FFAG has very strong focusing and defocusing optics and can accelerate particles fast. This makes it compact and unlike synchrotrons, does not require ramping of the magnets to keep the beam inside. The complex focusing and de-focusing optics are the key and keep the system acceptance large. These accelerators are being studied for proton and heavy ion therapy applications for both normal and superconducting magnet structures (Misu et al., 2004; Antoine et al., 2009; Peach et al., 2013). Furthermore, a superconducting FFAG gantry design has been proposed for proton and heavy ion therapy based on FFAG beam optics (Trbojevic et al., 2007). The beam optics with alternative gradients and high energy radio-frequency generators are complicated to design (Schippers, 2012). These systems are under investigation. They may compete with synchrotrons for heavy ion therapy, but robustness of cyclotron based PT systems exceeds here too.

Linear particle accelerators: Linear accelerators have also been explored for the use in ion beam therapy (Garonna et al., 2010; Schippers, 2012). In this scheme, a relatively compact superconducting (radio-pharmaceutical) cyclotron with up to 60 MeV maximum proton energies (or 120 MeV/u for carbon C^{6+} ions) is used as an injector to a high frequency linear accelerator which boost the ion energy to a desired value, with a maximum limit of 230 MeV for protons (and/or 400 MeV/u for C^{6+} ions). The length of the linear ac-

celerator in case of a proton only machine would be around 13.5 m and in case of dual ion option (protons and C^{6+} ions) the length would be around 25 m. The main advantage of this approach is that it combines the best output parameters available from cyclotron and synchrotron based solutions, i.e. the beam is always present (unlike synchrotron), the energy can be adjusted electronically (unlike cyclotron) and the energy shifts can be provided in about 1 ms (which is 50 times faster than cyclotron and about 1000 times faster than synchrotron). They could be technically advanced and provide better beam without external ESS but the accelerating system alone would require far bigger hospital buildings. On top, the magnetic transfer beamlines and associated gantries would be the same. This makes cyclotron based PT systems commercially still more appealing.

Gantry mounted cyclotrons: Recently, a compact PT system has become operational, which is produced by Mevion Medical Systems (Mevion Medical Systems, 2017; Zhao et al., 2016). This system consists of a compact superconducting synchrocyclotron² which is directly mounted on a gantry. The superconducting synchrocyclotron has a diameter of about 2 m and weighs about 22 tons. The gantry has a diameter of 8.5 m, length of ~ 10 m and requires ~ 11 m width for rotation. It can rotate in a limited range from -5° to 185° . The proton beam is accelerated to 250 MeV energy and has no dipole based ESS. However, it has a series of absorbing materials to reduce the beam energy to the required energies for tumour irradiation, and uses passive collimation to limit the size of the beam. The degradation of energy widens the beam spectrum and this needed to be accounted for each gantry rotation and all treatment options (i.e. field sizes and penetration depths). The company has recently designed and installed an active spot scanning option (called HyperScan) in a clinical facility, named MedStar Georgetown University Hospital in USA. HyperScan utilizes a new adaptive aperture multileaf collimator system, and it is planned to treat patients with this technology in the middle of 2018 (Mevion Medical Systems, 2018). This one-room PT system is the most compact commercially available system. However, still requires a considerable space and require one superconducting accelerator for each gantry option.

2.3 Alternative approaches for PT machines

All of the above mentioned solutions focused on improving the acceleration systems and beam parameters via conventional technologies. The associated heavy magnetic transferlines and the gantries are still massive and huge. There are two new ion beam acceleration schemes being explored for medical applications, which may provide much more compact and lighter solutions in the future. A brief introduction to these new concepts is presented below:

Dielectric wall accelerators: An exciting concept of dielectric wall induction linear accelerator has been presented for PT applications and is under development at Lawrence Livermore National Laboratory, USA (Caporaso et al., 2007; Chen et al., 2009). In this

²A synchrocyclotron is a cyclotron in which the frequency of the driving radio-frequency electric field is varied to compensate for relativistic effects of proton velocity, in contrast to the classical cyclotron, where the frequency is held constant.

concept, protons can be accelerated in multiple stages, by inducing a travelling electromagnetic wave in a dielectric tube. High gradient insulators are stacked in-between which could provide a factor 5 more in the surface breakdown field than vacuum gaps (which is 10 – 20 MV/m), and can provide a 100 MV/m average accelerating field (Caporaso et al., 2010). Theoretically, this would allow to reach 200 MeV proton energy in about 2 m accelerating length. This can be mounted directly on a gantry, i.e. must be mounted in length wise, also one must consider the distance required after a scanning system to cover a clinically relevant irradiation field sizes. This could make this a compact and light weight design. However, this technology has critical hurdles to overcome, mainly insulation issues at breakdown voltages between induction cells. Only a few MeV of proton energies have been shown. There has been no advances made in nearly a decade in this technology and it is waiting for a breakthrough.

Laser-driven accelerators: Another promising and exciting field is the particle acceleration by using high power laser pulses. If the electromagnetic field of the laser pulse is intense enough then it can ionize a solid target and can accelerate particles on μm scale. The first experiments in 2000 showed the prospects of acceleration of protons and ions from thin solid targets by high-power intense laser pulses (Hatchett et al., 2000; Snavely et al., 2000). The progress in the development of high-power laser systems, in the range of few hundreds of terawatt (TW) to even petawatt (PW) power, has progressed the field of laser-driven proton acceleration, and has triggered research and development in a number of potential applications, naming a few here: laser physics (Daido et al., 2012; Borghesi, 2014) itself, fast ignition fusion (Roth et al., 2001; Bychenkov et al., 2001; Dunne, 2006), injectors (Krushelnick et al., 2000; Busold et al., 2015), isotope production and positron emission tomography (Ledingham et al., 2004; Clarke et al., 2006a), neutron sources (Umstadter, 2000; Ledingham et al., 2003), radiation biology (Clarke et al., 2006b; Kraft et al., 2010; Yogo et al., 2011; Richter et al., 2011; Doria et al., 2012; Brückner et al., 2014) and radiation therapy (Bulanov et al., 2002; Malka et al., 2004; Ledingham and Galster, 2010; Limpert et al., 2011; Daido et al., 2012; Schreiber et al., 2016).

The laser-driven technology has attracted interest in the medical and laser communities for its potential to facilitate a more compact and lower cost PT facility. It is estimated that a dedicated high power laser system for radiation therapy application can be provided for less than 10 million Euros (Limpert et al., 2011). However, size of the associated gantries would still be problematic for overall size reduction. The aim of this thesis is to explore the possibility to utilize LAP beams via new gantry system for PT applications, thus, a focused discussion about laser-driven acceleration mechanisms, and status and prospects of LAP beams is presented in the following section.

2.4 Laser-driven proton acceleration

The physical processes of laser proton, or ion, acceleration are described in this section, along with some important parameters of laser systems and laser-accelerated beams. The two acceleration regimes, namely target normal sheath acceleration (TNSA) and radiation pressure acceleration (RPA), are also described as their characteristic beam

features will be utilized later in the beamline designs (in chapters 4 and 5). Excellent descriptions of the various physical processes contributing in laser accelerations, and providing basis for different acceleration regimes and techniques, have been presented by different authors, such as Borghesi (Borghesi, 2014), Daido et al. (Daido et al., 2012), and in the PhD theses by Zeil (Zeil, 2013), Jung (Jung, 2012) and Henig (Henig, 2010). The main descriptions presented below have been adapted from the above mentioned literature.

Laser induced plasma: When an intense laser pulse impinges on a target (from here on called laser-target), it ionizes the material. The physics of ion acceleration emerges from the behavior of the ionized material, i.e. plasma, under laser irradiation. The basic understanding can be developed by considering a hydrogen atom with the Bohr radius (a_B), which is given as:

$$a_B = \frac{4\pi\epsilon_0\hbar^2}{m_e e^2} \simeq 5.3 \times 10^{-11} \text{ m}, \quad (2.1)$$

where \hbar is reduced Planck's constant, ϵ_0 is permittivity of free space and m_e and e are the electron mass and charge, respectively. Accordingly, the electric field strength in the Coulomb potential ϵ_a between positively charged nucleus and negatively charged electron is given by:

$$\epsilon_a = \frac{e}{4\pi\epsilon_0 a_B^2} \simeq 5.1 \times 10^9 \text{ Vm}^{-1}. \quad (2.2)$$

The corresponding intensity at which the laser field equals the binding strength of the electron to the nucleus is referred to as the atomic intensity I_a and is calculated to be:

$$I_a = \frac{\epsilon_0 c \epsilon_a^2}{2} \simeq 3.5 \times 10^{16} \text{ Wcm}^{-2}, \quad (2.3)$$

where c is the speed of light. Laser fields with intensities of $I_L = 10^{18} \text{ Wcm}^{-2}$ would be sufficient to ionize a material and generate a plasma. Moreover, processes such as multi-photon ionization, tunneling & barrier suppression ionization and collisional ionization, would play parts in plasma generation. The plasma is generated instantly either by the (strong enough) pre-pulse or the rising part of the main pulse of the laser.

Electron dynamics in the plasma: The electrons from the ionized laser-target would now experience the intense laser pulse. The laser pulse can be characterized by wavelength λ_L , angular frequency ω_L , the electric field component as $\epsilon_L = \epsilon_{L,0} \cos \Theta$ and magnetic field component as $B_L = B_{L,0} \cos \Theta$, where $\Theta = \omega_L t - k_L z$, t is time, $k_L = 2\pi/\lambda_L$ and propagation is in z -direction. The motion of an electron in such a laser light field can be described by the Lorentz equation:

$$\mathbf{F} = \frac{d\mathbf{p}}{dt} = -e(\epsilon_L + \mathbf{v} \times \mathbf{B}_L), \quad (2.4)$$

where \mathbf{F} is the Lorentz force, \mathbf{p} ($\mathbf{p} = \gamma_r m_e \mathbf{v}$) is the momentum and $\gamma_r = (1 - v^2/c^2)^{1/2}$ is the Lorentz factor and v is the electron velocity. The maximum kinetic energy of the electrons can be given as:

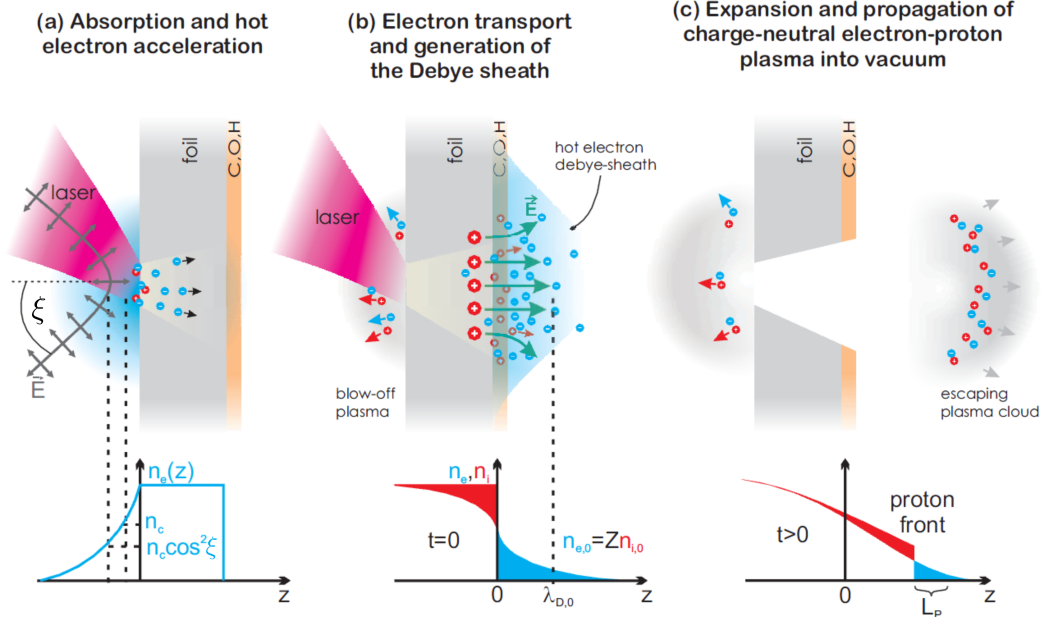


Figure 2.4: Illustration of the target normal sheath acceleration (TNSA) process from (a) to (c). The laser pulse impinges with incidence angle ξ , is reflected at the critical density (n_c) surface at the target front side. The extreme field strength of the laser generates a plasma, and the laser pulse is absorbed by the plasma and hot electrons are accelerated into the target. Those electrons travel through the foil and exit at the rear side, forming an electron cloud with an extension of about a Debye length $\lambda_{D,0}$. As a result a large quasi-static electric field is set up (\sim TV/m) that leads to ionization of light ions of the contaminant layer on the rear side and acceleration of those ions to MeV energy in the quasi-neutral plasma cloud escaping from the target. In the bottom part of the figure the evolution of the electron and ion density (n_e, n_i) with time is shown. At $t > 0$, L_p denotes the plasma scale length and is given by $L_p = \lambda_{D,0}(n_{e,0}/n_e)^{1/2}$. The image and description is adapted from Zeil (Zeil, 2013).

$$\hat{E}_{\text{kin}} = \frac{a_0^2}{2} m_e c^2, \quad (2.5)$$

where a_0 is the dimensionless electric field strength originating from the laser light field. In order to express it in a more useful quantity:

$$a_0 = \left[\frac{I_L \lambda_L^2}{1.37 \times 10^{18} \text{ Wcm}^{-2} \mu\text{m}^2} \right]^{1/2}, \quad (2.6)$$

where $I_L = \frac{1}{2} \epsilon_0 c \epsilon_{L,0}^2$ is the laser intensity. This means that for an optical wavelength $\lambda_L \approx 1 \mu\text{m}$ and light intensities above 10^{18} Wcm^{-2} (called relativistic intensities), the electron would be accelerated and receives kinetic energy which exceeds its rest mass energy and becomes relativistic while the electron velocity approaches c . It can be seen that the direct acceleration of ions to velocities approaching the speed of light $v_i \leq c$ implies:

$$\frac{Z m_e}{M_i} a_0 \approx 1, \quad (2.7)$$

where M_i denotes the ion mass and Z the ion charge number and thus would require a_0

of about 2000, or intensities in the region of $I_L > 10^{24} \text{ Wcm}^{-2} \mu\text{m}^2$, respectively. Thus, with the currently available laser intensities of I_L in the range of $10^{20} - 10^{22} \text{ Wcm}^{-2}$ laser-driven ion acceleration is only feasible via an indirect process. Due to the high inert masses of the ions, they can only be accelerated when the electrons acquire a net drift velocity in the direction of propagation of the laser pulse, when laser amplitudes are with $a_0 \gg 1$, generating a strong quasi-static charge separation field for the ions. In a simple model a plasma is characterized by an electron population of density n_e , which when pushed by the laser pulse, is pulled back by the Coulomb force arising from the quasi immobile positive ions and thus the electrons oscillate with the plasma frequency (ω_p) given as:

$$\omega_p = \sqrt{\frac{n_e e^2}{\epsilon_0 \gamma_r m_e}}, \quad (2.8)$$

Together with the frequency ω_L of the laser (and for simplicity neglecting any collisional effects), the refractive index of the plasma is given as:

$$n(\omega_L) = \sqrt{1 - \frac{\omega_p^2}{\omega_L^2}} = \sqrt{1 - \frac{n_e}{n_c}}, \quad (2.9)$$

where n_c is the critical density which in practical units (for $\gamma_r = 1$) is given as:

$$n_c = \frac{\epsilon_0 \gamma_r m_e \omega_L^2}{e^2} = 1.1 \times 10^{21} (1 \mu\text{m}/\lambda)^2 \text{1/cm}^3. \quad (2.10)$$

Electron heating: In plane waves, electrons starting from rest return to that state when the external field is turned off. No net gain in energy takes place. However, a real laser pulse is finite in space and time, and has a fast varying intensity envelope through tight focusing and short pulse duration, which is necessary for achieving high intensities in the experiments. This generates a strong radial intensity gradient. The laser field amplitude, and therefore a_0 , depends on the spatial coordinate and as soon as an electron reaches a point with less field strength during a laser cycle, it experiences less restoring force and cannot return to its initial position. The electron is therefore pushed to regions of less intensity or, in other words, of less electric field pressure. This exerts a non-linear force, so-called pondermotive force, on the electrons, resulting in a net energy gain. The pondermotive force (F_{pond}) is given as:

$$F_{\text{pond}} = -\frac{e^2}{4m_e \omega_L^2} \nabla \epsilon_L^2. \quad (2.11)$$

Furthermore, electrons gain energy via multiple mechanisms, including resonance absorption when laser interacts with the target at an angle ξ and excite electron oscillations. Also, by so-called $j \times B$ heating (where, j is the electron current density). In this type of heating large a_0 laser amplitudes make electrons gain energy via the $v \times B$ term of the Lorentz force. This also means electrons accelerating in the direction of laser propagation, loses focus due to the strong $v \times B$ part of the force. Thus, electrons accelerate into the laser-target and have an average kinetic energy of $k_B T_h$ (where, k_B is the Boltzmann constant and T_h represents hot electron temperature) which can be described mathemat-

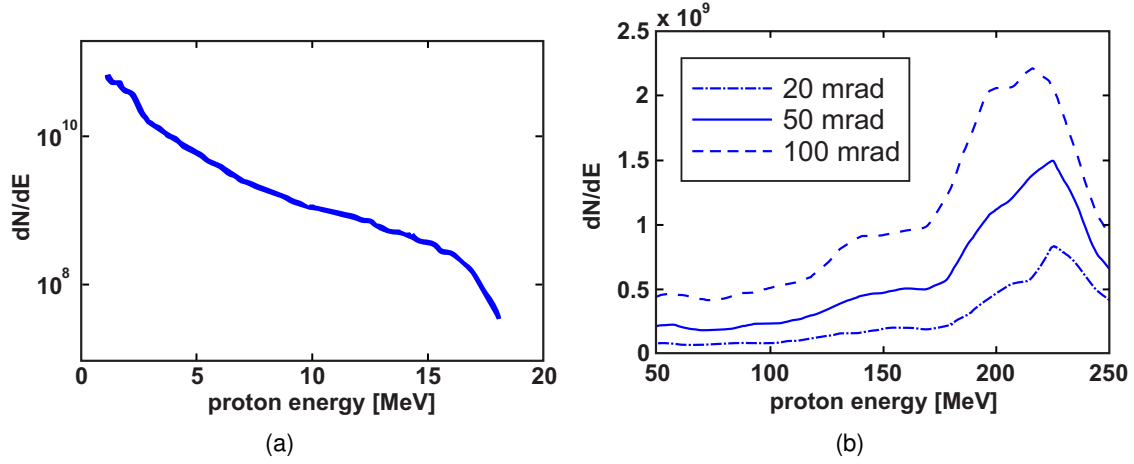


Figure 2.5: (a): LAP exponential energy spectrum (with a cut-off maximum energy of about 18 MeV) obtained via TNSA scheme, with the ultra-short pulse (30 fs), 150 TW laser system DRACO (DResden laser ACceleration sOurce) at HZDR, with laser peak intensities of $I_L = 10^{21} \text{ Wcm}^{-2}$ and 3 J of energy. This image is adapted from Kraft et al. (Kraft et al., 2010). (b): Predicted LAP energy spectrum obtained via 2D particle-in-cell simulations with 10 PW (620 J), 66 fs laser pulse with peak $I_L = 3 \times 10^{21} \text{ Wcm}^{-2}$. The different spectra show protons detected in different opening angles. This image is adapted from Hofmann et al. (Hofmann et al., 2011).

ically as:

$$k_B T_h = m_e c^2 \left(\sqrt{1 + \frac{a_0^2}{2}} - 1 \right). \quad (2.12)$$

2.4.1 Target normal sheath acceleration

When $\omega_p > \omega_L$, or $n_e > n_c$, the plasma is dense or overcritical which is the prevalent scenario of the laser matter interaction in the target normal sheath acceleration (TNSA) regime, see figure 2.4. The plasma becomes opaque for the laser. Within the laser-targets (in the order of μm thickness) the heated, or so-called hot, electrons travel *normally* (i.e. perpendicularly) inside the laser-target and reach the rear side of the target, where they form a sheath, hence the name *target normal sheath acceleration*. This electron cloud generates a strong charge separation field E_s . The extent of this field is given by the Debye length λ_D given as:

$$\lambda_D = \sqrt{\frac{\epsilon_0 k_B T_h}{e^2 n_e}}. \quad (2.13)$$

The charge separation field hence scales as:

$$E_s \approx k_B T_h / e \lambda_D. \quad (2.14)$$

E_s typically has a length of a few μm and gives rise to a quasi-static accelerating field of the order of TV/m. Due to the highest mass-to-charge ratio (for the positive ions present to be accelerated by E_s), the protons are preferentially accelerated. Along with the ex-

planation from equation 2.7, this is the main reason for laser-driven protons being the primary focus for the therapy applications, and not heavier ions like carbon. These protons come either from the contamination layers of hydro-carbons on the rear side of the laser-target (Hatchett et al., 2000; Snavely et al., 2000) or pure solid (frozen) hydrogen targets can be used (Obst et al., 2017). The energy spectra of these accelerated protons can be generally characterized by an exponentially decaying function with some maximum cut-off energy, see figure 2.5(a). Moreover, due to the transverse extent of E_s these protons have large divergences as well.

2.4.2 Radiation pressure acceleration

Another acceleration mechanism, which has drawn a lot of attention recently, is the radiation pressure acceleration (RPA) mechanism (Esirkepov et al., 2004; Macchi et al., 2009; Henig et al., 2009; Macchi et al., 2010). RPA could achieve up to 40 times increased laser to particle energy conversion efficiency than the robust TNSA (Henig et al., 2009) and, more importantly, provide improved beam parameters, like less initial divergence and energy spread. RPA can inherently accelerate the whole target as a single block of plasma by the laser light pressure. For laser intensities of the order of 10^{23} Wcm^{-2} protons can gain relativistic energies immediately even with linearly polarized light (Esirkepov et al., 2004). However, for laser intensities of about 10^{20} Wcm^{-2} the use of circular polarized light can also provide the similar acceleration regime (Klimo et al., 2008; Macchi et al., 2009). At first, the laser pulse rapidly ionizes the front surface of the target and compresses and pushes electrons deeper into the overdense target until the radiation pressure is balanced by the increasing charge separation field. The electrons remain cold, i.e. $j \times B$ heating is nearly absent because of the absence of an oscillatory component in the longitudinal electron motion (Henig, 2010), and the electrons are pushed in a layer as snow-plow. This results in an electron depletion area at the plasma surface, which is followed by the electron compression area. Due to the lack of hot electrons, and the coherent acceleration of the layer by the laser, the E_s can be very sharp and the accelerated protons can theoretically have mono-energetic spectra. The critical points for RPA are high contrast laser pulses, i.e. a sharp rise in the laser intensity (ideally with no pre-pulse) and laser-target thickness of the order of nm. The LAP spectra (peak proton energies) then can be tuned by the laser parameters, like I_L which can be varied by focusing, and thus can change the maximum LAP energies (Hofmann et al., 2011). RPA has not yet been confirmed experimentally but many investigators have been focused on the experimental verification of RPA. Figure 2.5(b) shows a RPA like spectrum for proton energies generated via simulations (Hofmann et al., 2011), and it can be seen that even though a mono-energetic spectrum could be predicted theoretically, however, realistic simulations show a peak energy region with long low energy tail.

2.4.3 LAP beam status and properties

In the laser-driven acceleration, not just protons are accelerated, but the accelerated bunch contains initially accelerated electrons and also ions, which were present either in

Table 2.2: Currently available LAP beam properties.

Parameters	Beam properties
Protons per bunch	in the order of 10^{11-12}
Beam frequency	maximum 10 Hz
Beam current	in the order of nA
Peak dose rate	about 10^{11} Gy/s
Average dose rate	same as cyclotron beams
Energy width	100% (i.e. 0 to cut-off energy)
Divergence	$5^\circ - 10^\circ$ (half-angle)

Note: The intense LAP bunches over time (per second) deliver beam currents similar to beams from cyclotrons, and hence similar average dose rates. The beam frequency for LAP beams is associated with the repetition rate of the laser system. The energy width follows a certain distribution, and divergences depend upon the laser-acceleration scheme and proton energies, as discussed in section 2.4.

the laser-target itself or from the contamination layer outside, see figure 2.4. The laser-target is destroyed after the LAP bunch is generated and it leaves debris around. The laser-target needs to be replaced for the next LAP bunch, which can be done via moving laser-targets on tape or foil, or via a spaghetti like laser-target production, such as frozen strip of hydrogen pressed out from a nozzle (Obst et al., 2017). Nevertheless, a particle selection system becomes indispensable to separate desired protons to characterize them and to utilize them for further applications.

Recently, protons with maximum cut-off energies of up to 90 MeV with a TNSA like exponential energy spectra have been experimentally observed by 10^{20} Wcm^{-2} intensity laser pulses from TW class laser-driven accelerators (Wagner et al., 2016). Although, the generation and reproducibility of LAP beams for full therapeutic energy range, are still to be established, the scaling models predict higher energies are reachable with increased laser power (Kluge et al., 2011; Zeil, 2013) and/or with new laser target geometries (Kluge et al., 2010; Zeil et al., 2014; Garcia et al., 2014). The development of the next generation PW laser systems (Danson et al., 2015; Schreiber et al., 2016) presents the prospects of laser-driven PT in near future, see figure 2.6. Several groups in the world are focused on developing these lasers (Siebold, 2013; Cirrone et al., 2013; Yong et al., 2014; Danson et al., 2015; Kiriya et al., 2016) and explore the possibilities of laser-driven PT applications.

Nevertheless, LAP bunches exhibit very different beam properties than beams from conventional accelerators, i.e. they are ultra-intense proton bunches of ps pulse duration, with up to 10^{12} protons per bunch (Daido et al., 2012; Wagner et al., 2016) and with up to 10^4 times better beam emittances (Cowan et al., 2004), however, have broad energy spread (up to 100%, i.e. energy spectrum ranges from 0 to maximum cut-off energy) and large divergence angles ($\sim 5 - 10^\circ$), and can be delivered with only low repetition rate of up to 10 Hz (this limit comes from the high-power laser systems), also see table 2.2. On

the other hand, conventional beams (e.g. from clinical cyclotrons) are quasi-continuous, well-collimated (divergence $< 0.2^\circ$ at maximum energy) mono-energetic pencil beams ($\Delta E/E_0$ of $< 1\%$), also see table 2.1. These particular properties make it challenging to adapt LAP beams directly for medical applications with existing PT equipment and dose delivery approaches which were developed over time for conventional beams. Therefore, new optimized transport beamline solutions are needed to control and utilize LAP beams for efficient and precise dose delivery to match clinical standards.

2.5 Dose delivery systems

2.5.1 Conventional dose delivery systems

There are two basic techniques for dose delivery being used in conventional systems for clinical proton beam applications, namely passive scattering and active beam scanning (for further details please see references (Goitein et al., 2002; Schardt et al., 2010; Slopeema, 2012; Schippers, 2012)). The basic aim is to deposit a homogeneous dose to the tumour either simultaneously to the whole volume or in spots stacked in transverse slices and layers in depth. The proton beam enters a specialized equipment at the end of the gantry called nozzle (see figure 2.3), which can either shape the beam by passive scattering or scan the beam via dipole magnets.

In the scattering approach, the mono-energetic pencil proton beam is broadened laterally usually by a double scattering system³, see figure 2.7. Scatterers are made of high-Z materials which provide high scattering angle for the lowest energy loss per unit length traversed and a binary set of scatterers (with increasing thickness) can be used to maintain scattering power for different proton energies. The depth dose of a mono-energetic proton beam (i.e. pristine Bragg peak, see figure 2.1) is too sharp to cover the full extend of a tumour. The energy of the beam is modulated by traversing through a range modulator and shifters inside the nozzle, to obtain homogeneous dose over the axial (depth) extent of the tumour. This beam then reaches the treatment site after the patient specific hardware downstream, such as collimators and range compensator, to match the individual 3D tumour volume. This scheme is simple to implement and verify, as well as more robust in treating moving targets, however, it limits the physical benefits of proton therapy because of the high doses to the healthy tissue volume in the proximal region (see figure 2.7). Also, it is only about 10 – 15% efficient⁴ due to the unavoidable proton loss in scatterers, range modulator, shifters, compensator and collimators, which result in the generation of secondary radiation close to the patient.

The specific disadvantage of high proximal doses via passive beam shaping can be avoided by utilizing modern beam scanning option. In a scanning system, a mono-

³A flat single scattering foil can also be used which could provide sharper lateral penumbra and limit proton loss, however, only for small field sizes. A double scattering system is more complex and may have different configurations, such as first flat scatterer with contoured, dual ring or occluding ring as second scatterers, however, can provide large irradiation field sizes.

⁴This number relates to the losses inside the nozzle only, i.e. behind the last turn in the gantry and before the isocentre.

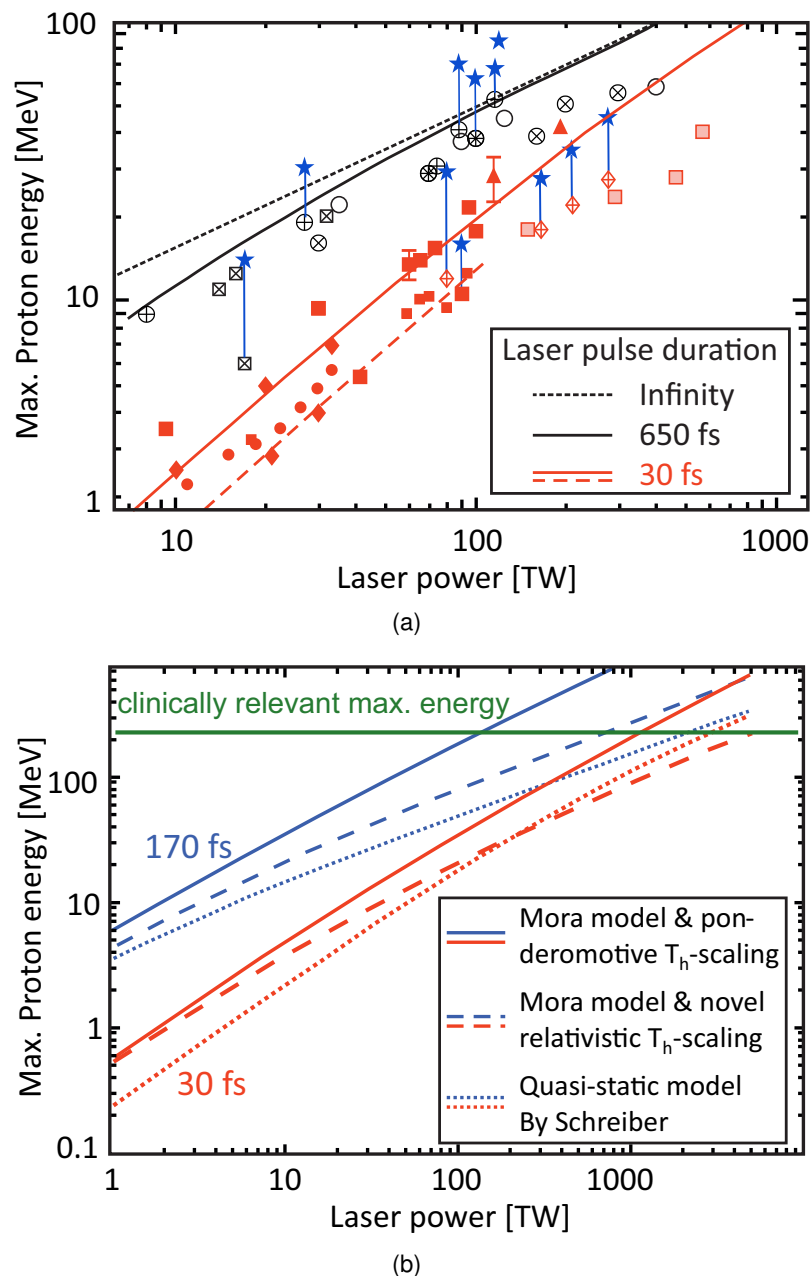


Figure 2.6: (a): Scaling fits to the achieved maximum cut-off proton energies in dependence of laser power and laser pulse duration, based on the experimental data. Laser systems with short laser pulse duration are designed for a repetition rate of about 10 Hz (red points) and long pulse laser systems for only about one pulse per hour (black points). Blue points connected by a line to another point are taken from the same laser system with a structured target instead of a foil. Additionally, the influence of thickness for foils used as laser target is shown by the red solid ($2\ \mu\text{m}$) and dashed ($5\ \mu\text{m}$) line. This image is adapted from Schramm et al. (Schramm et al., 2017), also please see the reference for further details about the symbols used in the figure. (b): Different theoretical scaling models for different laser parameters, which predict the maximum achievable proton energies as a function of laser power. The green line shows that the clinically relevant maximum energy could be reachable with petawatt class lasers. This image is courtesy of Zeil (Zeil, 2013), for *Mora model* please see references (Mora, 2003; Kluge et al., 2011) and for *Schreiber model* see reference (Schreiber et al., 2006).

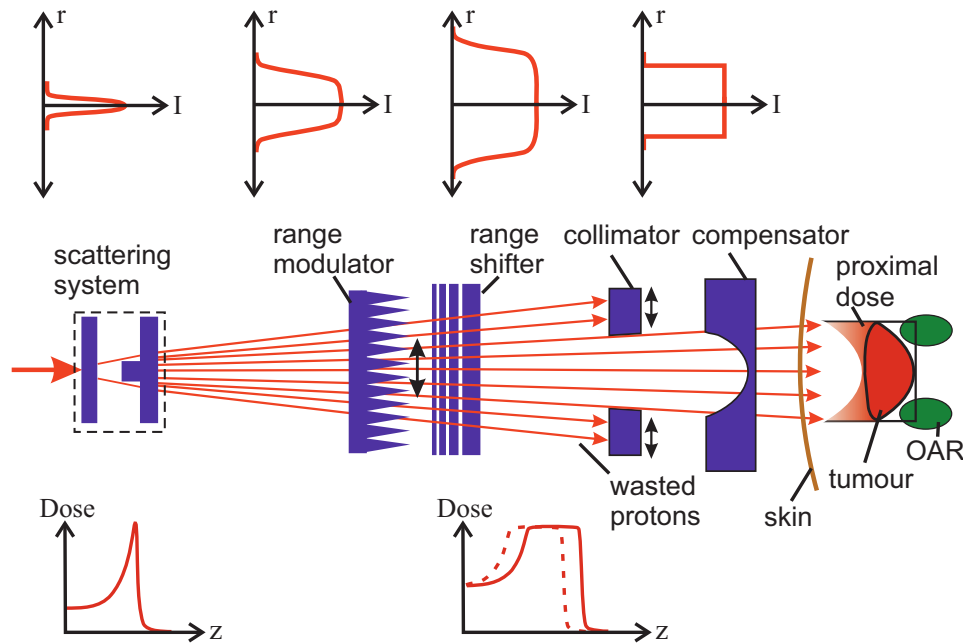


Figure 2.7: Sketch of a beam shaping system via passive scattering. The incoming mono-energetic pencil-like beam (red arrow) is broadened laterally by a scattering system and adapted to the target volume by various passive beam shaping devices (middle row of the figure). The incoming beam is usually with higher energy than required to reach the maximum range (distal end) of the tumour, and range modulator and shifters are used to broaden the beam in energy and deliver SOBP. Adaption of the dose field to the distal contour of the target volume is achieved by a compensator, to avoid doses to organs at risk (OAR) behind the tumour, but results in unwanted high normal-tissue dose in the proximal part. The lateral spread is restricted by the use of collimators, which are defined by the largest lateral extent of the tumour. The schematic evolution of the beam intensity profile (I) as a function of beam radius (r) is shown on top, as it passes through different nozzle components. Whereas at the bottom, the evolution of a mono-energetic pristine Bragg peak into SOBP, via modulation and shifters, is illustrated. Figure is taken from Schardt et al. (Schardt et al., 2010).

energetic pencil-like beam is scanned laterally via scanning magnets over the full transverse extent of the tumour volume. Also, in depth by varying the beam energy from the accelerator (e.g. synchrotron) or selected by the ESS or by range shifters inside the nozzle (in case of a cyclotron), see figure 2.8. Pencil beam scanning results in higher tumour conformity, however, with the beam spot-size of about 0.5 – 2 cm at full width at half maximum (FWHM), thousands of spots are needed to be irradiated to cover typical tumour volumes. Pencil beam scanning is more complex⁵ and it is more challenging to incorporate tumour motion.

These two schemes have been developed for continuous mono-energetic pencil-like beams from conventional accelerators. Both schemes have specific advantages over the other and, in conventional nozzles, it is not possible to use both beam scanning and scattering options at the same time, i.e. one cannot modulate beam size and position si-

⁵Pencil beam scanning would require a complete characterization of many variables and factors, such as time structure of the beam and may be motion of the organ, scan patterns, beam spot-size at every energy and transverse dose modulation, repainting options etc. Please see the reference (Flanz, 2012) for further description.

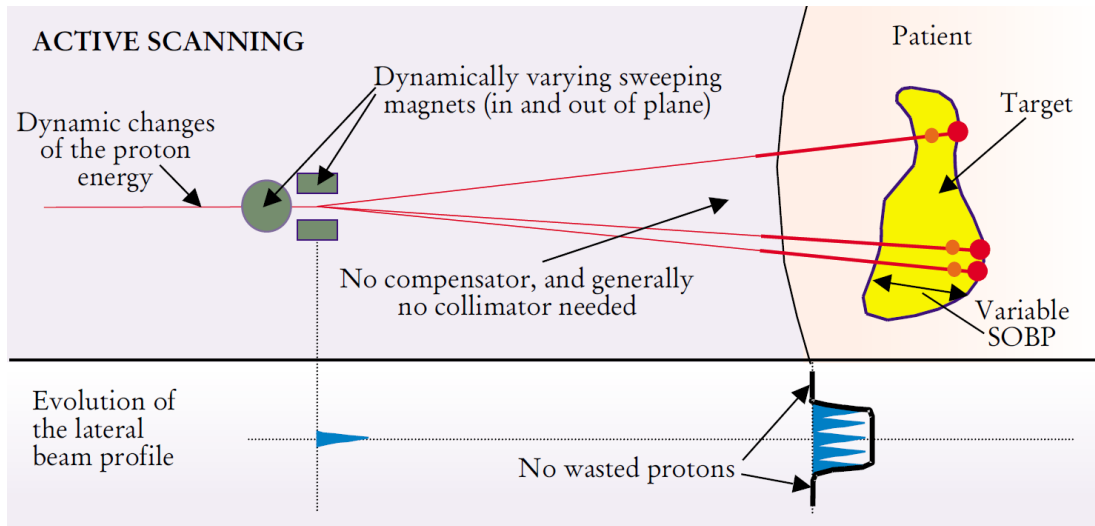


Figure 2.8: Sketch of the basic principles of an active scanning system. The proton mono-energetic pencil-like beam that emerges from the accelerator is applied directly to the patient. Lateral spreading is achieved by deflecting the beam with magnets. Adjusting the depth of the Bragg peak is done either by changing the energy of the beam or by dynamically adding material in front of the patient with a range shifter (inside the nozzle). The scan may be performed in discrete steps (spot scanning) or continuously (raster scanning). By changing the scanning speed or beam intensity, the dose delivered at each point in the target is controlled. The sketch and description is adapted from Goitein et al. (Goitein et al., 2002).

multaneously. In universal nozzles, a rather long time is required to physically switch between these two options (as it requires manual exchange of heavy parts like holders and compensators). But one thing is clear that, for a full coverage of the tumour, the mono-energetic beam is modulated to provide a specific energy width (and certain weighted intensity per energy peak). The laser-driven beams are far from mono-energetic and may already contain the required energy width within the initial spectrum. However, they may not have the same spectral distribution as required for a specific SOBP. Thus, an ESS must be an integral part of any laser-driven PT solution, with an intensity control. Also, due to the time structure (i.e. maximum 10 Hz repetition rate), it may require a long treatment time in particular with beam scanning. Thus, the above mentioned conventional dose delivery schemes, which require pencil-like mono-energetic beams would be inefficient and time consuming. Therefore, LAP beams require new dose schemes and new equipment.

2.5.2 Advanced dose models for LAP beams

The unique features of the LAP beams are very different from the conventional beams and require specialized beamline solutions and also can be used to develop new dose delivery strategies. The critical limit comes from the repetition rate of the high-power laser systems, i.e. maximum 10 Hz, and this would limit the treatment time. In principle, it is possible to use both conventional schemes for LAP beams as well if a mono-energetic spectrum is filtered out from the initial broad energy spectrum. A scattering system for LAP beams, with conventional components, will hugely reduce the efficiency in dose delivery and increase the treatment times given the low repetition rate. If a conventional

scanning system is to be considered for LAP beams (i.e. with small beam sizes), then the time structure of the individual LAP bunches, i.e. few ns bunch lengths, would not allow to sweep the large number of protons per bunch to spread the dose, like conventional raster or line scanning schemes. However, as mentioned above, LAP beams have intrinsic broad energy spectrum which can be utilized to irradiate several slices simultaneously. In addition, it is possible to spread the large number of protons (i.e. dose) laterally via increasing the beam spot-size. These two basic concepts could help utilize LAP beams efficiently.

A new 1D dose model, so-called Broad Energy Assorted depth dose Deposition (BEAD) model, was developed in the framework of this thesis, which is explained in detail later in section 4.2.1. However, it is relevant here to mention that it can achieve homogeneous SOBPs via several broad-energetic proton beams, with up to 20 times broader than conventional mono-energetic beams. Furthermore, this model gave the basic criteria for the beamline design. However, this 1D dose model was not developed further for advanced beamline and dose delivery design. Because in parallel to the development of BEAD, a dose model based on a similar concept for LAP beams was presented by Schell and Wilkens (Schell and Wilkens, 2010) from the Department of Radiation Oncology, Klinikum rechts der Isar, Technical University Munich, Germany. Their dose model was already advanced with 3D dose calculation capabilities on real patient data. Thus, it was logical to develop a collaboration with the Department of Radiation Oncology, Technical University of Munich, to study the 3D depth dose distributions from the output LAP beams from gantry simulations within this thesis. The work done under the collaboration benefited in improving this 3D TPS and feedback from clinical studies helped improved the gantry design, the major works were presented in these references (Hofmann et al., 2015; Masood et al., 2017a). The technical criteria and some results from the collaboration are also presented and discussed in chapter 5. However, the main features of this dose model are presented in this section, because, this can provide a foundation to compare conventional dose schemes and also LAP beamline designs being developed by other groups (discussed in the next section 2.6).

This advanced dose model is a 3D TPS based on the computational environment for radiotherapy research (CERR)⁶ and developed for pulsed LAP beams, and hence called LAP-CERR. The description is mainly adapted from Schell (Schell, 2011) and Hofmann (Hofmann, 2015). It is possible to show via the LAP-CERR TPS that advanced dose delivery schemes can be devised and implemented in between conventional schemes, i.e. spot scanning and whole tumour volume irradiation in passive beam scattering, see figure 2.9. These advanced dose delivery schemes can be described as below:

- (a) The figure 2.9(a) illustrates the *spot-based* delivery scheme which is similar to the conventional active spot scanning technique. Also, it is assumed that intensity modulation, i.e. variable dose, within the spots can be delivered by a beamline control.

This would allow for the most flexible dose delivery with many degrees of freedom.

⁶CERR is an open source, Matlab based, computational environment for radiation therapy research, and it is capable to import 3D computer tomographic (CT) data of patients and calculate absorbed doses from the user defined beams, even for intensity modulated radiotherapy (IMRT)

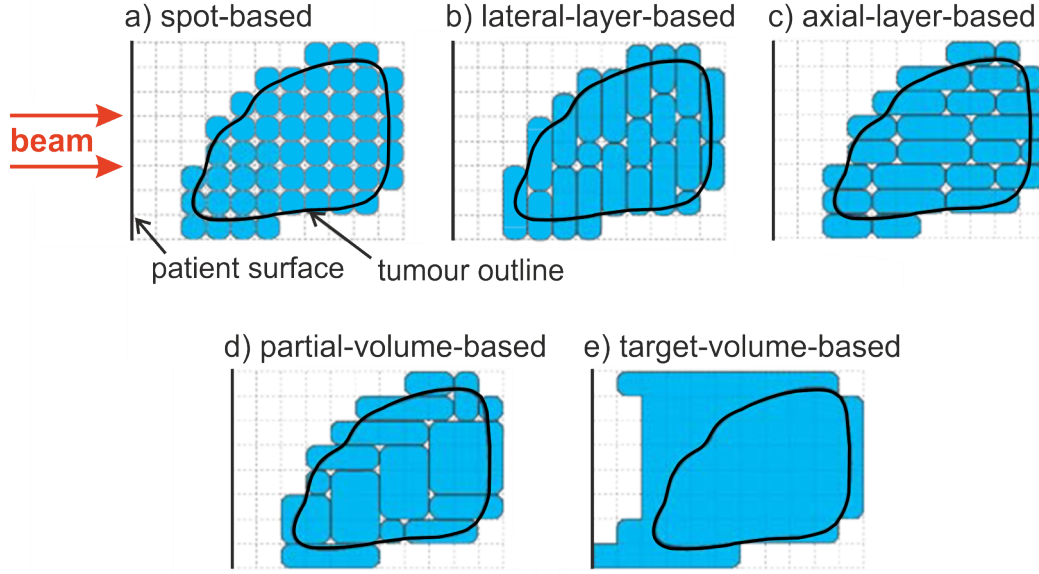


Figure 2.9: Sketch of five different dose delivery schemes for laser-driven protons. The delivery schemes are shown for one beam direction (red arrows) and a water equivalent patient, shown here axially (in-depth) as a 2D grid. Each enclosed blue area in the grid (called cluster) can be irradiated by one filtered LAP bunch. From (a) to (e) the bunch can be spread to irradiate several clusters simultaneously, i.e. laterally by beam spot-size and in-depth by broad energies per bunch. The sketch and description is adapted from Hofmann (Hofmann, 2015).

However, this may restrict the use of LAP beams spectral properties by only deploying quasi mono-energetic spectral widths, and also, due to the high intensity of LAP bunches, most of the protons need to be wasted for small spot-sizes.

- (b) The figure 2.9(b) illustrates the *lateral-layer-based* delivery scheme. In this scheme, the quasi-monoenergetic LAP bunch can be spread laterally to cover a part of, or even a whole slice in the tumour. This efficiently uses the available fluence per MeV energy band, and may decrease the required LAP bunches, and hence laser pulses.
- (c) The figure 2.9(c) illustrates the *axial-layer-based* delivery scheme. In which the fact that LAP beams occur with a broad spectrum has been taken into account. The small spot-size bunches, however, with broad energy spectra are scanned over the target laterally and deliver a certain dose in a cluster of arbitrary axial length.
- (d) The figure 2.9(d) illustrates the *partial-volume-based* delivery scheme. This scheme essentially combines both of the above mentioned *lateral-* and *axial-layer-based* clustering schemes. Thus, it can best utilize the beam properties, i.e. broad energy spectra and available high fluence in that energy range. This could deliver faster treatments due to the big cluster sizes and may require less number of LAP bunches.
- (e) The figure 2.9(e) illustrates whole *target-volume-based* delivery scheme. In which it is possible to irradiate the whole tumour simultaneously by several energy filtered LAP bunches to create a SOBP. This technique can be compared to the conven-

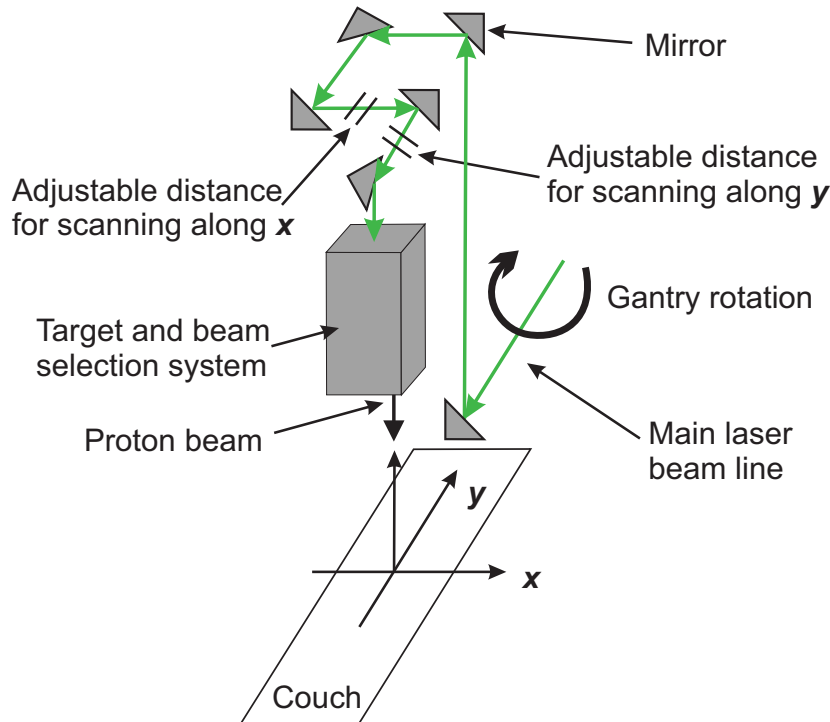


Figure 2.10: An optical gantry layout presented by authors from Fox Chase Cancer Center, USA. The laser pulses were assumed to be guided to the very last bend via optical mirrors just before the laser-target and beam selection system. There were two arms in the gantry with mechanically adjustable lengths. The precise movement of these two arms would move the whole laser-target assembly and the beam selection system, and consequently scan the filtered beam in x - and y -directions. The image is adapted from Luo et al. (Luo et al., 2005).

tional passive scattering scheme, and similarly, may delivery higher doses to proximal healthy tissue.

The LAP-CERR can be optimized to use laser-accelerated, pulsed beams with different specific input spectra and is able to calculate and optimize dose distributions on real patient data based on above mentioned advanced dose schemes. LAP-CERR was optimized for the output beam parameters of the designed gantry and nozzle system and then utilized to perform studies to show the clinical feasibility of the designed gantry.

2.6 Previously published beamline solutions

The beamlines and gantry concept discussed in this section are all aimed to meet the needs of future PT applications for LAP beams with energies up to 250 MeV. The first conceptual design of an ESS mounted inside a 360° gantry for laser-driven sources for PT applications was presented by a research group at Fox Chase Cancer Center, Philadelphia, USA (Fourkal et al., 2003; Luo et al., 2005; Ma et al., 2006; Fan et al., 2007). They considered that when laser pulses enter their gantry system, via optical transferlines⁷ from laser system to the gantry, they are reflected again using optical transferlines to

⁷optical transferlines can be described as vacuum tubes with reflecting mirrors to guide the light through desired path in straight sections

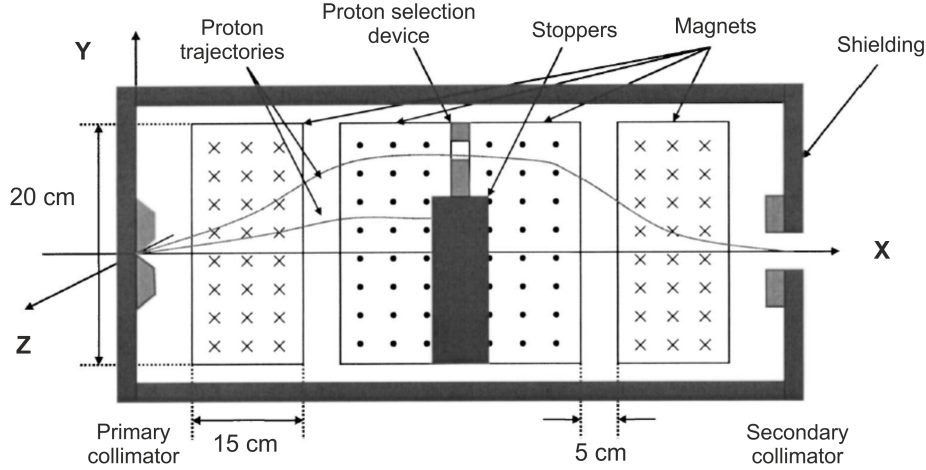


Figure 2.11: Schematic description of the laser-driven proton beam selection system presented by Fox Chase Cancer Center, USA, also see figure 2.10. After protons are generated by laser, on the left side, they enter the selection system through the primary collimator, then the beam passes through four separated dipole magnetic regions, set to form a chicane style ESS. The protons with low divergences filtered through the primary collimator deflect in the field from the central axis (x -axis) and then return to the x -axis after traversing through all four sections of magnetic field. In the middle of the selection system, the protons dispersed spatially following different curved paths according to their energies. Then protons with certain energy width can be selected via the proton selection device, i.e. the collimator. The unwanted particles are either stopped by the stoppers and collimators, or absorbed by the surrounding shielding, close to the patient site. The image is adapted from (Luo et al., 2005).

the laser-target and beam selection system, see figure 2.10. Two optical arms were considered to be mechanically adjustable, so that the whole beam generation and selection systems can be moved step-wise to scan the output beam along x - and y -directions. The laser pulses are guided by the optical system into the laser-target assembly, where LAP bunches were supposed to be generated which enter the *beam selection system*. This is the main component of their gantry design, which is based on four dipole field sections to essentially form a chicane style ESS, see figure 2.11. The dipole fields were assumed to be generated by superconducting magnets, with up to 4.4 T magnetic strength, for a compact system. The divergence of the initial LAP beam entering the *beam selection system* was limited by the use of a small aperture *primary collimator*, with an opening angle of only 0.6° . This allowed only a very small portion of the beam to pass through. The beam was then dispersed spatially behind the second magnetic section, as different energies follow different paths in the magnetic field. At this point a movable aperture, marked as *proton selection device* in the figure 2.11, permitted protons with only a narrow energy band as a function of the radius and position of the aperture. The last two dipole magnetic sections recombine the beam, canceling the spatial dispersion produced by the first two sections, and the filtered LAP bunch leaves the system for patient irradiation.

It is worthwhile to mention here that although the authors here have provided a number for the transport efficiency but the definition of the transport efficiency is not clear. For example, in their publications they have mentioned that only about 0.02% of all the pro-

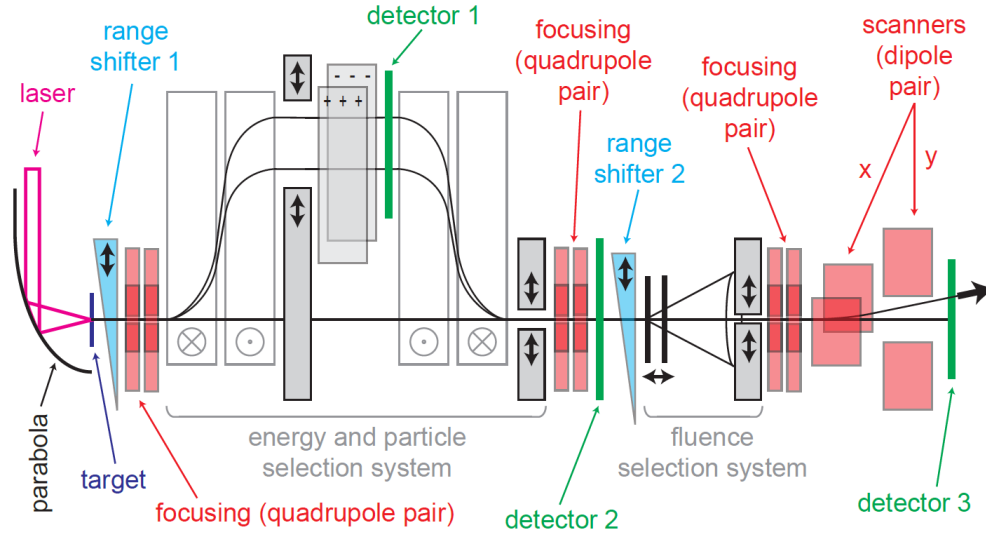


Figure 2.12: Schematic drawing of a potential treatment head for a laser-driven PT system. A setup with an active scanning apparatus is shown. If the collimator of the fluence selection system was a multileaf collimator, the last (most downstream) focusing element and the scanners could be removed. Then, the setup would be a passive scattering one. The image is taken from Schell (Schell, 2011).

tons in the initial bunch could reach the exit window (Fan et al., 2007), but as it would be the main function of the ESS to block all protons with energies not relevant to tumour irradiation, this would always show a very small number. Also for further comparison, different beamlines select different distributions and different energy bandwidths, and different initial distributions may result in different output results. Therefore, a simpler definition of the transport efficiency η can be used, which is defined as the percentage ratio of the transported and initial number of protons in a 1 MeV band around the desired nominal energy. This would be a better way to compare different beamlines and for different input beam parameters. Thus, from the result figures in their publications, e.g. Ma et al. (Ma et al., 2006), a number of about 3 – 4% for transport efficiency was determined.

This gantry concept was surely compact, however, has a few basic issues. First, due to the small acceptance of the *primary collimator*, it rejects most of the fluence. If a larger aperture size was used then the energy selection resolution of the *proton selection device* would be lower and would not allow filtering of mono-energetic beams (with low energy spread) for pristine Bragg peaks, as intended by the authors. Secondly, for the final dose delivery to the patient, only mono-energetic beams were filtered out to implement a conventional SOBPs scheme. This would result in long treatment times, as discussed in the previous section. Thirdly, the beam scanning by moving the entire beamline was suggested, in contrast to the prevailing use of magnetic fields. The precise motion of the massive laser target assembly, along with the magnetic ESS, for accurate scanning of about $20 \times 20 \text{ cm}^2$ field size through pencil like beams of about 1 cm spot size would put tremendous mechanical efforts. Finally, no design consideration was given to the laser-target assembly, as they can be complicated, including vacuum chambers, diagnostics, laser-target feeding systems, focusing system for laser pulses etc., and need space.

An attempt to improve this gantry concept was made by a research group from the Department of Radiation Oncology, Technical University Munich, Germany (Schell, 2011; Hofmann et al., 2012b), the same group who published the advanced dose schemes, LAP-CERR (see section 2.5.2). They presented a concept to improve the efficiency of the *beam selection system* with the same optical gantry layout. They introduced a few magnetic elements in front (upstream) and behind (downstream) the chicane style ESS, with a passive scattering system for fluence control, see figure 2.12. A couple of quadrupoles were considered to capture the diverging beam, instead of limiting the beam with the low acceptance *primary collimator* as done in the original design, to improve the overall transport efficiency. A movable and variable opening size aperture was assumed in the middle of the ESS instead of the fixed aperture size in the original design. Furthermore, a scattering fluence reduction system was introduced with a variable collimator, to control the intensity of the beam for intensity modulated proton therapy (IMPT) application. Also, a conventional active scanning system was considered, instead of the mechanical movements in the original design. The authors argued that this conceptual design may be able to deliver the beams needed to implement the advanced dose schemes they have developed for the LAP beams. However, no mathematical model for the magnetic field requirements or particle simulations were performed to establish the workings and scaling of the components of the gantry. The chicane style systems work best with on-axis particles or with beams with very small size and divergences, the reason why the original design used a small *primary collimator* (Fourkal et al., 2003). Moreover, the compact dimensions of the magnetic elements, apparent from the figure 2.12, seem highly optimistic. The *fluence selection system* would generate secondary radiation in the direction of the patient and close to the patient site.

An European collaboration, named ELIMED, at ELI-Beamlines in Prague, Czech Republic⁸ has also been dedicated to laser-driven PT applications. ELIMED have also adapted the chicane based beamline design, however, based on normal conducting magnets. Their first prototype would not be a gantry, but a fixed straight beamline. The development and experimental testing of their adaptation of the chicane beamline resulted in even lower transport efficiencies (less than 1%) (Cirrone et al., 2013; Scuderi et al., 2014). They later attempted to improve their design by adding magnetic quadrupoles and scattering system (probably swayed by the design by Schell (Schell, 2011)), which was optimized to filter and deliver LAP beams with up to 70 MeV energies for eye treatment applications (Tramontana et al., 2014). However, in reality, this straight fixed beamline ended up with a length of about 8 m. This beamline design will not be applicable as a rotating gantry in future PT applications, as it will require even longer lengths for 250 MeV protons and end up in a gantry with more than 16 m diameter. Also, it is not likely to be able to deliver

⁸The interest of high-power laser research has led to the establishment of ELI (Extreme Light Infrastructure), which is an European large scale infrastructure development. It is based on three laser facilities located in three different countries. One of these facilities, named ELI-Beamlines, is being developed in Prague, Czech Republic, which, among other interests, also focuses on the research and development of all aspects of laser-driven hadrontherapy applications. ELIMED (MEDical application at ELI-Beamlines) is a part of the ELI-Beamlines project dedicated to the research and development of transport beamlines and experimental facility for medical applications, see reference (Cirrone et al., 2013; Schillaci et al., 2014) and references within for further details.

advanced dose schemes for efficient treatment times.

In parallel to the above mentioned concepts and development, a new approach to utilize high-field pulsed magnets was developed by onCOOPtics. The idea was that one must collect all the available diverging protons and control the beam divergence over long distances, i.e. the *capture* of LAP bunches. The pulsed solenoid was proposed as a symmetric capturing lens and to collimate the beam for efficient transport. This idea was proposed as early as 2009, and later inspired Hofmann et al. (Hofmann et al., 2012b) and ELIMED groups to include some kind of collection systems in their concepts as well. The equipment, including pulsed solenoid (with as high-fields as 20 T) and compact pulsed power supply, was designed and developed at HZDR. To establish the efficient capture and transport of LAP beams, several successful experiments were performed at laser facilities at HZDR and GSI-Helmholtzzentrum für Schwerionenforschung, Darmstadt, Germany, with currently available laser-driven proton energies of 20 – 30 MeV (Harres et al., 2010; Burris-Mog et al., 2011; Busold et al., 2013, 2014b, 2015).

The work from Burris-Mog (Burris-Mog et al., 2011; Burris-Mog, 2012) focused on the design and experimental verification of a pulsed solenoid as capturing lens for LAP beams of up to 30 MeV and was done in the framework of the onCOOPtics project. The first successful experiments established the use of a pulsed magnet for LAP beams, and Burris-Mog et al. (Burris-Mog et al., 2011), on the basis of this experience, suggested for the first time that a gantry based on high-field pulsed magnets may provide a compact gantry solution for future applications. Later, two conjoint subprojects (thesis works) were designed under onCOOPtics project, first one dealing with the design, manufacturing and characterization of all the required new pulsed magnets for future applications, i.e. to investigate higher field pulsed magnets for proton energies as high as 250 MeV. And the second subproject was dealing with the design of the gantry with new optimized schemes for efficient clinical applications. Although, the framework of this thesis is dedicated to the second project, assistance and contributions were provided to the first subproject. A substantial contribution was made in the design and testing of new pulsed magnet types and testing of pulsed beamlines. Both subprojects complimented each other, and the experience from the first project helped determine the realistic and achievable pulsed magnets parameters for gantry design. The design and manufacturing of such high field iron-less pulsed magnets have been very challenging and were unprecedented at the beginning of this work (further discussed in section 3.3).

2.7 Challenges and prospects

Laser-driven beams have been proposed and intensively discussed for cancer therapy application since about 2000 (Snively et al., 2000; Bulanov et al., 2002; Bulanov and Khoroshkov, 2002; Malka et al., 2004, 2008). These early authors over-estimated the progress in the field of high-power lasers and laser-driven acceleration development. Even after almost two decades, the basic research and development towards the goals are lagging behind, however, still is an ongoing topic of interest. Linz and Alonso in their article in 2007 (Linz and Alonso, 2007) and then later in 2016 (Linz and Alonso, 2016),

have summarized the status and progress, and have articulated the main challenges and hurdles laser-driven systems need to overcome to qualify for radiation therapy application. The critical issues, challenges and respective prospects, along with some possible solutions are summarized and briefly discussed below:

1. **LAP energy and stability:** The still low energies of LAP beams, stability and reproducibility of laser-driven accelerators have been the key challenge. It is critical for LAP beams to reach therapeutic energies of up to about 250 MeV. The laser physicists are focused to address this issue via the development of higher power laser systems, exploring new laser-targets and investigating the stability and reproducibility issues (as discussed in section 2.4.3). An intermediate future could be to establish LAP beams with 100 – 150 MeV range so that basic clinically relevant research and development can go further, and even could find intermediate applications in the treatment of tumours with lower depths, e.g. brain or head and neck cases.
2. **Costs:** It could be possible to match the cost of a high-power laser-driven accelerator with the conventional, circular accelerator. However, the high stability and up-time, and thus providing lower running costs are the strong suits of conventional accelerator based systems, which make them cost efficient in the long run. This is a crucial challenge and the laser physicists must investigate this issue, and the future laser-driven systems must match these reliability terms in order to compete.
3. **Size:** It is clear that reducing the footprint of the PT systems will bring down the initial investment costs. Therefore, size and costs are related. One solution to lower the costs with the laser-driven systems is to replace magnetic transferlines with less cumbersome optical transferlines, and then to develop a gantry system. However, the critical point has been that a gantry must be compact and must match the high clinical standards in dose delivery and reasonable treatment times. The answer must surely be a compact, light weight and reliable gantry system, which can exploit the unique properties of LAP beams for efficient and must match the high clinical standards set by the conventional PT systems in conformal dose delivery.
4. **Monochromaticity:** LAP beams observe large energy spectra and in current clinical practices only mono-energetic beams are being used for dose applications (see section 2.5.1). Therefore, at first, it was demanded by the critics and the medical community that either stable LAP beams must also be generated with monochromaticity or must be filtered to mono-energetic beams. The first option would be the Holy-Grail for the laser physicists, and many authors have been working in this direction, e.g. (Schwoerer et al., 2005; Eliasson et al., 2009; Zhuo et al., 2010; Fiuza et al., 2012; Haberberger et al., 2012). However, a stable and reproducible acceleration regime has not yet been experimentally established. The later option was deemed most viable and the beamline proposals, e.g. from Fox Chase Cancer Center and ELIMED, were based on the mono-energetic filtering. But, it was later argued that broad energetic beams can also be used for clinical applications and would be

more efficient given the low repetition rates of LAP beams. As mentioned before (in section 2.5.2), a 1D broad-energetic dose scheme (i.e. BEAD) was developed in this thesis to support this argument and to provide basic criteria for designing the new large acceptance gantry and dose delivery systems.⁹

5. **Beam intensity:** One of the critical points is the treatment delivery time. Because of the limited repetition rate of 10 Hz for high-power lasers and if only mono-energetic beams from the initial, wide spectrum were filtered and used, the resultant beam currents would not be sufficient to deliver prescribed doses to large tumours in acceptable duration. As mentioned in the previous point, by using not just mono-energetic beams but also broad-energetic beams, it is possible to utilize the maximum allowed proton fluence per laser pulse. To implement such dose techniques, a gantry is needed with variable energy selection with variable energy widths, intensity modulation scheme, large acceptance transport and new dose delivery (nozzle) equipment to shape and scan the beam according to the tumour requirements.
6. **Dose quality:** Due to the unique LAP beam properties, such as large beam divergences and broad energy spectra, any new laser-driven PT solution must establish that it can meet the high quality standards in dose delivery set by the conventional PT systems. This means the gantry must be able to deliver (or scan) the beam with the desired beam properties (i.e. proton fluence, size, energy width and scan angles) to the tumour location for prescribed doses. Furthermore, this must be supported by dosimetric evaluation on real patient data, like a 3D treatment planning system.
7. **Beamlines:** The associated energy selection systems and transport beamlines including gantry systems have to compete with the commercially available PT systems. The efficacy of laser-driven systems would strongly diminished if the associated gantries are still large. Thus, the new gantry must include above mentioned features/functionalities and must be compact and light weight.

The first two of the above mentioned points are related to the development of high-power lasers and laser-target systems, which is out of the scope of this thesis. Although, there are many aspects which need exploring for the establishment of a laser-driven PT system, such as dosimetry, radiation biology etc., the remaining points described above are in the context of beamline design. These all points have been tackled in the framework of this thesis.

⁹The 1D BEAD model was developed in parallel to the advanced dose models proposed by Schell and Wilkens, as discussed in detail in section 2.5.2.

Chapter 3

Beam optics

For the design of any beamline it is essential to understand the initial charged particle source properties and the output beam parameters required for a desired application. Then, the beamline can be designed to control and manipulate the in-flight particles to achieve those output parameters. The specifics of the laser-driven proton sources and the output beam parameters required for the PT applications are discussed in chapter 4. But first, in this chapter, the basics of the control and manipulation of the transverse beam properties are discussed. Such beam controls can be managed via different magnetic field elements, and the arrangement of these magnetic elements along the desired beam path forms a beamline. The study of controlling charged particle beams via magnetic fields/forces is known as transverse beam optics¹ and in this chapter the theory of transverse beam dynamics is introduced. This theory is used to develop the controls and manipulate LAP beams presented in the following chapters. At least three types of magnetic field elements, namely solenoid, dipole and quadrupole, were required to design the beamlines and these are the focus while discussing the theory of beam optics. The description is heavily influenced by the excellent literature from the references (Wiedemann, 2007; Reiser, 2008). Furthermore, the pulsed nature of the LAP beams allowed to utilize relatively new type of magnets, so-called pulsed magnets. Pulsed magnets can achieve much higher magnetic field strengths than conventional, direct current, resistive magnets, however, for short durations only. These high-field magnets impose new challenges in construction and operation. Before utilizing them for beamline design studies, it is of utmost importance to understand the properties, performance and limits of these magnets, which are discussed at the end of this chapter.

3.1 Transverse beam optics

LAP beams are generally characterized by intense particle bunches with large spectral distribution and divergence angles. For PT applications the control over these diverse properties is of sheer importance. The transport, controls and manipulation of particle beams can be understood by the theory of transverse beam optics. In any beamline

¹It is also common to refer magnets as optic elements, or simply optics. A distinction is suggested here to not to confuse with the optical transferlines used for laser pulses mentioned earlier.

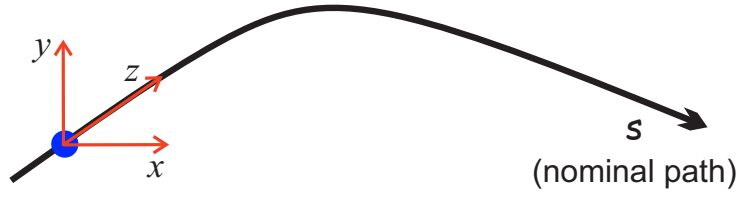


Figure 3.1: A charged particle (blue) with space coordinates (x, y, z) following a nominal path s . The choice of coordinate system here would be curvilinear system as the beam bends along the nominal path, traveling through bending magnets. The particle can be considered nominal when $x = y = 0$ and has no divergence.

design it is imperative to steer the charged particles along a certain designed path, also called the nominal path (see figure 3.1). Before dealing with a beam (i.e. collection of particles), first look into single charged particle dynamics. The force \mathbf{F} experienced by a charged particle with charge q and velocity \mathbf{v} , due to the magnetic field strength \mathbf{B} is given by the magnetic component of the Lorentz force:

$$\mathbf{F} = q \mathbf{v} \times \mathbf{B}. \quad (3.1)$$

The equation 3.1 shows that a charged particle entering a magnetic field with an angle (i.e. not parallel) would follow a curved path and the centrifugal force providing the necessary acceleration for the bend in the particle trajectory is given by:

$$\mathbf{F} = \frac{\mathbf{p}\mathbf{v}}{\rho} = \frac{\gamma_r m_0 v^2}{\rho} \quad (3.2)$$

$$\begin{aligned} \text{with } \mathbf{p} &= \gamma_r m_0 \mathbf{v} \\ \gamma_r &= (1 - \beta_r^2)^{-1/2} \\ \beta_r &= v/c, \end{aligned} \quad (3.3)$$

where p is the momentum of the particle with m_0 its rest mass and v its velocity, ρ is the bending radius of the curvature and c is the speed of light. γ_r and β_r are the Lorentz factor and the ratio of velocity to the speed of light, respectively.² From equations 3.1 and 3.2, an important term known as magnetic rigidity ($B_0\rho$) of the beam can be obtained:

$$(B_0\rho) = \frac{p}{q}. \quad (3.4)$$

The magnetic rigidity ($B_0\rho$) is an important parameter and it describes the magnetic field strength B_0 required to bend a particle with a certain momentum p and a charge q in a curvature of radius ρ . Equation 3.4 also describes an important condition which is higher magnetic fields are necessary to design more compact systems. The magnetic rigidity ($B_0\rho$) is frequently used to normalize the magnetic strength of the magnets according to

² Note: the subscript r in γ_r and β_r is only used here to clarify the difference between Lorentz factors and Twiss parameters, as same symbols are used in literature to describe both. Twiss parameters are introduced and discussed later in section 3.2

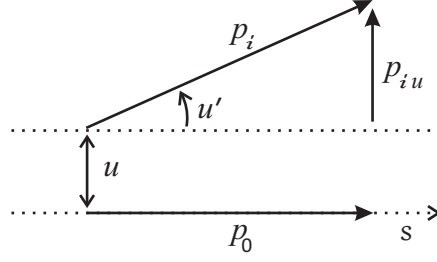


Figure 3.2: Geometric illustration of momentum coordinates and the divergence of a particle in a beam. u is a general term representing either x or y transverse directions. p_0 is the nominal momentum of the ideal particle following the nominal path along s , whereas another particle with momentum of p_i is moving with a certain divergence with respect to the nominal particle.

the ideal (or called nominal) momentum p_0 . Note here that the nominal particle is a particle with p_0 momentum and strictly follows the nominal path, i.e. $x = x' = y = y' = 0$, where $' = d/ds$ represents divergence. Now, consider a charged particle inside the beam with momentum p_i and with initial parameters $(x, x', y, y', z, \delta)$, where, x and y are transverse coordinates in the real space, z is the longitudinal coordinate along the nominal path s , x' and y' are the divergences (flight directions) and $\delta = \Delta p/p_0$ is the momentum deviation from the nominal momentum p_0 . The divergence of this particle in x -direction, $x' = dx/ds$, can also be described in terms of momentum as $x' = \tan^{-1}(p_{ix}/p_0)$, where, p_{ix} is the momentum component of the particle i along the x -axis, (see figure 3.2). Similarly, the divergence of this particle in y -direction is $y' = dy/ds$. For simplicity, u is used as a general term for either x or y transverse directions. Now, the general equation of motion for this charged particle can be described by a second order homogeneous differential equation, known as Hill's equation:

$$u'' + K u = 0. \quad (3.5)$$

The Hill's equation represents an harmonic oscillator with a restoring strength of K , which is provided by the magnets. The general solution for the equation 3.5 is given as:

$$u(s) = a_1 \cos(\sqrt{K}s) + a_2 \sin(\sqrt{K}s), \quad (3.6)$$

where a_1 and a_2 can be determined by applying the initial boundary condition:

$$s = 0 \rightarrow \begin{cases} u(0) = u_0 & , \quad a_1 = u_0 \\ u'(0) = u'_0 & , \quad a_2 = \frac{u'_0}{\sqrt{K}}. \end{cases} \quad (3.7)$$

$$(3.8)$$

The above set of equations are used to determine the influence of a particular magnetic field element on the motion of a charged particle. Three types of linear magnetic field elements, namely quadrupole, dipole and solenoid, have been used to design the beamlines for LAP beams. The beam optics of these individual magnets are discussed below.

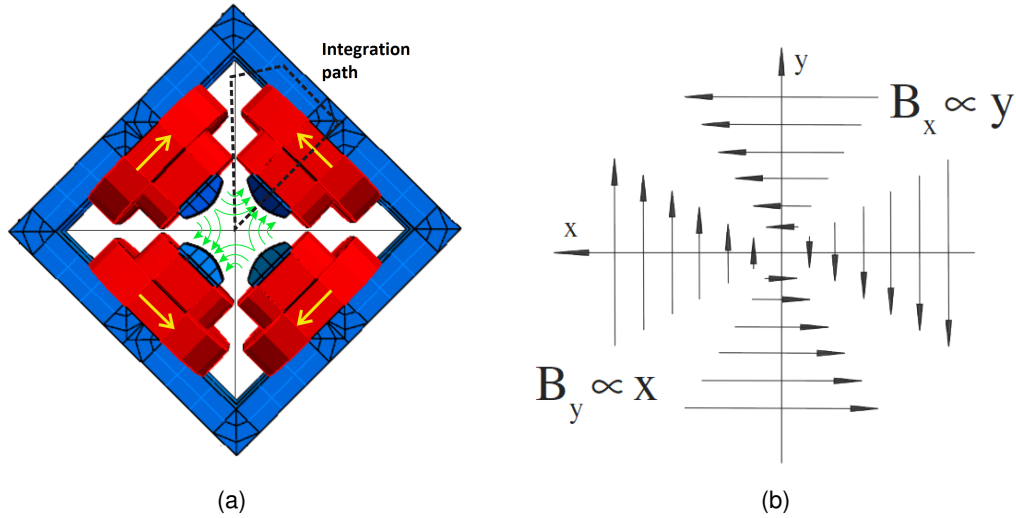


Figure 3.3: (a): Conventional quadrupole structure with iron core (blue) and the current carrying coils (red). The direction of current and resultant magnetic field are shown with yellow and green arrows, respectively. (b): Simplified magnetic field pattern inside a conventional quadrupole magnet. Figure (a) is adapted from an example from Radia: A 3D magnetic field computing code (Chubar et al., 1998) and figure (b) is taken from Wiedemann (Wiedemann, 2007).

3.1.1 Quadrupoles

Quadrupole magnets are used as strong focusing elements in magnetic beamlines. The magnetic field strength, inside a quadrupole, is distributed in such a way that it decreases from the pole to the center such that it has magnetic field gradient $g = B_0/R$, where R is the radius of the aperture of the quadrupole (see figure 3.3). The normalized strength³ k_Q and the focal length f of the quadrupole of length l_Q can be described as:

$$k_Q = \left[\left| \frac{g}{(B_0 \rho)} \right| \right]^{1/2} \quad \text{and} \quad f^{-1} = \pm k_Q^2 l_Q. \quad (3.9)$$

Here the \pm sign shows focusing in one direction and de-focusing in the other. Now, by replacing the \sqrt{K} in the equation 3.6 with k_Q and applying the initial boundary conditions, the equations of motion for the particle traversing through a horizontally focusing quadrupole, i.e. with positive K , are given as:

$$\begin{aligned} x(s) &= x_0 \cos(k_Q l_Q) + x'_0 \frac{1}{k_Q} \sin(k_Q l_Q) \\ x'(s) &= -x_0 k_Q \sin(k_Q l_Q) + x'_0 \cos(k_Q l_Q). \end{aligned} \quad (3.10)$$

The magnetic field is mirrored in x - and y -directions, hence, a quadrupole principally focuses in one transverse direction and de-focuses in the other. However, the motion in each transverse plane is independent and not coupled. Thus, for a horizontally focusing quadrupole, the equations of motion in vertical (de-focusing) plane will change and the

³Note: there are two definitions of k_Q in the literature, one is mentioned in the equation 3.9 (Crandall and Rusthoy, 1997) and another is simply $k_Q = g/(B_0 \rho)$ (Reiser, 2008). If one uses the second definition then in the solutions, given in equations 3.10 and 3.11, one must replace k_Q with $\sqrt{k_Q}$. First definition is used in this work because many particle tracking simulation softwares uses this definition.

Hill's equation now becomes $y'' - K y = 0$ (as the restoring strength K becomes negative), and then the solutions can be given as:

$$\begin{aligned} y(s) &= y_0 \cosh(k_Q l_Q) + y'_0 \frac{1}{k_Q} \sinh(k_Q l_Q) \\ y'(s) &= y_0 k_Q \sinh(k_Q l_Q) + y'_0 \cosh(k_Q l_Q). \end{aligned} \quad (3.11)$$

Now, consider a charged particle with initial parameters $(x_0, x'_0, y_0, y'_0, z_0, \delta)$ at $s = s_0$ traversing through a horizontally focusing quadrupole, then the particle parameters $(x, x', y, y', z, \delta)$ behind the quadrupole, let's say at $s = s_1$ (where, $l_Q = s_1 - s_0$), can be obtained via the matrix equation (3.12) given below:

$$\begin{pmatrix} x \\ x' \\ y \\ y' \\ z \\ \delta \end{pmatrix}_{s_1} = M_{\text{Quad}} \begin{pmatrix} x_0 \\ x'_0 \\ y_0 \\ y'_0 \\ z_0 \\ \delta \end{pmatrix}_{s_0}. \quad (3.12)$$

This is the usual way in beam optics to mathematically represent a magnetic element, i.e. matrix system. Thus, a quadrupole can be described as following:

$$M_{\text{Quad}} = \begin{pmatrix} \cos(k_Q l_Q) & \frac{1}{k_Q} \sinh(k_Q l_Q) & 0 & 0 & 0 & 0 \\ -k_Q \sin(k_Q l_Q) & \cos(k_Q l_Q) & 0 & 0 & 0 & 0 \\ 0 & 0 & \cosh(k_Q l_Q) & \frac{1}{k_Q} \sinh(k_Q l_Q) & 0 & 0 \\ 0 & 0 & k_Q \sinh(k_Q l_Q) & \cosh(k_Q l_Q) & 0 & 0 \\ 0 & 0 & 0 & 0 & 1 & l_Q/\gamma_r^2 \\ 0 & 0 & 0 & 0 & 0 & 1 \end{pmatrix}. \quad (3.13)$$

Quadrupoles do not have a net effect on the momentum spread δ , as represented in the last row of the above equation 3.13. Furthermore, the z in equation 3.12 represents the particle's longitudinal position, which is of minor importance here (i.e. no accelerating/de-accelerating forces are present in a transport beamline to influence change in velocity or energy). Nevertheless, the fifth row in the transfer matrix represents the effect of a magnetic element, in this case quadrupole, along the longitudinal direction. This only depends on the particle's own energy, and any deviation from the nominal momentum will result in elongation of the initial bunch (i.e. $\Delta v/v = (\Delta p/p)/\gamma_r^2$).

3.1.2 Sector magnets

Sector magnets provide a bending Lorentz force via a dipole field, which is spread along the bending plane in a circular sector, hence the name. The bending force, i.e. $\mathbf{F} = q \mathbf{v} \times \mathbf{B}_{\text{SM}}$, where, \mathbf{B}_{SM} is the magnetic field inside the sector magnet, and bends

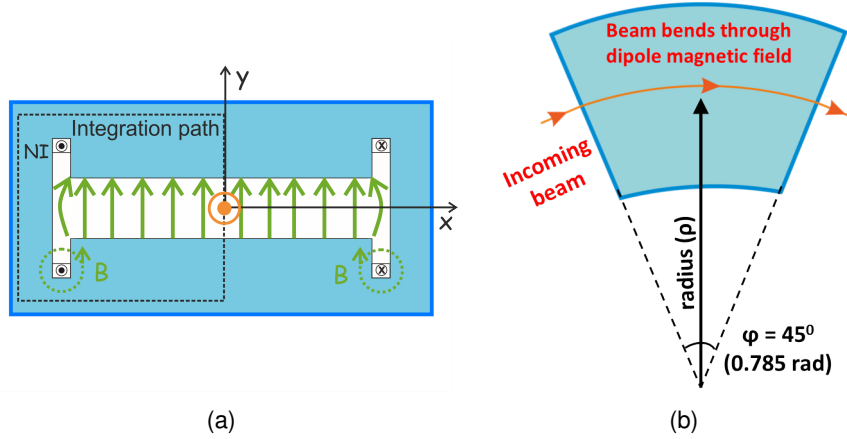


Figure 3.4: Schematic layout of a dipole field arranged in a sector, hence known as sector magnet. (a): Layout in xy -plane, or beam's eye view. Conventional dipole magnetic field is generated in a gap inside an iron core (blue) via the current carrying coils (marked as ampere turns NI). The magnetic field strength can be determined by utilizing the Stokes theorem along the integration path. (b): Layout in the deflecting plane, a narrow beam following the nominal bending path while maintaining a right angle to the entry and exit edges of the sector magnet. Ideally, the beam is not changed in the non-deflecting plane and a sector magnet only acts as a drift element in this plane.

the traversing charged particles so that they follow a desired path in a transport beamline, see figure 3.4. The restoring factor K_{SM} and the bending angle φ can be described as:

$$K_{SM} = \frac{1}{\rho_0^2} \quad \text{and} \quad \varphi = \frac{l_{SM}}{\rho_0}, \quad (3.14)$$

where l_{SM} is the arc length through the nominal path inside the magnet. In the ideal sector magnet, the restoring factor K_{SM} is bending the beam along the nominal path s , and not changing the transverse parameters of the particles with respect to the nominal particle. In the non-deflecting plane the magnet behaves like a drift length with l_{SM} , whereas the solution for Hill's equation in the bending plane (x -plane) can be given as below:

$$\begin{aligned} x(s) &= x_0 \cos \varphi + x'_0 \rho_0 \sin \varphi \\ x'(s) &= -x_0 \frac{1}{\rho_0} \sin \varphi + x'_0 \cos \varphi. \end{aligned} \quad (3.15)$$

However, the particle beams are not truly mono-energetic and have a certain momentum spread $\delta = \Delta p/p_0$. In case of bending sector magnets, the momentum spread introduces a perturbation in the equation of motion and now the Hill's equation can be given as:

$$u'' + K(s)u = \frac{1}{\rho_{0u}(s)} \delta. \quad (3.16)$$

The general solution of the equation of motion becomes (Wiedemann, 2007):

$$\begin{aligned}
u(s) &= aC_u(s) + bS_u(s) + \delta D_u(s) \\
u'(s) &= aC'_u(s) + bS'_u(s) + \delta D'_u(s) \\
\text{with } D_u(s) &= \int_0^s \frac{1}{\rho_{0u}(\tilde{s})} [S_u(s) C_u(\tilde{s}) - C_u(s) S_u(\tilde{s})] d\tilde{s}, \\
C_u(s) &= \cos(\sqrt{K_{SM}} s) \quad \text{and} \quad S_u(s) = \frac{1}{\sqrt{K_{SM}}} \sin(\sqrt{K_{SM}} s),
\end{aligned} \tag{3.17}$$

where C_u and S_u mean cosine and sine like functions, respectively and $D(s)$ and $D'(s)$ are the dispersion functions. Physically, when the particle with some momentum error δ traverse through a bending magnet with B_0 designed for the nominal particle with p_0 momentum, then this off-momentum particle deviates from the reference path. The difference between the deviated and reference path Δx describes the dispersion function, $D(s) = \Delta x / \delta$. For the system of equations 3.17, the dispersion function can be solved for a sector magnet, with $\rho(s) = \rho_0 = \text{const.}$, as follows:

$$\begin{aligned}
D(s) &= \sin \varphi \int_0^{l_{SM}} \cos \varphi d\tilde{s} - \cos \varphi \int_0^{l_{SM}} \sin \varphi d\tilde{s} \\
&= \rho_0 [1 - \cos \varphi] \\
D'(s) &= \sin \varphi.
\end{aligned} \tag{3.18}$$

Using the similar approach as equation 3.13 for transformation matrix, the above mentioned sets of equations 3.14, 3.15 and 3.18 can be written as:

$$M_{SM} = \begin{pmatrix} \cos \varphi & \rho_0 \sin \varphi & 0 & 0 & 0 & \rho_0 [1 - \cos \varphi] \\ -\frac{1}{\rho_0} \sin \varphi & \cos \varphi & 0 & 0 & 0 & \sin \varphi \\ 0 & 0 & 1 & l_{sm} & 0 & 0 \\ 0 & 0 & 0 & 1 & 0 & 0 \\ -\sin \varphi & -\rho_0 (1 - \cos \varphi) & 0 & 1 & 1 & l_{sm}/\gamma_r^2 - \rho_0 (\varphi - \sin \varphi) \\ 0 & 0 & 0 & 0 & 0 & 1 \end{pmatrix}. \tag{3.19}$$

Note here that a sector magnet only behaves like a drift space in the non-bending plane and this fact is mathematically represented in the above transfer matrix in rows 3 and 4 (column 3 and 4), which is the basic transfer matrix of a drift space (i.e. without any magnetic field effect) of certain length (in this case l_{SM}), further explained in the section 3.1.4. As the whole beam is deflected through a bend, the nominal path also changes in the bending plane, which is presented by (5×1) and (5×2) terms (i.e. first and second terms of the 5th row) of the transfer matrix M_{Sect} , while the term (5×6) shows the effect on off-momentum particles, i.e. the particle bunch elongates.

3.1.3 Solenoid

A solenoid is a magnetic lens with an axis-symmetric magnetic field which focuses traversing charged particles in both x - and y -directions simultaneously, see figure 3.5.

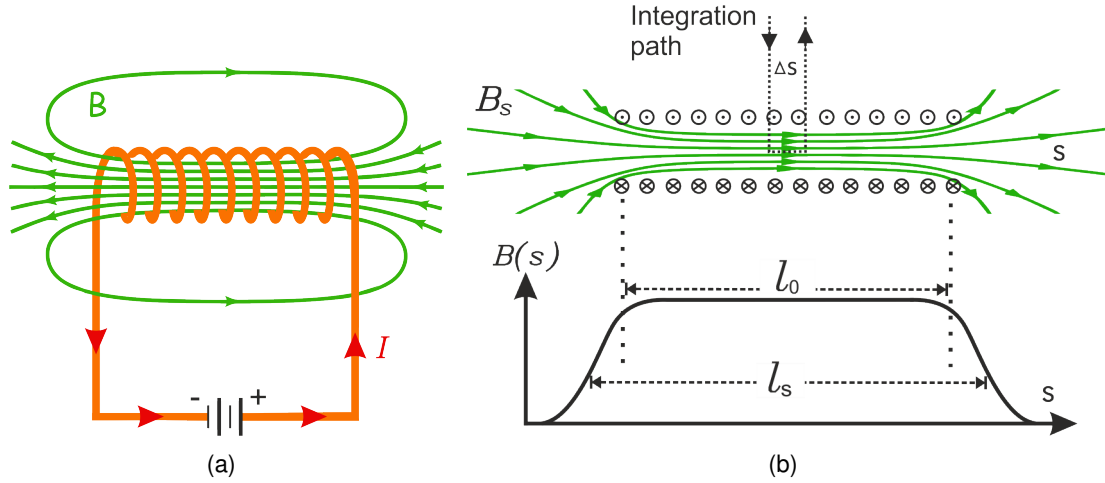


Figure 3.5: (a): A simple coil winding (orange) capable of generating a solenoidal magnetic field pattern (green). (b): Evolution of the magnetic field strength $B(s)$ along the central axis s in conjunction with the effective length of the solenoid l_s , whereas the physical length of the solenoid is l_0 . Figures are adapted from Wiedemann (Wiedemann, 2007) and Reiser (Reiser, 2008).

There are two field components in a solenoid, the longitudinal magnetic field $B(s)$, which is along the traversing axis s and the radial magnetic field component. The longitudinal magnetic field peaks at the center of the solenoid and decreases toward the edge of the solenoid, and approaching zero far away from the solenoid. The charged particles follow a helical path inside the solenoid. The beam dynamics have been explained extensively in the literature, such as Wiedemann (Wiedemann, 2007), Reiser (Reiser, 2008) and Kumar (Kumar, 2009). However, the detailed description of motion inside a solenoid is of no importance here, and only a brief description of the effect of a solenoid as a focusing lens in a beamline is presented here, which was used later in the calculations. Figure 3.5(a) shows a typical solenoidal field pattern originating from a coil. The magnetic field strength B_{sol} at the center of a solenoid can be determined by utilizing the Stokes theorem along the integration path as shown in the figure 3.5(b).

$$\oint \mathbf{B} ds = B_{sol} \Delta s = \mu_0 \mu_r J \Delta s \quad (3.20)$$

$$B_{sol} = \mu_0 \mu_r J,$$

where $J = (N/l_0)I$ is the solenoid current per unit length for N number of turns carrying current I , μ_0 , μ_m and μ_r are the permeability of free space, the permeability of the medium and the relative permeability of the medium (in this case air) respectively, which are related as $\mu_r = \mu_m/\mu_0$. Although, the magnetic field $B(s)$ has a rise and fall at the edges of the solenoid, however, a constant magnetic field strength B_{sol} (i.e. at the central axis for $x = 0, y = 0$) can be assumed for an effective length of l_s to determine the focusing strength of the solenoid with physical length of l_0 (where $l_s > l_0$). The focusing strength (f^{-1}) then can be given as:

$$f^{-1} = \frac{q^2}{4p_0^2} B_{\text{Sol}}^2 l_S = k_S^2 l_S \quad (3.21)$$

where $K = k_S^2 = \frac{q^2 B_{\text{Sol}}^2}{4p_0^2} = \frac{B_{\text{Sol}}^2}{4(B_0 \rho)^2}.$

The solutions for the equations of motion from the Hill's equation for a solenoid can be obtained in similar way as done for quadrupole and sector magnets. The resultant transfer matrix for a solenoid M_{Sol} can be given as:

$$M_{\text{Sol}} = \begin{pmatrix} \cos(k_S l_S) & \frac{1}{k_S} \sin(k_S l_S) & 0 & 0 & 0 & 0 \\ -k_S \sin(k_S l_S) & \cos(k_S l_S) & 0 & 0 & 0 & 0 \\ 0 & 0 & \cos(k_S l_S) & \frac{1}{k_S} \sin(k_S l_S) & 0 & 0 \\ 0 & 0 & -k_S \sin(k_S l_S) & \cos(k_S l_S) & 0 & 0 \\ 0 & 0 & 0 & 0 & 1 & l_S/\gamma_r^2 \\ 0 & 0 & 0 & 0 & 0 & 1 \end{pmatrix}. \quad (3.22)$$

Note here that the solenoid exerts force symmetrically in both x - and y -directions, also the dispersion terms are zero as there is no net bending term from an on-axis solenoid. A solenoid behaves the same way as a quadrupole in the longitudinal direction.

3.1.4 Drift space

A drift space is also a part of a beamline, i.e. a space without any magnetic field, where charged particles can fly free of external forces. Drift spaces can be provided in-between magnetic elements to achieve certain beam properties, which were induced by a upstream magnetic field element. For example, charged particles exit a focusing solenoid with a net deflection towards the central axis as dictated by the equations 3.21, however, they require a drift space of certain length to achieve the smallest spot-size. A transfer matrix can be deduced for a drift space M_{Drift} , with a length of l_D :

$$M_{\text{Drift}} = \begin{pmatrix} 1 & l_D & 0 & 0 & 0 & 0 \\ 0 & 1 & 0 & 0 & 0 & 0 \\ 0 & 0 & 1 & l_D & 0 & 0 \\ 0 & 0 & 0 & 1 & 0 & 0 \\ 0 & 0 & 0 & 0 & 1 & l_D/\gamma_r^2 \\ 0 & 0 & 0 & 0 & 0 & 1 \end{pmatrix}. \quad (3.23)$$

3.2 Beam Dynamics

In the previous section 3.1 the transfer matrices for the individual beam optic elements, i.e. quadrupole, sector magnet, solenoid, were introduced. Individual particles with specified initial parameters now can be traced through these magnets. However, a beam con-

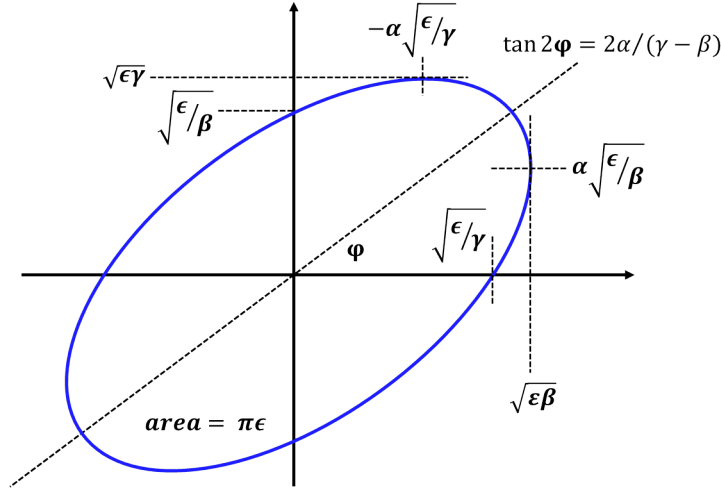


Figure 3.6: Phase space ellipse (blue) which would enclose a certain distribution of particles of the beam at a given position. Along with determinable Twiss parameters (α, β, γ) and emittance ϵ from the orientation of this ellipse. The horizontal axis is usually the transverse coordinates of the particles, i.e. either x or y , while the vertical axis is usually the respective slope parameter, i.e. x' or y' . It is also a common practice to use respective momentum values of the particles along the vertical axis, however, in this work slopes are used. Figure is adapted from Wiedemann (Wiedemann, 2007).

tains a large number of particles with a certain distribution, and it is impractical to solve for individual particle trajectories through a collection of magnets which forms a beamline. Liouville's theorem is very well known in the theory of beam dynamics (in classical statistical mechanics) and it provides an important mathematical tool to describe particles in a beam as a whole in a transverse phase space (i.e. (x, x', y, y')), and extends to describe the evolution of beam parameters through a magnetic element or combination of them, i.e. conservative forces. This theorem states that the particle phase density stays constant under the influence of magnetic (conservative) forces (Wiedemann, 2007). And, it infers that a distribution of particles with certain initial parameters constituting a beam would occupy a certain area in the phase space which would remain constant while traversing through a magnetic transferline. This area covering all particles is commonly described by an ellipse (also see figure 3.6), which can be described as:

$$\gamma u^2 + 2\alpha uu' + \beta u'^2 = \epsilon_u, \quad (3.24)$$

where α , β , γ and ϵ are ellipse parameters and are also known as Twiss parameters⁴. ϵ is the beam emittance and α , β and γ determine the shape and orientation of the ellipse and are connected by the expression $\gamma\beta - \alpha^2 = 1$. The beam can be represented by a beam matrix σ , given as:

$$\sigma_u = \epsilon_u \begin{pmatrix} \beta_u & -\alpha_u \\ -\alpha_u & \gamma_u \end{pmatrix}. \quad (3.25)$$

⁴The Twiss parameters must not be confused with the Lorentz factor γ_r and β_r .

If a Gaussian particle distribution is assumed, then the beam matrix components in equation 3.25 can be calculated statistically, by the set of equations 3.26 given below:

$$\begin{aligned}\langle u_i^2 \rangle &= \epsilon_u \beta_u \\ \langle u_i'^2 \rangle &= \epsilon_u \gamma_u \\ \langle u_i u_i' \rangle &= -\epsilon_u \alpha_u\end{aligned}\tag{3.26}$$

with emittance $\epsilon_u = \sqrt{\langle u_i^2 \rangle \langle u_i'^2 \rangle - \langle u_i u_i' \rangle^2}.$

And, standard deviation in the beam in transverse directions can be written as:

$$\sigma_x = \epsilon_x \beta_x \quad \text{and} \quad \sigma_y = \epsilon_y \beta_y.\tag{3.27}$$

Furthermore, the envelope of the beam which encloses all the individual charged particle trajectories can be written as:

$$env(s) = \pm \sqrt{\epsilon \beta(s)},\tag{3.28}$$

where \pm indicates the symmetric behavior on both sides of the center of the beam. The envelope can also be determined by the phase space ellipse at any point in the beamline, see figure 3.6.

Now, a particle bunch (or initial beam source at the start $s = 0$) can be described by the following 6D matrix:

$$\sigma_0 = \begin{pmatrix} \epsilon_x \beta_x & -\epsilon_x \alpha_x & 0 & 0 & 0 & D(s) \\ -\epsilon_x \alpha_x & \epsilon_x \gamma_x & 0 & 0 & 0 & D'(s) \\ 0 & 0 & \epsilon_y \beta_y & -\epsilon_y \alpha_y & 0 & 0 \\ 0 & 0 & -\epsilon_y \alpha_y & \epsilon_y \gamma_y & 0 & 0 \\ 0 & 0 & 0 & 0 & L^2 & 0 \\ 0 & 0 & 0 & 0 & 0 & \delta^2 \end{pmatrix},\tag{3.29}$$

where L is the bunch length (defined by bunch duration) and $\delta = \Delta p/p_0$ is the momentum deviation. The equation 3.29 represents the collective behavior of all the particles in a bunch. Now, this particle bunch can be conveniently tracked through any magnet or collections of magnets, described by a 6×6 matrix M , from a position s_0 to another position downstream s_f :

$$\sigma_f = M \sigma_0 M^T,\tag{3.30}$$

where the transfer matrix M for an arbitrary beamline section can be obtained by multiplying the individual transfer matrices of the respective beamline elements, for example $M = M_{\text{Quad}} M_{\text{Drift}} M_{\text{SM}} M_{\text{Drift}} M_{\text{Sol}} M_{\text{Drift}}$. This method is frequently used in the next two chapters to determine gantry sections for specific desired conditions.

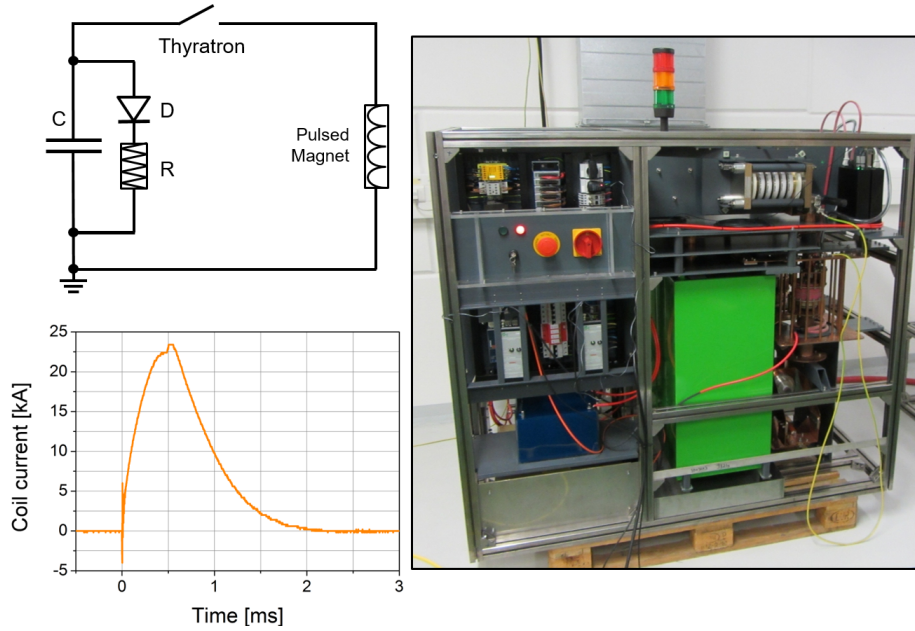


Figure 3.7: Schematic electrical circuit (upper left corner), in which a capacitor C with capacitance C (or even multiple capacitors in parallel) discharge through a switch (thyatron) via a pulsed magnet with certain inductance L_{ind} . The current through the circuit rises (according to the angular frequency of the $L_{\text{ind}}C$ circuit given by $\omega = 1/\sqrt{L_{\text{ind}}C}$). After, the flow of maximum current the voltage shifts and then diode D damps the current through R . The evolution of the current as a function of time (lower left corner) measured with a pulsed solenoid magnet. A portable compact capacitor-bank (right) which was designed and built at HZDR for the experimental characterization of pulsed magnets.

3.3 Pulsed magnets

To physically implement the afore mentioned magnetic field types for beam controls different types of magnets can be employed. However, the pulsed structure of the LAP beams allows to utilize high-field pulsed magnets for a compact design. Pulsed magnets have been favored for this work because the magnetic rigidity ($B_0\rho$) of the protons with therapeutic energies require high magnetic field strength B_0 for a small bending radius ρ , which predominantly determines the size of any PT gantry. In conventional systems, room temperature iron-core magnets are being used in which the achievable maximum magnetic field strength B_{max} is limited to a maximum value of about 2 T, due to the saturation of the magnetization of the iron-core. The core saturation limitation can be avoided by removing the iron-core, by air-core designs. By doing so, pulsed magnets can achieve peak magnetic field strengths 6 times, or even higher, than iron-core magnets. It is worthwhile to mention that abandoning the iron-core not only elevates the field strength but also makes pulsed magnets much lighter in weight, e.g. a 45° pulsed bending magnet with ~ 10 T field strength is more than 60 times lighter than a 45° 2 T iron-core magnet for a similar bending angle. This in turn would lower the mechanical constraints on the support structures and the architecture of the therapy buildings.

However, the ampere turn for equal magnetic flux (e.g. see equation 3.20) is much smaller for iron-core magnets (where, $\mu_r \gg 1$) compared with air-core (where, $\mu_r \sim 1$)

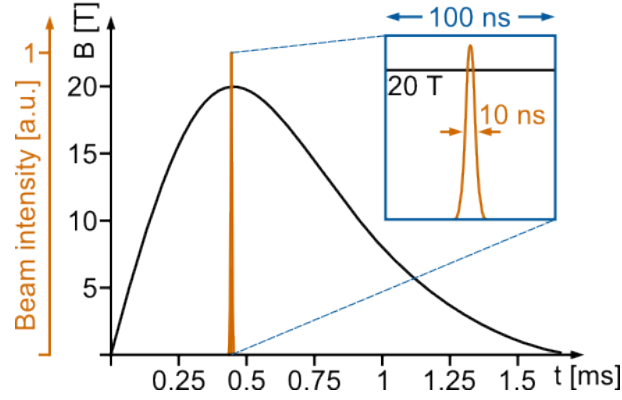


Figure 3.8: Evolution of magnetic field strength (black line) inside a pulsed magnet (in this case, measured in a pulsed solenoid) as a function of time. The rise time for the magnetic field usually ranges between 200 – 700 μs , depending upon the magnet type. However, the LAP bunch (orange line) traversing through the magnet only require propagation time in ns range. The magnetic field can be considered uniform and static during the passage of the LAP bunch, as shown in the blown-up part of the figure. Figure courtesy of F. Kroll.

(Humphries, 1986). This means an air-core magnet would require higher current values for similar magnetic field strength. Moreover, the iron-core not only supports the returning magnetic flux with low reluctance but also can be shaped precisely near the gap to provide accurate field gradients and field orientations. On the other hand, pulsed magnets must use thick current carrying wires for higher current values and must be laid out in a special orientation to retain the returning flux in air-core, which means that the flowing current can result in magnetic field regions with correct gradients and orientations (further discussed for each magnetic type in subsequent subsections). This is extremely challenging and unprecedented for high magnetic field types, which would be required for the gantry design. Nevertheless, the electrical energy E_{ind} (given as $E_{\text{ind}} = \frac{1}{2} L_{\text{ind}} I^2$) can be supplied by high-power capacitor-banks and B_{max} achievable with air-core pulsed magnets is mainly limited by the inductance L_{ind} and the peak current I required.

To provide the necessary electrical energies, compact and portable high-power capacitor banks have been designed at HZDR, see figure 3.7. This power supply is capable of delivering 94 kJ electrical energy with a maximum voltage of 24 kV, via two parallel capacitors of 163 μF capacitance⁵ each. It can handle a current of 200 kA via a fast thyra-tron switch. The current rise time, $t_{\text{rise}} = \pi/2\sqrt{L_{\text{ind}}C}$, is usually in the range of 200 – 700 μs for pulsed magnets with inductances in the range of 100 – 500 μH (for different types of magnets) and the total pulse duration is a few ms. The LAP bunches can be synchronized so that when they reach the magnet they see the peak in the current pulse, hence, the peak in magnetic pulse inside the pulsed magnet, see figure 3.8. For example, consider LAP bunch with bunch duration of about 1 ns and with a lower E_0 of 80 MeV with $\Delta E/E_0$ of about 20% (these would be the slowest moving protons in the therapeutic range) enters a pulsed magnet. The traversing time inside a pulsed magnet of about 40 cm length is about 3 ns, then it experiences the magnetic field only for this period of

⁵Capacitance of a capacitor is denoted as C with units Farad (F), i.e. 1 F is equal to 1 Coulomb per volt, and the inductance L_{ind} of a magnet has units Henry (H), i.e. 1 H is equal to 1 Ω s. Both quantities F and H are large in SI units and usually mentioned in smaller quantities such as μH and μF .

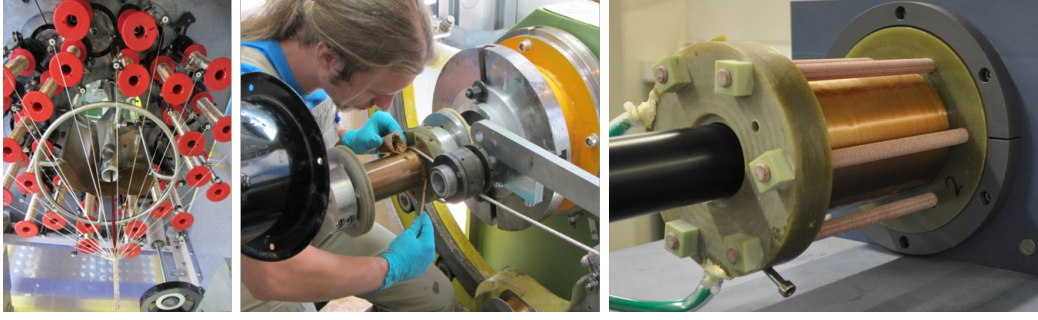


Figure 3.9: Construction process of a 20 T pulsed solenoid. A 4 mm thick solid copper wire, which is already insulated with a thin layer of Kapton, covered in a mesh of Zylon fibers (left). The wire is then carefully wound by hand around a hollow polyurethane plastic tube (which is a high tensile plastic material with excellent insulation properties and act as beampipe) using G-10 glass reinforced epoxy (middle). Also, Kapton layers are used in between layers for strength and insulation. Finished solenoid (right) is then further reinforced by a polyurethane structure. Note here that, due to the high magnetic flux, sharp rise times and insulation issues, metals are generally avoided around the construction of any pulsed magnet. Images courtesy of F. Kroll.

time. Even though magnetic field strength is evolving with time, however, for the ns long LAP bunch the magnetic field can be considered flat and uniform. Even if this lower energy LAP bunch traverses through a 7 m drift length (approximate traversing length of the prospective beamline design) before entering a pulsed magnet, only a maximum increase of about 8 ns is expected in its bunch length, and the pulsed magnetic field can be considered uniform for up to few hundreds of ns. The higher energy protons will take even lesser time. This also makes it less complicated to sequence the trigger for a series of magnets along the prospective beamline, as LAP bunches will take only few tens of ns to traverse through the beamline and peak magnetic fields can be considered uniform for an order of magnitude higher than the traversing time. Thus, the shape of the current pulse, and hence the magnetic pulse, stays constant for the traversing ns LAP bunches and hence all the particles would experience the same Lorentz force. There is no practical need to solve equations of motion for varying dB/dt magnetic fields and the solutions presented in the section 3.1 and 3.2 for designing beamlines remain valid.

The design and development of pulsed magnets poses two major challenges. First, the missing iron-core means thick current carrying wires are required to be wound to shape a specific magnetic field region of interest. This is in contrast to conventional resistive magnets where the iron-core can be shaped precisely to shape complicated magnetic field regions, e.g. hyperbolic curved poles with tangential shimming in quadrupoles to ensure fine magnetic field adjustments. Secondly, the pulsed magnets require energies E_{ind} in the range of few tens of kJ per pulse, thus, the mechanical stability of the magnet structure should be capable of withstanding pressures in the range of GPa. It is crucial to know the realistic limits of the individual pulsed magnets, i.e. solenoid, sector magnet and quadrupole, before using these values for the beamline design.

3.3.1 Pulsed solenoid

A pulsed solenoid was proposed as early as 2009 for capturing LAP bunches and to

control their initial divergence for efficient transport over large distances (up to few meters), as briefly mentioned in section 2.6. The solenoid is a symmetric lens, which means it can provide equal beam control in both x - and y -directions. This allows to use only one solenoid for capture and to make the bunch collimated around a specific energy. The pulsed solenoid with magnetic strength as high as 20 T, with a length of about 15 cm, has been a compact and robust solution. The design, construction and experimental characterization of pulsed solenoid, for capturing of LAP beams of up to 30 MeV energies, has been the topic of several studies, a few are presented in these references (Harres et al., 2010; Burris-Mog et al., 2011; Busold et al., 2015). These experiments established the functioning of the single solenoidal lens and its benefits, i.e. transport efficiency of 34% over more than 2 m with 5 mm diameter beam spot-size. A LAP bunch with a maximum divergence of about 10° (half-angle) otherwise would have a diameter of about 75 cm at this distance, which is practically not useable.

Burris-Mog et al. (Burris-Mog et al., 2011; Burris-Mog, 2012) showed that a pulsed solenoid, for LAP capturing experiment, would require a peak current of about 16 kA at which solenoid (with inductance of about 250 μ H) would experience up to 70 kN radial forces. To deliver such peak currents and to contain such high magnetic pressures special construction methods are required. Figure 3.9 shows the construction of a pulsed solenoid with reinforced insulation layers around thick copper wires. This gives the structure the required strength and stability, and these pulsed solenoids have been very well established in many experimental campaigns (Burris-Mog et al., 2011; Busold et al., 2013, 2014a,b, 2015).

Due to the use of thick (about 4 mm) insulated copper wires and reinforced insulation layers, the solenoid's magnetic field B_{Sol} is not as straightforward as equation 3.20 and one must account for the geometric configurations, for details see (Herlach, 1999). However, B_{Sol} can be determined either via 3D COMSOL (COMSOL, 2017) simulations or Hall effect sensor measurements. The pulsed solenoid used in recently performed and ongoing experiments has the following main characteristics:

- B_{Sol} of about 20 T
- Peak current I of 24 kA (at 24 kV)
- Inductance of 270 μ H
- 120 windings in 4 layers
- Aperture size of 4 cm
- Holds up to 3 GPa radial magnetic pressure.

Equation 3.21 shows that the required magnetic field, for a set focusing strength, is directly proportional to the momentum of the protons (i.e. $B_{\text{Sol}} \propto p_0$). Now, to scale for therapeutic proton energies, i.e. up to 250 MeV, the same solenoid would require up to 50 kA of peak current to reach about 42 T magnetic strength (discussed further in sections 4.2.3 and 5.3.2). This translates up to 12 GPa pressures inside the solenoid structure. This limit has been discussed with colleagues at HZDR and considered to be achievable⁶.

⁶In section 5.3.2 it has been further argued and recommended to use 160 winding solenoid instead of 120 windings, this would potentially bring the structure demand down to 9.5 GPa.

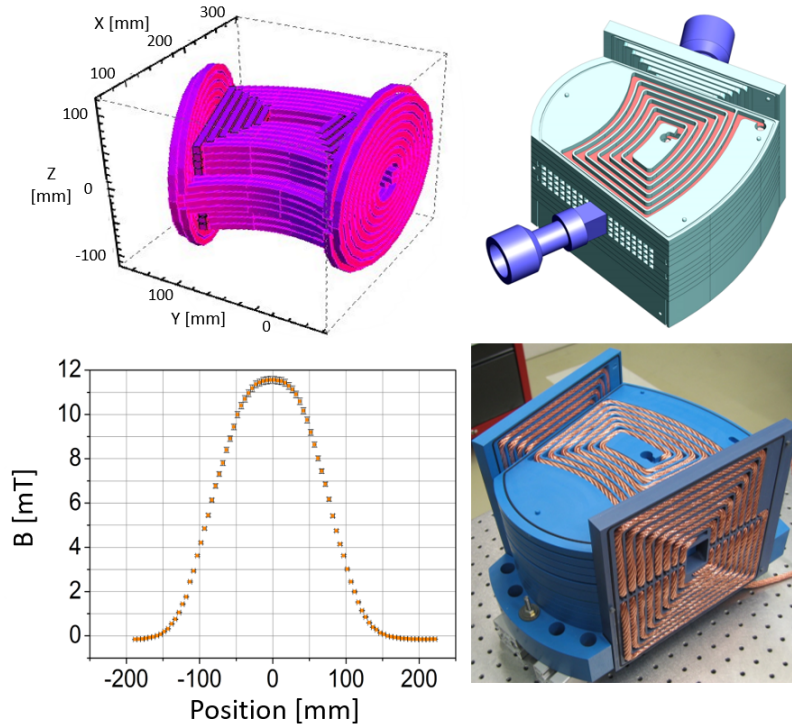


Figure 3.10: 3D simulated current carrying wires in a race-track style geometry (top left) arranged in 20 layers to generate a dipole field region along the beampipe in the middle. 3D model geometry (top right) of solid layers which would provide housing for the wires, insulation and structure integrity to hold immense magnetic pressures. Arrangement of stranded copper rope type wire in the polyurethane housing milled according to the 3D model geometry (bottom right). The magnetic field strength measured with a Hall effect sensor (bottom left), where zero represents the center of the magnet. The maximum field of 11.6 ± 0.2 mT was measured at 20 A (direct current), which would translate to 10 T peak field at 17.24 kA peak current in pulsed mode. Images courtesy of M. Schürer and L. Karsch.

3.3.2 Pulsed sector magnet

The second type of pulsed magnet, which is required for beam deflection around a designed path and crucially for an energy selection system, is a dipole sector magnet. Due to the lack of an iron-core, the current carrying wires must be laid out such that they generate a dipole type magnetic field region of interest in a curved path. For this purpose, an innovative design and construction technique was developed, which lead to a patent design (Schuerer et al., 2016). Please see figure 3.10 for the outline of the design. A race-track style of copper windings were arranged in 20 layers, separated by thin layers of polyurethane plastic. The direction of the current in the windings always compliment the resultant magnetic field lines inside the beampipe. For manufacturing, stranded copper rope was used in a continues manner and hand pressed into the polyurethane layers, which were milled in precise shape to construct a sector shape layout in each layer. The design parameters for the first prototype pulsed sector magnet are as follows:

- Maximum field strength up to 12 T
- Peak current I of 22 kA

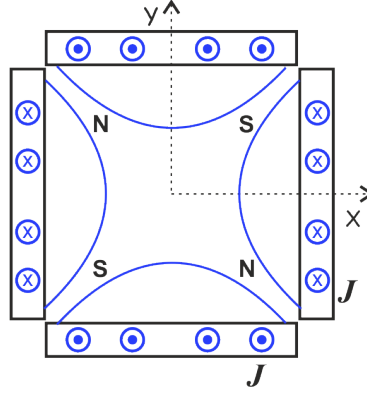


Figure 3.11: Schematic layout of a Panofsky quadrupole, with square box enclosed by current carrying sheets. Iron plates were used in the original design. The current density J is same in the adjacent sides of the square, however, in opposite directions. This results in a quadrupole field inside the box, with zero magnetic strength in the middle and increasing strength towards the current sheets, thus, generating the characteristic magnetic gradients, for further details see (Hand and Panofsky, 1959).

- Inductance of about 420 μH
- Race-track windings in 20 layers
- Bending radius ρ of 30 cm
- Bending angle φ of 50°
- Aperture size of the beampipe of 3 cm.

The first prototype has been successfully tested with up to 5 T. This magnet can theoretically reach up to 12 T peak field values, as per designed parameters. However, it has not been tested yet to its maximum value. Figure 3.4 shows an elliptical beam path inside the sector magnet, rather than the usual circular arc length. For the equations of motions, described in section 3.1.2, the total bending radius ρ_0 would remain the same, as it is only measured in between the entry and exit points. However, the arc length l_{SM} would be slightly longer. For first order beamline calculations this has been ignored. A second prototype pulsed sector magnet is being designed for 90° bending angle and with improved features, such as water cooling mechanism and larger aperture size. The preliminary results show that it is feasible to design and construct a 90° sector magnet with up to 10 T.

3.3.3 Pulsed quadrupole

The final magnetic element for the beamline is a pulsed quadrupole. The pulsed quadrupole was designed in this thesis. Again, no iron-core means the typical quadrupole field (see figure 3.3) must be shaped via the current carrying wires in the similar manner as pulsed solenoid and pulsed sector magnet constructions.

For the basic design, a Panofsky quadrupole layout has been preferred here over the conventional design in which four hyperbolic poles carry the magnetic flux, shown in figure 3.3. A Panofsky quadrupole is a box type magnet enclosed by thin sheets of current carrying plates (Hand and Panofsky, 1959). When the direction of current is opposite,

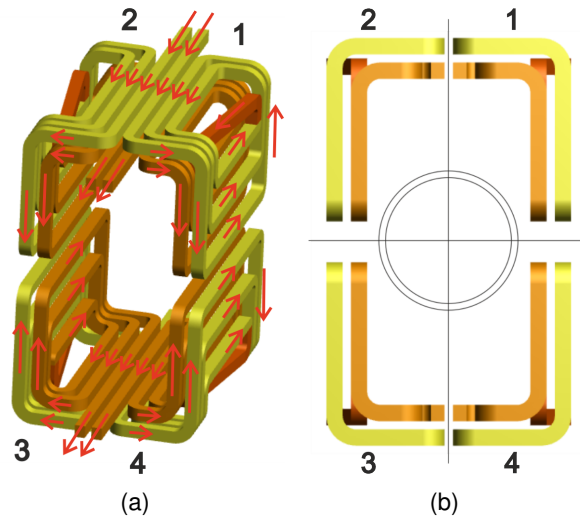


Figure 3.12: (a): 3D structure of a prototype pulsed quadrupole with two layers, and 4 quadrants (marked with numbers 1 to 4). The direction of current is shown with red arrows. Each quadrant has one input connection and one output connection, i.e. two input and output connections per side of the rectangular layout. All 4 quadrants are fed current simultaneously. (b): Beam's eye view of the quadrupole, the black circle shows the beampipe and represent the region of interest, where the magnetic field gradients must provide uniform quadrupole type focusing.

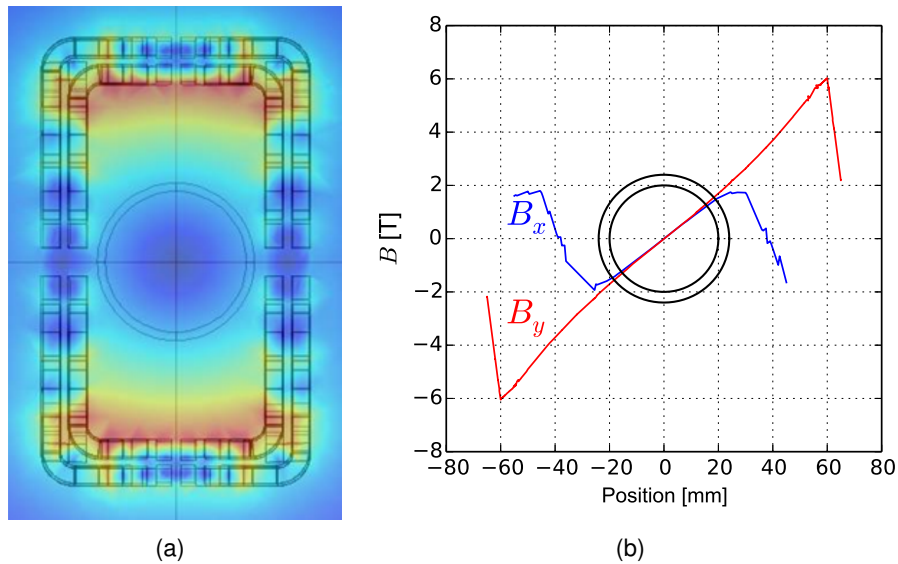


Figure 3.13: (a): Magnetic field map along the central plane, calculated via 3D COMSOL simulations for the 3D geometry shown in the figure 3.12. The black circles in the middle represent the beampipe aperture, with inner and outer radii of the beampipe. (b): Magnetic field as a function of position in the central plane, i.e. B_x as a function of the position along the x -axis (blue line) and B_y as a function of the position along the y -axis (red line). The black circles represent the beampipe as in (a).

with same current density, in two adjacent sides then it results in a quadrupole type field inside the (square) box, see figure 3.11. For the design of the pulsed type quadrupole, the current carrying plates have been replaced by current carrying copper wires, and the square shape is changed to a rectangular shape. Due to the rectangular shape, the length of one side needs to be twice that of the adjacent side and the short side has twice the current density. This means that the magnetic gradients in both directions remain the same.

The preliminary design was developed using a 3D magnetic field computing code called Radia (Chubar et al., 1998). The basic design requirements were that the wires must be thick, at least 4 mm, to carry large values of current and there must be a minimum gap of 2 – 3 mm between wires so that insulating materials can be inserted in the construction phase. The main challenge was to design a layout so that the direction of the current in one side always remains the same. To achieve higher current density, two layers of wires were considered (for the first prototype design) and the difference in current density between two adjacent layers was maintained by twice the gap size between the wires along the longer side compared to the short side of the rectangle. Each side has two input connections and the current flows in four sections (called quadrants), please see the figure 3.12 for the detailed view of the geometry layout. After, the preliminary study the design was converted into 3D COMSOL model (COMSOL, 2017), which allowed for the detailed study of the magnetic field strengths, maps and current values, please see figure 3.13 for details. The main design features are:

- Field gradient up to 150 T/m
- Peak current I of 40 kA
- Inductance of about 30 μ H
- 4 quadrants and 2 layers
- Aperture size of the beampipe of 4 cm.

This model was then used for the construction design, which was mainly done at the engineering department at HZDR, where it was suggested and decided to use thick copper sheets instead of wires. The copper sheet was cut, via laser-cutting, in a flat wire like pattern and then bend to form a corner, i.e. constitute part short side and long side of the rectangular design. Two of these corners were welded with a small bridge connecting them (and to allow the flow of current) to form one quadrant with two layers, see figure 3.14. Four of these welded quadrants would then form a full rectangular pulsed quadrupole. Such construction type was never been used before for magnets, designed to hold current values in the range of tens of kA. The single prototype quadrant (shown in figure 3.14) was constructed and tested by supplying pulsed currents of up to 20 kA (which was at the limit provided by the capacitor bank for low inductances). The prototype quadrant held physically the flow of high peak currents and then the construction of the full quadrupole was begun. Figure 3.15 shows the 3D construction model with polyurethane and Kapton insulation layers, necessary for the structural integrity. The first prototype quadrupole has been manufactured and is ready to be tested. The design features can cater for LAP beams with up to 100 MeV energies (i.e. magnetic rigidity ($B_0\rho$))

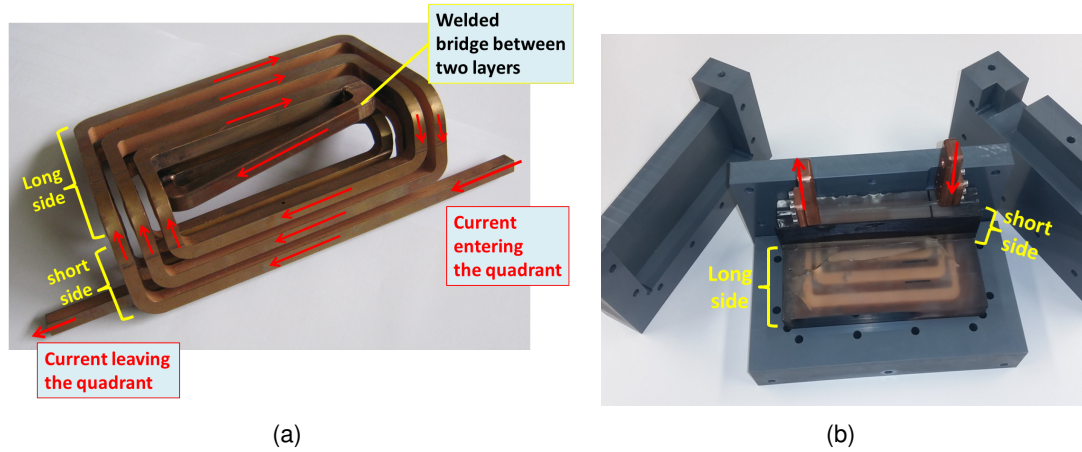


Figure 3.14: (a): Single quadrant of a pulsed quadrupole, with two layers welded together via a bridge connection, also see the figure 3.12(a). Each layer was cut via laser-cutting out of a solid copper sheet, and then 90° bend was made for the rectangular geometry. The direction of current are shown in red arrows. (b): Same quadrant in an epoxy for insulation and test-bed for testing, and with terminals designed for providing current pulses (red arrows).

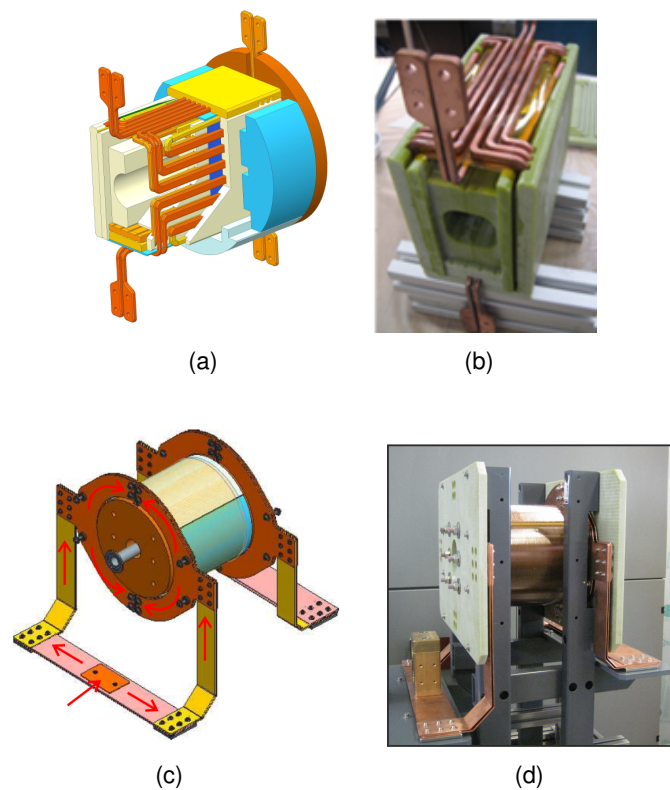


Figure 3.15: (a): 3D design layout of the coils of the quadrupole along with the insulation layers in between. The insulation layers consist of many polyurethane and Kapton pieces. (b): Physical construction of the designed model. (c): Concealed 3D construction model of the quadrupole coils. The direction of the current (red arrows) which can be supplied through the specially designed copper plate terminals. (d): Completed and ready for test quadrupole with the test-stand. Images courtesy of M. Sobiella.

Table 3.1: Upper limits for different types of pulsed magnets which are to be used for the gantry design studies.

Magnet type	Maximum k strength [m^{-1}]	Maximum magnetic field strength [T]
Solenoid	$k_S = 8.64$	$B_{\text{Sol}} = 42$
Sector Magnet	-	$B_0 = 10$
Quadrupole	$k_Q = 10$	$B_{\text{pole}} = 12$

of 1.432 Tm). The second prototype pulsed quadrupole is being designed for 250 MeV proton beams, which may have up to 4 layers (perhaps a square form rather than rectangular layout) and could reach gradients of about 250 T/m, i.e. k_Q of about 10 m^{-1} , and with larger beampipe aperture to cater larger beam sizes.

3.3.4 Limits for gantry design studies

The demand from a compact gantry design would push pulsed magnet designs to achieve higher magnetic field strengths with compact and efficient designs. The design studies of current and future pulsed beamlines and the advancement in pulsed magnet technology go hand-in-hand. However, the gantry design being developed here must assume realistic and achievable pulsed magnet parameters. Furthermore, currently high-field pulsed magnets have low repetition rate, of about 0.1 Hz, which mostly is limited by the charging of the capacitor banks. Research and development of highly efficient, 10 Hz, high-power, compact capacitor banks to power multiple pulsed magnets is also being done (Wettengel, 2014). A 10 Hz system can be achievable in foreseeable future. Therefore, on the basis of the recent experiences in the development of pulsed magnet technology, the upper limits for the pulsed magnets with 10 Hz repetition rate are shown in table 3.1. Those have been considered for designing the gantry system.

Chapter 4

Preliminary Gantry Solution

4.1 Motivation

The concept to employ high-power laser pulses to generate energetic proton beams on μm scale and to utilize these LAP beams for PT to reduce the size and associated costs, has been presented in detail in chapter 2. A new compact 360° rotatable gantry design based on high-field pulsed magnets for laser-driven sources is presented here. LAP beams have different features than conventional beams, i.e. intense ps – ns bunches, large initial divergence, broad energy spectrum, and thus require a gantry with multiple integrated functionalities to control the LAP bunches, e.g. capture controls, energy selection, achromatic beam transport of broad energy bandwidths.

A basic 1D dose model is presented which was developed to generate clinically relevant flat-top SOBP using LAP bunches with filtered large energy bandwidths. This dose model provided the basic criteria for the ESS and acceptance of the gantry beamline in question. Principal requirements are summarized and then a first approximation gantry design which has multiple integrated functionalities is presented. This preliminary solution shows the possibility of a compact gantry system which can fulfill the rudimentary clinical requirements.

4.2 Materials and Methods

4.2.1 Broad energy assorted depth dose deposition model

In conventional PT, the depth dose deposition calculations consider mono-energetic Bragg peaks and their weighted superposition to achieve a flat-top SOBP to cover the full extend of a tumour (as explained in the section 2.5.1). Nevertheless, SOBPs require a certain energy range which is provided by degrading the mono-energetic beam through a passive system in cyclotron based PT systems. The required extent of the energy window may already be available in the initial LAP spectra, and the available number of protons per bunch can be utilized efficiently to achieve similar SOBPs.

A new depth dose deposition model has been devised, in which 1D SOBPs were realized by the superposition of the depth dose profiles of individual LAP bunches with

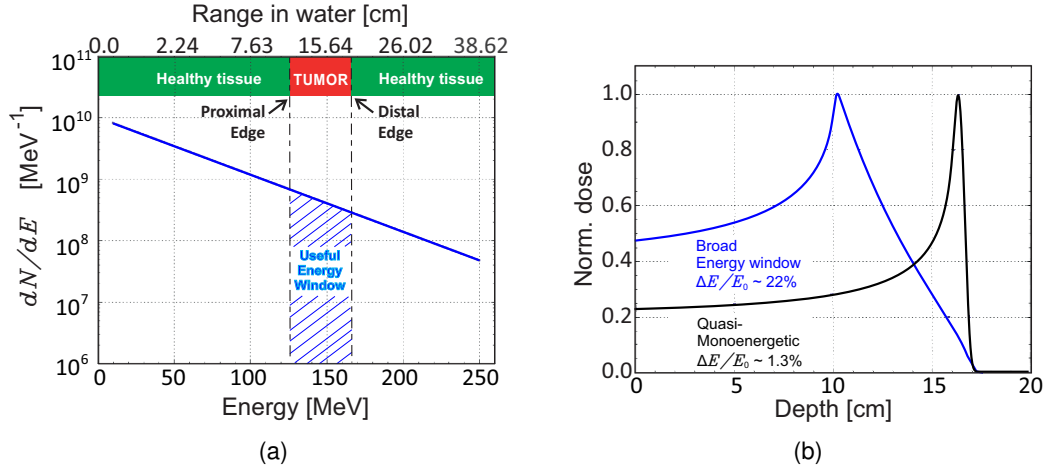


Figure 4.1: (a): TNSA like scaled exponential function (solid blue line) for energy spectrum of laser-accelerated protons. The top horizontal axis displays the range in water for protons with corresponding energies given on the bottom axis. The tumour position, as an example, is marked by a red bar, while the “useful energy window” corresponding to the tumour extent is hatched in blue. (b): Comparison between depth dose profiles of two LAP shots with a broad energy band of $\Delta E/E_0$ of about 22% (blue line) corresponding to the “useful energy window” in (a), and a narrow energy band of $\Delta E/E_0$ of about 1.3% (black line) similar to a pristine Bragg peak as used in conventional PT systems.

varied energy bandwidths. In the following, this technique is referred to as Broad Energy Assorted depth Dose deposition (BEAD) model. In order to understand the BEAD model, let us consider an arbitrary TNSA like LAP source capable of delivering clinically relevant proton energies and a tumour to be irradiated with certain depth and extent, see figure 4.1. The energy windows to be selected to create a SOBP within the tumour region must lie within the proton range set by the minimum energy E_{\min} , corresponding to the depth of the proximal edge of the tumour, and the maximum energy E_{\max} , corresponding to the depth of the distal edge of the tumour. The energy window thus defined by $\Delta E = E_{\max} - E_{\min}$ with centered nominal energy of $E_0 = (E_{\max} + E_{\min})/2$ can be referred to as the “useful energy window” within the initial spectrum. If this $\Delta E/E_0$ band could be filtered out, its depth dose profile is neither a flat-top SOBP nor a pristine Bragg peak, but displays a peak and bounded plateau situated within the tumour region, see figure 4.1(b). In this example, it is assumed that a single filtered LAP bunch does not deliver the clinically prescribed dose and multiple LAP bunches are required to be superimposed to achieve this dose level. Also, as one LAP bunch can be filtered out to limit the energy window to specific settings, this is from here on referred to as *shot-settings*, and multiple LAP bunches can be filtered through single shot-setting.

The figure 4.2 shows a schematic example, representing a single field uniform depth dose regime with the BEAD model by superimposing several individually filtered LAP bunches. The first LAP bunch was filtered through a specific shot-setting, say shot1, with energy windows $\Delta E_{\text{shot1}}/E_{0(\text{shot1})}$ of 21.4%, required to produce a baseline dose profile covering the entire tumour depth. The second LAP bunch was delivered with a narrowed energy window setting (shot2) of ΔE_{shot2} , as compared to the shot1 while increasing

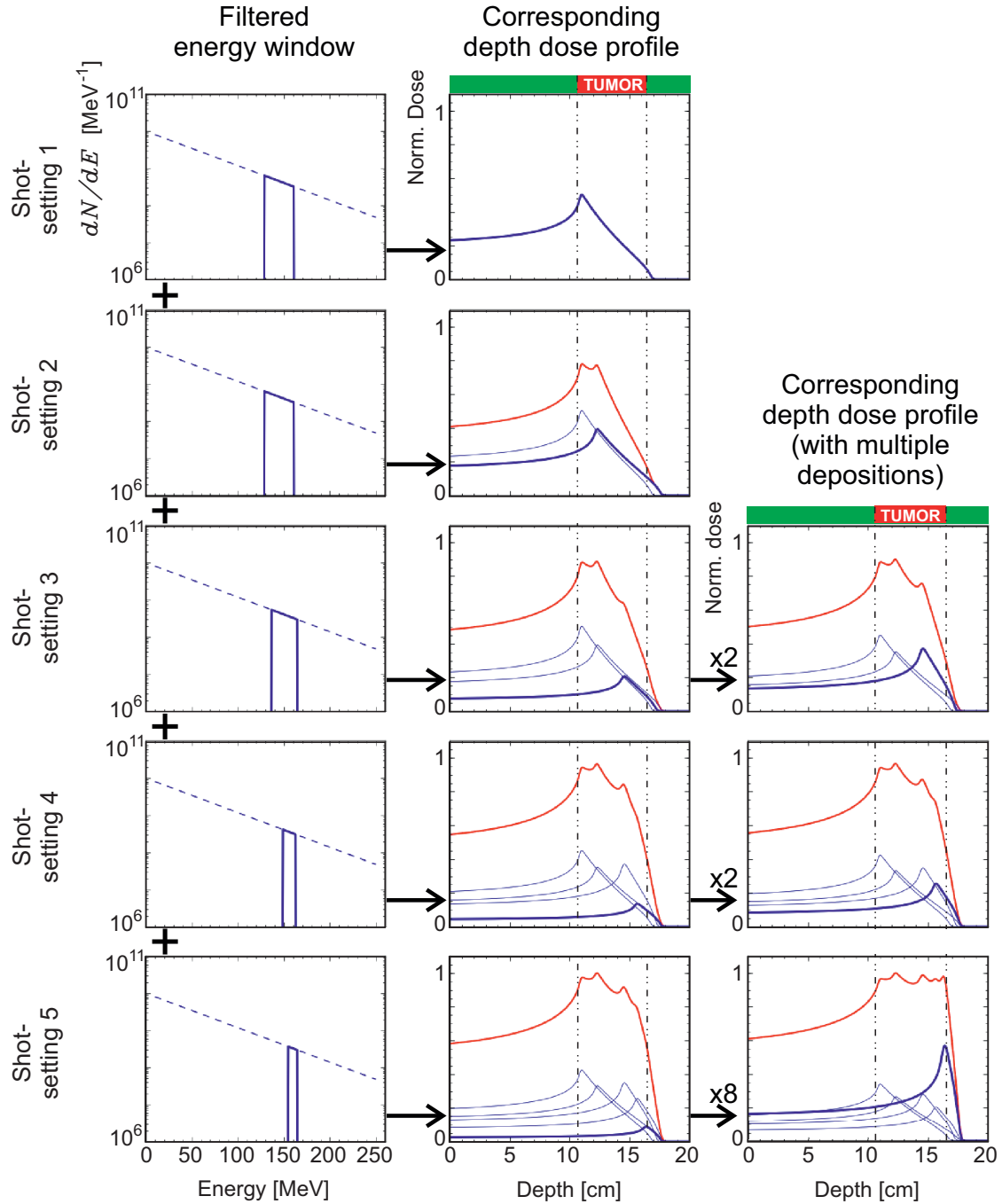


Figure 4.2: Illustration of the BEAD model. The resultant SOBP (red line) as it evolves due to superimposing energy-filtered individual LAP bunches. The column of figures marked as *filtered energy window* shows the initial energy spectrum (dashed blue line) and filtered energy window (solid blue line). The next column of figures show *corresponding depth dose profile* of that energy window (bold blue line). *Shot-settings 1 – 5* represent different settings required for filtering the corresponding width of the energy window. The last column (right most) shows dose profiles when multiple LAP bunches were filtered through the same corresponding *shot-settings* and deposited.

nominal energy $E_{0(\text{shot}2)}$ to fill the shallow dose region towards the distal edge. This implies E_{\min} for the next consecutive shots to be greater than the previous shot, such as $E_{\min(\text{shot}1)} < E_{\min(\text{shot}2)} < E_{\min(\text{shot}3)} \dots < E_{\min(\text{shot-last})}$. The second shot-setting (shot2) was set so that a LAP bunch with $\Delta E_{\text{shot}2}/E_{0(\text{shot}2)}$ of 18.5% was filtered and superimposed on shot1 (second row in the figure 4.2). Due to the exponentially decreasing energy spectrum, LAP bunches with shot-settings of smaller $\Delta E/E_0$ windows and with increasing E_0 contain less protons, and thus multiple deposition of LAP bunches would be needed to flatten the cumulative dose profile. For this reason, two LAP bunches were needed for each of the shot-setting 3 (with $\Delta E_{\text{shot}3}/E_{0(\text{shot}3)}$ of 8.60%) and shot-setting 4 (with $\Delta E_{\text{shot}4}/E_{0(\text{shot}4)}$ of 6.0%). The last shot-setting (shot5) was used to deposit eight LAP bunches, because of relatively smaller $\Delta E_{\text{shot}5}/E_{0(\text{shot}5)}$ of 3.60% containing less protons, to achieve a flat-top SOBP.

The flatness (or dose homogeneity) of the resultant SOBP could be enhanced by decreasing the energy step between two consecutive shots, i.e. decreasing $E_{0(\text{shot } i+1)} - E_{0(\text{shot } i)}$. The total number of LAP bunches, N_{LAP} , required would also then increase, which would directly translate into longer treatment times. Thus, for a specific treatment plan, there is a trade-off between required flatness and treatment time. In this example, a total of 14 individual LAP bunches were needed for a normalized SOBP with an acceptable uniformity of less than $\pm 4\%$, using 5 different shot-settings.

It was found that $\Delta E/E_0$ of 22% to 3% bands were sufficient to produce a normalized SOBP of ~ 5 cm width at depths of 5 – 25 cm. The total number of LAP bunches N_{LAP} required to deliver a homogenous dose to the complete depth of the tumour for a prescribed dose depends on three sets of factors:

1. LAP bunch properties, such as characteristic slope of the spectrum, total number of protons per energy range and repetition rate.
2. Tumour related aspects, such as tumour width and depth, and required uniformity of the delivered dose.
3. Beamline (gantry) parameters, such as energy acceptance, capture and transport efficiencies per energy window.

The first set could be considered predetermined due to the features of the laser-particle accelerators, while the second set could also be considered fixed due to the clinical requirements. However, the third set rely on the transport beamline and gantry system. The conventional beam optics and beamlines have been developed only for small sized beams, i.e. with $\Delta E/E_0$ of about 1%. Although, large transportable $\Delta E/E_0$ windows would provide efficient proton use for larger tumours, it is challenging to control and transport of large $\Delta E/E_0$ bandwidth beams. Therefore, as a trade-off, in the case for the intended gantry design, beams with large $\Delta E/E_0$, ranging from 22% to 3% bands for all therapeutic proton energies, could be considered for designing efficient, large acceptance beamlines for efficient dose delivery for acceptable short treatment times.

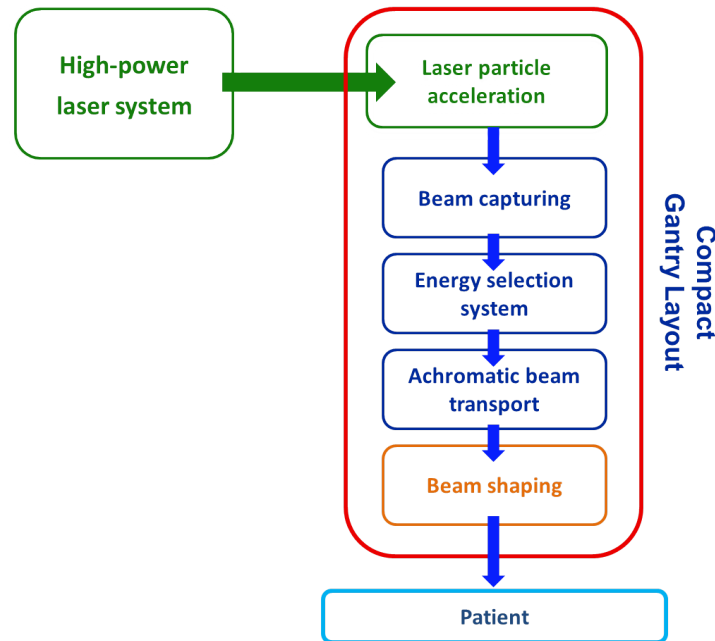


Figure 4.3: Schematic illustration of a laser-driven PT system concept. Intense laser pulses from a high-power laser system are delivered to the laser-target chamber via optical transferlines (green arrow). For a compact layout the laser-target chamber has been considered as a part of the gantry (represented by the red box). The laser-driven protons (represented with blue arrows) generated in the chamber then enter in the magnetic part of the gantry (represented with blue boxes). LAP bunches must be captured, energy sorted and then transported. Before exiting the gantry beam shaping equipment (orange box) could be used to match the beam laterally to the tumour dimensions. Then the beam can exit the gantry and reaches the patient site (light blue box).

4.2.2 Principal requirements from the gantry

A large acceptance compact gantry system is required with multiple functionalities to utilize LAP bunches for clinical applications with maximum possible transport efficiency η .¹ The required functionalities are schematically illustrated in figure 4.3, and the principal requirements are listed below:

1. The first function is to capture the LAP bunches and to control the intrinsic, large divergences and transverse dimensions, as discussed in the sections 2.4.3 and 2.6. This is necessary for maximum beam transport efficiency and control of the LAP beam downstream.
2. Secondly, an ESS is necessary to filter variable energy widths per bunch (ranging from 22% to 3%) from the initial broad-energetic spectrum of the LAP bunches, as discussed in the above section 4.2.1. This is a necessary function for efficient and precise dose delivery and to restrict already present protons with unwanted energies.
3. The large beams (in size and energy width) tend to blow up, especially behind a

¹Transport efficiency is defined in section 2.6, as the fraction of transported protons with respect to the initial number of protons in a 1 MeV band around the desired nominal energy E_0 .

dispersive magnet (i.e. sector magnet) which is necessary for ESS. Therefore, the whole beamline should be achromatic for all beamline settings, i.e. canceling the dispersive effects introduced by the energy selection. This is a crucial function for the delivery of homogeneous beams and thus homogeneous dose distributions.

4. Different beam sizes are required in clinical settings and a beam shaping device must also be included to restrict the lateral extent of the beam. A physical collimator, similar to the conventional passive scattering systems, could work.
5. It is also necessary that the whole gantry must have large acceptance, this means all the magnets and drift spaces must have large beampipe radius, to transport beams with large $\Delta E/E_0$ and size (further explained in section 4.2.3).
6. Finally, all elements must be arranged in a gantry formation to rotate these beams around an isocentre for multi-directional tumour irradiation.

Now, the first step is to develop a mathematical model for the gantry design based on the first order linear beam optics, presented in chapter 3. In the design studies, few models were devised and calculated with the beam optics formalism, with different layouts of the magnetic elements, but tracking simulations showed undesired results, as the beams with large spectral distributions are not always well-described by the linear model and become difficult to control. Here, only the best agreed design is presented. The main functions of this gantry model are explained below one-by-one, along with the matrix formalisms.

4.2.3 One-step beam capture and collimation

The LAP bunches require efficient capturing due to the large initial divergences to control and prevent losing the beam. A single pulsed solenoid has already been investigated and established as a LAP beam capturing lens in many experiments (Burris-Mog et al., 2011; Busold et al., 2013, 2014a,b, 2015) and has been proven to conserve and transport about 20 – 30 times more protons than a collimator system (no magnetic capturing element) over a distance of 1 – 2 m. Therefore, it is a good place to start for the capturing system for the gantry design.

A solenoid acts as a symmetric chromatic focusing lens, as discussed in section 3.1.3. The magnetic field strength B_{Sol} can be adjusted via the provided current $I = 2GB_{\text{Sol}}/\mu_m n$, where G is the geometric factor, μ_m is the permeability of the air-core and n is the number of windings per meter. For the capturing system of the gantry, a single pulsed solenoid has been considered with an aperture diameter of 4 cm and is positioned at 7.5 cm downstream from the LAP source, see figure 4.4. A 4×30 windings solenoid structure was considered, with solenoid length l_S of 18 cm. These parameters have been taken from the solenoid which has been routinely used in the experimental campaigns (cf. section 3.3.1). The transfer matrices for solenoid M_{Sol} and drift space M_{Drift} (see equation 3.22 and 3.23) have been used to define this first beamline section M_{Capt} .

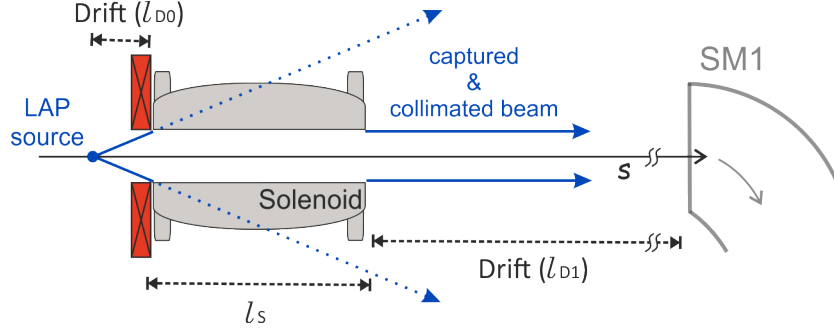


Figure 4.4: Schematic illustration of a single lens capture and collimation system based on a pulsed solenoid. The dotted blue lines show the beam without a capturing solenoid, while the solid blue lines show the captured and collimated beam. The red rectangle represents an aperture to restrict the stray particles with higher divergences than the collection angle of the solenoid and to protect the solenoid. It is evident that without a capturing lens the beam size would grow and most of the beam would be lost. The collimated beam is then transported to the following beamline element, in this case a 90° bending sector magnet (SM1).

$$M_{\text{Capt}} = M_{\text{D1}} M_{\text{Sol}} M_{\text{D0}} \quad (4.1)$$

and $\sigma_1 = M_{\text{Capt}} \sigma_0 M_{\text{Capt}}^T,$

where σ_0 represents the initial LAP beam parameters while σ_1 represents the beam parameters behind the beamline section M_{Capt} , M_{D0} represents the drift space D0 of length l_{D0} of 7.5 cm between proton source and the solenoid and M_{D1} represents the drift space D1 with length l_{D1} between solenoid and the next magnetic element, which was chosen to be 50 cm. The focusing strength of the capturing solenoid k_s was now calculated by using the equation 4.1 for the condition that $\epsilon\gamma$ is minimum behind the solenoid. This means the beam is collimated (i.e. has minimum divergence) around E_0 symmetrically in x - and y -planes. The set of equations 4.1 can be solved for this condition and then M_{Capt} is used to extend the beamline further. This step wise problem solving technique has been used throughout. The solenoid can only be optimized for collimating protons of single energy E_0 , the protons with $E > E_0$ experience less focusing strength and protons with $E < E_0$ experience higher focusing strength. Beams with large momentum spread δ grow in size with drift length, which directly relates to the large $\beta(s)$ values, i.e. large beam envelope. The acceptance A of any magnetic element is the size of the beampipe running through the magnet and can be defined as:

$$A = R^2/\beta(s) \quad [\text{mm mrad}], \quad (4.2)$$

where R is the inner radius of the aperture of the beampipe. It is difficult to control the Twiss parameters for the large δ beams (i.e. with large momentum spread). Furthermore, it is important to keep the radius R of the beampipes large enough for maximum transport efficiency and small beam envelopes. This demands larger magnetic field region from all magnetic elements, which would complicate the design requirements of the pulsed magnets. Therefore, a maximum value of $\Delta E/E_0$ of about 22% to be filtered and transported to the patient site would be a good compromise between equipment design, beam control

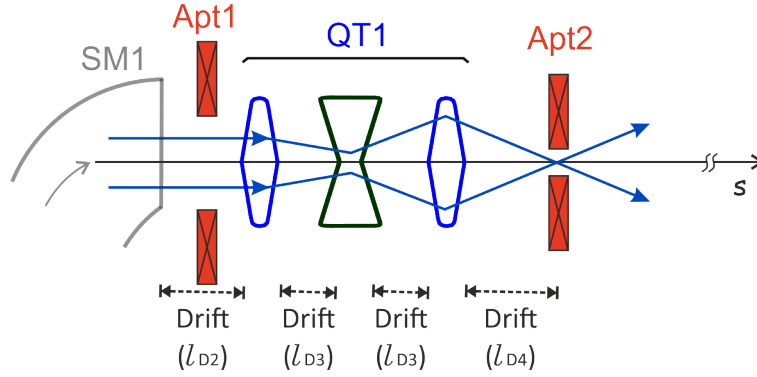


Figure 4.5: Schematic illustration of the energy selection system, i.e. ISESS, behind the beam bending magnet SM1. The blue arrows represent the proton beam with nominal energy in the bending plane, downstream of the capturing system (shown in figure 4.4). The first aperture Apt1 (red squares) is to limit protons of much higher or lower energies than desired energy bandwidths. Quadrupole triplet QT1, consisting of three quadrupoles with focusing, de-focusing and focusing strengths in x -direction, respectively. Focusing quadrupoles are represented by convex lenses (blue) and the de-focusing quadrupole is represented by a concave lens (dark green) (these symbols are used through out this work). QT1 focuses the beam at the center of the energy selective aperture Apt2.

and transport, and for efficient treatment dose delivery options.

4.2.4 Energy selection system

Laser-driven sources have large energy spread and require an efficient energy selection system. An energy filtering system has been devised and incorporated in the gantry design. This Integrated Shot-to-shot Energy Selection System (ISESS) is based on a 90° bending sector magnet SM1 (with the bending radius ρ_0 of 30 cm) and a quadrupole triplet QT1 with two physical apertures, see figure 4.5. A 90° dipole bending magnet provided two integrated functionalities, i.e. it bends the beam, which is necessary for an isocentric gantry arrangement, and the dispersion introduced in the beam allows energy selection. The dispersion (equation 3.18) introduced by the bending magnet can also be described as:

$$D(s) = \Delta x / \delta, \quad (4.3)$$

where Δx is the separation of the mean position of the particles with Δp momentum difference from the ideal momentum p_0 particle on the ideal path defined by the B_{SM} of the bending magnet. This energy dependent spatial spread provides the necessary condition for energy selection, however, the beam diameter at this point is large due to the solenoid's large inner radius which was necessary for maximum capture efficiency, therefore, high resolution energy selection is not possible with SM1 only. An Aperture (Apt1) is placed after SM1 to restrict the further transport of protons of much higher or lower energies than the desired energy bandwidths. For fine-tuned selection a pulsed quadrupole triplet (QT1) follows SM1 which acts as a strong chromatic focusing lens. The magnetic gradients can be tuned to focus protons with E_0 at 15 cm behind QT1. An aperture (Apt2)

with variable opening radius R_{Apt2} is placed at this focal point. The objective is to select momentum spread δ (hence $\Delta E/E_0$) as a function of the radius R_{Apt2} of the principal energy selective aperture (Apt2) behind the QT1. This would effectively filter protons around p_0 (hence around E_0). The imaging parameters of the QT1 and the drift length in-between can be calculated by the following matrix equation:

$$M_{\text{ESS}} = M_{\text{D4}} M_{\text{QuadX3}} M_{\text{D3}} M_{\text{QuadY2}} M_{\text{D3}} M_{\text{QuadX1}} M_{\text{D2}} M_{\text{SM1}} M_{\text{Capt}} \quad (4.4)$$

and $\sigma_2 = M_{\text{ESS}} \sigma_0 M_{\text{ESS}}^T.$

In the equation 4.4 M_{SM1} represents the first 90° sector magnet, matrices M_{D2} , M_{D3} and M_{D4} represent drift spaces D2, D3 and D4 of lengths l_{D2} , l_{D3} and l_{D4} , respectively. M_{QuadX} represents the transport matrix for a focusing quadrupole in x -direction and M_{QuadY} represents the transport matrix for a focusing quadrupole in y -direction. The numbers 1, 2 and 3 in the subscripts in the quadrupole matrices specify different quadrupoles with respective focusing strengths, i.e. k_{Q1} , k_{Q2} and k_{Q3} . These three quadrupoles with the drift space D3 in-between them constitute the quadrupole triplet QT1, note here that the drift space D3 is used twice in-between for symmetry. σ_2 represents the beam after the beamline M_{ESS} , whereas, M_{Capt} represents the previous beamline section from the set of equations 4.1. Now, the equation 4.4 can be solved for drift lengths and focusing strengths of individual quadrupoles such that the phase space ellipse parameter $\epsilon_u \alpha_u$ is minimum at the centre of Apt2. Thus, the equation 4.4 can be specifically solved for the following condition:

$$\epsilon_x \alpha_x = \epsilon_y \alpha_y = 0. \quad (4.5)$$

This means that behind the drift length l_{D4} the beam is tightly focused and the beam-waist is symmetric in both x - and y -directions. The energy resolution at this point could be described as:

$$\delta = 2R_{\text{Apt2}}/D(s = z_{\text{Apt2}}), \quad (4.6)$$

where z_{Apt2} is the position of the aperture Apt2 and $D(s)$ is the dispersion function. The equation 4.6 shows that if the radius R_{Apt2} is matched to the beam envelope $env = \sqrt{\epsilon \beta}$ (see equation 3.28) of the beamlet² then only specific momentum spread δ is allowed to pass through the aperture. The R_{Apt2} could be varied for each shot-setting which in turn determines the energy width filtered from the initial spectrum.

4.2.5 Achromatic beam transport

The tightly focused beam behind the energy selective aperture Apt2 would now diverge again. A second quadrupole triplet (QT2) after Apt2 can be placed which would recapture the filtered bunch, followed by a second 90° bending sector magnet (SM2)

²beamlet is the interested part within the whole beam

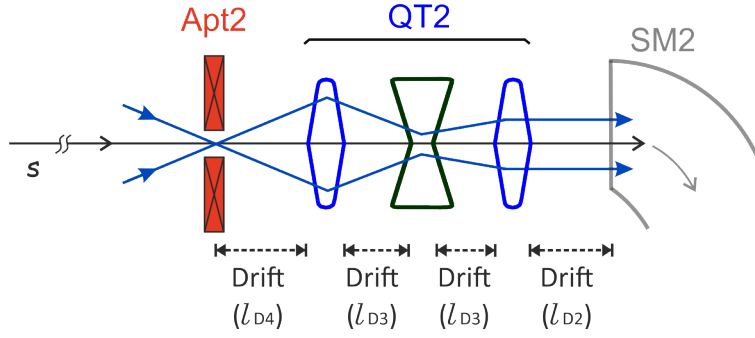


Figure 4.6: Schematic illustration of the recapture and beam bending for achromatic transport, as explained in section 4.2.5. This beamline section mirrors the previous beamline section shown in the figure 4.5. The second 90° bending sector magnet SM2 bends the beam towards the patient site.

which bends the beam towards the patient table, see figure 4.6. The matrix equation now can be extended from equation 4.4 as:

$$M_{BL} = M_{SM2} M_{D2} M_{QuadX6} M_{D3} M_{QuadY5} M_{D3} M_{QuadX4} M_{D4} M_{ESS} \quad (4.7)$$

and

$$\sigma_3 = M_{BL} \sigma_0 M_{BL}^T.$$

Similar to the set of equations 4.4, M_{QuadX} and M_{QuadY} represent focusing quadrupoles in x - and y -directions, respectively. Matrices M_{D2} to M_{D4} represent drift spaces of lengths l_{D2} to l_{D4} , respectively, and have been chosen to be similar to equations 4.4 for symmetry. M_{ESS} represents the previous beamline section and M_{SM2} represents the second 90° sector magnet SM2. σ_3 represents the beam after the beamline M_{BL} . The drift spaces D2, D3 and D4 are used multiple times for symmetry. Now, the above equation 4.7 can be solved for $D(s) = 0$ and $D'(s) = 0$ (called a double-achromatic condition). This magnetic arrangement would cancel the spatial energy dispersion introduced earlier while bending the beam for energy selection in the SM1, hence achieving a double-achromatic transport beamline.

Now, a third set of quadrupoles, quadrupole doublet QD1, was introduced after SM2 which in principle could match the output beam profile in x - and y -directions, for a uniform field size at the isocentre. The final matrix equation for the complete beamline is now:

$$M_{G01} = M_{D7} M_{QuadX8} M_{D6} M_{QuadY7} M_{D5} M_{BL} \quad (4.8)$$

and

$$\sigma_f = M_{G01} \sigma_0 M_{G01}^T,$$

where M_{D5} and M_{D6} represent drift spaces D5 and D6 with lengths l_{D5} and l_{D6} , respectively. M_{G01} represents the whole beamline and σ_f represents the final output beam properties. Now, the above equation 4.8 can be specifically solved for the following conditions:

$$\epsilon_x \alpha_x = \epsilon_y \alpha_y. \quad (4.9)$$

The above condition implies that beam size is symmetric in x - and y -directions, and also

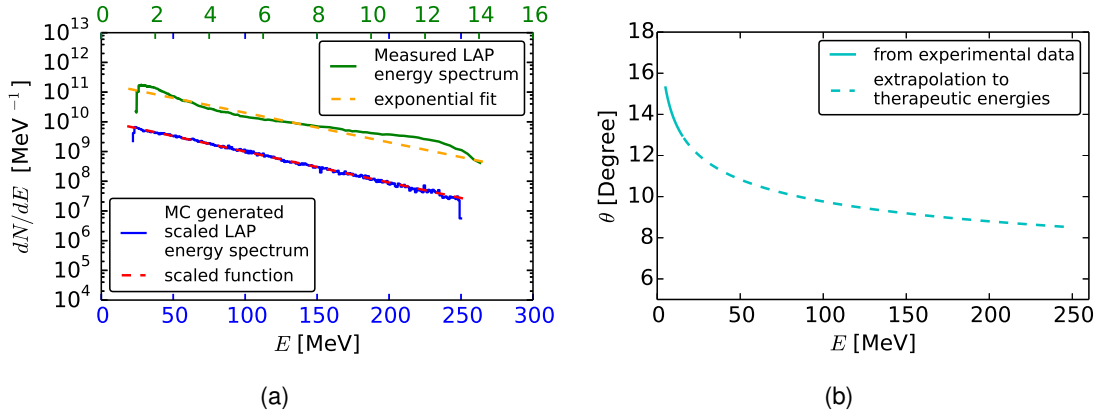


Figure 4.7: (a): Average proton energy spectrum (green line with energy axis on top) measured at the DRACO laser system at HZDR with an exponential fit (dashed orange line with energy axis on top). The scaled function predicts a proton spectrum over therapeutic range and is shown as the dashed red line (with energy axis on bottom), while the blue line shows the spectrum (with energy axis on bottom) of a proton bunch generated via a Monte-Carlo (MC) code. (b): Energy dependent half-angle divergence observed in the experiments (solid cyan line) which was then extrapolated to the therapeutic energies (dashed cyan line).

for the condition:

$$\epsilon_x \gamma_x = \epsilon_y \gamma_y = 0, \quad (4.10)$$

this means that beam is parallel, with minimum divergence. According to this mathematical model, presented by the above set of equations, should now give a well-collimated and uniform output beam from the gantry for the patient irradiation.

4.2.6 Simulated LAP sources

To design a beamline solution for laser-driven PT system, initial beam parameters are required to be used as input. However, to design and investigate a gantry, it is not necessary to consider a specific laser acceleration mechanism and to have pre-determined beam properties. A broad set of characteristic parameters can be defined for the design study, and a robust design would then have the flexibility for optimization once experimental data is known. The intended gantry design must cater therapeutic proton energy range, i.e. 70 – 250 MeV. Therefore, two LAP sources, namely target normal sheath acceleration (TNSA) and radiation pressure acceleration (RPA) like sources, have been simulated with scaled proton energies to the therapy range. These simulated sources gave the initial beam parameters, i.e. σ_0 , needed for mathematical model calculations which then were used in the beam tracking simulations later.

TNSA source: Currently, there is no experimental data available for LAP in the therapeutic energy range. However, for this study the experimental data from the Dresden laser ACceleration sOurce (DRACO) at HZDR, which is a 10 Hz 150 TW ultra-short (~ 30 fs) pulsed laser system (Zeil et al., 2010), has been used and scaled to higher energies. The proton energy spectra from five LAP bunches were averaged and then scaled

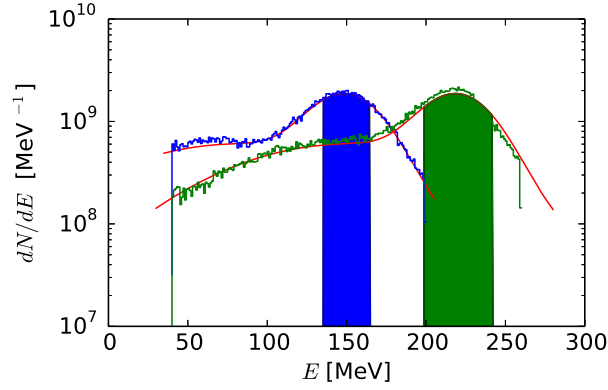


Figure 4.8: Predicted RPA like initial energy spectra (red lines) following the equation 4.13. These functions were then used to generate proton bunches via a MC code, shown by blue and green lines for peak energies E_0 of 150 MeV and E_0 of 220 MeV, respectively. The shaded areas under the respective curves represent proton spectra in the $\Delta E/E_0$ of about 22% energy width, which as an example here was selected to be captured and transported, later, via the gantry design in question.

to the energy range required for therapy, using a similar approach presented in the reference (Burris-Mog et al., 2011), also see figure 4.7 for details. An exponential decay function was fitted to the averaged data, which can be described by:

$$dN/dE = N_0 e^{-\kappa E}, \quad (4.11)$$

where N_0 is the initial (highest) number of protons with a value of about 2×10^{11} (see green line in the figure 4.7), κ is the fit parameter representing the slope of the function with a value of 0.43 and E is the energy of the protons in the spectrum. For scaling this spectrum to therapeutic energy range, the proton energies E observed in the experiments were increased by a factor of $250/14 = 17.86$, and the slope κ was decreased by the same factor. The total number of protons under the fit function 4.11 can be calculated by integrating the function between E_{\min} of 1.28 MeV and E_{\max} of 14 MeV, which is about 3×10^{11} . Now, assuming that the total number of protons available for acceleration is conserved, the scaled function with $\kappa_{\text{scaled}} = 0.024$, $E_{\min} = 22.8$ MeV and $E_{\max} = 250$ MeV, yields a drop in the scaled N_0 to $\sim 1 \times 10^{10}$ (shown in figure 4.7(a) as red dashed line).

Moreover, TNSA sources exhibit energy dependent large divergences, which decreases with increasing proton energies within a bunch. For realistic scaling, this angular dependence of the LAP spectrum has to be accounted for. The half-angle divergences observed in experiments can be defined by a power fit as:

$$\theta(E) = a_{\theta} E^{\kappa_{\theta}}, \quad (4.12)$$

where a_{θ} and κ_{θ} are the fit parameters with values of 19.48 and -0.15 , respectively. The same fit function 4.12 was simply extrapolated to higher E values, i.e. up to 250 MeV, see figure 4.7(b). These scaled functions were then used to generate LAP bunches for simulation inputs by a Monte-Carlo (MC) code, explained later in this section.

RPA source: A RPA like laser-driven source has also been generated. The RPA beam

spectral intensity distribution is described, by Hofmann et al. (Hofmann et al., 2012a), as a bi-Gaussian fit to the simulated results presented by Yan et al. (Yan et al., 2009). This bi-Gaussian fit is:

$$N(E) = N_0 [e^{-((E-E_0)/30)^2} + 0.4 \times e^{-((E-(E_0-70))/100)^2}], \quad (4.13)$$

where $N_0 = 1.5 \times 10^9$. Additionally a maximum divergence half-angle θ of ± 100 mrad ($\sim 5.7^\circ$) was assumed.³ In this acceleration model, the laser parameters, e.g. laser intensity on laser-target, were assumed to be adjustable for controlled acceleration, so that a LAP bunch with $N(E)$ distribution has a selectable peak energy E_0 . This means that E_0 could be shifted via changing the focused laser intensity, which could allow to squeeze maximum number of protons around the E_0 . Although, a RPA like source has superior $N(E)$ distribution, it still contains protons with a wide range of energies, see figure 4.8. ESS is still necessary for any laser-driven PT solution, even for the best known laser-driven sources.

Monte-Carlo LAP bunch generation: Now, what is needed are the Twiss parameters to determine the initial beam parameters σ_0 for the mathematical model calculations. For this reason a MC code was written in Python programming language (version 2.7.8) (Python Software Foundation, 2015) to generate proton bunches with a spectral intensity distribution following equation 4.11 for scaled TNSA like sources and equation 4.13 for RPA like sources. The MC code generated ASCII files with randomly distributed spatial (x, y, z) and momentum coordinates $(\gamma_r \beta_{rx}, \gamma_r \beta_{ry}, \gamma_r \beta_{rz})$, where $\gamma_r = (1 - \beta_r^2)^{-1/2}$, $\beta_r = v/c$ and c is the speed of light. The bunch spot-size (x, y) was set with Gaussian deviation of $2\sigma_g$ of $1.4 \mu\text{m}$ (see figure 4.9) and the bunch length z was set to be ± 1 nm with uniform distribution. These simulated LAP bunches were then used in the calculations and for the beam tracking simulations to mimic laser-driven sources, further discussed in the next sections 4.2.7 and 4.2.8.

4.2.7 Gantry model simulations

To solve the mathematical model developed for the gantry in the last sections, an algorithm was written in the Mathematica computational program (Wolfram Research Inc., 2015) to step wise solve the set of equations 4.1, 4.4, 4.7 and 4.8. This algorithm also included all the beam optics formalisms derived in section 3.1. The initial LAP bunch parameters generated with the MC code (see section 4.2.6) can also be defined by six-dimensional phase space (x, x', y, y', z, p) . This 6D phase space is then used to determine the Twiss parameters $(\alpha, \beta, \gamma$ and $\epsilon)$ using the set of equations 3.26. The beam optics formalism works best with narrow Gaussian beams, therefore, as the first approximation these formalisms were first solved for δ of 1% and then for δ of 50%, this means when the Twiss parameters were determined only particles with specified momentum range were selected. Now, this would statistically define the beam at the initial position $s = 0$.

³There might be an energy dependent divergence, similar to TNSA, however, it is not known at present. Also from the figure 4.7(b) it can be seen that in the higher energy range the divergences do not change much.

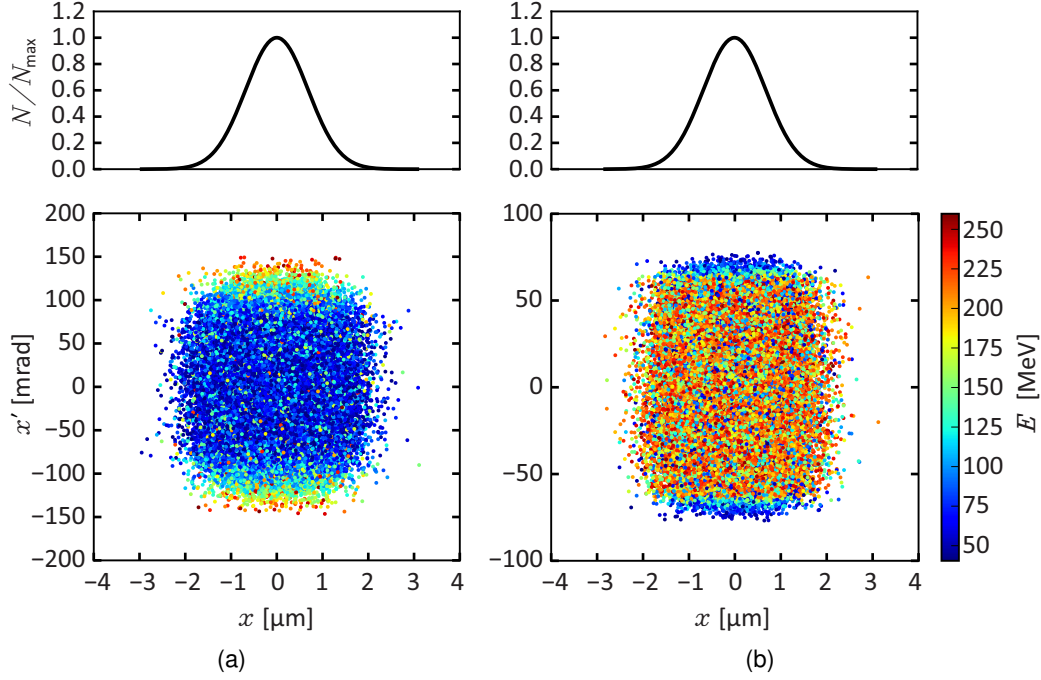


Figure 4.9: MC generated LAP bunches. (a): TNSA like source and (b): RPA like source, as explained in the section 4.2.6. The beam is symmetrical in transverse planes. The graphs on top show the Gaussian profiles of the accumulated beam spot, for all particles of all energies. The TNSA like source has larger divergences compared with the RPA like source (note here that x' axis scales are different and both figures share the energy scale shown on the right side).

Also, the bunch length L can be determined from the 6D phase space (in this case was set to 2 nm in the MC code). This is all the information needed to determine the initial σ_0 representing the beam (also see the equation 3.29), which was the initial information needed for the algorithm. Some of the parameters were chosen to be fixed, e.g. length of the solenoid, quadrupoles, bending radius and arc length for the sector magnets etc., and then solved for the magnetic strengths for each magnetic elements. Few solutions were obtained, however, these formalisms considered hard edge magnetic models and small size beams with narrow momentum spreads. Therefore, it is essential to verify the solutions with beam tracking simulations. The results from this mathematical model are presented in the section 4.3.1.

4.2.8 Beam tracking simulations

In the beam optics formalism Twiss parameters are generally defined for a specific energy with small $\Delta p/p_0$ values. However, in laser accelerated beams, there is a large dependence of transverse characteristics upon the energy of the protons. It is necessary to verify the gantry design determined by the mathematical model via full beam tracking simulations. General particle tracer (GPT) simulation package version 3.01 (Pulsar Physics, 2014) has been used for this purpose. GPT is capable of simulating beams with large spread in beam energy and transverse characteristics, and is fully capable of simulating 3D magnetic fields and other beamline elements such as apertures and collimators.

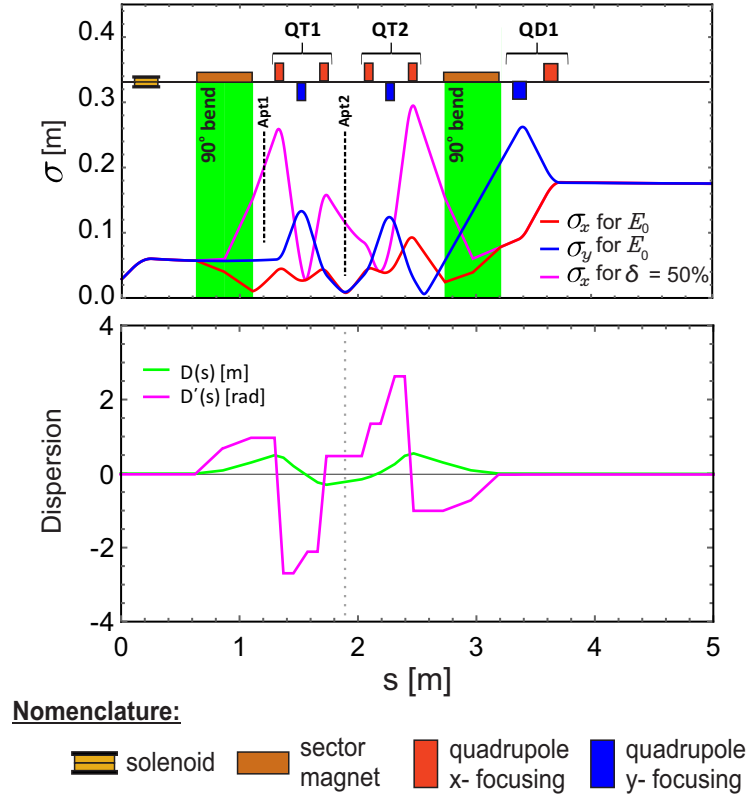


Figure 4.10: Evolution of the beam through the gantry model. The magnetic elements are drawn which were used to manipulate the beam properties, also see the table 4.1. The plot on top shows the evolution in the beam according to the equations 3.27, red and blue lines represent beam in x and y transverse planes respectively, for the beam with the nominal energy, and the magenta line represents the beam in the bending plane, i.e. x -plane, with 50% momentum spread. The bottom plot shows the evolution of dispersion functions along the beamline. This model was then used for the particle tracking simulations, please see figure 4.11 for corresponding magnet positions on the simulated particle tracks and for the whole gantry layout.

GPT uses a fifth-order Runge-Kutta method to solve equations of motion for each particle in the beam (Geer and Loos, 2013). The laser-driven beam sources generated via the MC code (described in section 4.2.6) were converted into GPT readable source files. The magnets were then laid out along the nominal path with magnetic field strengths calculated via the mathematical model of the gantry. Then, the GPT simulations were used to track the beam through the whole gantry in predefined time steps, which were set to be 1×10^{-12} s.

The high performance computing (HPC) facility at HZDR was utilized for the GPT simulations. One simulation would track one LAP bunch (with full energy spectrum and up to 10 million particles per bunch) through the gantry with one set of parameters, i.e. magnetic fields strengths optimized for one nominal energy, aperture sizes etc. One computing node at HPC was used to perform one simulation, and one node consists of 2 – 4 CPUs (Central Processing Units) with AMD Opteron 16-core processors. One simulation could take up to 100 hours to complete, and each simulation writes an output file with the information about $(x, y, z, \beta_{rx}, \beta_{ry}, \beta_{rz}, \gamma_r, m_0, q)$ of every particle in each time step (i.e. few GB of size). Several tens of single simulations needed to be performed in order to

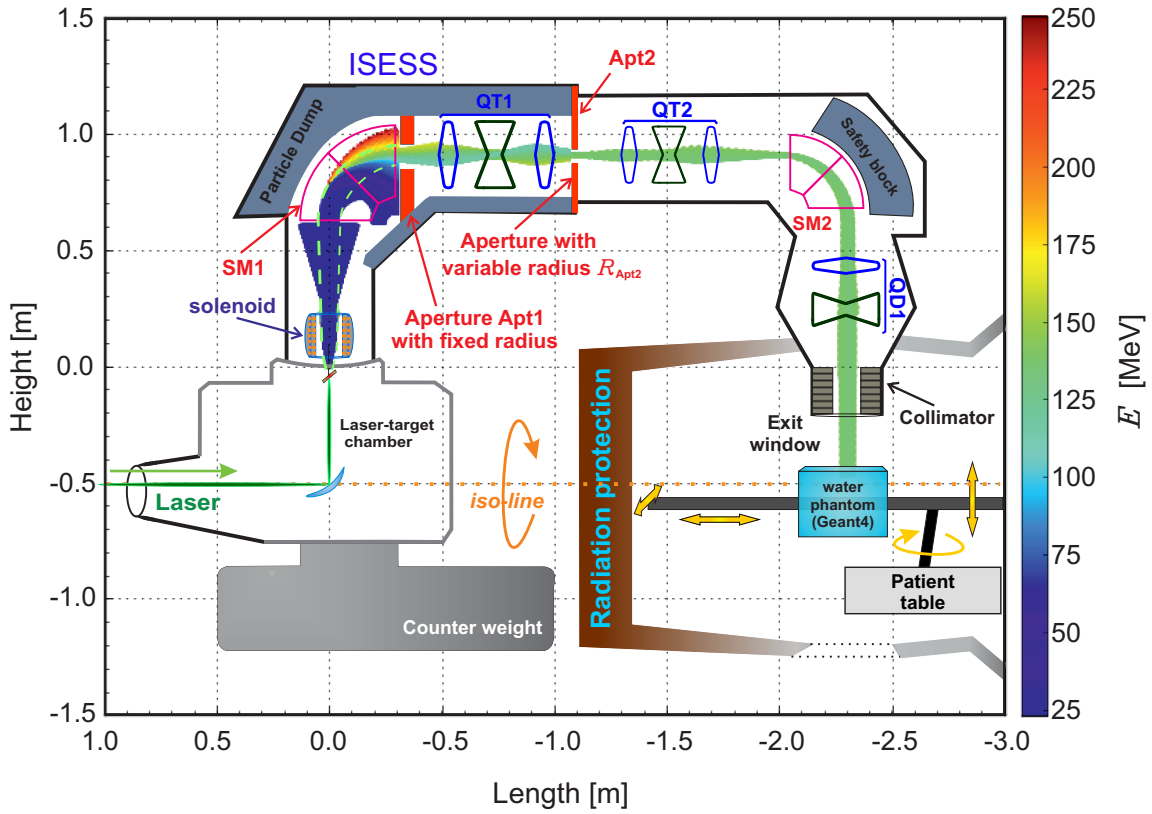


Figure 4.11: Schematic representation of 360° isocentric preliminary gantry design. It also shows the schematic layout of the treatment room including a radiation protection cave around the patient table. For a compact arrangement the idea is to transport laser pulses from the laser system directly into the gantry via optical lines into an integrated rotatable laser-target chamber. Laser pulses could be focused on the laser-target generating LAP bunches. MC generated LAP bunches were tracked through the design. The particle tracks along the beamline are shown with a color map representing the proton energies. The beamline elements are drawn on the tracks to illustrate their positions (also see figure 4.10) with simulated parameters listed in the table 4.1. A water phantom underneath the exit window represents the setup used for the depth dose simulations.

verify different gantry settings. For further analysis of the output data, codes were written in the Python programming language. The results of the mathematical model and tracking simulations are further discussed in detail in the next section 4.3.

4.3 Results

4.3.1 Solution for the gantry model

The mathematical model for the gantry was solved in steps by solving for the desired beam parameters for each function of the beamline, i.e. beam capture, energy selection, dispersion free transport and homogenous field size. The equation 4.1 was solved for the magnetic strength k_S of the solenoid to capture and collimate the beam around E_0 , the results were then plugged into the following beamline section, i.e. energy selection

Table 4.1: List of beamline elements used for the preliminary gantry design, along with the corresponding lengths, start position in the beamline and magnetic strengths for corresponding magnetic elements.

Main beamline component	Beamline element	Start position [cm]	Length [cm]	Normalized strength [m^{-1}]
LAP beam source	-	0	-	-
Capture & collimation section	D0	0	$l_{D0} = 7.5$	-
	Solenoid	7.5	$l_S = 18.66$	$k_S = 4.60$
	D1	26.16	$l_{D1} = 50.0$	-
90° beam bending magnet	SM1	76.16	$\rho_0 = 30.0$ $l_{\text{arc}} = 47.0$	-
Beam restricting aperture	Apt1	123.16	$l_{\text{Apt1}} = 5.0$	-
Beam focusing via QT1 for energy selection	D2	123.16	$l_{D2} = 20.0$	-
	QuadX1	143.16	$l_Q = 7.5$	$k_{Q1} = 10.0$
	D3	150.66	$l_{D3} = 8.5$	-
	QuadY2	159.16	$l_Q = 12.0$	$k_{Q2} = 8.513$
	D3	171.16	$l_{D3} = 8.5$	-
	QuadX3	179.66	$l_Q = 7.5$	$k_{Q3} = 11.0$
	D4	187.16	$l_{D4} = 15.0$	-
Energy selective aperture	Apt2	197.16	$l_{\text{Apt2}} = 5.0$	-
Beam control via QT2 for achromatic transport	D4	202.16	$l_{D4} = 15.0$	-
	QuadX4	217.16	$l_Q = 7.5$	$k_{Q4} = 9.805$
	D3	224.66	$l_{D3} = 8.5$	-
	QuadY5	233.16	$l_Q = 12.0$	$k_{Q5} = 8.90$
	D3	245.16	$l_{D3} = 8.5$	-
	QuadX6	253.66	$l_Q = 7.5$	$k_{Q6} = 9.491$
	D2	261.16	$l_{D2} = 20.0$	-
90° beam bending magnet	SM2	281.16	$\rho_0 = 30.0$ $l_{\text{arc}} = 47.0$	-
Beam control via QD1 for beam shape and size	D5	328.16	$l_{D5} = 15.0$	-
	QuadY7	343.16	$l_Q = 7.50$	$k_{Q7} = 5.90$
	D6	350.66	$l_{D6} = 16.0$	-
	QuadX8	366.66	$l_Q = 12.0$	$k_{Q8} = 4.02$
	D7	378.66	$l_{D7} = 70.0$	-

Note: The parameters in black were selected as input values while parameters in blue have been calculated via the mathematical model. The drift spaces D2, D3 and D4 are used multiple times for the sake of symmetry, as described by the equations 4.4 and 4.7. The position of all the magnetic elements are shown graphically in figures 4.10 and 4.11.

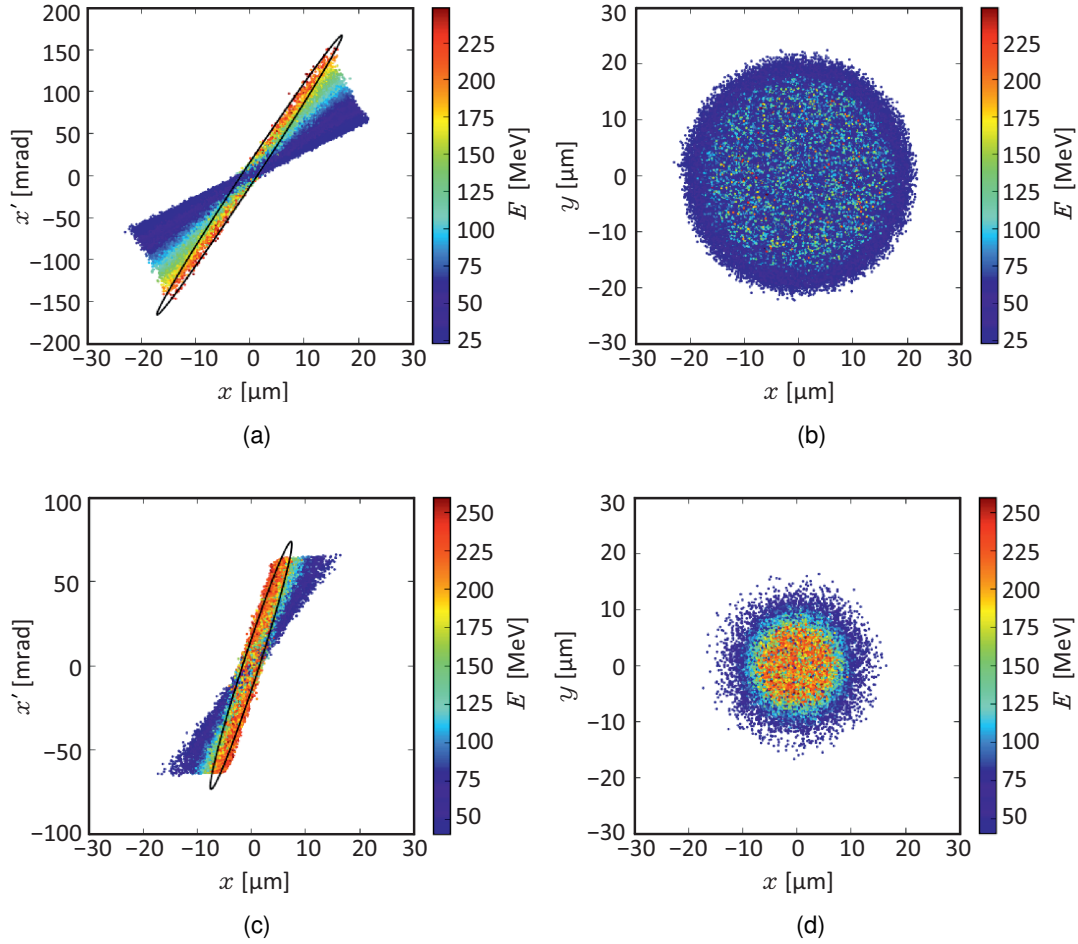


Figure 4.12: Transverse LAP beam profiles after traversing 100 μm in the nominal direction in the GPT simulations. (a) and (b) show beam profiles of a TNSA like source, while (c) and (d) show beam profiles of a RPA like source. The black ellipses show the protons with $\Delta E/E_0$ of about 20% energy width at $E_0 = 220$ MeV, this is to illustrate the usable particle phase space per LAP bunch.

system. The equation 4.4 was then solved for the beam waist and the individual strengths k_Q of the three quadrupoles (in the quadrupole triplet QT1), and the length of the drift spaces between the magnets have also been calculated. The calculated parameters were then plugged into the equation 4.7 to solve for the condition of dispersion free transport. Then equation 4.8 was solved for the homogenous field size at the isocentre. Table 4.1 lists the individual magnetic elements and drift spaces, in order starting from the LAP source, with their respective calculated magnetic field strengths and lengths, along with their position.

The evolution of the initial beam parameters through this gantry model is shown in figure 4.10. The figure shows the size of the beam beam (see equation 3.27) of the beamlet with E_0 energy in x - and y -directions, along with the portion of the beam with 50% momentum spread. The magnetic elements are clearly shown, along with the positions of the apertures. In the mathematical model, the apertures were not used, however, they were implemented in the beam tracking simulations. The solution of the mathematical model was then translated into the GPT tracking code, please see the figure 4.11 for the

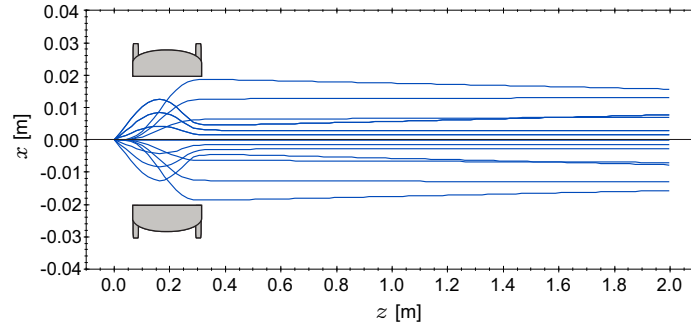


Figure 4.13: Particle tracks of a mono-energetic diverging proton beam (of an arbitrary energy), illustrating the beam capture and collimation by a single solenoid lens (also see figure 4.4).

full layout of the preliminary gantry design. The GPT simulation results are presented in the following sections.

4.3.2 One-step beam capture and collimation

The GPT simulations were set up to track the LAP beams with its full spectral distributions (for both TNSA and RPA like sources) through the calculated preliminary solution for the gantry design. First, the LAP bunches which were generated via the MC code were implemented in the tracking simulations. Figure 4.12 shows the evolution of the bunch just after 100 μm of the start position, i.e. $s = 0$, cf. figure 4.9.

The first magnetic element is the beam capturing single solenoid, which acts as an axially symmetric chromatic lens. To illustrate the function of the solenoid as a capture and collimation lens, the proton trajectories of a diverging mono-energetic beam are shown as an example in the figure 4.13. The size of the collimated beam behind the solenoid can get as large as the solenoid bore size for maximum capture, depending upon the initial divergence and the source to solenoid distance. However, the diverging beam can be efficiently captured and restricted for further transport, as was illustrated in figure 4.4.

A large inner radius of 2.5 cm was used for the solenoid for maximum capture efficiency, which then resulted in a large beam diameter of the collimated beam. Figure 4.14 shows the collimated LAP bunch behind the solenoid. Now for the GPT tracking simulations both TNSA and RPA like sources were tracked. Figure 4.14 shows the energy spectra behind the solenoid for both types of sources after being captured and transported to 50 cm (downstream from the LAP start position, i.e. $s = 0$). The current setting in the solenoid was tuned for each shot-setting for the desired E_0 value. Figure 4.14 shows that the capture efficiency of almost 100% around the selected E_0 could be achieved with a large bore sized solenoid. Furthermore, the ellipses in the phase space diagrams in figures 4.14(b) and 4.14(d), which show the protons with E_0 with $\pm 1\%$ energy width, could be well-collimated and can be contained for longer distances. In-fact a slight converging bunch was favored in this case for further transport. However, protons with lesser or higher energies than E_0 could not be well contained and the beam would grow spatially with the distance, and will hit the beampipe and be lost. The spot-size of the beam from two different LAP sources can be seen from real space axis (i.e. x -axis) in the phase space plots. The TNSA beam, due to the larger initial divergences, is larger than the RPA

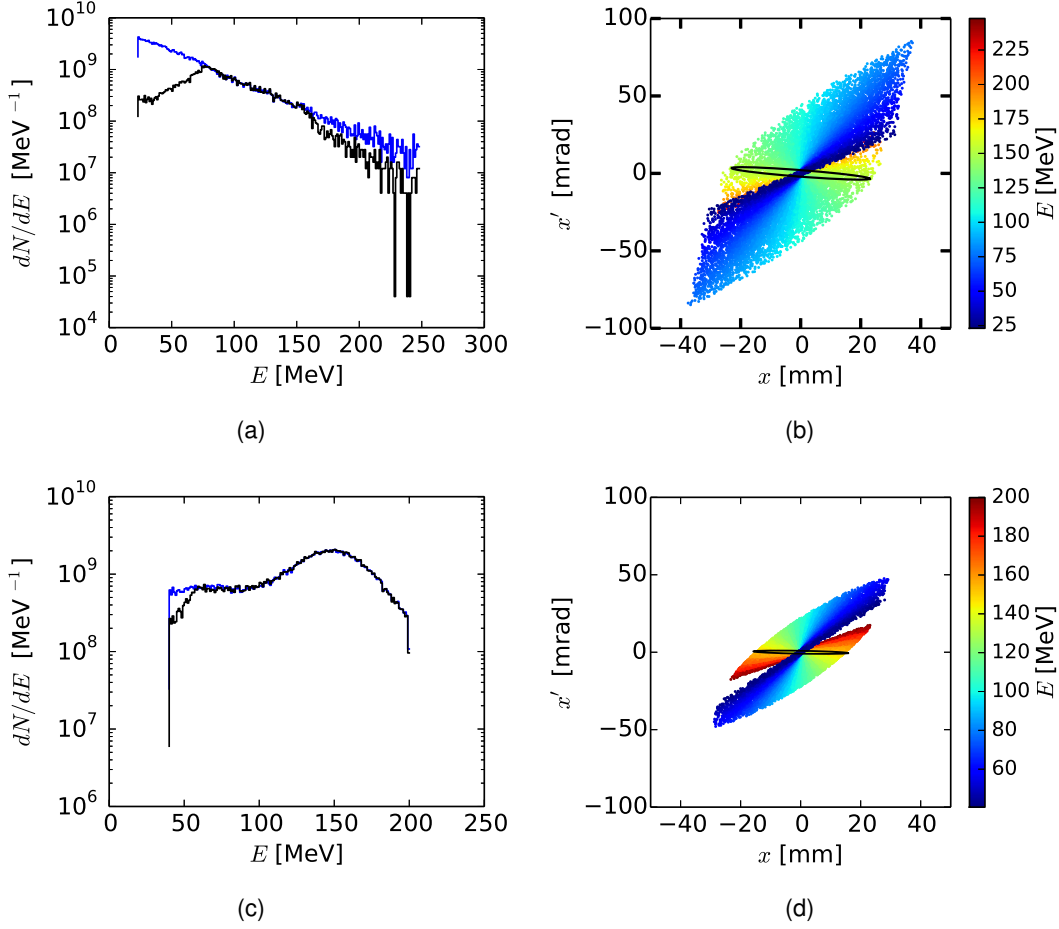


Figure 4.14: (a) and (b) show the energy spectra and phase space in (x, x') (which is symmetric in (y, y')) behind the capturing solenoid for a TNSA like LAP source, while (c) and (d) show a RPA like LAP source. The blue lines in (a) and (c) show the MC generated initial LAP bunch spectra taken as input for the GPT simulations, while the black lines show the respective spectra 50 cm behind the solenoid. The black ellipses in (b) and (d) enclose protons with E_0 with $\pm 1\%$ energy width (in this case E_0 of 150 MeV), and show that the beam has been well-collimated around the nominal energy.

beams, even though they have similar initial spot-size. The magnetic field strength B_{Sol} of the solenoid of about 42 T was determined to be required for protons with 250 MeV energy. At this point in the tracking simulations, the beam is well-collimated and enters the following magnetic element, which is the first 90° sector magnet (SM1).

4.3.3 Energy selection system

The capturing solenoid delivers a well-defined beam, i.e. close to a parallel beam around any chosen E_0 . A high resolution energy filtering system, ISESS, follows the capturing lens which consists of a 90° sector magnet (SM1) and a quadrupole triplet (QT1), see figure 4.11. The magnetic field B_{SM1} is tuned so that a nominal particle with energy E_0 would follow the nominal path. SM1 introduced the dispersion in the beam according to the energy of the protons, this allowed energy selection. An aperture Apt1 with a large bore was used behind the SM1 to limit the unwanted protons from traversing

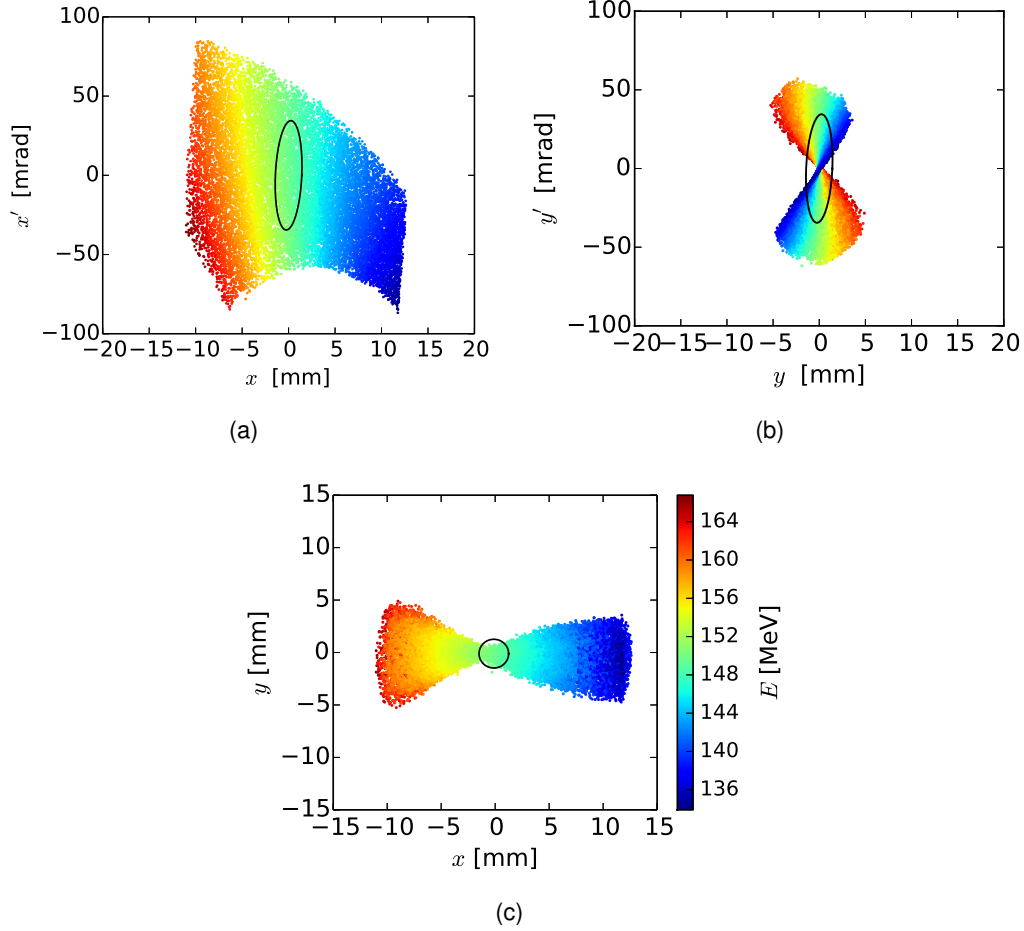


Figure 4.15: LAP bunch profile (from a RPA like source) at the position of the energy selective aperture Apt2 (also see the figures 4.10 and 4.11). Protons are spatially spread with respect to their energy due to the dispersion. (a) and (b) show the beam in phase space, and (c) shows the beam spot in real space. The black ellipses in (a) and (b) represent the acceptance of the aperture Apt2 with R_{Apt2} of 1.2 mm, which is shown by a black circle in (c). All figures share the energy scale shown next to (c).

further into the beamline, see figures 4.10 and 4.11. Behind that, the dispersed beam enters the quadrupole triplet (QT1) which strongly focuses the beam, to a focal spot with minimum beam waist (symmetrical in x - and y -directions) at a distance of 15 cm behind QT1, see figure 4.10 and table 4.1. An aperture Apt2 with variable opening radius R_{Apt2} has been placed at this focal spot, which then effectively filters protons around E_0 with the bandwidth $\Delta E/E_0$ depending on the R_{Apt2} size. The figure 4.15 shows the beam at the focal spot at the Apt2 position, due to the dispersion produced by the SM1 in the bending direction, i.e. x -direction. The beam spreads spatially in x -direction only, see figure 4.15(a), while the beam remained compact and centered without spatial dispersion in the y -direction, see figure 4.15(b). The ellipse in these pictures represents the acceptance of the R_{Apt2} to select, in this case set to filter about 2% energy band around the nominal energy E_0 of 150 MeV. Whereas the black circle in the figure 4.15(c) represents the R_{Apt2} in the real transverse space, corresponding to the phase space ellipse. The size R_{Apt2} of the aperture Apt2 can be varied for each bunch and thus, the size of R_{Apt2} would de-

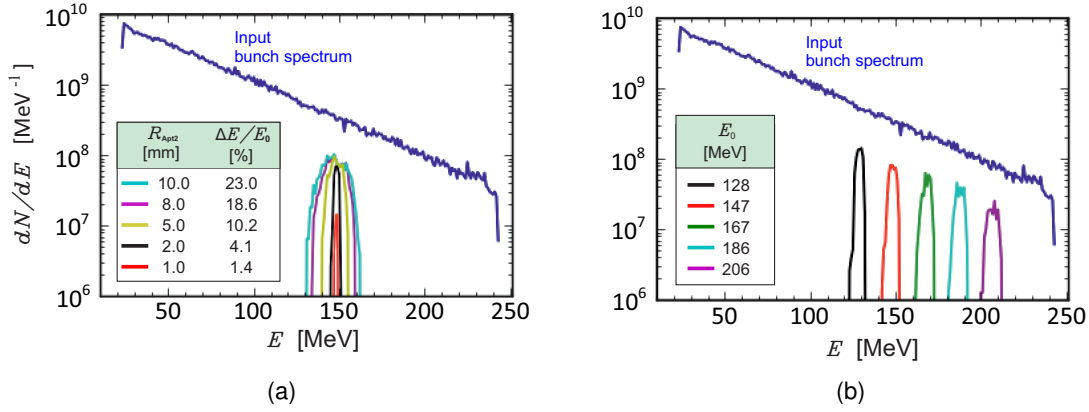


Figure 4.16: MC generated TNSA like LAP bunches (blue line) transported through the gantry in GPT simulations and measured at the isocentre. (a): Results with ISESS set to deliver $E_0 = 148$ MeV with five R_{Apt2} settings for five consecutive LAP bunches. (b): Filtered spectra through ISESS at fixed $R_{\text{Apt2}} = 3.0$ mm while E_0 values were varied through selecting optimized magnetic field strengths for each magnetic element of the beamline. Both figures share the same y -axis.

termine the allowed energy bandwidth $\Delta E/E_0$ to pass through Apt2. Also, it is clear from the figures 4.15(a) and 4.15(b) that for small R_{Apt2} the transport efficiency drops, due to the low acceptance.

The separation between the centroid of the protons with 1% energy difference was about 0.5 cm, which shows a dispersion value of 0.5 m (see equation 4.3). This agrees with the mathematical model based on the transverse beam optics, see figure 4.10. As mentioned in the section 4.2.8, it was important to verify the model with beam tracking simulations, which shows that the tracking simulations essentially agree with the presented mathematical model.

Two sets of simulations were performed. In the first set, the capability of the ISESS, to filter $\Delta E/E_0$ bandwidths was investigated while the radius R_{Apt2} of the aperture Apt2 was varied from 12 mm to 1 mm. The magnetic field values in each of the magnets were optimized for a desired nominal energy E_0 . Figure 4.16 and 4.3.3 show the beam tracking simulation results with E_0 of 148 MeV (as an example). ISESS was able to filter a spectrum out of the input bunch spectrum (for both TNSA and RPA like input bunches) with a peak at the selected E_0 while the bunch was transported through the beamline from laser-target chamber to the patient table. In case of the TNSA like spectrum, the filtered bandwidth $\Delta E/E_0$ decreased from 25% at $R_{\text{Apt2}} = 12.0$ mm to 1.4% at $R_{\text{Apt2}} = 1.0$ mm. The transport efficiency η for R_{Apt2} of 12 – 3 mm was about 22%, and dropped quickly for R_{Apt2} of 2.0 mm and below, due to the chromatic spread at the focal point, to about 5% for $\Delta E/E_0$ of 1.4% at $R_{\text{Apt2}} = 1.0$ mm.

In case of the RPA like spectrum, the filtered bandwidth $\Delta E/E_0$ decreased from 19% at $R_{\text{Apt2}} = 12.0$ mm to 2% at $R_{\text{Apt2}} = 1.0$ mm, with almost constant transport efficiency $\eta \approx 85\%$ for $R_{\text{Apt2}} = 12 - 3$ mm, and dropped for below $R_{\text{Apt2}} = 2.0$ mm to about 40% for $\Delta E/E_0 = 2\%$ at $R_{\text{Apt2}} = 1.0$ mm. A satisfactory control over $\Delta E/E_0$ as a function of R_{Apt2} was established over a wide bandwidth range of 3 – 22%.

The second set of simulations was performed to establish a control to select desired

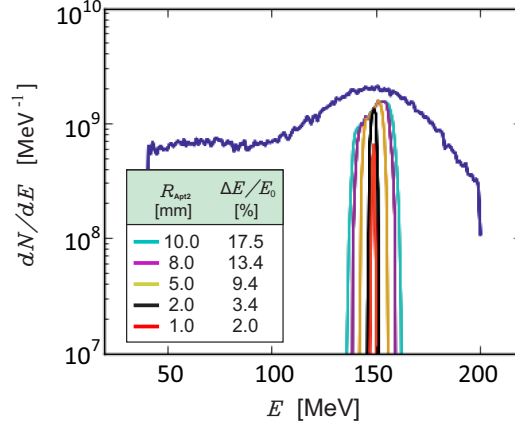


Figure 4.17: Energy spectra at the isocentre of the MC generated RPA like LAP bunches transported through the gantry in the GPT simulations, with ISESS set to deliver $E_o = 148$ MeV with five R_{Apt2} settings for five consecutive LAP bunches.

value of E_0 . Normally, 1.0 to 1.5 mm range steps are used in conventional PT to scan the complete depth of the tumour which would require ~ 0.5 MeV controllable energy steps. This translates to a requirement of a controllable step change in magnetic field values in each magnet with an accuracy of 10^{-2} T, which is achievable with present day technology in pulsed powered magnets, and thus assumed as an incremental change in E_0 . One MC generated LAP bunch was transported, with fixed R_{Apt2} aperture size, and the magnetic fields for all the magnets in the gantry were optimized for a nominal energy, say E_{o1} . For the next shot-setting, for the next consecutive LAP bunch, the magnetic strengths were reduced for a nominal energy, say E_{o2} , such that $E_{o2} < E_{o1}$. Figure 4.16(b) shows the results, as an example, of five tracking simulations, with $R_{Apt2} = 3.0$ mm, and the gantry was optimized for transporting LAP bunches with five different values of E_0 . The output spectra were measured at the isocentre. These simulation results established the control for selecting a desired energy window for each bunch and show the capability and functionality of the energy selection system.

4.3.4 Beam tracking through the whole gantry

Behind the energy selective aperture Apt2, a quadrupole triplet QT2 collects the yet again diverging beam. QT2 was then followed by the second 90° sector magnet SM2, which bends the beam towards the patient table. The arrangement of QT2 and SM2, with drift spaces in-between, was calculated to cancel the dispersion. Behind the SM2 the beam size was not symmetric in the transverse directions, see figure 4.10. A third quadrupole set, a doublet QD1, was then used to make the beam uniform in transverse directions. The individual proton tracks of a LAP bunch simulated in the GPT simulation are shown in the figure 4.11, along with the schematic layout of the gantry. Figure 4.11 also shows the integrated laser-target chamber, layout of the magnetic elements along the nominal path along with the apertures and collimator. The layout of the magnets allows to arrange an isocentric 360° gantry formation, with enough space around for possible beam dumps, and a treatment room with the patient table inside a radiation protected

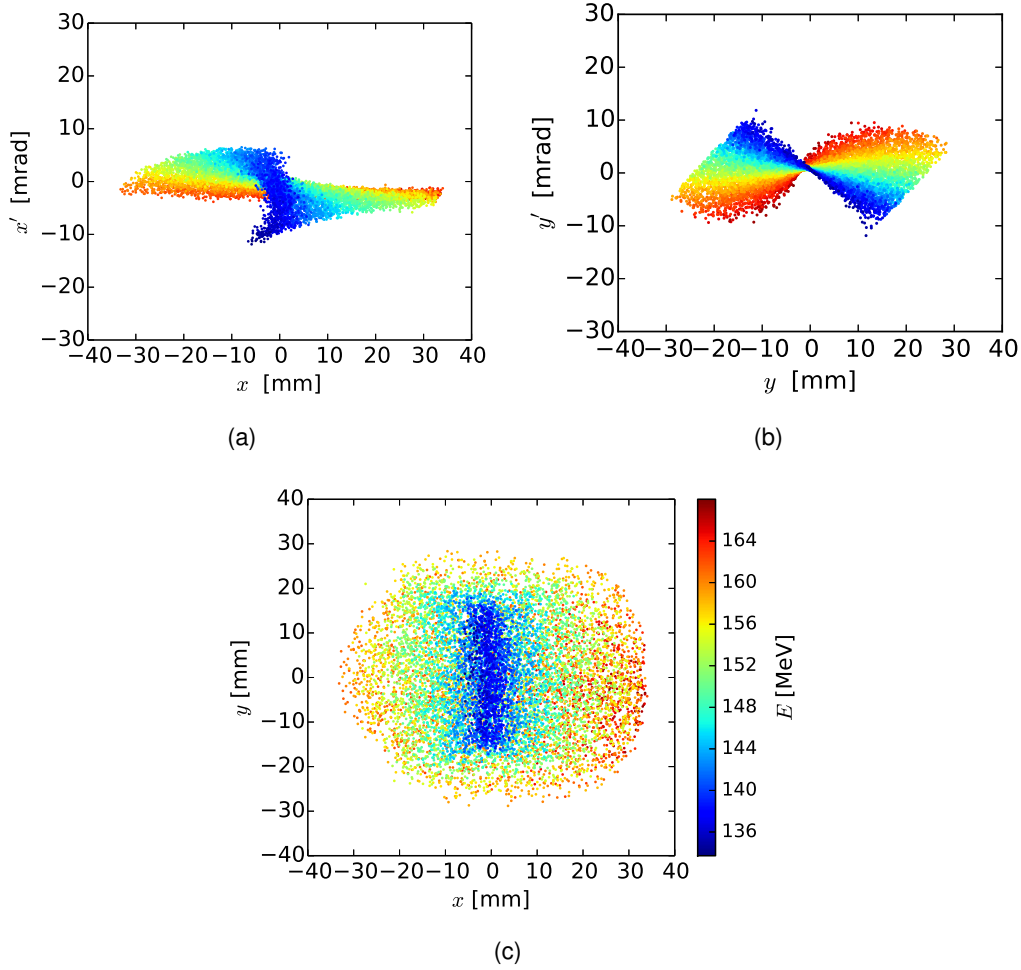


Figure 4.18: Output beam profile at the isocentre with $\Delta E/E_0$ of $\sim 19\%$ at $E_0 = 150$ MeV. The beam in the phase space shows that the dispersion has been canceled out with centered beam and in both directions. However, (a) shows slight aberrations in the lower energy range. (c) Beam spot in the real transverse space, and shows that the spatial spread is energy dependent. All figures share the same energy scale.

bunker. The gantry could also have a collimator system to reduce the size of the beam if required due to the the smaller tumour sizes.

The LAP bunches were tracked through the whole gantry, and figure 4.18 shows the beam spot at the isocentre, with $\Delta E/E_0$ of 19% as one example. The beam was spatially centered, i.e. $(x, y) = (0, 0)$, in the isocentric plane as was calculated. The xx' phase space plot (figure 4.18(a)) shows a controlled beam with almost zero dispersion, and the yy' phase space plot (figure 4.18(b)) shows a slight offset from the center $(0, 0)$. This was observed due to the small drift spaces D2 and D5 (see table 4.1) which resulted in the superposition of dipole and quadrupole magnetic fields. The small values for these drift lengths were used for two main reasons. First, it keeps the system compact, and secondly, the more important reason that the large beam sizes behind the capturing solenoid starts to get bigger due to the large $\Delta E/E_0$ values. Moreover, it is evident from figure 4.18(c) that protons with different energies occupy different envelopes within the irradiation field, i.e. the spatial spread is energy dependent. This would make the irradiation field rather

inhomogeneous, which was not evident simply from the mathematical model. The beam spot-size at the isocentre is about 6 cm, see figure 4.18, therefore, a physical collimator would be indispensable. Also, to cover the lateral extent of the larger tumours, the patient table was assumed to be movable to scan the beam across the tumour volume and to apply multiple laterally adjacent fields to homogenize dose over larger volumes.

4.3.5 Dose delivery

Lastly, it was investigated if the energy filtered LAP bunches, with varied bandwidths, from the gantry could reproduce the flat-top SOBP shown in the 1D BEAD example in the section 4.2.1 (in the figure 4.2). For this purpose, depth dose profiles of the individually filtered LAP bunches and superimposed dose distributions from multiple filtered bunches were simulated in a $10 \times 10 \times 30 \text{ cm}^3$ water phantom placed at the isocentre using the Geant4 simulation code⁴. The proton positions, energy and velocity components of the filtered LAP bunches, at the exit window of the gantry from GPT simulations were taken as input to the Geant4 simulations. The SOBP shown in the BEAD single field example (figure 4.2) was as an example simulated, first in the GPT simulations for filtering LAP bunches and then followed by Geant4 simulations for depth doses. The SOBP was achieved by superimposing multiple LAP shots with 5 different optimized beamline settings of $\Delta E/E_0$, as given in the example. The simulated 1D depth dose profiles in the water phantom are shown in figure 4.19. It took a total number of filtered LAP bunches, $N_{\text{LAP}} = 19$, to reach a normalized SOBP, with flatness of less than $\pm 3\%$, for the same shot-settings as in the BEAD example (from the figure 4.2). The required number of LAP bunches from beam tracking simulations (i.e. $N_{\text{LAP}} = 19$) were slightly higher than the predicted $N_{\text{LAP}} = 14$ from the BEAD example. The reason is that due to the acceptance of the energy selective aperture Apt2 mentioned in the section 4.3.3, the transport efficiency dropped for the lower $\Delta E/E_0$ transportable energy windows. Therefore, for the last two shot-settings, i.e. with shot-settings 4 and 5, two and three more bunches, respectively, were required to achieve the desired flat-top SOBP.

4.4 Features and limitations of the gantry solution

A new compact gantry has been designed and simulated for the unique laser-driven proton sources. This gantry has integrated multiple functionalities, i.e. integrated laser-target chamber for proton acceleration, large acceptance LAP beam capturing, energy selection system and achromatic beam transport, and it is also capable to deliver 1D dose deposition model BEAD for broad-energetic LAP bunches, i.e. for filtered $\Delta E/E_0$ in the range of 3 – 22% with energy steps of 0.5 MeV. This was the first complete beamline design which showed that it is possible to capture, filter and transport bunches with varied large energy bandwidths. The estimated dimensions of the gantry are a height of 1.8 m

⁴Geant4 is a toolkit for the simulation of the passage of particles through matter. It is based on object-oriented C++ programming language, and has been extensively utilized in various fields, from astrophysics to medical sciences. Please see the references (Agostinelli et al., 2003; Allison et al., 2006) for further details.

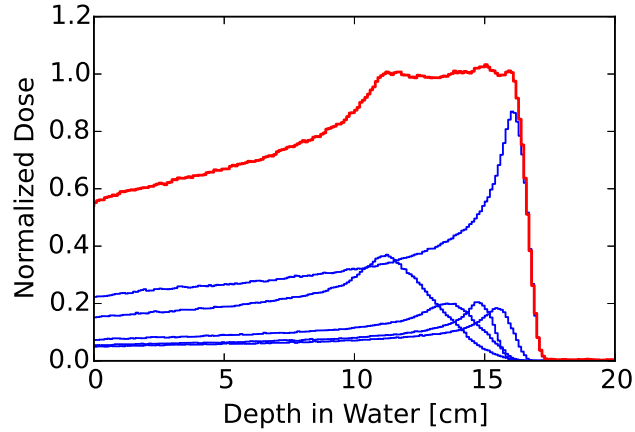


Figure 4.19: Depth dose profiles of individual LAP bunches (blue) in water, filtered through ISESS with five different shot-settings and transported to the patient site via the simulated gantry. A total of $N_{\text{LAP}} = 19$ shots were required to be superimposed to reach SOBP (red) of 5.4 cm width with flatness of about $\pm 3\%$.

and a length of ~ 3.0 m (see figure 4.11), which is about 2.5 times smaller in height and about 3.5 times shorter in length than the installed conventional PT gantries, as explained in section 2.1.

In this design, much focus was given to reduce the overall size, which in-turn increased the demands on shorter drift spaces between magnets and higher magnetic strength values (see table 4.1). The disadvantages of shorter drift spaces are that the high magnetic fields in individual magnets can superimpose generating non-linear effects, and also, it might be difficult to physically pack and install these components along with power cables and beam monitoring devices. Therefore, the overall dimensions of the gantry might increase by a few percent, nevertheless, would still be a considerable reduction in the size compared to the conventional gantries. The magnetic field strength values has been kept under the advised limits, presented in the section 3.3.4, except one of the quadrupoles has $k_Q = 11 \text{ m}^{-1}$ which might be possible to achieve in the future, or this value can also be lowered to 10 m^{-1} by increasing the length of this quadrupole.

The layout of the gantry is such that the LAP bunches would be generated in the direction opposite to the final output beam for patient irradiation. This would ensure that the contaminant radiations (e.g. x-rays, electrons, neutrons and other ions), generated along with the accelerated protons via laser-matter interactions, would not pose radiation protection issues for the patients. Furthermore, the layout of the gantry also ensures that any unwanted radiation, from blocking the unnecessary part of the LAP spectra via the energy selection system, must not directly face towards the patient table, and that there is sufficient space between beam dumps and the patient site to add sufficient shielding, see figure 4.11. The secondary radiations from the laser proton acceleration and the beam dumps must be blocked by the radiation protection walls of the bunker enclosing the patient table⁵.

However, the main limitation of this gantry design is the lack of output beam controls,

⁵A detailed study of radiation protection for laser-based gantry systems is in progress.

i.e. the control over size of the output beam and lack of beam scanning to cover larger tumour sizes. Furthermore, the output beam at the isocentre behind the exit window shows a rather poor beam quality as can be seen in the spatial distribution of the different energies of the large E/E_0 filtered output LAP beams (figure 4.18(c)). These output beam features were similar for both TNSA and RPA like sources. This was not foreseeable from just the mathematical model and was only became evident with the tracking simulations. Although, the output beams were good enough to produce uniform SOBPs in 1D BEAD model, however, homogenous 3D lateral dose distributions would require more effort and many filtered bunches to be superimposed. Furthermore, there is no scheme to select the number of particles deliverable per bunch to the patient, i.e. intensity modulation. This is a clinically very important aspect of the beam delivery, as it would provide precise control over deliverable dose per bunch. The output beam has a fixed field size of about $6 \times 6 \text{ cm}^2$ and to deliver doses to the tumours with smaller lateral dimensions a physical collimator is assumed to be able to reduce the size of the beam (similar to the conventional scattering systems, see figure 2.7). This would reduce the efficiency and pose radiation shielding issues close to the patient. And, to deliver doses to the tumours with larger lateral dimensions, than the deliverable output beam size, lateral field patching via precise patient table movement was assumed to provide the solution.

This gantry design provided a proof-of-principle solution to incorporate multiple functionalities demanded by the unique properties of the LAP beams, into a compact 360° rotatable gantry layout. Furthermore, it provided key parameters for parallel development of pulsed magnets, for example the need for sector magnets and quadrupoles and their respective parameters. This study provided the basis for the research and development of individual pulsed magnets which was presented in the section 3.3. It also showed the possibility to control and manipulate LAP bunches for clinical dose delivery options and encouraged further research in the beamline and dose delivery options, as there were no showstoppers identified. Although, this preliminary gantry design study was important, it is not clinically attractive due to the limited control over the output beam parameters, i.e. lateral spread, spatial distribution, intensity modulation control and lateral beam scanning. Therefore, an advanced gantry solution was then designed which could fulfill the above mentioned beam requirements and is able to deliver advanced 3D clinical treatment plans.

Chapter 5

Advanced Clinical Gantry Design with Novel Nozzle

5.1 Objective

The preliminary gantry design presented in chapter 4, provided the first basic proof-of-principle multi-functional beamline solution. However, to overcome the limitations of the preliminary design, an advanced gantry design is required with additional features for improved output beam quality and, more importantly, an advanced beam control and active scanning system. This is necessary to deliver state-of-the-art 3D clinical treatment plans. Therefore, in this chapter an advanced clinical gantry solution with novel dose delivery system, i.e. nozzle, is presented. From the previous chapter, it is clear now how to develop a mathematical model for beamlines and how to verify via particle tracking simulations. In this chapter, similar materials and methods have been utilized to design the advanced gantry. The methods already mentioned in the previous chapter will be glided over swiftly, and detailed description is presented only for the new features, conditions and equipment design.

5.2 Materials and Methods

5.2.1 Clinical requirements from the gantry

Similar to the preliminary gantry design, a large acceptance transport beamline system with multiple functionalities is required, however, with additional, advanced features to fulfill state-of-the-art clinical requirements. Those are illustrated in figure 5.1 and listed below:

1. The first function is to capture the LAP bunches and to control the intrinsic large divergences and transverse dimensions. The large acceptance of the single solenoid lens used in the previous gantry design, which was necessary for maximum capture efficiency, resulted in a collimated but with a large beam spot-size. A small sized beam would be easier to maintain for improved beam quality. Thus, an improved capture and collimation system is required.

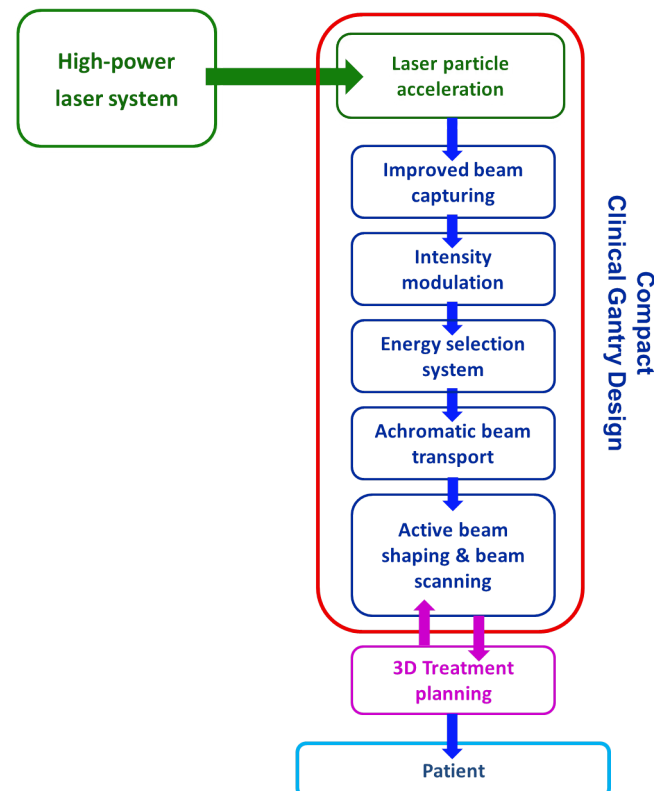


Figure 5.1: Schematic illustration of the advanced gantry design (cf. figure 4.3). A capturing system is an essential feature, and now, for clinical applicability an intensity modulation scheme has been added. Followed by an energy selection system and large acceptance, achromatic beam transport. An active beam shaping and scanning must now be included for precise tumour conformal dose delivery, moreover, the features, limits and output beam parameters must be incorporated in an advanced 3D treatment planning system for a comprehensive laser-driven PT solution.

2. An energy selection system is still necessary to filter variable energy widths (ranging from 22% to 3%) from the initial, broad spectrum of the LAP bunches.
3. Furthermore, it is imperative to be able to vary the beam spot-size for clinical tumour irradiation. This functionality would allow to utilize the maximum number of protons possible per bunch for efficient 3D advanced dose delivery (as described in the section 2.5.2). This demands a beam shaping system, preferably active (i.e. magnetic) without the need to use physical scatterers and collimators.
4. It is also crucial to be able to scan the beam, to the spots (and/or sub-volumes of tumour) for conformal tumour irradiation with high precision and accuracy. This demands a novel beam scanning system with large acceptance, i.e. large beam sizes with broad energy widths.
5. It became clear in the 3D dose verification studies for LAP beams (Hofmann et al., 2015; Masood et al., 2017a) that the control of the intensity of the bunch is necessary for efficient and precise 3D tumour conformal dose delivery. Therefore, an intensity modulation scheme must be incorporated in the new advanced gantry design.

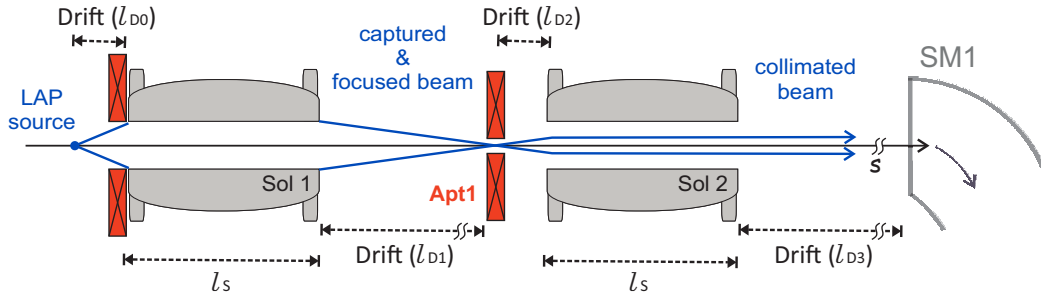


Figure 5.2: Schematic illustration of the two-step capturing and collimation system based on two pulsed solenoids. The solid blue lines represent LAP beam. Apertures are shown as red rectangles, the first one behind the LAP source is used only to restrict stray particles outside the acceptance of the first solenoid Sol1. The aperture Apt1 has been placed at the focal spot of Sol1. Second solenoid Sol2 re-captures the beam and keeps it small in transverse directions. The collimated beam behind the second solenoid has smaller transverse dimensions than the single solenoid based system, cf. figure 4.4.

6. Finally, similar to the previous design, the whole beamline should be achromatic for homogeneous dose distribution for all beamline settings, and all elements must be arranged in a gantry formation to rotate these beams around an isocentre for multi-directional tumour irradiation.

Similarly to the design approach used for the preliminary gantry design, the first step is to develop a mathematical model based on the first order linear beam optics. The main functions of this gantry model are explained below step-by-step, along with the matrix formalisms.

5.2.2 Two-step beam capturing and collimation

It has been established that the LAP bunches require capturing due to their large initial divergences, and an efficient capturing system is needed which is capable of keeping the beam small and collimated. A single large aperture pulsed solenoid was investigated for the preliminary gantry design as a capturing lens. Although, it provided efficient capturing, the size of the collimated beam was relatively large. It is desired to keep the beam spot-size small, which will be beneficial in all downstream beamline sections and for output beam characteristics.

An improved two-step capturing and collimation system has been developed to overcome this problem and which would provide enhanced control over the captured beam, see figure 5.2. It is based on two pulsed solenoids. The first solenoid, with an aperture diameter of 3 cm, was positioned (start of the solenoid) at 3 cm downstream from the laser-target. The laser-target to solenoid distance is considerably less than the single lens capturing, cf. section 4.2.3. This would allow to keep the beam small and capture efficiency high. This parameter was discussed with the experimental team at HZDR and considered achievable, and would allow to keep the beam small from the start. Furthermore, a 4×40 windings solenoid structure was considered here instead of 4×30 windings solenoid. This will lower the magnetic strength B_S requirement as now the length l_S is increased from 18 cm to 22 cm.

The diverging LAP bunch interacts with the first solenoidal field which bends the protons symmetrically, however, chromatically towards the central axis. The focusing strength of the first solenoid (Sol1), i.e. the capturing lens, can be adjusted to achieve a minimum beam waist around desired nominal energy E_0 at 1 m downstream from the laser-target source position. The focusing strength k_{S1} of Sol1 can be calculated from the following transfer matrix equation for Twiss parameters $\epsilon\alpha = 0$ (which is the condition for beam waist) at 1 m:

$$\begin{aligned} M_{\text{Capt}} &= M_{D1} M_{\text{Sol1}} M_{D0} \\ \text{and} \quad \sigma_1 &= M_{\text{Capt}} \sigma_0 M_{\text{Capt}}^T, \end{aligned} \quad (5.1)$$

where σ_0 represents the initial LAP beam parameters, while σ_1 represents the beam parameters behind the beamline section M_{Capt} . M_{Sol1} represents the first solenoid Sol1, M_{D0} represents the drift space D0 with drift length l_{D0} of 2 cm between proton source and the solenoid, and M_{D1} represents the drift space D1 with drift length l_{D1} between solenoid Sol1 and the aperture Apt1, which was chosen to be 76 cm. At the focal-spot an aperture (Apt1) was positioned to limit the proton energy spectra. Behind this point the beam starts to diverge again and a second solenoid (Sol2) was placed which would re-capture and collimate the beam around E_0 . In this way, the first solenoid can be optimized for maximum capture efficiency, by allowing maximum opening angle, independent of the second solenoid. The second solenoid (Sol2) was placed as close as possible to the focal point so that it could re-capture the beam at minimum transverse dimensions. Focusing strength k_{S2} of Sol2 was then optimized to deliver a collimated beam for further transport. The focusing strength k_{S2} can be calculated from the matrix equation below, now for the condition for collimated beam, i.e. $\epsilon_u \gamma_u = 0$:

$$\begin{aligned} M_{\text{Coll}} &= M_{D3} M_{\text{Sol2}} M_{D2} \\ \text{and} \quad \sigma_2 &= M_{\text{Coll}} \sigma_0 M_{\text{Coll}}^T, \end{aligned} \quad (5.2)$$

where M_{Sol2} represents Sol2, M_{D2} represents the drift space of length l_{D2} of 15 cm, and M_{D3} represents the drift length l_{D3} between solenoid Sol2 and the next magnetic element, which was set as 40 cm. The second solenoid was optimized for collimating protons of energy E_0 , the protons with $E > E_0$ experience less focusing strength and protons with $E < E_0$ experience higher focusing strength. Thus, the beam will grow in size with traversing distance, therefore, small drift spaces in-between magnetic elements are desirable. However, larger drift spaces than in the preliminary gantry design are considered here for practical reasons, as mentioned in the section 4.4.

5.2.3 Energy selection system

Laser-driven sources have large energy spread and, even after a two-step collection system, a beamline would require an efficient energy selection system. A gantry Integrated Shot-to-shot Energy Selection System (ISESS) was presented in the section 4.2.4

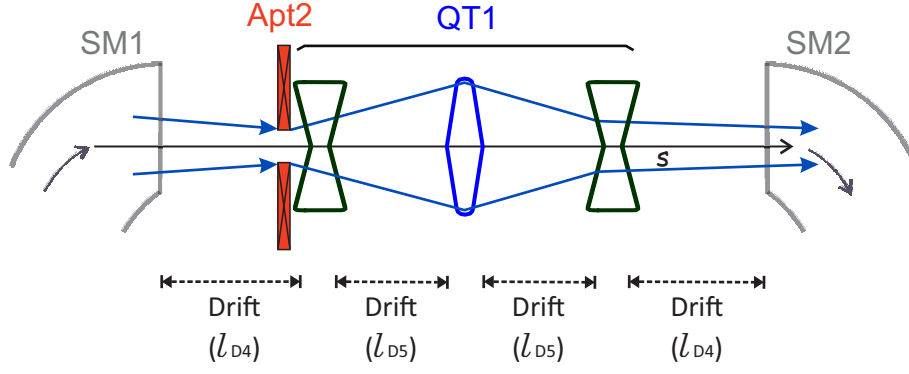


Figure 5.3: Schematic illustration of the beamline downstream from the two-step collimation section. The blue arrows represent the proton beam with nominal energy in the bending plane, red rectangles shows the energy selection aperture Apt2. Bending magnets SM1 and SM2 are shown in grey. The quadrupole triplet QT1 is also shown with concave shape (dark green) representing de-focusing and convex shape (light blue) representing focusing in x -direction (i.e. the bending direction), respectively.

which included a 90° bending magnet in combination with a quadrupole triplet. For this gantry design, the ISESS has been simplified by eliminating the need of the set of three quadrupoles behind the dipole, see figure 5.3. Now the energy selection is only done by the dispersion provided by a 90° dipole sector magnet (SM1). This could show that a similar energy selection resolution can be achieved with the well-collimated, small size beams from the two-step capturing system and provided twice the drift length behind the sector magnet. The beamline matrix equation up to the principal energy selective aperture Apt2 can be written as:

$$M_{\text{ESS}} = M_{\text{D4}} M_{\text{SM1}} M_{\text{Coll}}$$

and $\sigma_3 = M_{\text{ESS}} \sigma_0 M_{\text{ESS}}^T,$ (5.3)

where M_{SM1} represents the first sector magnet SM1 and M_{D4} represents the drift space D4 of length l_{D4} . The energy dependent spatial spread, provided by the dispersion function introduced by the sector magnet, would be the necessary condition for energy selection and the objective is to select δ (or $\Delta E/E_0$) (similar to the arguments provided in the section 4.2.4). The radius R_{Apt2} of the principal energy selective aperture Apt2 behind SM1 (i.e. $R_{\text{Apt2}} = \sqrt{\epsilon\beta(z_{\text{Apt2}})}$) is required to match the $env = \sqrt{\epsilon\beta(z_{\text{Apt2}})}$, where z_{Apt2} is the position of the Apt2 behind the SM1. The value of z_{Apt2} is chosen where $D(s)$ is relatively large and env is preferably equal in both x - and y -directions for efficient and symmetric energy filtering. The R_{Apt2} could be varied for each shot which in turn determines the energy width filtered from the initial spectrum. Here also, a maximum value of $\Delta E/E_0 = 22\%$ would be considered to be filtered and transported to the patient site.

5.2.4 Achromatic beam transport

For a homogenous beam profile at the isocentre, it is crucial to cancel the dispersion functions, $D(s)$ and $D'(s)$, introduced by the 90° bending magnet (i.e. the spatial

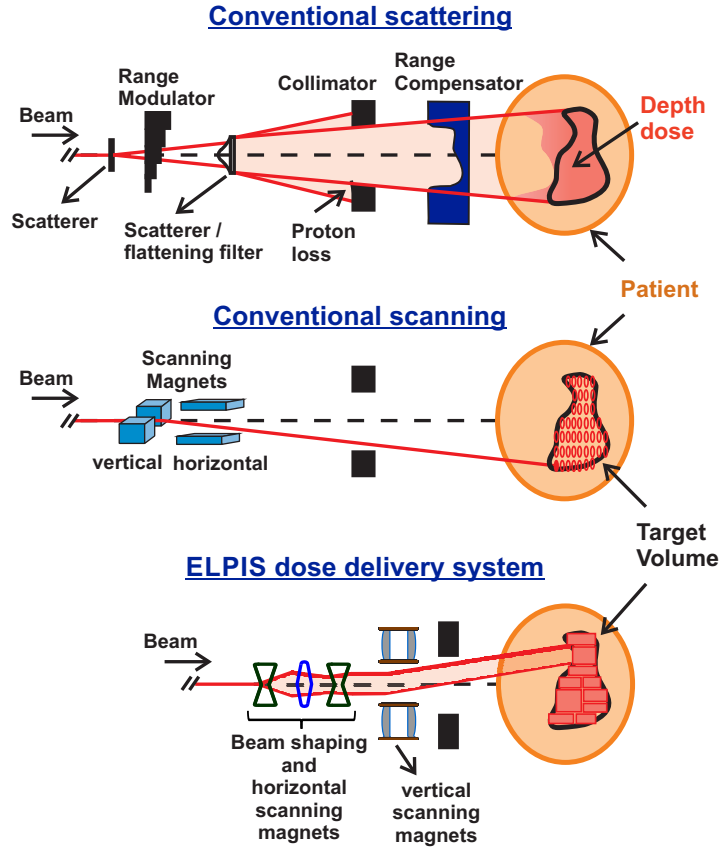


Figure 5.4: Schematic layout of the beam delivery approaches, comparing the two conventional approaches, passive beam scattering (top) and active pencil beam scanning (middle), along with the new ELPIS system (bottom). The conventional approaches has been designed for mono-energetic pencil-like beams and has been described in detail in section 2.5.1. They are shown here again for side-by-side comparison. In the ELPIS system, the spectrally large proton beams can be spatially broadened via quadrupole magnetic fields, i.e. without the need to traverse through any physical material, while actively scanning the variable sized and shaped beams. With high-field pulsed magnets higher bending angles can be achieved, thus, the length of the scanning system can be reduced for similar irradiation fields, i.e. lateral extents.

spread of the beam as a function of the energy). This requires beam control via magnetic quadrupoles and a second 90° bending magnet. A quadrupole triplet (QT1) has been introduced to control the spatially resolved beam.¹ Also, a second 90° bending magnet SM2 was introduced, which was necessary to bend the beam towards the patient site, see figure 5.3. Thus, all the elements now form a rotatable, isocentric gantry formation. The drift spaces and the individual strengths of QT1 quadrupoles can be calculated by solving the following equation for the $D(s) = 0$ and $D'(s) = 0$ double-achromatic condition:

$$M_{BL} = M_{SM2} M_{D4} M_{QuadY1} M_{D5} M_{QuadX1} M_{D5} M_{QuadY1} M_{ESS} \quad (5.4)$$

$$\text{and} \quad \sigma_4 = M_{BL} \sigma_0 M_{BL}^T, \quad (5.5)$$

where M_{QuadX} and M_{QuadY} represent focusing quadrupoles in x - and y -directions, re-

¹Please note here that the quadrupole triplet is abbreviated as QT in general, however, the functions of the first quadrupole triplet QT1 and the second quadrupole triplet QT2, are entirely different from the preliminary gantry design in chapter4.

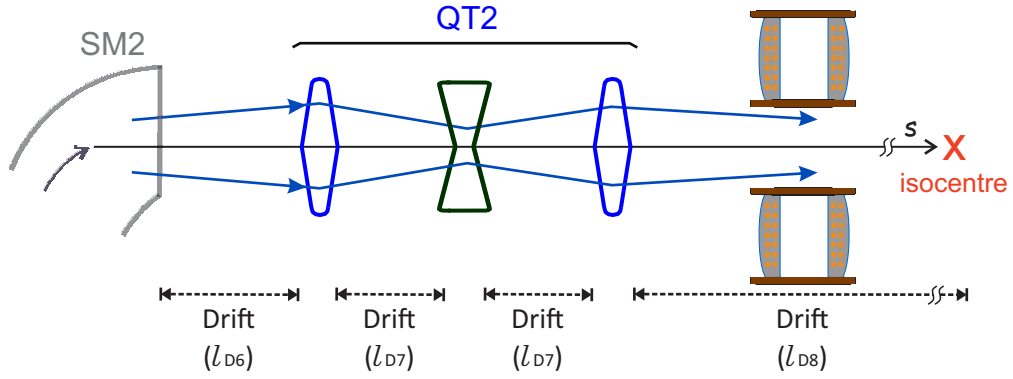


Figure 5.5: Schematic illustration of the beam shaping and scanning, ELPIS, system. The blue lines represent the nominal energetic proton beam in the bending plane, also see figure 5.4 (bottom) to compare the beam in bending and non-bending planes. The quadrupole triplet QT2 can shape the beam in different elliptical shapes and sizes. The solenoid-pair at the end can scan the beam in the non-bending plane, i.e. in y -direction (also see figure 5.6).

spectively, and matrices M_{D4} and M_{D5} represent drift spaces D4 and D5 of drift lengths l_{D4} and l_{D5} , respectively (note here that similar quadrupoles and drift spaces have been chosen for symmetry). The beamline parameters were optimized to keep the beam small in transverse dimensions before the beam shaping and dose delivery system behind the second bending magnet SM2.

5.2.5 Advanced nozzle system – ELPIS

At this point, the beam is required to be spatially matched in x - and y -directions, and furthermore, required to be shaped according to the tumour dimensions. Conventional beam delivery systems, i.e. nozzles, can provide spatially and spectrally broad beams via passive scattering or small spot-size mono-energetic beams via active beam scanning, described in detail in the section 2.5.1. Also, in conventional nozzles, it is not possible to use the beam scanning option with scattering at the same time, thus one cannot modulate beam size and position simultaneously. Furthermore, the conventional system cannot be deployed to deliver advanced dose models for LAP beams, described in the section 2.5.2.

A novel broad-Energetic Large acceptance beam delivery via magnetic field shaPing, Integrated with short-throw Scanning (ELPIS) system has been designed which can overcome the beam delivery limitations of the preliminary gantry design and is able to deliver advanced dose schemes, see figure 5.4. ELPIS includes a quadrupole triplet (QT2) and a solenoid-pair with a gap, for the beam shaping and scanning technique, see figure 5.5. The advantages of both conventional scattering and scanning schemes have been combined in the new ELPIS system.

The beam shaping can be done via the beam imaging parameters of QT2, which can be adjusted so that the beam transverse size forms a uniform spot at the isocentre, and also, these parameters can be adjusted per LAP bunch for different selectable beam spot-sizes. The matrix equation for the final beam section behind the last bend now can

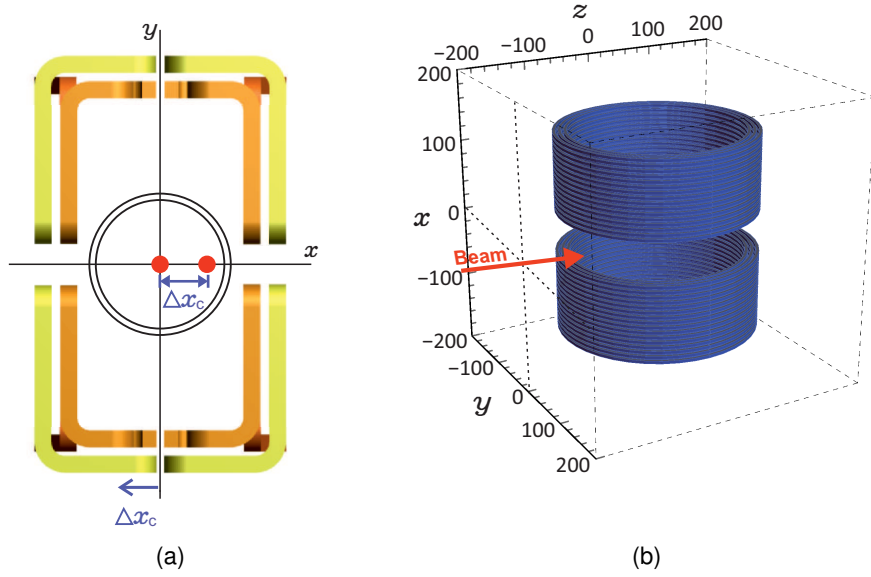


Figure 5.6: (a): Illustrates the beam spot (shown in red) relative to the centre of the quadrupole. If the quadrupole is shifted left by Δx_c then the beam spot would move right by the same amount. As the magnitude of the magnetic field increases from centre to the pole of the quadrupole (cf. figure 3.3(b)), the beam experiences an extra dipole-kick proportional to the amount of the shift. (b): A pulsed solenoid-pair with a gap in-between. With the same direction of current, a dipole field region is generated in the gap, also see figure 5.7 for the magnetic field region and proton beam traversing through the gap of the solenoid-pair.

be written as follows:

$$M_{G02} = M_{D8} M_{\text{QuadX4}} M_{D7} M_{\text{QuadY3}} M_{D7} M_{\text{QuadX2}} M_{D6} M_{\text{BL}} \quad (5.6)$$

$$\text{and} \quad \sigma_f = M_{G02} \sigma_0 M_{G02}^T, \quad (5.7)$$

where M_{D6} , M_{D7} and M_{D8} represent drift spaces D6, D7 and D8 of lengths l_{D6} , l_{D7} and l_{D8} respectively. M_{G02} represents the whole beamline and σ_f represents the final output beam properties. Now the above equation 5.7 can be solved for $\epsilon_x \sigma_{xf} = \epsilon_y \sigma_{yf}$, i.e. symmetric field shape in x - and y -planes, at the isocentre and with $\epsilon_x \gamma_x = \epsilon_y \gamma_y = 0$ for a parallel beam. These can be considered as default beam settings, which means without beam scanning and additional beam shaping. The final matrix equation in the previous gantry design (equation 4.8) was solved to deliver one field size and the physical collimators were considered to shape the beam further. However, the quadrupoles can also be used to change the shape of the beam. Therefore, the above equation 5.7 can also be solved for a range of field sizes, and this was the reason to use three quadrupoles with larger drift spaces in-between for more versatility. This also means that the condition $\epsilon_x \gamma_x = \epsilon_y \gamma_y = 0$ (condition for parallel symmetric beam) does not necessarily hold true for different beam shapes. However, a parallel output beam at the isocentre can be considered as the default beam setting when the aforementioned condition is met and with no beam scanning applied.

Thus, the last quadrupole triplet QT2 provided the basis to magnetically shape the

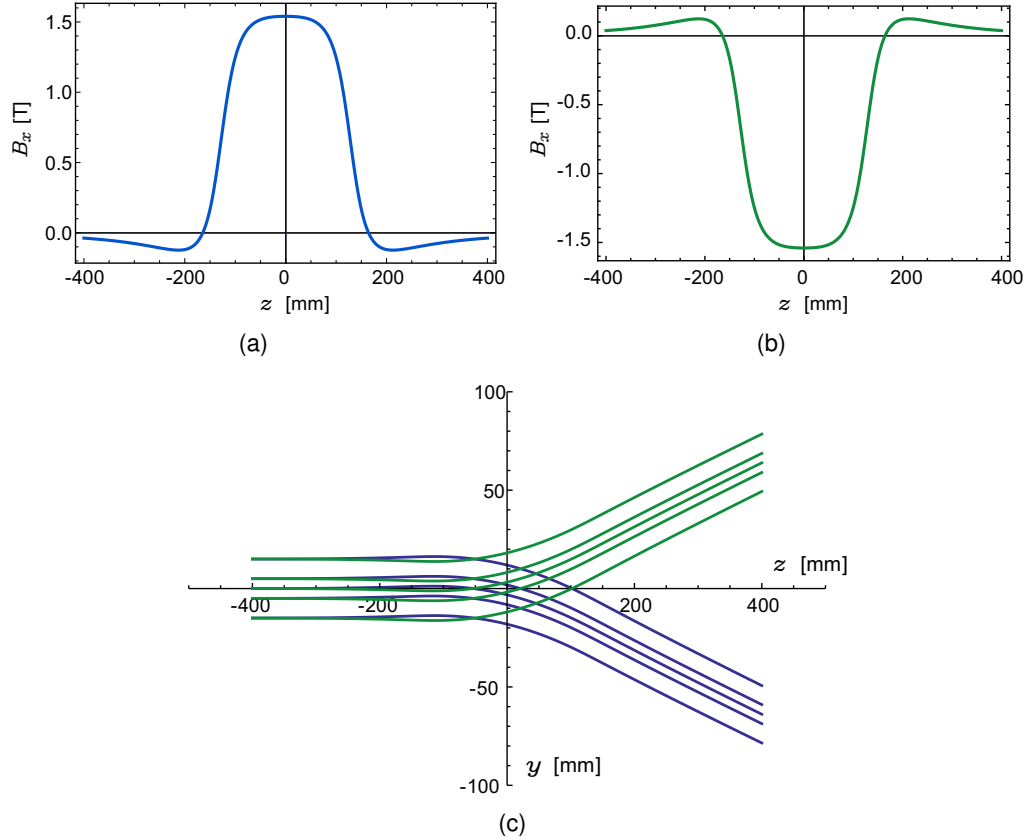


Figure 5.7: (a): Magnetic field strength inside the gap of a solenoid-pair (as shown in the figure 5.6(b)) with the same direction of current in each solenoid of the pair. (b): If the direction of current is reversed in both solenoids then the magnetic field strength can be reversed in the gap. The direction of the deflection can be controlled via the direction of provided current. (c): A parallel mono-energetic proton beam (green and blue lines) can be deflected when traversing through the gap, with the deflection direction controlled by the provided magnetic field strength.

beam to circular or elliptical forms and to different sizes. This would provide a new feature which has never been implemented in any medical gantry before. By selecting the peak nominal energy E_0 and the energy width $\Delta E/E_0$ via the ISESS, along with the transverse beam spot-size via the QT2 of ELPIS system, for each LAP bunch, different unequal spots or sub-volumes of the tumour can be irradiated, which would result in the conformal irradiation of the full extent of a tumour volume. Furthermore, beam shaping now can be performed without traversing through any physical materials, as it is done in all conventional scattering systems. This would preserve the proton fluence and reduce secondary radiation generation close to the treatment site.

Now, for scanning the beam in the transverse (i.e. x - and y -) directions, two separate approaches have been included in the ELPIS system. For scanning in x -direction, the fact that the offset in the quadrupole position with respect to the beam centre delivers a dipole-kick to the beam has been utilized. This is usually a misalignment issue in beamlines, however, here it can be utilized as an advantage. If Δx_c is the offset (please see the figure 5.6(a) for illustration) in a quadrupole position with respect to the beam then the dipole kick θ_Q can be given by:

$$\theta_Q = k_Q l_Q \Delta x_c \quad [\text{radian}], \quad (5.8)$$

where k_Q is the normalized quadrupole strength and l_Q is the length of the quadrupole. However, this dipole-kick would introduce an additional dispersion term behind the last 90° bending magnet (i.e. after the achromatic conditions were met). In conventional active beam scanning systems the dispersion effect is ignored due to the fact that the conventional mono-energetic pencil beams tend not to blow up with slight dispersion terms. However, in this case beams have about 20 times larger $\Delta E/E_0$ values and up to 10 times larger spot-sizes compared to the conventional scanning beams. The dipole-kick cannot be ignored and can be quantified by using the transfer matrix equation 3.19 of the dipole bend with $\rho_0 = l_Q/\theta_Q$ and multiplying it with the transfer matrix of the quadrupole (equation 3.13):

$$\begin{aligned} D(s) &= \frac{l_Q}{\theta_Q} \cos(k_Q l_Q) (1 - \cos \theta_Q) + \frac{1}{k_Q} \sin(k_Q l_Q) \sin \theta_Q \\ \text{and} \quad D'(s) &= -\frac{k_Q l_Q}{\theta_Q} (1 - \cos \theta_Q) \sin(k_Q l_Q) + \cos(k_Q l_Q) \sin \theta_Q. \end{aligned} \quad (5.9)$$

The above equation 5.9 shows the dispersion functions for the x -focusing quadrupole. The dispersion functions for the same off-set in the y -focusing quadrupole is:

$$\begin{aligned} D(s) &= \frac{l_Q}{\theta_Q} (1 - \cos \theta_Q) \cosh(k_Q l_Q) + \frac{1}{k_Q} \sin \theta_Q \sinh(k_Q l_Q) \\ \text{and} \quad D'(s) &= \cosh(k_Q l_Q) \sinh \theta_Q + \frac{k_Q l_Q}{\theta_Q} (1 - \cos \theta_Q) \sinh(k_Q l_Q). \end{aligned} \quad (5.10)$$

The beamline parameters before were calculated for the double-achromatic condition by solving the equations 5.5 and 5.7, i.e. the default settings without scanning. Now, i.e. for beam scanning, the quadrupole set QT2 is assumed to have mechanically controlled shifts $\pm \Delta x_c$, and the beam can be given a controlled dipole-kick in $\mp x$ -direction. The dispersion thus produced, see equations 5.9 and 5.10, needs to be canceled. A shot-to-shot dispersion correction can be implemented within the quadrupole set QT1 upstream of the last bending magnet SM2, so that the double-achromatic condition can be met for each scanning spot, i.e. for the required dipole-kick θ_Q , downstream of the ELPIS system.

For beam scanning in y -direction the bending term ($\mathbf{v} \times \mathbf{B}$) of the Lorentz force has been utilized, by a dipole field generated in-between two pulsed solenoids, i.e. a solenoid-pair. The two solenoids of the pair are placed such that their apertures face each other separated by a gap. With the same direction of current a dipole field region is generated perpendicular to the beam traversing axis. The beam traverses through the gap and experiences a net bending force in y -direction. The 3D magnetic field computing code called Radia (Chubar et al., 1998) was used to simulate the solenoid-pair. It was found that each solenoid in the pair with 3×16 windings and with an inner radius of 12 cm could be used for the said purpose, see figures 5.6(b) and 5.7. The bending angle can be controlled via the amount and direction of the current provided to the solenoids, about 5 times

larger bending angles than conventional systems, could be achieved. Thus, short-throw scanning could be delivered without the need to increase the height of the gantry, i.e. the distance between the last bending magnet SM2 and the isocentre. This solenoid-pair was used as the last magnetic element in the gantry, and it was not included in the mathematical model but was investigated via the beam tracking simulations. The results from the beam tracking simulations are presented in the section 5.3.4.

5.2.6 Gantry model and beam tracking simulations

The mathematical model developed in the previous sections, i.e. sections 5.2.2 to 5.2.5, was solved for the MC generated LAP sources step-by-step by the algorithm written in Mathematica, similar to the preliminary gantry design solution (see section 4.2.7). Then the optimized solution of the advanced gantry model was translated to GPT simulation code for full beam tracking simulations, also similar to the previous gantry design (see section 4.2.8).

Although, more than one type of LAP sources can be simulated via MC code and the details in the mathematical model could be optimized for each particular source. The principal solution can be verified via the beam tracking simulations by using only one type of source. The design can be optimized for any other (future) sources, however, this is omitted here to avoid redundancy and because no major changes were found between TNSA and RPA like sources, except small optimizations in magnetic field strengths and drift spaces. Therefore, the results presented in the section 5.3 were only optimized for RPA like LAP sources (section 4.2.6). As mentioned earlier in section 4.2.8, the beam tracking simulations took a long time (up to four days) to simulate one full LAP bunch, therefore, the number of protons per bunch has been reduced here by a factor of 4×10^6 to require less computational power and save simulation time. Qualitatively, the tracking results do not differ, however, they must be multiplied by the same factor to compare with the original sources. The beam tracking results for different beamline functions are presented in the section 5.3.1, however, the results have not been multiplied by the factor and results are shown as obtained from the simulations.

5.2.7 Clinical applicability of the gantry design via 3D dose verification

The further development of the BEAD model, i.e. from 1D to 3D, was halted in favor of the advanced 3D dose schemes presented by Schell and Wilkens (Schell and Wilkens, 2010), described in the section 2.5.2. The 3D treatment planning system (TPS), called LAP-CERR, was developed for pulsed LAP beams at the Department of Radiation Oncology, Klinikum rechts der Isar, Technical University Munich, Germany, and a collaboration was established to further the research in the TPS and gantry designs via clinical studies. This advanced 3D TPS is based on an open source software, i.e. Matlab based computational environment for radiotherapy research (CERR), and it is capable to import 3D computer tomographic (CT) data of patients and provide tools to delineate organs at risk (OAR), planning target volume (PTV), clinical target volume (CTV) etc. LAP-CERR can calculate absorbed doses from the user defined beams and even for intensity

modulated proton therapy (IMPT). LAP-CERR was designed to calculate advanced dose delivery schemes, i.e. spot-based, lateral-layer-based, axial-layer-based, partial-volume-based and target-volume-based. The first clinical study was conducted to verify the clinical applicability of the pulsed high intensity LAP sources and the filtered output beams, presented in the reference (Hofmann et al., 2015). For this study, the basic output parameters were taken from the preliminary gantry design (presented in the previous chapter), i.e. it was considered that a gantry can filter and deliver bunches with $\Delta E/E_0$ in the range of 24 – 4% in 2% energy steps with 2 cm (FWHM) beam size. The shape and quality of the output beam was ignored at that time. Only the axial-layer-based dose delivery scheme was utilized, as the other advanced dose schemes were not functional in the TPS at that time.² In this study two patients with brain tumours (with relatively small sized tumours of about 275 cm³) were selected (who were previously treated at the Department of Radiation Oncology, Klinikum rechts der Isar, Technical University Munich, Germany) and treatment plans were made using conventional proton beams, axial-layer based LAP beams and also state-of-the-art volumetric modulated arc therapy with photon beams. All plans were clinically approved by an oncologist, on the basis of tumour coverage, conformity and homogeneity, and then were compared to each other. This study showed that the LAP beams can be utilized in clinical radiotherapy and can provide treatment plans with high clinical standards. Furthermore, this study concluded that the pulsed, high-intensity LAP bunches, when applied to the tumour volumes with large energy widths do not necessarily impair the quality of the treatment plans. This has been a main criticism towards the clinical application of LAP beams, as presented in detail in section 2.7. This work was crucial and provided the encouragement to continue research and development as no clinical showstoppers were identified. However, to deliver a clinically relevant treatment plan about 9650 filtered LAP bunches were required, which corresponds to a delivery time of about 16 min (at a repetition rate of 10 Hz). The distinctive feature of LAP-CERR is that it can optimize dose distributions for the best tumour coverage and dose conformity on 3D patient data by combining several scanning spots axially (and/or laterally) to be irradiated simultaneously by one energy filtered LAP bunch. However, the several combined spots may require different doses to achieve 3D dose homogeneity. It was further noted in this study that if LAP-CERR was allowed to modulate the intensity of the individual LAP bunches then the total number of required LAP bunches could be reduced to 3641 (i.e. about 6 min delivery time), which is a reduction to about 38%. Thus, showing the importance of beam control (i.e. transverse beam size and scanning) and intensity modulation scheme from the beamline, which were not included in the preliminary gantry design.

An advanced clinical gantry capable of delivering all of the aforementioned advanced dose schemes was not available. This presented the clinical need of an advanced beam delivery system to be included in this advanced clinical gantry design. The new ELPIS system is now able to shape and scan such broad beams and capable of delivering the advanced dose models for LAP beams. Although systematic 3D TPS studies including different tumour types and dose delivery approaches are beyond the scope of this thesis,

²Further work in research and development of the LAP-CERR is still going on to incorporate and made all the advanced dose schemes, presented in the section 2.5.2, functional.

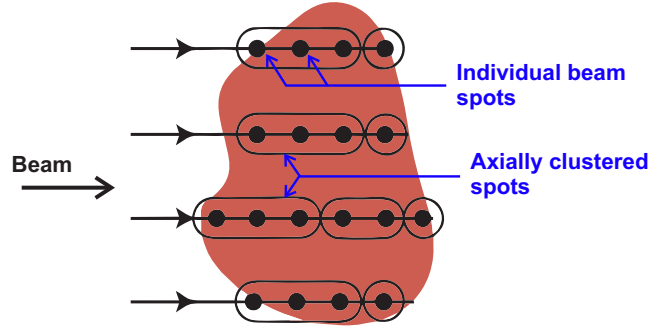


Figure 5.8: Illustration of axial clustering used in 3D plan calculations. In conventional active scanning systems, tumour volume is scanned sequentially with individual beams with fixed spot-size (shown by black dots). However, to reach a similar dose distribution several spots can be combined axially (i.e. axial clustering), and can be irradiated simultaneously with one filtered LAP bunch with specified large energy window.

however, one feasibility study is presented as an example to illustrate the functionality of the ELPIS system.

A head and neck patient with a large tumour volume (of about 600 cm^3) was selected for this feasibility study, who was previously treated with conventional megavoltage x-rays at the Department of Radiation Oncology at Technical University of Munich, Germany. Only the axial-layer-based dose delivery scheme was utilized, as in the first clinical study. The larger tumour volume was chosen to determine limits of the treatment times for 10 Hz LAP beams. The simulated input LAP spectra (i.e. RPA like source, presented in the section 4.2.6) and the output beams from the results of the tracking simulations through the advanced clinical gantry were incorporated in the LAP-CERR in a form of a library. That is, for this study detailed input beam quality and output beam shape, size and energy widths were implemented in the LAP-CERR for the verification of the clinical applicability of this advanced gantry and the ELPIS system, and not just the clinical application of LAP beams in general. Now, LAP-CERR could choose from the energy range and filtered energy windows $\Delta E/E_0$ per bunch, and divide the tumour volume accordingly, as illustrated in the figure 5.8. This means LAP-CERR would axially cluster the scanning spots so that no cluster is longer than the allowed maximum transportable $\Delta E/E_0$ and the smallest scanning spot is not smaller than the minimum transportable $\Delta E/E_0$ from the gantry. Furthermore, the spectral distribution of each transportable $\Delta E/E_0$ window was cataloged and then the dose distribution of these filtered bunches were simulated in Geant4 simulation package for characteristic depth dose profiles. Now, LAP-CERR could choose from the depth dose profiles of the individual bunches and generate 3D dose plans on the CT data of the patient. Several constraints were applied so that OAR and healthy tissues around the marked tumour volume would not receive more than an allowed dose.

The LAP-CERR plans were analyzed on clinically relevant parameters like tumour coverage TC and the conformation number CN , which can be given as:

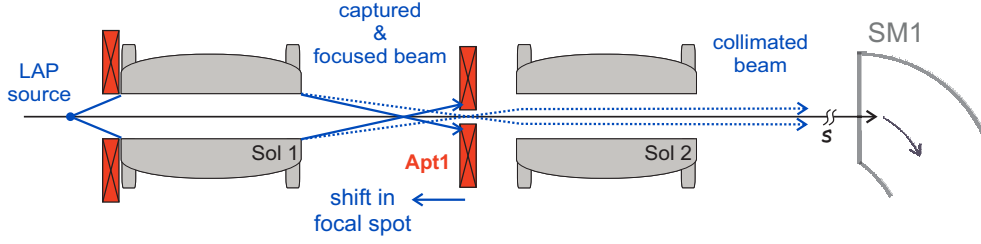


Figure 5.9: Schematic illustration of the intensity modulation scheme via the two-step capturing and collimation system. The dotted blue lines, behind the solenoid1, represent the trajectory of protons with energy E_0 as designed for maximum transport efficiency, cf. figure 5.2. The blue solid lines show the effect of a stronger focusing strength applied by the solenoid1. This would decrease the transport efficiency, also see figure 5.10 for the effect in the phase space.

$$TC = \frac{V_{T,p}}{V_T} \quad (5.11)$$

and

$$CN = \frac{V_{T,p} \cdot V_{T,p}}{V_T \cdot V_p}$$

where V_T is the target volume, V_p is the whole volume receiving at least the prescribed dose and $V_{T,p}$ is the target volume receiving at least the prescribed dose (for details see reference (Lomax and Scheib, 2003)). With the help of these parameters as well as by the dose volume histograms it was ensured that the generated plans were similar to clinically accepted plans. The results are presented in the section 5.3.5.

5.2.8 Integrated intensity modulation scheme

In the state-of-the-art intensity modulated PT, a 3D TPS can calculate different doses to different scanning spots from different angles to achieve the best tumour conformity and dose homogeneity while sparing the healthy tissues around. In conventional PT systems, such calculated doses can be delivered by modulating the number of protons for each scanned spot by modulating the time for the beam to stay ON per scanned spot. It is relatively straight forward to modulate number of protons as a function of beam-ON time for quasi-continuous, stable beams from conventional accelerators.

However, LAP beams consist of ns bunches with a very high number of protons and with a maximum repetition rate of 10 Hz only. It is not possible to modulate the number of protons within a single bunch as a function of beam-ON time. Therefore, previously published studies (presented in the section 2.6) considered either the use of integral number of shots or proposed to use conventional beam shaping tools close to the patient site, such as range shifters and physical scatterers to reduce the beam intensity. Moreover, it was shown that integrating an intensity modulation scheme in a laser-driven PT system could increase the treatment delivery efficiency to about 30 – 40% (Hofmann et al., 2015). This is because while optimizing the dose the LAP-CERR system could reject intense bunches completely, however, with intensity modulation included it would have the option to select a reduction of proton number in the same bunch and then utilize the bunch. Therefore, there was a need to design an equipment able to modulate intensity within the presented gantry design. The beam shaping capabilities of the ELPIS system are highly

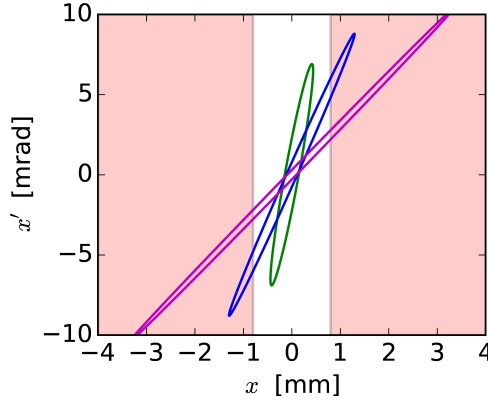


Figure 5.10: Schematic illustration of the phase space ellipse rotation as an effect of a stronger focusing by the first solenoid Sol1. The green ellipse represents the protons with the selected E_0 at the centre of the aperture Apt1 for default focusing strength of the first solenoid. The red shaded area represents the area restricted by Apt1. The increased solenoid focusing strength rotates and stretches the green ellipse, i.e. into blue and magenta ellipses, and thus blocks the parts of the rotated ellipse which would decrease the transport efficiency.

desirable as it can efficiently distribute the protons per bunch to unequal sub-volumes for the best overall achievable 3D dose distributions, as the fluence changes inversely with the beam size. However, due to intense LAP bunches, it is likely to exceed prescribed doses for small beam sizes, which could restrict the use of smaller beam sizes. Smaller beam sizes would be required for best possible 3D conformity of irregular tumour volumes, especially at the edges of the tumour volume. Thus, it could limit the homogeneity of the 3D dose distributions, and force the LAP-CERR to choose larger beam sizes which would produce undesirable results.

Therefore, an intensity modulation scheme is necessary to modulate the deliverable number of protons per bunch, and hence, to control the dose deliverable per bunch. The two-step capturing system, described in the section 5.2.2, has been optimized for maximum transport efficiency around the nominal energy E_0 by focusing the beam via the first solenoid on to the centre of the aperture Apt1. However, if the focal length is decreased by increasing the current in the first solenoid, this will shift the focal spot of the protons with energy E_0 , upstream from the aperture Apt1, and consequently decrease the transport efficiency. Thus, it is possible to modulate the intensity of each bunch. Figure 5.9 illustrates this intensity modulation scheme, while figure 5.10 shows the effect of the increasing focusing strength of the first solenoid on the clipping of the phase space ellipse of the nominal energy. This clipped beam is then collimated to the same beam parameters as before via the second solenoid. This beam is then transported through the ISESS and the ELPIS systems to the isocentre. This would provide an efficient solution for intensity modulation controlled by the magnetic strength in the beginning of the beamline, rather than the physical scatterers at the end of the beamline.

5.2.9 LAP beam fluctuations

The LAP beams are well-known (or notorious) to have large shot-to-shot fluctuations

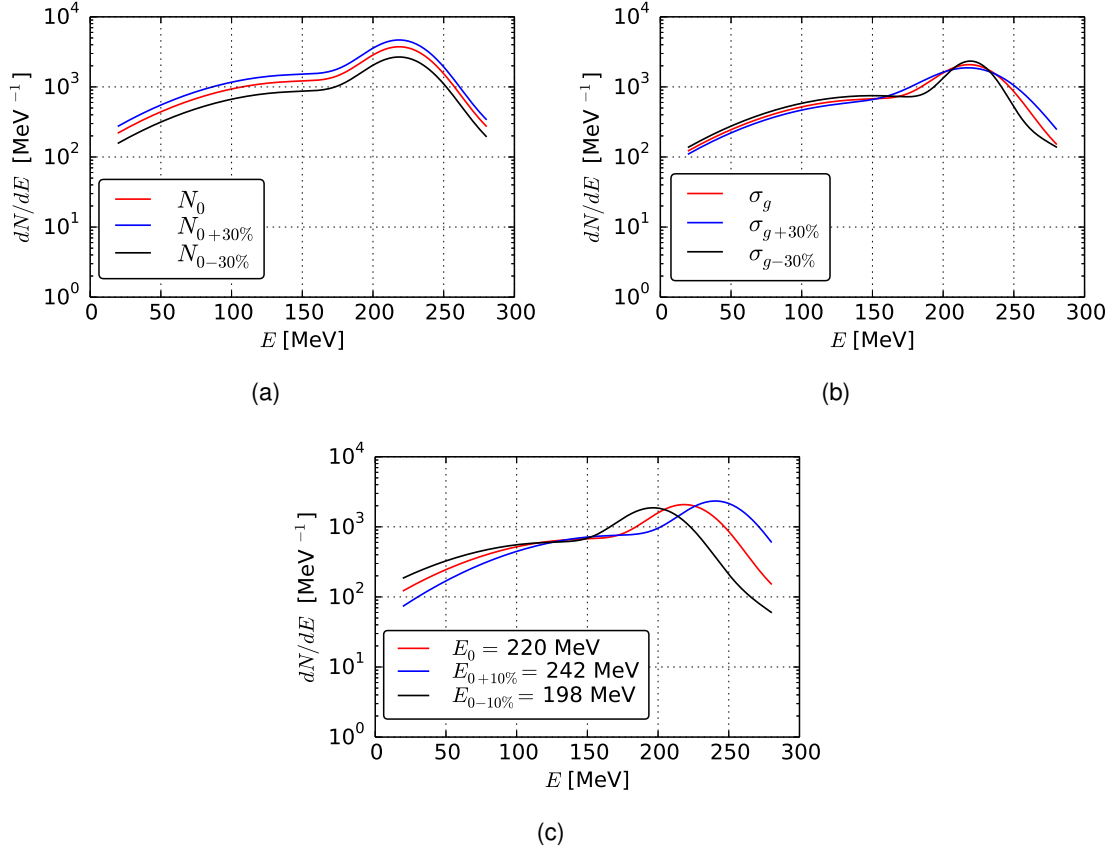


Figure 5.11: RPA like input energy spectra of the LAP bunches with fluctuations described in section 5.2.9. (a): $\pm 30\%$ variation in the total number of protons in the bunch. (b): $\pm 30\%$ variation in the spread of the spectrum in the higher energy region. (c): $\pm 10\%$ change in the E_0 value.

due to the non-linear acceleration process by the high intensity laser pulses. Although, the fluctuations in the source cannot be eliminated by any beamline, however, it is interesting to characterize the output of the gantry design for possible fluctuations, i.e. how the output beam is affected by what type of fluctuations in the source. A set of simulations were made to observe this. The RPA like source which has been described, in the section 4.2.6, by a bi-Gaussian fit (see equation 4.13), can also be written as:

$$N(E) = N_0[ne1 + ne2] \quad (5.12)$$

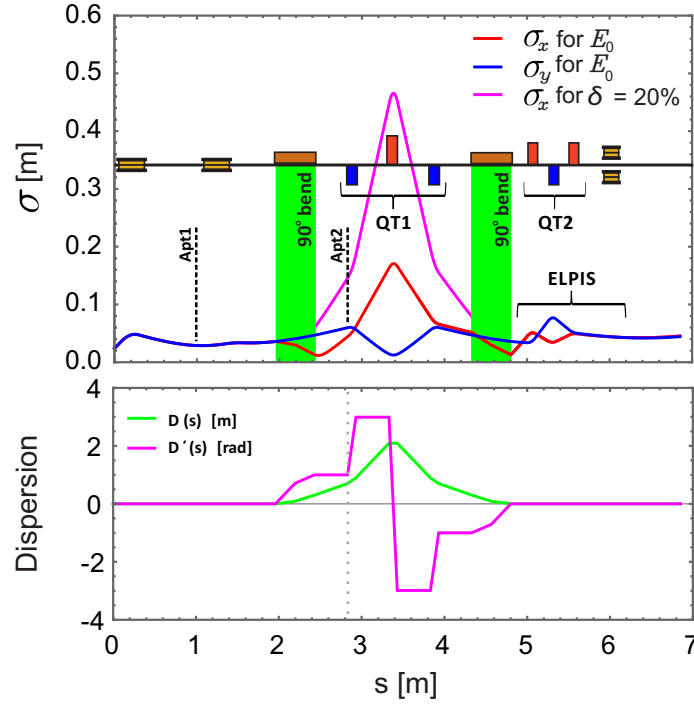
where

$$ne1 = e^{-((E-E_0)/30)^2} \quad (5.13)$$

$$\text{and} \quad ne2 = 0.4 \times e^{-((E-(E_0-70))/100)^2},$$

with $ne1$ and $ne2$ being the two individual Gaussian curves and N_0 is the number of protons in the bunch. Three main types of fluctuations were considered for these simulations, which are given below:

1. Fluctuation in the total number of protons per bunch, i.e. N_0 , in the same opening angle for the same overall distribution as in equation 5.12. Three RPA like sources have been generated via the MC code following three curves described by equa-



Nomenclature:



Figure 5.12: The beam evolution through the advanced gantry model has been graphically shown here. The magnetic elements have been drawn along the nominal beam path, as used in the model to manipulate the beam properties. The plot on top shows the beam shape according to the equations 3.27, red and blue lines represent beam nominal energy in x - and y -directions, while the magenta line represents the beam in x -direction with 20% momentum spread. The bottom plot shows the evolution of the dispersion functions along the beamline in the default settings, i.e. with parallel beam at the isocentre without scanning. These plots change slightly with scanning option, see figure 5.22. This model was then translated to the particle tracing simulation code, please see figure 5.13 for corresponding magnet positions on the particle tracks.

tion 5.12 for $E_0 = 220$ MeV with N_0 , $N_0 + 30\%$ and $N_0 - 30\%$ (see figure 5.11(a)).

2. Fluctuation in the energy distribution around the nominal energy. The Gaussian curve $ne1$ mainly describes the proton distribution in the higher energy range, i.e. around the nominal energy E_0 . When compared with the standard form of the Gaussian beam with centre at the origin, i.e. $g(x) = e^{-(x^2/2\sigma_g^2)}$, the nominal Gaussian sigma for the RPA like source can be obtained, which would be $\sigma_g = 21.21$ MeV. Now, a fluctuation in the spectrum around E_0 means fluctuation in σ_g . A $\pm 30\%$ fluctuation in the Gaussian sigma is considered. Three RPA like sources have been generated via the MC code following three curves described by equation 5.12 for $E_0 = 220$ MeV with σ_g and $\sigma_g \pm 30\%$, i.e. $\sigma_{+30\%} = 27.57$ MeV and $\sigma_{-30\%} = 14.85$ MeV (see figure 5.11(b)).
3. Fluctuation in the nominal energy E_0 . It is possible that the whole spectrum shifts, right or left, on the energy axis, that means E_0 . To simulate this, three RPA like sources have been generated via the MC code following the curves for $E_0 = 220$ MeV

and $E_0 \pm 10\%$, see figure 5.11(c).

The generated new sources were then used in tracking simulations with the default settings for the nominal energy $E_0 = 220$ MeV. The reason why a value of $\pm 30\%$ was chosen for the first two points was to compare the results with the dose fluctuation studies performed in the first clinical feasibility study for LAP beams (Hofmann et al., 2015), in which the effect of (10 – 30%) fluctuation in the proton number in the bunch on the 3D treatment plan by LAP-CERR was discussed. A $\pm 10\%$ value was chosen for the nominal energy E_0 to keep the main beam in the acceptance of the gantry, more than this value the output beam would not be suitable for dose delivery. The results are presented and discussed in the section 5.3.7.

5.3 Results

5.3.1 Solution for the gantry model

The mathematical model developed for the advanced gantry was solved in steps by solving for the desired beam parameters for each section of the beamline and then plugging them into the following beamline section. This is the same method described for the preliminary gantry model solution in section 4.3.1. Table 5.1 lists the individual magnetic elements and drift spaces, in order starting from the LAP source, with their respective calculated magnetic field strengths and lengths, along with their position in the beamline.

The evolution of the initial beam parameters through this advanced gantry model is shown in figure 5.12. It shows the evolution of the beamlet with E_0 energy in transverse planes, along with the portion of the beam with 20% momentum spread. The magnetic elements are clearly shown, along with the positions of the apertures. Figure 5.12 shows an output beam with default settings, i.e. parallel beam with equal beam size in both transverse directions. In the mathematical model, the apertures were not used, however, they were implemented in the beam tracking simulations. Also, the beam shaping and scanning parameters were characterized in the tracking simulations. The solution of the mathematical model was then translated into the GPT tracking code (see figure 5.13 for the full layout of the gantry design). The GPT simulation results are presented in the following sections.

5.3.2 Two-step beam capturing and collimation

The diverging LAP beam is focused tightly around selected E_0 at 1 m from the laser-target, by the first solenoid Sol1. The second solenoid Sol2 then recaptured and collimated the beam. To illustrate the functioning of the two-step capture and collimation system compared with a single solenoid lens (cf. 4.3.2), the proton trajectories of a diverging beam with a single energy are shown as an example in the figure 5.14. The transverse size of the collimated beam behind the two-step system is smaller than the single solenoid capturing lens of the preliminary gantry design. Furthermore, it was possible in the two-

Table 5.1: List of beamline elements used for the advanced gantry design, along with the corresponding lengths, start positions in the beamline, and magnetic strengths for corresponding magnetic elements.

Main beamline component	Beamline element	Start position [cm]	Length [cm]	Normalized strength [m^{-1}]
LAP beam source	-	0	-	-
Two-step capture & collimation section	D0	0	$l_{D0} = 3.0$	-
	Sol1	3.0	$l_S = 22.0$	$k_{S1} = 4.45$
	D1	25.0	$l_{D1} = 75.0$	-
	Apt1	95.0	$l_{Apt1} = 5.0$	-
	D2	100.0	$l_{D2} = 15.0$	-
	Sol2	115.0	$l_S = 22.0$	$k_{S2} = 2.26$
	D3	137.0	$l_{D3} = 40.0$	-
90° beam bending magnet	SM1	177.0	$\rho_0 = 30.0$ $l_{arc} = 47.0$	-
Energy selective aperture	D4	224.0	$l_{D4} = 40.0$	-
	Apt2	259.0	$l_{Apt2} = 5.0$	-
Beam control via QT1 for achromatic transport	QuadY1	264.0	$l_Q = 10.0$	$k_{Q1} = 5.05$
	D5	274.0	$l_{D5} = 40.0$	-
	QuadX2	314.0	$l_Q = 10.0$	$k_{Q2} = 5.28$
	D5	324.0	$l_{D5} = 40.0$	-
	QuadY1	364.0	$l_Q = 10.0$	$k_{Q1} = 5.05$
	D4	374.0	$l_{D4} = 40.0$	-
90° beam bending magnet	SM2	414.0	$\rho_0 = 30.0$ $l_{arc} = 47.0$	-
Beam shaping via QT2	D6	461.0	$l_{D6} = 20.0$	-
	QuadX3	481.0	$l_Q = 10.0$	$k_{Q3} = 7.20$
	D7	491.0	$l_{D7} = 15.0$	-
	QuadY4	506.0	$l_Q = 10.0$	$k_{Q4} = 6.40$
	D7	516.0	$l_{D7} = 15.0$	-
	QuadX5	531.0	$l_Q = 10.0$	$k_{Q5} = 4.30$
	D8	541.0	$l_{D8} = 150.0$	-

Note: Parameters in black were selected as input values while the parameters in blue have been calculated via the mathematical model developed for the advanced gantry design. The position of all the magnetic elements are graphically shown in the figure 5.12 and figure 5.13. The solenoid-pair used for the beam scanning in the y -direction is not mentioned in this table. The parameters of the solenoid-pair were not calculated via the mathematical model but were simulated in the beam tracking simulations, further discussed in the section 5.3.4.

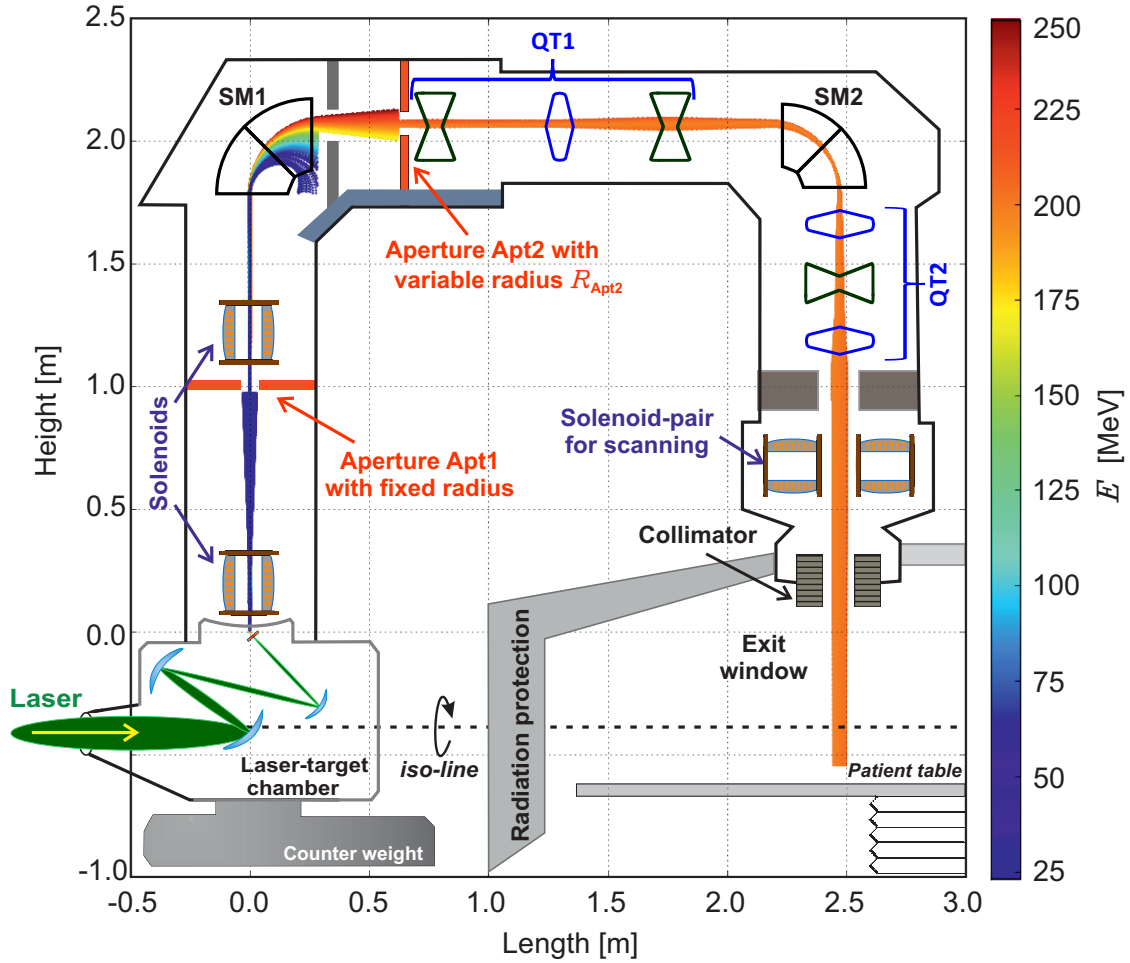


Figure 5.13: Schematic representation of 360° isocentric advanced clinical gantry design with new nozzle system. It also shows the schematic layout of the laser-target chamber and the treatment room. Laser pulses could be focused on the laser-target generating LAP bunches, which are then captured, energy sorted and transported to the patient site. MC generated RPA like LAP bunches were tracked through the design. The particle tracks along the beamline are shown with a color map representing the proton energies. The beamline elements are drawn on the tracks to illustrate their positions (also see figure 5.12) with simulated parameters listed in the table 5.1. Note here that in tracking simulations LAP bunches were starting from $(x = 0, y = 0)$ and the *iso-line* (i.e. the rotational axis) is shown 40 cm below it, where the laser pulses enter the gantry.

step scheme to adjust the drift length $D2$ (see figure 5.2) along with the size and current of the second solenoid Sol2, independent of the initial capturing solenoid Sol1 parameters.

Figure 5.15 shows the energy spectra behind the second solenoid Sol2 for a full LAP bunch tracking simulation. The ellipse in figure 5.15(b) represents the acceptance of the beamline which can contain the protons with E_0 with 22% width, in this case $E_0 = 220$ MeV. The second solenoid has rotated the phase space such that protons with E_0 have minimum divergence (i.e. have been collimated).

5.3.3 Energy selection system

The beam was transported to the first 90° bending magnet SM1 behind the two-step beam capturing and collimation system. The magnetic fields in the following beamline

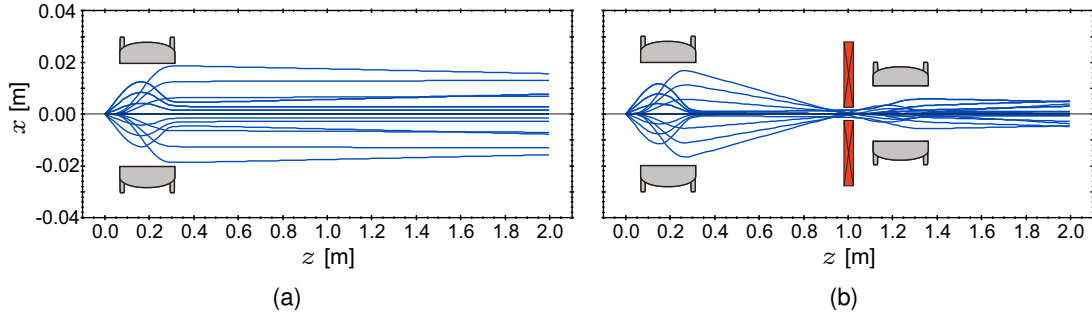


Figure 5.14: Comparison between (a) one-step and (b) two-step capture and collimation schemes. (a) is same as figure 4.13, and is shown here again for the side-by-side comparison. The proton trajectories, with arbitrary single energy, of a diverging beam (blue lines) show schematically that the two-step system can deliver a well collimated beam with smaller transverse dimensions with similar collection angles as the one-step scheme.

sections has been tuned for the same E_0 as the capturing system. An aperture Apt2, with 5 cm thickness and variable opening radius has been placed at 35 cm behind the SM1 just before the first quadrupole, see table 5.1. Also, figures 5.12 and 5.13 show the position of Apt2. Due to the dispersion the beam spreads spatially in the bending plane (as a function of energy and distance), which would allow to select the beam as a function of the radius R_{Apt2} of the aperture Apt2, see figure 5.16. Thus, the radius R_{Apt2} of the aperture Apt2 was varied for filtering specific $\Delta E/E_0$ energy windows. The filtered bunch was then transported through the gantry and the spectra were measured at the isocentre.

The filtered $\Delta E/E_0$ windows could be selected ranging from about 3 – 19% in 1% steps, see figures 5.17. Although, a larger $\Delta E/E_0$ filtered window of about 22% was expected, the simulation results showed that only 19% could be transported. The transport efficiency $\eta(E_0)$ was different for each selected window, i.e. the efficiency decreases with reduced filtered energy widths. For the energy widths in the range of 19 – 14% the $\eta(E_0)$ was as high as 97%, for the range 13 – 10% the $\eta(E_0)$ decreases from 95% to 70%, and for the range 9 – 3% the $\eta(E_0)$ dropped down to 20%, which was expected. The filtered energy spectra, nevertheless, have certain distribution which could be approximated by a higher order parabolic function, as given below:

$$dN/dE_{\text{filtered}} = a_{\text{filtered}} (E - E_0)^6 + ke, \quad (5.14)$$

where a_{filtered} is related to the shape of the curve and was determined for each curve (i.e. output beam spectrum) from the tracking simulations, whereas, ke is related to the transport efficiency η (see figure 5.18). It was beneficial to describe the output of the gantry in such form, as these curves were then used to create a library for the 3D TPS LAP-CERR (see sections 5.2.7 and 5.3.5).

5.3.4 Achromatic beam delivery via the ELPIS system

For a homogenous beam profile at the isocentre, the dispersion introduced for energy selection was canceled via the quadrupole triplet QT1 and the second 90° bending

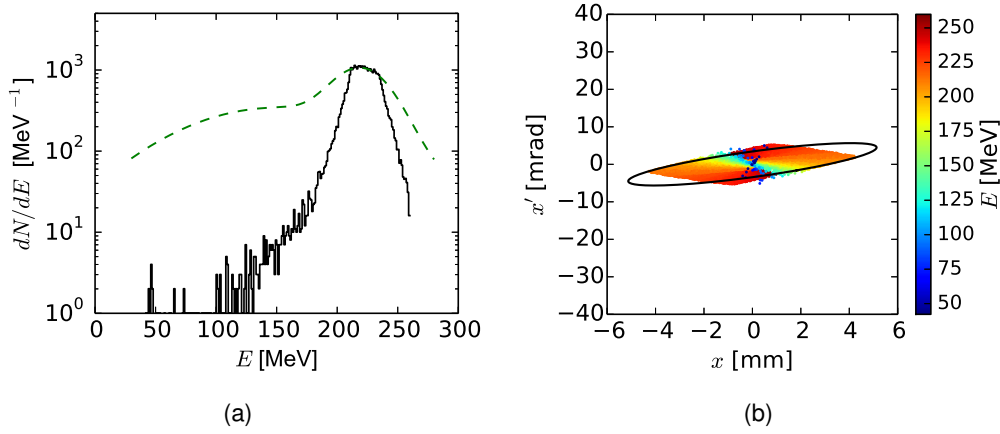


Figure 5.15: (a): Initial energy spectrum of a LAP bunch (green dashed-line) entering the gantry simulations, with the spectrum (black line) after the two-step capture and collimation system (here, for $E_0 = 220$ MeV), just before the first sector magnet SM1. (b): Corresponding proton distribution (color scale) in the transverse phase space (beam is symmetric in both transverse directions), while black ellipse represents the acceptance of the following magnetic energy selection system, i.e. for $\Delta E/E_0$ of about 22%.

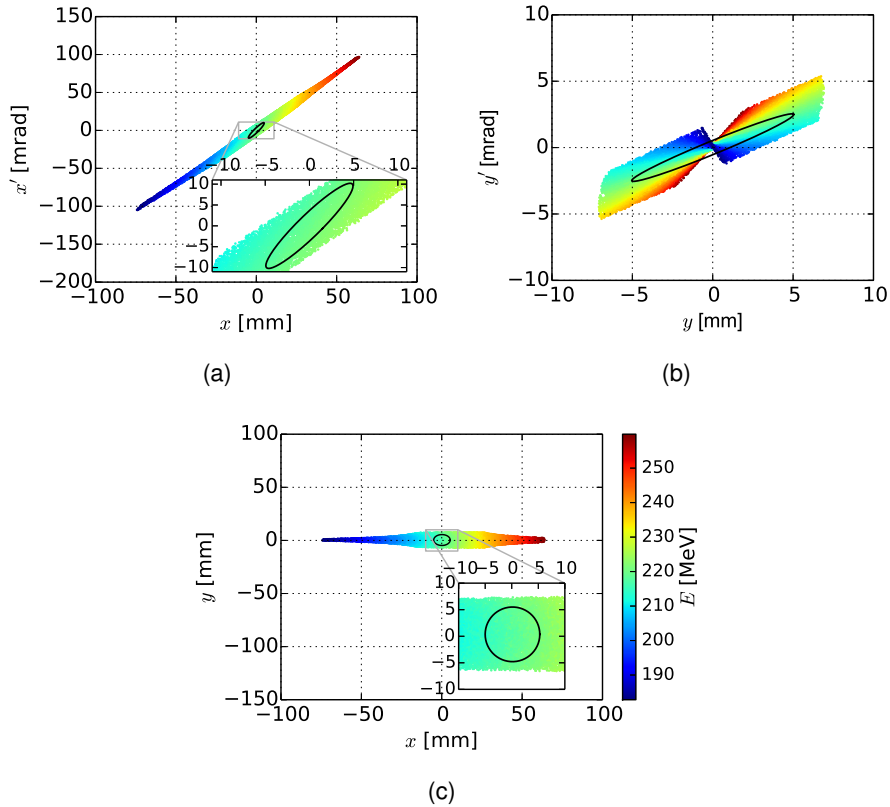
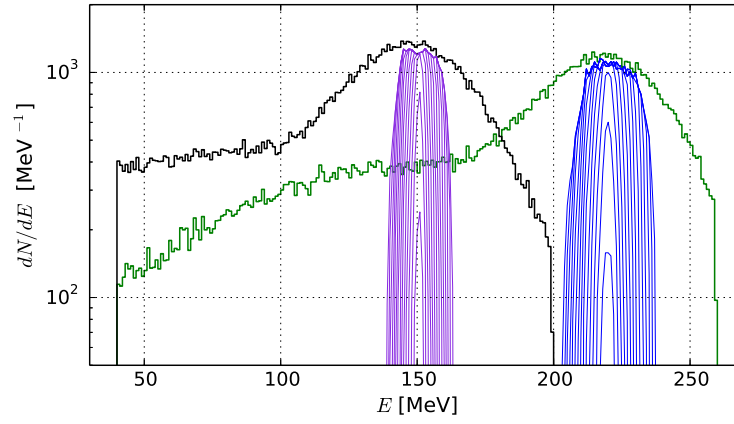
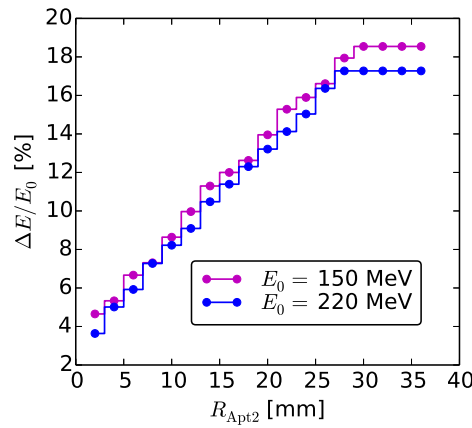


Figure 5.16: Beam profile at the centre of the aperture Apt2, used for energy selection. (a): phase space in the x -plane. (b): phase space in the y -plane. The spatial energy spread due to the dispersion is only in x -direction, i.e. bending plane. The black ellipse represents the acceptance of Apt2 with $R_{\text{Apt2}} = \sqrt{\epsilon\beta} = 5$ mm. (c): Beam spot in real space and the black circle shows the acceptance of Apt2 for $R_{\text{Apt2}} = 5$ mm, i.e. only particles inside it would continue in the beamline and the rest will be stopped here. All figures share the same energy scale as shown in (c).



(a)



(b)

Figure 5.17: (a): The energy spectra when filtered and transported to the isocentre. The black and green spectra represent two exemplary LAP bunches with energy peaks (E_0) at 150 MeV and 220 MeV respectively. The magenta and blue set of curves, under the respective black and green initial proton distributions, show the filtered spectra transported for varied R_{Apt2} values selecting energy windows $\Delta E/E_0$ between 3% (inner line) and 19% (outer line). (b): Respective relationship between R_{Apt2} and filtered $\Delta E/E_0$.

magnet SM2. By introducing the second bending magnet SM2 the beamline now can be arranged in a rotatable isocentric gantry formation, similar to the preliminary gantry design. The drift spaces and the individual strengths of QT1 quadrupoles were calculated for $D(s) = 0$ and $D'(s) = 0$ and are given in the table 5.1. Figure 5.19 shows the beam profile at the isocentre. If compared with the output beam profile from the preliminary gantry design (see figure 4.18), it is clear that the output beam from this advanced gantry design has been improved and is more homogenous. All the protons in the large $\Delta E/E_0$ window cover a homogenous circular area in the irradiation field, with the dispersion values lower than 10^{-5} .

To efficiently deliver a tumour conformal dose distribution, the beam spot-size and shape can be varied by the ELPIS system, specifically via the quadrupole triplet QT2 settings as described in the section 5.2.5. Figure 5.20(a) shows a LAP bunch from the GPT particle tracking simulations and shows the evolution of beam size controlled by the

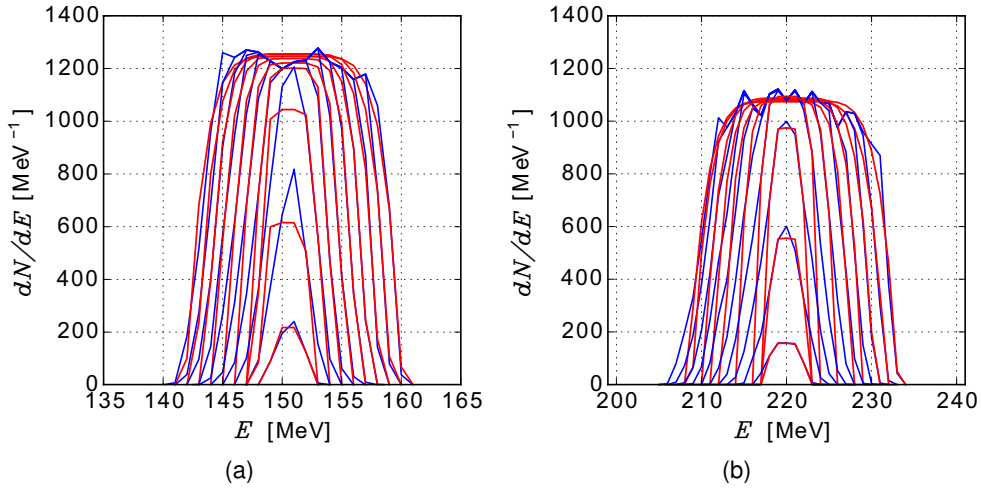


Figure 5.18: Simulated output beam spectra of the filtered LAP bunches with varied $\Delta E/E_0$ windows (blue lines). (a) and (b) show the spectra with E_0 at 150 MeV and 220 MeV, respectively (also see figure 5.17(a)). These bunches have certain dN/dE_{filtered} distribution which can be approximated by a parabolic function (red lines) for each output beam, as described by the equation 5.14.

QT2 parameters. Figure 5.20(b) shows different spot-sizes in elliptical shapes achievable at the isocentre via different QT2 settings. The beam spot size could be chosen from diameter 20 cm down to 1 cm. This means for the gantry setting to deliver a specific $\Delta E/E_0$ window, i.e. with the same η , then by changing the size of the beam spot the fluence is changed. This needs to be taken into account while calculating the dose distribution by a 3D treatment planning system such as LAP-CERR for using advanced dose delivery methods.

The ELPIS system is also designed to scan the beam in both transverse directions, i.e. scan in x -direction via the mechanical shifts of QT2 with respect to the beam and scan in y -direction via the applied current in the solenoid-pair, described in section 5.2.5. Figure 5.21 shows the functionality of the scanning system with a small sized beam with the position of the centre of the beam as a function of QT2 shifts and as a function of the current provided in each solenoid of the solenoid-pair. These are the two parameters required for scanning the beam over the full extent of the irradiation field, of about $20 \times 20 \text{ cm}^2$. Figure 5.21(a) shows that if the quadrupole triplet QT2 is mechanically shifted by 1 mm steps then the beam can be scanned in x -direction in about 2.3 mm steps. Figure 5.21(b) shows that if the current in the solenoid-pair is modulated by 100 A steps then the centre of the field in y -direction can be scanned in about 2.7 mm steps. These parameters, i.e. shifts and current steps, can be delivered by existing technologies and show the performance of the ELPIS system. They are illustrated by the red lines, i.e. the step functions, in figures 5.21(a) and 5.21(b).

In clinical settings with pencil beam scanning, the beam size from cyclotron based systems is a function of beam energy (as the passive beam degraders deteriorates the beam profile more for lower energies). The beam spot-size can be in the range of 5 – 12 mm FWHM at the isocentre. This means that two side-by-side beam spots must be separated by at least 5 mm (to match high clinical standards being practiced), i.e. the

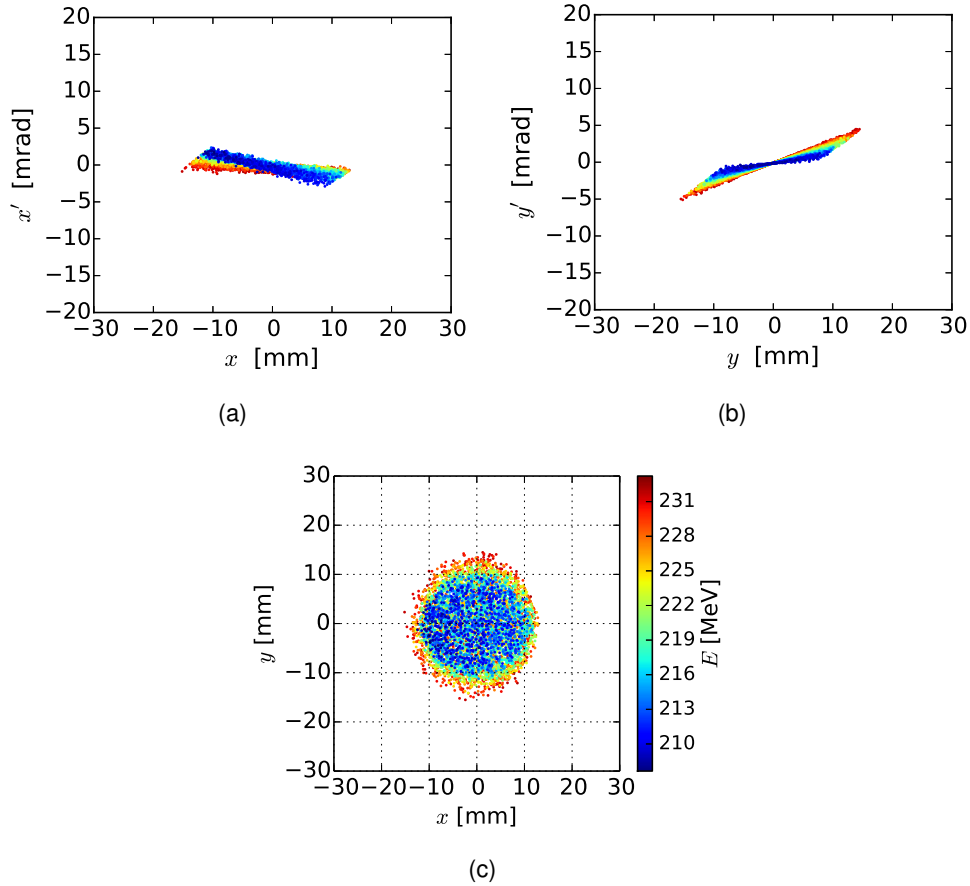


Figure 5.19: The output beam profile from the advanced clinical gantry at the isocentre, and in this particular example with $\Delta E/E_0$ of 19% at $E_0 = 220$ MeV. The beam profiles have been vastly improved compared with the preliminary gantry design output, cf. figure 4.18. (a) and (b) show beam in phase space and (c) shows the beam spot in real space. Energy scale is same for all figures.

minimum distance between the centres of two beam spots with the size of 5 mm FWHM.³ If considering the Gaussian beam spot profile for the output LAP beams, it can be considered here for argument that 5 mm steps (as minimum value) in scanning would be sufficient for clinical needs, which falls comfortably within the limits of the ELPIS system.

Figure 5.21(c) shows the beam spot scanned along the x -axis while the current in the solenoid-pair is zero, and similarly in y -axis while the shift in QT2 is zero. Furthermore, it shows scanning of the beam in all quadrants of the irradiation field by applying shifts and current simultaneously. Few beam spots are also shown outside the recommended 20×20 cm² field size in figure 5.21(c). It can be clearly seen that the dispersion introduced by the dipole fields of the ELPIS system produce a spatial energy dependent separation. Thus, even though ELPIS can scan beams beyond the recommended field size, the field size is limited due to the dispersion in the large $\Delta E/E_0$ filtered bunches.

The dispersion functions, $D(s)$ and $D'(s)$, become non-zero for scanned beams and increase with the field strength in ELPIS required to scan the beam farther from the

³Although, the spot-size varies with depth due to lateral spread, thus usually require even more separation between two side-by-side spots. However, the value of 5 mm is used here only as a minimum limit.

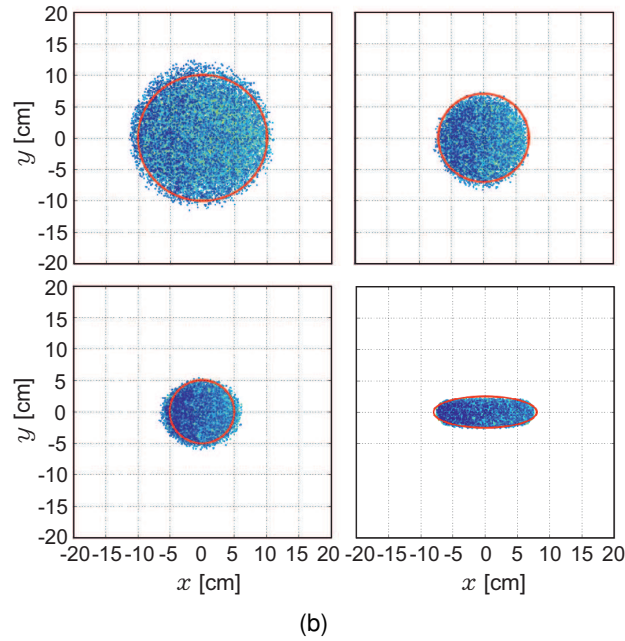
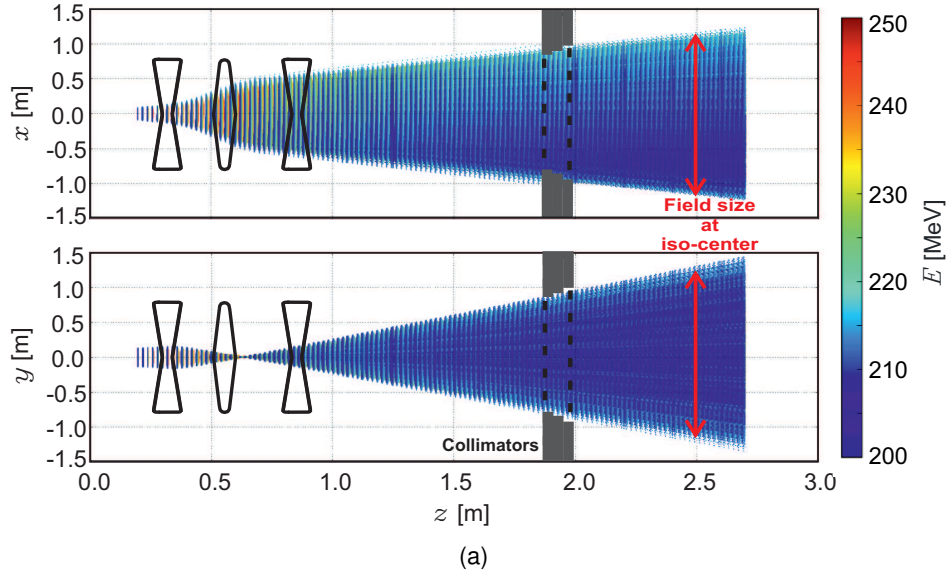


Figure 5.20: (a): The evolution of the transverse size of a LAP bunch, with $\Delta E/E_0$ of 19% at $E_0 = 220$ MeV, and represents the schematics of beam broadening via quadrupole triplet QT2 of the new dose delivery system, ELPIS. Please note here that due to the large number of protons used in the GPT simulations, (a) shows protons in time steps rather than the usual line trajectories. By changing the QT2 settings the beam spot-size and shape can be altered. (b): Four beam spots simulated at the isocentre for different QT2 settings, as an example to illustrate the beam shaping capability. Energy scale is same for all figures.

isocentre (as described in section 5.2.5). This resulted in a beam spot at the isocentre with energy dispersion, see figure 5.22 (top). A shot-to-shot dispersion correction technique was introduced to compensate the dispersion for each beam position in the scanning field, see figure 5.22 right bottom. This was done by the adjustment in the QT1 parameters upstream so that the conditions $D(s) = 0$ and $D'(s) = 0$ are satisfied after including the effect of the scanning. It was found via simulations that a maximum of $\pm 1.5\%$ change

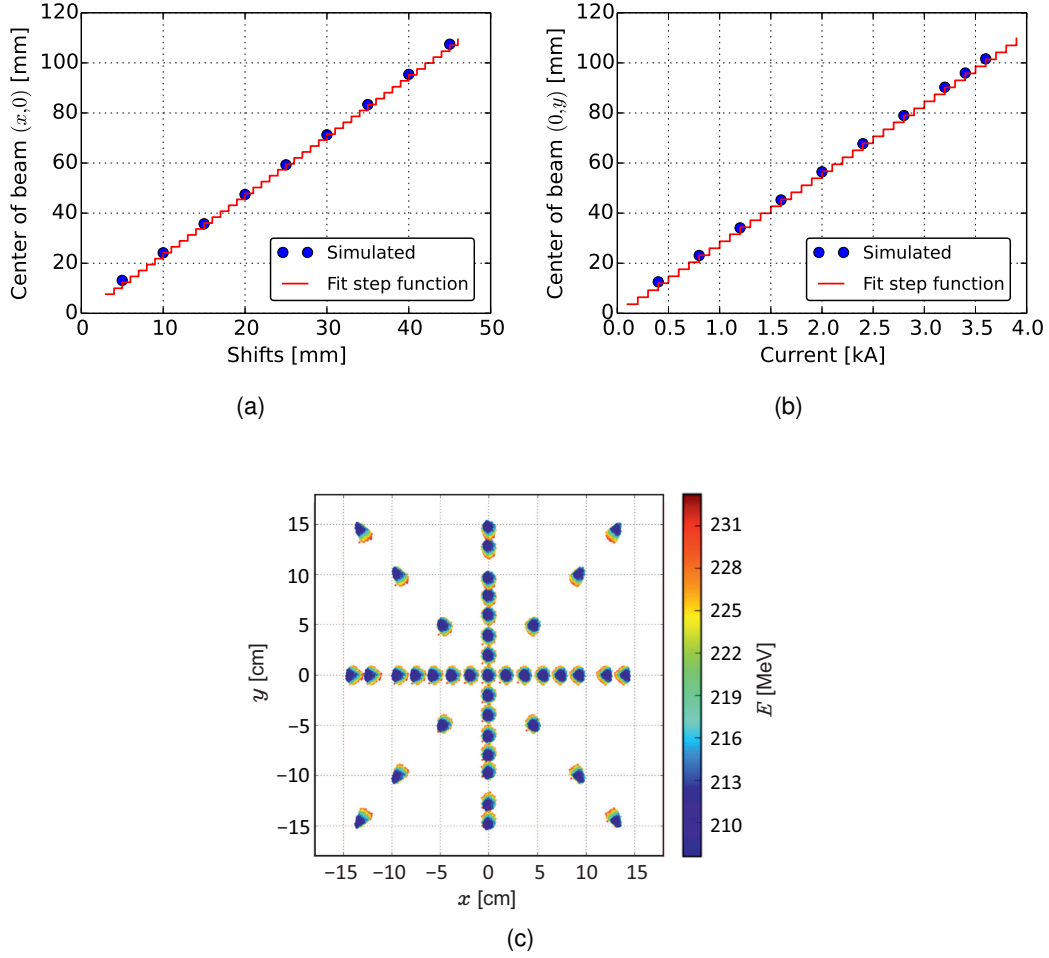


Figure 5.21: (a): The change in the centre of the beam in x -direction as a function of mechanical shifts in the quadrupole triplet QT2. (b): The centre of the beam in y -direction as a function of current in the solenoid-pair of the ELPIS system. The blue dots are from the GPT simulation results, the blue lines are the linear fits and the red lines are the step functions which depicts the physical minimum steps which can be applied via current and/or mechanical shifts. The beam scanning in the negative directions, i.e. $(-x, 0)$ and $(0, -y)$, can similarly be done by applying shifts and the current in the opposite directions. (c): The simulated beam spots scanned in x - and y -directions, by applying both QT2 shifts and solenoid-pair current simultaneously. Thus, the beam can be scanned in all quadrants of the irradiation field.

in k_{Q2} of quadrupole QuadX2 of QT1 triplet would restore the non-dispersion condition for a maximum scanning angle in x -direction, i.e. for the beam spot centre (x, y) at $(\pm 10 \text{ cm}, 0 \text{ cm})$. As all magnets are assumed to be pulse powered at a maximum of 10 Hz to match pulsed LAP beams, there is enough time to implement the shot-to-shot dispersion magnetic correction in between two LAP bunches and this would not complicate the pulsing system. However, the correction could only be applied in x -direction and the dispersion effect in y -direction needs to be accounted for either by restricting the scanning field to a maximum size y -direction of 10 cm, i.e. a maximum field size of $20 \times 10 \text{ cm}^2$, or by a clever 3D treatment planning system. Figure 5.23 shows the full functionality of the ELPIS system after the dispersion correction. The new ELPIS system can deliver advanced dose schemes via beams with large (selectable) spot-sizes with broad-energy windows and

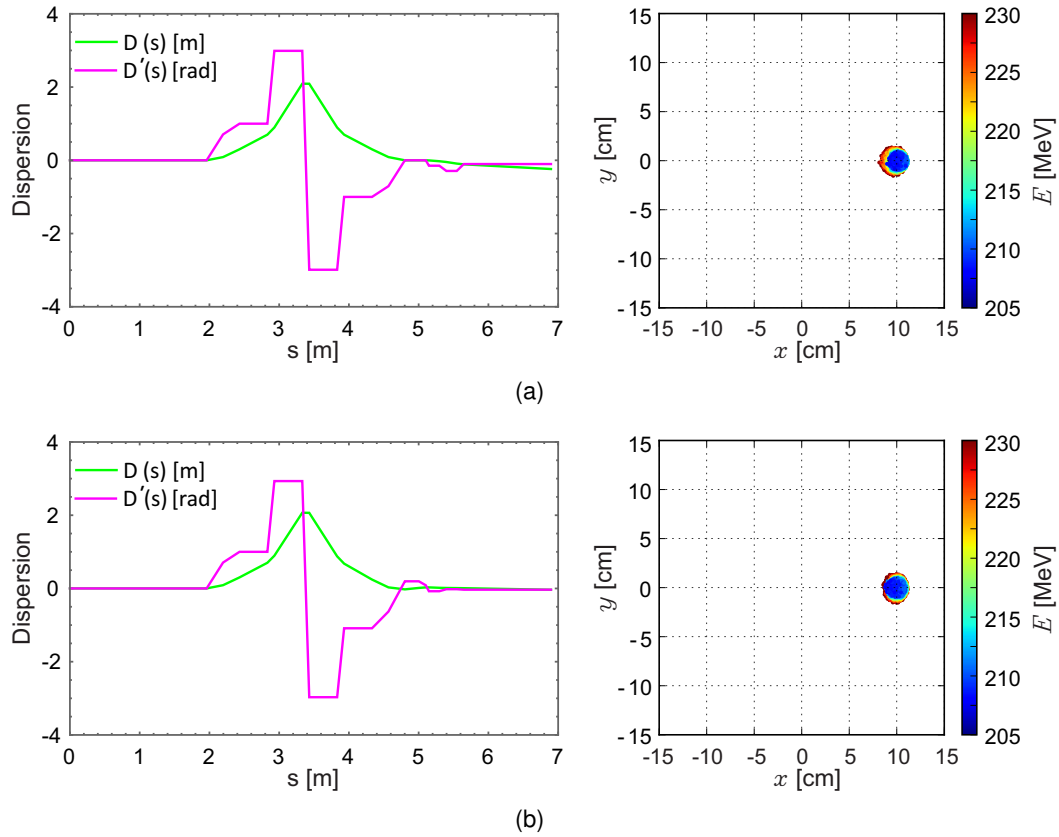


Figure 5.22: Dispersion plots (left) and the corresponding beam spots (right) for the scanned LAP beam with $E_0 = 220$ MeV and $\Delta E/E_0$ of 19%. (a): Scanned beam without dispersion correction. (b): Scanned beam after dispersion correction is applied.

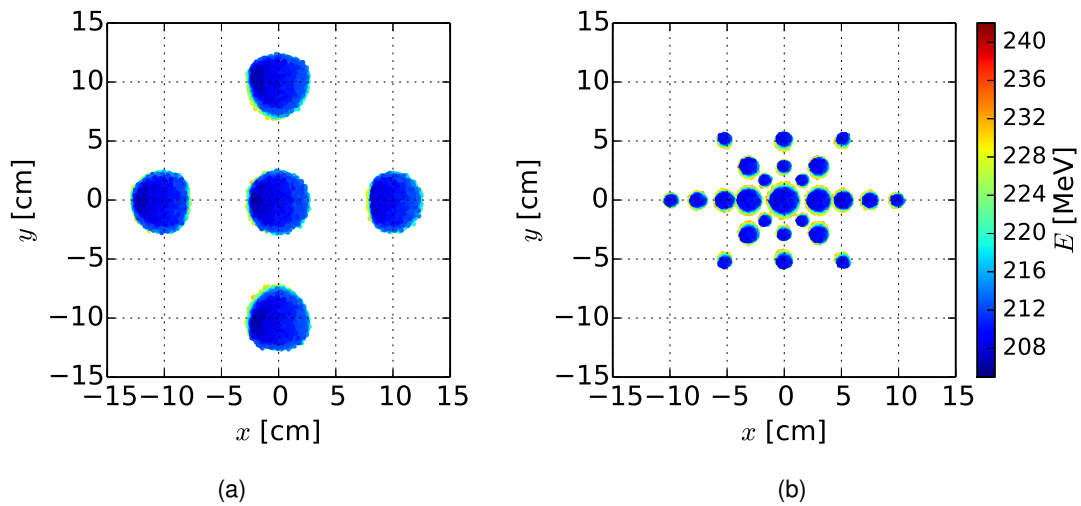


Figure 5.23: Simulation results for the different beam sizes at the isocentre for different transverse beam positions. The beam parameters of $E_0 = 220$ MeV and $\Delta E/E_0$ of 19% were selected and transported via the gantry and the integrated ELPIS system. (a): Scanning of large spot size beams. (b): Scanning of beams with varied spot sizes. The combination of different spot sizes with different energy windows could provide efficient dose delivery without compromising tumour conformity.

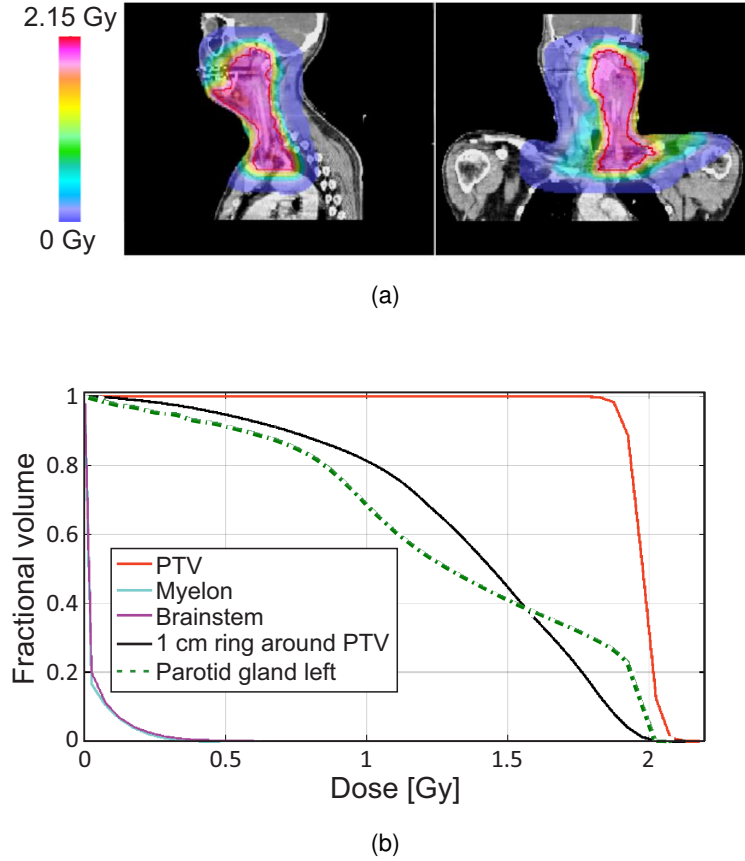


Figure 5.24: (a): Dose distribution for the laser-driven proton plan generated deliverable via the filtered beams from the advanced clinical gantry. (b): Cumulative dose-volume histogram (DVH). Sagittal and coronal views of the head and neck cancer patient in (a) show the dose map per fraction to the planning target volume (PTV) structure with red outline, for a prescribed dose per fraction of 2 Gy. The histogram for the 1 cm ring structure around the PTV is also shown which was used for dose optimization, as well as DVHs for surrounding organs at risk. The myelon and the brainstem being the most critical organs, show only a maximum dose as low as 0.48 Gy and 0.6 Gy per fraction, respectively, which is clinically acceptable practice.

can scan in both lateral (x - and y -) directions.

5.3.5 3D dose verification

In order to show the clinical feasibility of this advanced clinical gantry and the beam delivery system ELPIS, a treatment planning study was conducted on the 3D clinical data of a head and neck cancer patient with a large tumour volume of nearly 600 cm^3 . The axial clustering technique (from the advanced dose model for LAP beams, see section 2.5.2) was utilized to compute a laser-driven proton treatment plan. The 3D TPS LAP-CERR has been adapted for the input and output beam parameters of this advanced gantry design. In particular, LAP-CERR was constrained to utilize nominal energies ranging from 50 to 250 MeV in 1 MeV steps and to select energy windows $\Delta E/E_0$ in the range of 3 – 19% in 1% steps. Moreover, the transport efficiencies per selected energy window were implemented according to the simulation results, and a library of all possible beam spectral sizes (according to the equation 5.14) was created and simulated in Geant4

simulation package. Beams with 2 cm FWHM spot-size were employed to deliver the dose via the active beam scanning option of the ELPIS system. Now, LAP-CERR could choose from the library which spectral beams would be suited for tumour conformal doses.

The studied patient (see figure 5.24) was planned to be irradiated from two beam directions, namely 50° and 300° , which represents a realistic clinical proton therapy scenario where usually 1 – 3 beam directions are utilized. The LAP bunches are intense and with the improved transport efficiency of the gantry the delivered beams of 2 cm size still could reach much higher local doses than the prescribed dose for the tumour. Therefore, the fluence needed to be reduced in the TPS by a factor of 400 from the assumed initial proton number per bunch described by equation 4.13.

The dose distributions obtained in this study show promising results, like the optimal plan displayed in figure 5.24, with high dose conformity and good sparing of surrounding organs at risk. The corresponding tumour coverage and conformity indices of $TC = 98\%$, $CN = 87\%$ are comparable to conventional, clinically accepted treatment plans. In figure 5.24, the cumulative dose-volume histogram (DVH) per fraction is shown for the planning target volume (PTV) as well as exemplary organs at risk and a ring structure around the tumour with a thickness of 1 cm. The DVH of the PTV shows a steep fall-off with $Dose_{2\%} = 2.09$ Gy and $Dose_{98\%} = 1.90$ Gy per fraction with good sparing of organs at risks (where $Dose_{2\%}$ and $Dose_{98\%}$ are the minimum doses received by at least 2% and 98% of the tumour volume, respectively). However, it was found that an optimal treatment plan of clinically acceptable quality would require 12326 LAP bunches per fraction to treat this patient with a dose per fraction of 2 Gy (i.e. standard daily fractionation). Assuming an optimistic repetition rate of the laser system of 10 Hz, this would translate into a treatment time of about 20 mins.

It was found in the previous clinical study that a reduction in the required number of LAP bunches of the order of few tens of percent can be achieved if an intensity modulation scheme could be included in the gantry (Hofmann et al., 2015). This advocated strongly for an intensity modulation to be included in the advanced gantry design, and it was devised after the dose verification studies.

5.3.6 Integrated intensity modulation scheme

The intensity modulation scheme has been devised as presented in the section 5.2.8 and the results were obtained via GPT simulations. The GPT simulation results for the beam transport without intensity modulation, presented in section 5.3.3, show that the maximum part of the input LAP spectrum transported to the isocentre is about $\Delta E/E_0$ of about 20% around the selected E_0 . Therefore, the GPT simulations for the intensity modulation scheme were done with input spectrum width of only 40% around the selected E_0 . The protons outside this 40% window in the input bunch would not be transported but the reduced input spectrum width saves the computational power and simulation time.

Different sets of simulations were set up to verify the intensity modulation scheme at different E_0 values. Figure 5.25 shows, as an example, only one set of simulations which were optimized for $E_0 = 220$ MeV. At the default settings, i.e. magnetic field strengths as

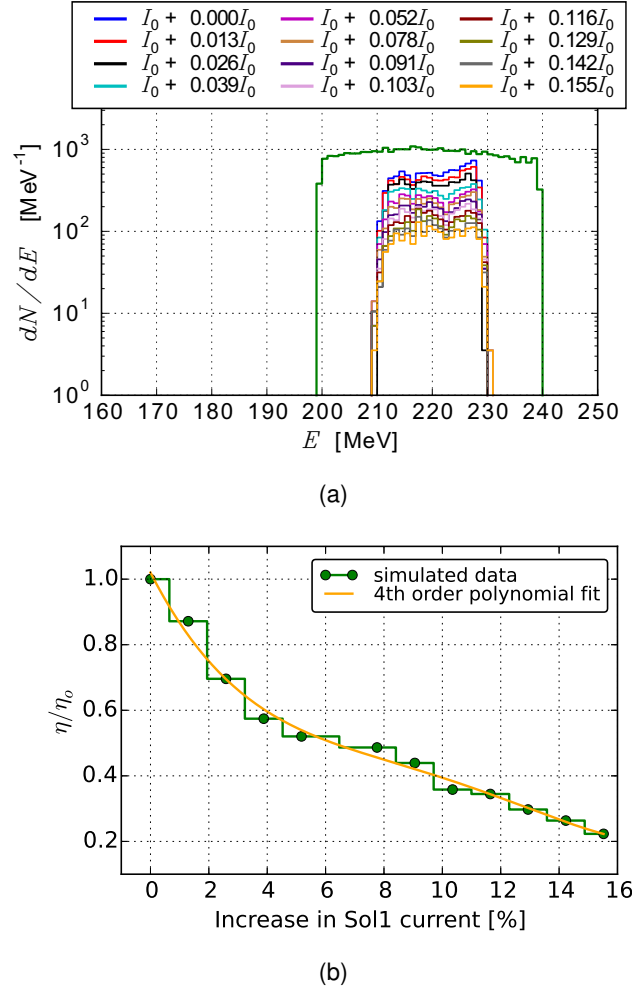


Figure 5.25: (a): Input LAP spectrum (green line) with the filtered spectra at the isocentre (different colors) under the green curve. An increase in the first Solenoid Sol1 current decreases the transport efficiency, however, the output $\Delta E/E_0$ window remains same. (b): The relationship between the drop in the transport efficiency η at the isocentre, normalized to the maximum transport efficiency η_0 for the protons with the nominal energy E_0 , in relation to the increase in the current in the Sol1.

listed in the table 5.1, the maximum value of $\Delta E/E_0$ at the isocentre was 19%. Now, the focusing strength k_{S1} of the first solenoid Sol1 was increased by providing increased current than the default settings. The $\Delta E/E_0$ value remains the same, however, the transport efficiency has now decreased (presented in detail in figure 5.25(a)). Nevertheless, the acceptance of the beamline maintains the output $\Delta E/E_0$ window. The default k_{S1} was provided via current I_0 , in this case $I_0 = 38.65$ kA, and then a current I with an percentage (p_c) increase in I_0 was provided, i.e. $I = I_0 + \frac{p_c}{100} I_0$, see figure 5.25(b). As the $\Delta E/E_0$ window at the isocentre is determined by the radius of the energy selective aperture Apt2 after the introduction of dispersion by the bending magnet SM1, there is no change in $\Delta E/E_0$ window and intensity can be modulated similarly for all $\Delta E/E_0$ windows, i.e. in the range of 3 – 19%. Thus, a simple increase in the focusing strength of Sol1 provides an efficient solution for modulating the intensity.

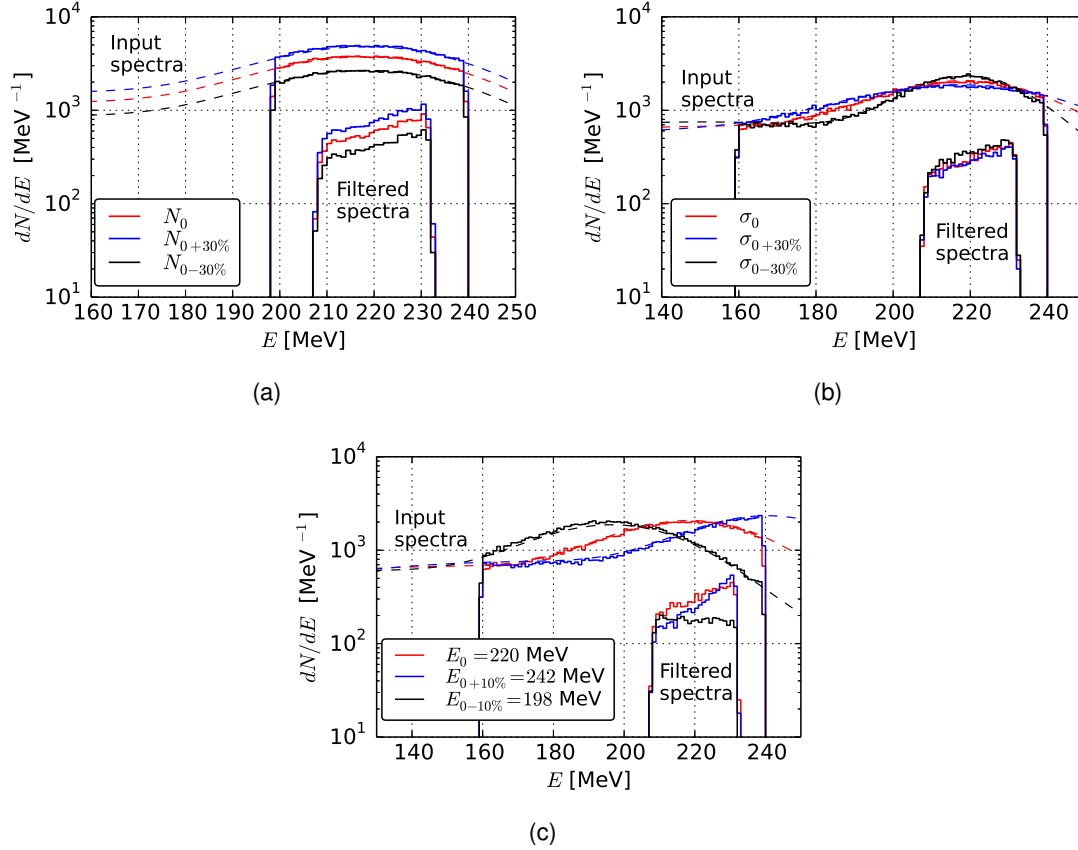


Figure 5.26: Shown here RPA like input energy spectra of the LAP bunches with fluctuations described in the section 5.2.9 (cf. figure 5.11). (a): a $\pm 30\%$ variation in the total number of protons in the input bunch, and respective spectra of the output filtered bunches. (b): a $\pm 30\%$ variation in the spread of the spectrum in the higher energy range. (c): a $\pm 10\%$ change in the E_0 value.

5.3.7 LAP beam fluctuations

The LAP beams are known to have high shot-to-shot fluctuations and simulations have been performed to inspect the behavior of the designed gantry under such fluctuations. The input spectra used for the tracking simulations were limited in the energy range with respect to the maximum possible output $\Delta E/E_0$ window, similar to the section 5.3.6, to save computational power and simulation time. Three types of fluctuations have been introduced in the input spectra as described in section 5.2.9. Three sets of GPT simulations were performed, one for each each type of fluctuation:

1. The first set of simulations were made with the total number of protons per bunch, i.e. N_0 , have been varied by $\pm 30\%$ within the same opening angle. Figure 5.26(a) shows simulation results, the number of protons in the output beam was simply proportional to the variation in the input spectrum, i.e. $\pm 30\%$ change in the input spectra show a direct $\pm 30\%$ change of proton number in the output spectra. It is obvious that the change in the total number of protons in the initial beam within the allowed window would simply be reflected in the output beam.
2. The second set of simulations were performed for the $\pm 30\%$ change in the Gaussian

spread (σ_g) around the peak energy E_0 in the initial input spectrum. A +30% change in the σ_g would spread the protons in the distribution, while, a -30% change in the σ_g would squeeze more protons around the E_0 , see figures 5.11(b) and 5.26(b). Therefore, in these cases, the output beam spectra vary slightly in shape also, although, the $\Delta E/E_0$ window remained unchanged. In case of -30% change in σ_0 , around 12% more protons were delivered in the filtered bunch (dN/dE_{filtered} , see equation 5.14). In case of +30% change in σ_0 , around 7% less protons were transported in the filtered bunch.

3. The third set of simulations were performed for the $\pm 10\%$ change in the E_0 value. The simulation results show that, although the width of the filtered $\Delta E/E_0$ window remained unchanged, however, in this case the shape of the output beam spectra have changed much more than in the case of σ_g variations, see figure 5.26(c). In case of +10%, there was a 10% decrease in the total number of protons in the filtered bunch dN/dE_{filtered} . And with -10% change in E_0 a 42% decrease in the total number of protons in the filtered bunch was recorded, as the output spectra follow the change in the input spectra.

The acceptance of the whole beamline would fix the maximum and minimum energy limits in the filtered energy window, i.e. $\Delta E/E_0$ limits. However, the shape of the spectra varies with the change in the shape of the initial spectra, which was an expected outcome. This would translate into dose variations. Later, some possible implications of the beam fluctuations on the 3D dose distributions are discussed in the section 5.5.

5.4 Realization of the gantry: First tests of a pulsed beamline section

The short pulsed characteristic of the intense LAP bunches allowed to utilize a relatively new kind of high-field magnets, namely pulsed magnets. Pulsed magnet beamlines have never been used for PT machines.⁴ The design, construction and experimental characterization of these magnets are under way, as explained in section 3.3. Due to the current status of available LAP beams, i.e. stability and shot-to-shot fluctuations and limited availability of beam-time at laser accelerator facilities, it is rather preferable to test and characterize the new pulsed magnetic components and beamline sections with stable conventional proton sources. An experiment was setup at the tandemron accelerator at HZDR (under the framework of onCOOPtics project). The main aim of this experiment was to establish pulse powering of more than one pulsed magnet, synchronizing traversing beam bunches and pulsing of magnets, and characterizing the beamline section. This proof-of-principle experiment provided the basic controls and hands-on experience to use these types of high-field magnets for complete beamlines.

⁴Few of the current PT facilities use small *kicker* magnet/s in the transport beamline, which can be operated in pulsed mode, however, no pulsed beamline (i.e. series of synchronized pulsed magnets) exists.

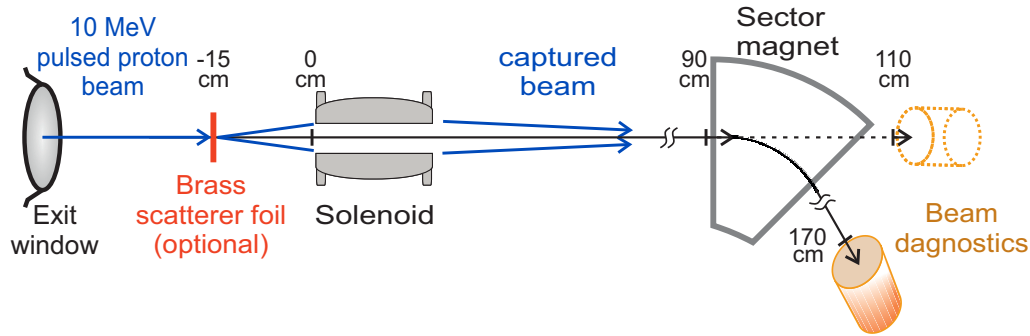


Figure 5.27: Illustration of the experimental setup. The mono-energetic proton bunches from the tandem accelerator exit from the accelerator window and enter into the pulsed beamline setup. In the first stage of the experiment, only a pulsed solenoid was operated and optimized. The solenoid focuses the beam on to the diagnostics site (shown as a dotted orange cylinder). In the second stage, the diagnostics were shifted (shown as a solid orange cylinder) after installing the pulsed 50° bending sector magnet. A 25 μm brass scatter foil was placed at 15 cm before the solenoid entrance, as an option to introduce divergence in the beam when both solenoid and sector magnet were used to capture and transport the beam around a bend. Also, see figure 5.28 for the actual setup.

5.4.1 Experimental setup

A pulsed solenoid and a pulsed sector magnet already designed and manufactured (as described in sections 3.3.1 and 3.3.2, respectively) were used to build a pulsed beamline section. This beamline was characterized at the 6 MV tandetron accelerator⁵ facility at HZDR. Although, the tandetron, or simply tandem, accelerator is capable of delivering 12 MeV proton beams, only 10 MeV proton beam was used due to safety reasons. The tandem accelerator was equipped with an electrostatic steerer, a fast high-voltage amplifier and an electric-pulse generator. This equipment was added behind the ion source and before the tandem accelerator. This steerer can steer the beam in and out of the accelerating structure at a maximum (adjustable) rate of about 1 kHz, thus, the continuous beam can be pulsed. This system can deliver accelerated output beams with high reproducibility and as small as 500 ns bunch durations. However, pulsed proton bunches with 20 – 70 μsec durations were used to characterize the pulsed beamline section.

The pulsed solenoid was placed outside the beam exit window of the tandem vacuum beamline, see figures 5.27 and 5.28 for the optimized experimental setup. The beamline, however, was extended with a polyurethane beam pipe with inner diameter of 35 mm which passes through the solenoid. In the first stage of the experiment, the solenoid positioning, synchronization of the pulsing with incoming pulsed proton bunches and magnetic field strengths were optimized. The pulsed solenoid was connected to a high-voltage pulse generator, as described in the section 3.3 (also, see figures 3.7 and

⁵Tandetron accelerators use a static electric potential to accelerate ions generating a continuous beam, i.e. with no micro or macro ion beam pulses as is the case in linear or circular accelerators. The negatively charged ions are accelerated towards the positive terminal and pass through a stripper, which strips off electrons and converts the negatively charged accelerating ions to positively charged ions, and the ions keep accelerating towards the negative terminal. This tandem accelerating structure therefore can accelerate ions to energies to two or more times than the single available acceleration voltage. The 6 MV tandetron, or simply tandem, accelerator at HZDR can provide H^+ ions up to 12 MeV maximum energy.

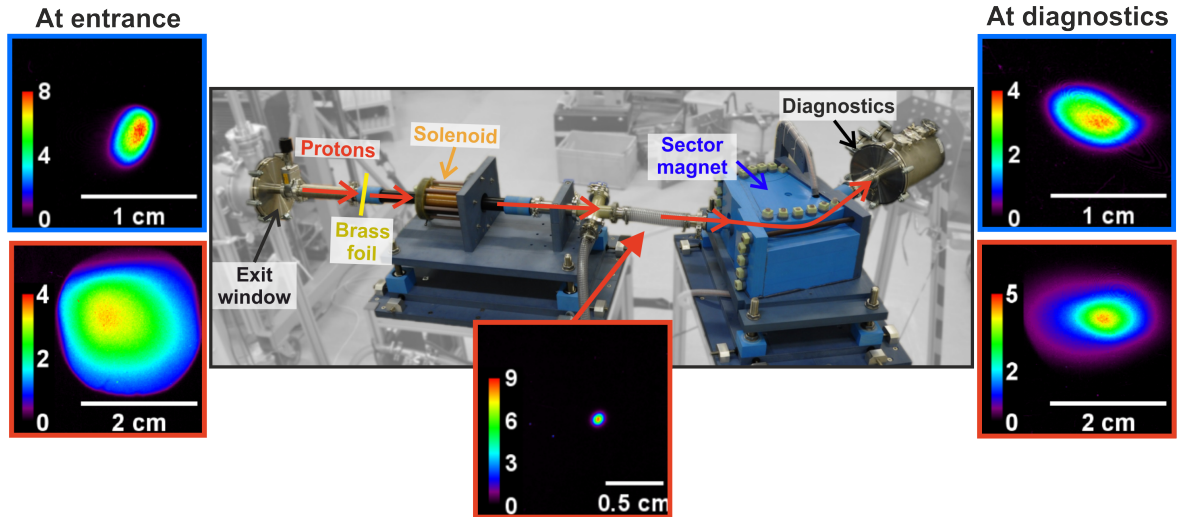


Figure 5.28: The experimental setup after optimization (middle picture in black frame) and typical lateral beam profiles for different beam parameters and at different positions along the beam-line. Pictures on left show the beam at the entrance of the solenoid behind the exit window. Top left picture (in blue frame) shows a parallel beam output from the accelerator and bottom left picture (in red frame) shows a broadened beam which was achieved by the use of a brass scatterer foil. Pictures on the right show the beam behind the sector magnet at the beam diagnostics site. The pictures framed in blue show beam profiles when only the sector magnet was operated for optimization and the pictures framed in red show beam profiles when both solenoid and sector magnets were operated together. The insets show the color coded absorbed dose in Gy and the spatial scale of the corresponding radiochromic films (RCF). As an example to show the beam transport, the broadened beam (bottom left) was focused by the solenoid (bottom middle) at ~ 80 cm downstream and then transported via 50° bending magnet (bottom right) to the beam diagnostics.

3.8). The solenoid was mounted on a movable platform, which was designed and built in-house, and allowed precise positioning of the solenoid with respect to the incoming proton bunches. Radiochromic films (RCF) and an online scintillation detector were used as beam diagnostic tools, which were placed 1.1 m downstream from the solenoid.

In the second stage of the experiment, the pulsed sector magnet (with 50° bending angle) was installed 90 cm behind the start of the solenoid. The diagnostics were also moved and positioned behind the 50° bend at 1.70 m downstream from the start. The alignment and magnetic field optimization of the sector magnet was done by transporting a parallel proton bunch through the magnet, with the solenoid turned off.

Once, the alignment and optimization of solenoid and sector magnet were done, a brass scatterer foil of $25\ \mu\text{m}$ was placed about 15 cm before the entrance of the solenoid. The well-collimated parallel pulsed proton bunches from the tandem accelerator pass through the scatterer and attained divergence angles. Figure 5.28 shows two beam sizes (on the left side under the label “at entrance”), the small beam size in the top left (with blue frame) was achieved by adjusting the quadrupole doublet imaging features in the tandem transport beamline, while the beam size in the bottom left (with red frame) was achieved by inserting a brass scattering foil which introduced an extra divergence in otherwise parallel beam. This was done to mimic a laser-driven proton source with stable

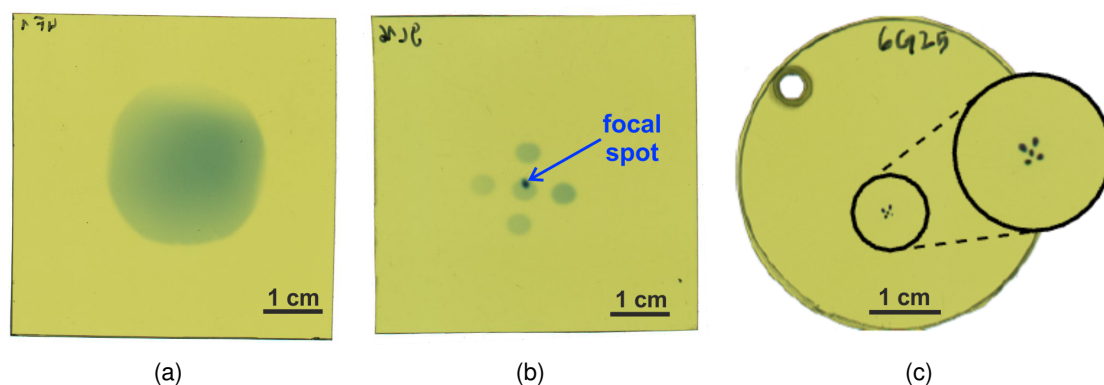


Figure 5.29: Radiochromic films exposed during the first stage of the experiment, i.e. solenoid optimization. (a): Lateral beam profile at the exit window of the accelerator, when a laterally broadened beam profile was selected via adjusting the imaging properties of the quadrupoles in the tandem transport beamline. (b): RCF positioned behind the solenoid at 1.1 m which was exposed twice, once with a five hole aperture at the exit window with no solenoid field, where the middle spot represents the centre of the incoming beam, and the same film was exposed a second time after the optimization of the solenoidal field for focused beam without the five hole aperture. (c): focused beam spot with the five hole aperture.

beam parameters, with controlled and limited divergences. In the third stage of the experiment, the diverging pulsed proton bunches were captured and focused by the solenoid, and then transported via the sector magnet to the diagnostic chamber 50 cm behind the sector magnet. The combination of two pulsed, i.e. capturing and bending, magnets used for transporting the diverging pulsed proton beams with high transport efficiency was established, and this setup provided the first prototype pulsed beamline section.

5.4.2 Experimental methods and results

It is necessary that the solenoid is well aligned with the incoming beam, i.e. the beam axis aligns with the central axis of the solenoid, so that the focused beam stays on the axis behind the solenoid. The beam was laterally broadened via adjusting the imaging features of the quadrupole doublet used to maintain beam parameters downstream from the tandem accelerator. The beam then travels through a long beamline until it reaches the exit window (the experiment site). With its very low divergence, the magnetically broadened beam can be considered as a parallel beam. Figure 5.29(a) shows the beam behind the exit window of the tandem accelerator. The parallel beam was about 25 mm in diameter (without the use of the brass scatterer foil). The solenoid alignment was achieved by putting an aperture with five holes inside the beamline prior to the exit window and then irradiating films with and without the solenoidal field turned on. After the five hole aperture was placed, another RCF was exposed behind the solenoid at 1.1 m downstream from the start of the solenoid, without the magnetic field (see figure 5.29(b)), in which the middle spot of the five hole beam exposure represents the central axis of the incoming beam. The optimization of the position was mainly achieved via using the online scintillation detector, instead of the RCF. The five hole image was marked on the display screen, and then the

aperture was removed and a proton bunch was focused to a minimum beam waist by turning on the solenoid and optimizing the field strength. The focal spot of 0.8 mm FWHM was achieved with a peak magnetic field strength of 2.7 T (at 3.27 kA provided peak current). If there was a misalignment of the beam and the solenoid axis then the beam would experience a slight bend and the focused beam would not match the centre of the five holes beam spot which was taken without the magnetic field. Several adjustments were made in the solenoid platform and finally a satisfactory position was achieved. Then, the RCF which was exposed with the five hole aperture and no solenoid field, was exposed again without the five hole aperture and with the solenoid field on. Figure 5.29(b) shows that the focal spot of the beam is close to the centre of the five spots of the unfocused beam. The difference in the centres of the focused and unfocused beam was about 0.8 mm, and with the standard deviation in the position of the unfocused beam being 0.2 mm (the standard deviation was measured by online scintillator images of 25 consecutive beam pulses, without any aperture). The solenoid now can be considered well aligned. Furthermore, the five hole aperture was utilized to optimize the focal spot of the beam by varying the solenoid field strength, see figure 5.29(c). This confirms the control over the beam bunches, synchronization of the beam bunches with peak solenoid field, and basic functionality and setup of the pulsed solenoid.

After the solenoid was setup and aligned, the pulsed sector magnet was installed, in the second stage of the experiment. The sector magnet was placed 90 cm downstream from the start of the solenoid. The parallel beam (without the scatterer foil) from the accelerator (top left picture in figure 5.28) was transported via the sector magnet to the diagnostic site, with the solenoid switched off. The position and alignment of the sector magnet was adjusted using the online scintillation detector. The magnetic field was optimized so that the beam can be bent and transported without any losses. The optimized peak magnetic field was 2.6 T at 4.5 kA peak current. The top right picture in the figure 5.28 (with blue frame, under the label “at diagnostics”) shows the transported beam spot at the diagnostics site. This confirms the synchronization of beam bunches with peak magnetic field and functionality of the pulsed sector magnet.

After the individual setup and alignment of the solenoid and sector magnet, both magnets were operated together to collect, focus and transport a pulsed beam through a bend. A brass scatterer foil was used to increase the size and divergence of the proton bunches, and to a limited extent mimic a stable mono-energetic LAP source. Unfortunately, at the time of the experiment only one pulse generator was available, and the two magnets had to be attached in series connection to operate them together. This had a drawback as the current amplitude would be equal in both magnets, and individual magnetic field optimization was not possible. The sector magnet needs to have the right magnetic field strength for precise bending of the beam, therefore, it took the priority. As a result, the solenoid peak magnetic field was fixed at about 1.9 T. As a consequence, a thicker brass foil to introduce larger divergence could not be used, because then the focal length was long and with a thin brass foil (or a parallel beam without scatterer foil) the focal length was about 50 cm downstream from the start of the solenoid, which allowed the beam to diverge again behind the focal spot for almost 40 cm before it entered the sector magnet. Consequently,

the beam was too large laterally to be contained in the beampipe. It was estimated via a GPT simulation that if a scatterer foil placed at 15 cm upstream of the solenoid with divergence angles of maximum 3° (half-angle) then the diverging beam could be captured and focused by the solenoid at about 80 cm downstream with 1.9 T magnetic field strength. It was estimated that a brass foil of 25 μm thickness should be sufficient for said needed divergence for 10 MeV proton bunches. This estimation was made via a SRIM simulation⁶. The bottom left picture in figure 5.28 (with red frame) shows a proton bunch scattered via a 25 μm brass foil entering the pulsed beamline section, while the picture in the middle in figure 5.28 (with red frame) shows the focused beam spot. The bottom right figure (with the red frame) shows the bended and transported beam spot. The transported beam was bigger in size (compared with the top right picture in figure 5.28) as the beam started to de-focus after the focal spot, and also the beam has been elongated slightly in the direction of the bend which was expected as after the scattering foil the dispersion of the dipole field would have some effect on the beam shape. Nevertheless, it was successfully concluded that the pulsed beamline section could be synchronized with the pulsed proton bunches, and can capture, focus, bend and transport diverging beam bunches with high transport efficiency (of almost 100%).

The experimental verification and characterization of higher magnetic field pulsed magnets will continue. Furthermore, the experiment will be moved in future to higher proton energy beamlines and also to laser-driven beams for further tests and development of pulsed beamline systems.

5.5 Highlight features of the advanced gantry design

In this chapter, an advanced isocentric gantry solution for laser-driven proton beams has been presented with a novel nozzle system, which is capable of delivering 3D tumour conformal dose distributions with high clinical standards. This advanced gantry solution has been designed as an improvement based on the preliminary gantry design. The two-step capture and collimation system provided well-collimated beams with smaller transverse sizes. Furthermore, the independent capture and collimation steps also allowed to incorporate a much needed active intensity modulation scheme. In this intensity modulation scheme, the beam can be modulated actively (without the need of any physical degraders) and is away from the patient for better secondary radiation protection issues. The smaller beam size at this stage also provided efficient energy selection and further transport through the beamline. The particle tracking simulation results advocate that the advanced gantry design has improved transport efficiency, which was increased from 85% to 97%, when compared to the preliminary gantry design (for the RPA like sources). Although, the transport efficiency depends upon the initial beam parameters and would be different for higher diverging sources. However, the two-step capture and collimation system allows the use of two different solenoid geometries which can be optimized separately. A few simulations were made for the advanced gantry with TNSA like

⁶SRIM is a collection of software packages which calculate many features of the transport of ions in matter (Ziegler, 2015).

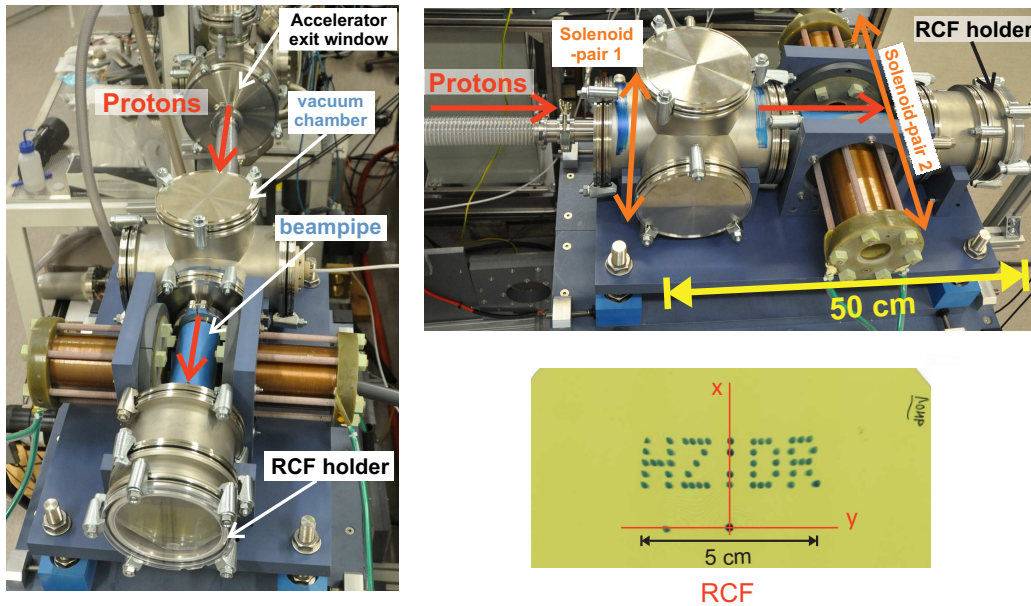


Figure 5.30: Experimental setup for beam scanning and a RCF exposed to demonstrate the beam control. The experiment was performed with 10 MeV proton bunches from the tandem accelerator at HZDR. Figure (left) shows the proton bunch entering into the experimental setup, first into a diagonal vacuum chamber which contains the first solenoid-pair (solenoid-pair1, cannot be seen). Protons traverse downstream inside a vacuum beampipe (blue pipe), which was placed in between the second solenoid-pair (solenoid-pair2). At the end of the beampipe was another vacuum chamber which could hold either a RCF or an online scintillation detector screen. Figure (top right) shows another view of the setup. The first solenoid-pair was placed perpendicular to the following second solenoid-pair. The solenoid-pairs were powered by separate pulsed power supplies, and therefore, could provide independent control over the generated magnetic fields. The proton bunches could be deflected in one direction, say x -axis, by the first solenoid-pair and in y -direction by the second solenoid-pair. The exposed RCF (bottom left figure) shows the deflected beam spots. Letters **HZDR** were written, letters **HZ** were written in the second quadrant, then the current direction was changed in the second solenoid-pair and the letters **DR** were then written in the first quadrant. A few shots were made with only one solenoid-pair to define the transverse axes, shown under the red lines.

sources, which have larger initial divergences than RPA like sources. In these simulations a solenoid with wider aperture and longer length was used as a capturing lens for maximum capture and with about 10 cm longer focal length. The second solenoid was then able to re-capture and provide small sized beams for further transport, similar to the presented RPA cases. The output maximum transport efficiency was increased from 22% (in case of preliminary gantry) to about 70%. This shows that with the change in the input characteristics available from the future sources, the two-step capture and collimation system can be optimized without the need to change the overall beamline design.

The most important feature of the clinical gantry design is the new dose delivery, ELPIS system. The ELPIS system is designed to combine not only conventional dose delivery options in one equipment, but also could provide LAP bunches with a wide range of optimizable parameters, i.e. shape, size and lateral position (and also axial width via $\Delta E/E_0$), which can all be varied simultaneously for one LAP bunch. Thus, there is no

need to physically switch between scanning and scattering options. Furthermore, advanced dose delivery schemes, like axial and lateral clustering and partial volume irradiation, can now easily be implemented. The mechanical shifts of the quadrupole triplet (QT2) used for beam scanning were assumed to have 1 mm steps. Technically it is possible, however, it can be argued that it would complicate the otherwise robust gantry design. The most viable alternative to this would be to add a second solenoid-pair, similar to the one used for the beam scanning in the y -direction, but with a 90° rotation (i.e. perpendicular to each other), as there is enough space between the last magnet and the treatment table, which was left in anticipation of implementation issues. The inclusion of the second solenoid-pair would only increase the height of the gantry by about 10 cm, however, can provide a robust solution. Particle tracking simulations were also done with such a system, i.e. two solenoid-pairs for separate beam scanning in x - and y -directions. There was no qualitative difference noted in the delivered beams. Furthermore, an experiment was also conducted with two solenoid-pairs arranged perpendicular to each other to demonstrate the pulsed dipole field generated in the gap in-between two solenoids is qualitatively feasible to provide control over the beam scanning. The 10 MeV pulsed proton beam from the tandem accelerator at HZDR was utilized (the same tandetron accelerator and the pulsed beam setup was used as described in the section 5.4.1). Figure 5.30 shows the experimental setup (see description in the figure caption) and the exposed RCF. A beam control for scanning was established using an online scintillation detector system and then a RCF was exposed to demonstrate the control by writing the letters HZDR on it. The deflection angle was limited to the size of the beam pipe, however, it clearly showed as proof-of-principle that such solenoid-pairs can be used to scan pulsed beams. The design parameters will change for clinical beams demanding higher proton energies, such as larger solenoids with larger gaps in between (see figures 5.6(b) and 5.7).

Chapter 6

Discussion

The laser-driven proton acceleration has captured the attention of both laser and medical physics communities for its potential to reduce the size and cost of existing PT facilities. The milestone of accelerating protons with lasers up to the proton energies of 250 MeV is still to be reached, which is a basic requirement for the clinical radiation therapy application. The development of new more powerful (i.e. next generation petawatt) laser systems is of high interest for not only radiation therapy applications but also for other research fields, from fast ignition fusion to basic radiation biology. The recent results from the ongoing research on laser-driven proton acceleration and laser systems exhibit the prospects of laser-driven PT, as discussed in section 2.4.3.

For radiation therapy applications, it is further necessary to develop concepts and equipment to utilize laser-driven proton beams which are characterized by specific beam properties, like very short, ultra intense bunches with large energy spread, large divergence and low repetition rate. The onCOOPtics project has been committed towards the advancement in the laser-driven PT applications via integrated multi-disciplinary research and development in all related fields, such as, the development of stable and reliable high-power laser systems and laser-targets (Zeil et al., 2010; Kluge et al., 2010; Metzkes et al., 2011; Kluge et al., 2011; Zeil et al., 2012; Zeil, 2013; Zeil et al., 2014; Siebold et al., 2014; Obst et al., 2017; Schramm et al., 2017), the beam monitoring and dosimetry equipment for intense pulsed broad-energetic beams (Kraft et al., 2010; Richter et al., 2011; Metzkes et al., 2012; Karsch et al., 2011; Kroll et al., 2013; Karsch and Pawelke, 2014; Metzkes et al., 2016), the *in vitro* and *in vivo* characterization for radio-biological effects for ultra-high dose rate regimes as LAP beams can reach up to several orders of magnitude higher peak dose-rates than conventional beams (Kraft et al., 2010; Zeil et al., 2012; Brückner et al., 2014; Oppelt et al., 2015) and the LAP beam transport systems along with the development of pulsed magnets and beam controls for radiotherapy applications (Schürer et al., 2012; Masood et al., 2014; Schürer et al., 2015; Hofmann et al., 2015; Schuerer et al., 2016; Masood et al., 2017a,b).

This thesis focused on the beam control and transport system for future laser-driven proton sources for PT applications, with expected therapeutic proton energies. This transport system must take into account the unique properties of LAP beams and include multiple functionalities in the transport beamline to control the beam, e.g. beam capture,

energy selection, beam size and shape, and to be able to deliver the beam from different angles for tumour conformal irradiation. For this purpose, a new 360° rotatable beamline, i.e. gantry, has been designed. For designing a beamline it is standard practice to utilize matrix formulation (described in sections 3.1 and 3.2) to develop a mathematical model and then solve this model to determine magnetic field strengths for individual magnets and also drift spaces in between, to obtain an output beam with certain desired properties. With the advancement of computing technologies, particle tracking simulation has also become a standard practice for characterizing new calculated beamlines. The mathematical method gives a very good approximation to a solution, however, it works best with narrow mono-energetic input beams. The particle tracking simulation codes, like GPT, solve equations of motion for each particle traversing in realistic magnetic field regions compared to the mathematical method where Twiss parameters are solved which represent the whole beam collectively, traversing through magnetic field regions of sudden rise and fall, i.e. rectangular fields. Therefore, the results from particle tracking simulations present a more realistic solution and beamline characterization tool. There are different particle tracking simulation packages available. Although, they differ in framework, input coding language and output result format, they produce similar beam optic results for output beams from one beamline. As a test, small beamline sections were simulated with three particle simulation packages, i.e. OPAL (Snuverink, 2018), Geant4 and GPT, and found that the output results were similar from these three packages. The choice of using GPT simulation package was made because it was readily available and due to its ease of use and capability to cater input beams with broad energy spectra and diverse beam properties and its ability to take input beams generated via external MC codes, like Python. GPT produces output files which can be plugged in to other softwares for further analysis, like Python or Mathematica, and even to use these files as input for other MC simulation codes, like Geant4. Separate Python calculation codes were written to analyse the GPT results.

Although materials and methods in general would be similar (with the choice of different softwares and simulation packages) in designing a beamline, the concept of a beamline layout can vary. For example, the gantries designed in this thesis assumed a rotatable laser-target assembly with integrated capture and collimation section, however, it is also possible to design a beamline with fixed laser-target assembly and capture and collimation section before a rotating gantry, like a concept given by Burris-Mog et al. (Burris-Mog et al., 2011). The concept of integrated laser-target was envisioned to keep the beamline compact and total traversing length short. The short traversing length allowed to transport maximum possible energy widths per bunch with minimum possible magnetic elements.

The gantry was designed in two stages, first a preliminary gantry solution was devised. The main purpose of this preliminary design was to determine if in principle it is feasible to control LAP beams, i.e. energy filtering, achromatic beam transport and beam delivery for efficient dose deposition. Two of the LAP beam properties – short pulsed bunches (in the range of ps) and low repetition rate (up to 10 Hz) – allowed to utilize relatively new high-field pulsed magnets. Therefore, this preliminary gantry study incorporated three main fields of research and development: beam optics and beamline design, magnet design

and development and clinical dose delivery and tumour irradiation. The requirements and limits of one of the aforementioned fields put constraints on the other two fields. For example, higher magnetic field strengths would allow more compact beamlines, however, reliable pulsed magnets are limited by physical constraints, or, clinical demands require efficient delivery of energetically broad beams, however, beamlines can only deliver certain beam shapes and a limited range of proton energies per bunch. The idea was to find a balanced solution which could provide the best possible clinical treatment plans.

The preliminary gantry design was important on two levels, first, it brought the existing experience in pulsed magnet design, construction and use in experiments, i.e. pulsed solenoid, and suggested to extent this technology for a pulsed gantry system with two new pulsed magnet types, i.e. pulsed sector magnet and pulsed quadrupole. The gantry design and pulsed magnet research and development took place in parallel and both fields benefited from each other. Compact gantry design demanded higher magnetic fields from 10 Hz pulsed magnets with larger acceptance (i.e. large bore of the beam pipe with large uniform good field region) and pulsed magnet development constrained to use unforeseeable magnet properties in the gantry design.

Secondly, it was imperative to characterize the gantry beamline design and to identify any limits and/or pitfalls on the basis of clinical requirements and applicability. The main result of the preliminary gantry design was that it is possible to capture diverging LAP beams and collimate them for efficient transport through a 360° gantry. This feature was a new concept in the gantry design and was not considered by the earlier attempts (discussed in section 2.6). The large acceptance energy selection in this preliminary design was designed to filter and transport a wide energy range which can be varied for each LAP bunch. This design was suggested by the concept of efficient dose delivery based on the BEAD model, presented in section 4.2.1. In contrast, the chicane system has a low acceptance by design and was intended to deliver only the conventional dose schemes via mono-energetic filtering of LAP beams, like conventional SOBP formation in the figure 2.1(a). The results obtained at ELI-Beamlines (Cirrone et al., 2013; Scuderi et al., 2014; Tramontana et al., 2014) showed that such beamline concept could only deliver LAP beams with less than 1% transport efficiency. In contrast, the simulation results from the preliminary gantry design showed the possibility to deliver LAP bunches with up to 22% transport efficiency (for TNSA like sources) with variable energy widths. All of this in a compact system with realistic magnetic field values and the capability to deliver basic clinical doses via the BEAD model. Thus, it showed that the superiority of this design concept over the chicane style design by avoiding the usual pitfalls and considering realistic limits.

A 3D TPS study was conducted in collaboration with the Department of Radiation Oncology, Klinikum rechts der Isar, Technical University Munich, Germany (please see section 5.2.7). The main result of this study was that if LAP bunches could be delivered with $\Delta E/E_0$ in the range of 24 – 4% in 2% energy steps (which were simulated via the preliminary gantry design for this study) then it is possible to deliver realistic tumour conformal 3D treatment plans with high clinical standards. This assured the clinical applicability of the gantry design concept and laid the foundation for further development of the

Table 6.1: Comparison between the two presented gantry designs.

Gantry Design	Magnet type	Maximum magnetic strength	Number of magnets	Size [m]	Beam shaping	Beam scanning
Preliminary design	Solenoid	$k_{S=} 4.6 \text{ m}^{-1}$	1	height: 1.8 length: 3.0	passive	not included
	SM	$B_{0=} 10 \text{ T}$	2			
	Quad	$k_{Q=} 11 \text{ m}^{-1}$	8			
Advance clinical design	Solenoid	$k_S = 4.5 \text{ m}^{-1}$	2	height: 2.5 length: 3.5	active	active
	SM	$B_0 = 10 \text{ T}$	2			
	Quad	$k_Q = 7.5 \text{ m}^{-1}$	6			
	Solenoid-pair	$k_S = 2.5 \text{ m}^{-1}$	1			

Note: The abbreviations SM and Quad mean 90° sector magnet and quadrupole, respectively. The solenoid-pair used for beam scanning in the advanced clinical gantry design can be considered as one magnet.

gantry concept and pulsed magnets, including experimental characterization of individual prototype magnets, a first pulsed beamline section and a new beam scanning design.

Further improvements were made to the preliminary gantry design which resulted in the advanced gantry solution based on a similar beamline concept. The total number of magnets used in the advanced gantry design is the same as in the preliminary design, however, the magnetic strengths of the individual magnets were reduced, see table 6.1. Also, the drift lengths between magnets have been increased for more convenient installation and reduced overlap of the magnetic fields. For example, in the preliminary gantry design only 20 cm of drift length was provided between the first sector magnet and the following quadrupole and only 8.5 cm between two quadrupoles, which was done to make the system as compact as possible. However, in the advanced gantry design 40 cm drift length was used between sector magnets and quadrupoles and also between quadrupoles. Also, 15 cm drift length was used between the quadrupoles of the ELPIS system without any compromises to the output beam. The overall size of the advanced gantry is about 2.5 m in radius (height) and about 3.5 m in length. This is about 2 times smaller in height, about 3 times shorter in length and about 4 times smaller in volume than most of the conventional isocentric gantries deployed in PT facilities. The height of the advanced clinical gantry design is about 70 cm higher than the preliminary gantry design. Figure 5.13 shows that there is about 70 cm drift space provided between the exit window of the gantry and the isocentre. In a final clinical implementation beam monitors and ionization chambers would be required using this free drift space. It is also possible that inclusion of necessary monitors and safe space between might increase the size of the gantry by few percent. The simulation results also advocate that the advanced gantry design has improved capture and transport efficiency, which is about 2 – 4 orders of magnitude higher than the low-acceptance chicane style designs (Cirrone et al., 2013; Fan

et al., 2007) with maximum transport efficiency increased to 97%.

The advanced gantry solution has been designed to deliver an achromatic beam with selectable large spot-size and broad $\Delta E/E_0$ windows. Furthermore, it has been shown that the dispersion produced in the bending plane by the scanning system can be corrected. The scanned irradiation field size is, however, limited by the extent of beam dispersion in the non-bending plane as no correction can be applied. While only a $20 \times 10 \text{ cm}^2$ beam scanning field can be applied with good beam quality, larger irradiation fields could be managed in principle by patching two fields. However, this is not an attractive solution in clinical practice. It might be possible that an optimized 3D TPS, like LAP-CERR, could account for small distortions in the beam spots while calculating depth dose profiles. Then it could be possible to irradiate even larger field sizes. This issue should be further investigated when clinical relevant LAP beams become available.

The feasibility of laser-driven PT would depend on the efficient use of the properties of LAP beams, i.e. large energy spread with variable beam sizes. Here it is important to mention that the main benefit would be the size and cost reduction of the PT facilities, if the LAP beams could match the high standards in 3D tumour conformal dose delivery of the conventional PT. The TPS study via the advanced gantry design demonstrated that the application of the axial clustering scheme could deliver clinically acceptable treatment plans. In the particular example, presented in sections 5.2.7 and 5.3.5, a large tumour (of about 600 cm^3) would require about 12300 LAP bunches per 2 Gy standard fraction, which means about 20 min irradiation time with 10 Hz repetition rate. Also, in a separate study conducted earlier with the preliminary gantry design parameters, it was demonstrated that a small tumour (about 275 cm^3) would require about 9700 LAP bunches per 2 Gy standard fraction which translates to about 16 min of irradiation time (Hofmann et al., 2015).¹ This irradiation time, or beam-ON time, is on top of the patient setup time (which is usually about 15 mins) and must be reduced to make laser-driven PT therapy a viable option.

In the aforementioned treatment planning study it was also shown that if an intensity modulation scheme could be included in the beamline with 10% intensity reduction steps, then the 3D TPS LAP-CERR can further optimize proton fluence delivery and a shot reduction to about 38% can be achieved (Hofmann et al., 2015). The small sized (brain) tumour would then require about 3640 LAP bunches per 2 Gy standard fraction, which means that irradiation time was reduced from 16 min to about 6 min. This result can be extended to the large sized tumour (presented in sections 5.2.7 and 5.3.5) and can be assumed that treatment delivery time could be reduced to about 8 mins from 20 mins. This is still about 2 – 3 times longer than the conventional treatment plans deliverable via conventional PT therapy systems.

The inclusion of other advanced dose schemes, like partial volume irradiation (discussed in section 2.5.2) can further increase the efficiency in dose delivery by simultaneous axial and lateral clustering of spots. This would give more flexibility in 3D TPS as the

¹This 3D clinical study was performed based on the assumption that a beamline could deliver broad-energetic beams with fixed beam sizes and ignored the actual beam quality from the gantry output at that time. The main results of this study would still be valid for the beams deliverable via the advanced clinical gantry design with ELPIS system.

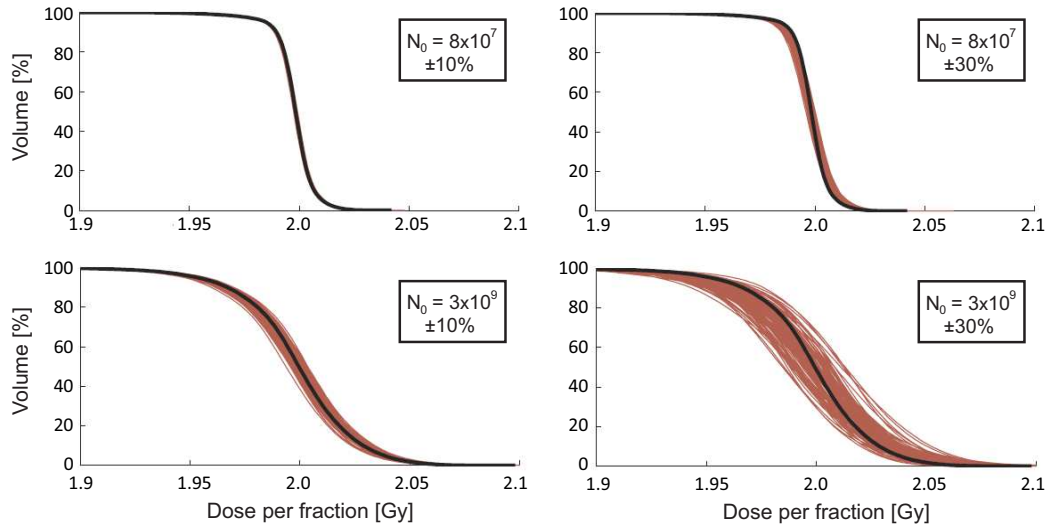


Figure 6.1: Dose volume histograms of the PTV for a reference plan (black) compared with 100 plans underlying random shot-to-shot fluctuations (colored lighter). Four comparisons are shown, two plots for a low (top) and two plots for a high (bottom) initial proton number N_0 , and two different severities of fluctuations, namely, up to $\pm 10\%$ (left) and up to $\pm 30\%$ (right). Image is taken from Hofmann et al. (Hofmann et al., 2015).

dose delivery system, ELPIS, is fully capable to shape and deliver variable size beams with variable energy widths and variable intensities. This may further reduce the treatment time. The research and development in the LAP-CERR is an ongoing project and is a crucial task to exploit other advanced dose schemes to bring the treatment time as low as possible for time efficient laser-driven PT clinical systems.

The advanced gantry solution allowed to restrict the energy window of the filtered bunches through the ISESS. Thus, shot-to-shot fluctuations may only influence the flux delivered with some change in the spectral distribution. This means as the selected energy window is chosen for specific tumour parameters, the fluctuations in the spectral distribution would mainly effect the dose to the tumour and not to the healthy tissue around it. The effect of fluctuations in the total number of protons per LAP bunch (N_0) on the 3D dose distribution on real patient data was also studied in the clinical feasibility study (Hofmann et al., 2015). This study demonstrated that as lower the initial proton number as more an averaging effect takes place due to the randomness of the fluctuations, as few hundreds of LAP bunches or more would then be required to deliver the same dose per fraction. Thus, a shot-to-shot fluctuation up to $\pm 30\%$ in the bunch intensity does not necessarily result in a fluctuation of $\pm 30\%$ on the dose received by the tumour in a single treatment fraction, see figure 6.1. The evaluated dosimetric parameters could be clinically acceptable for all treatment plans with 8×10^7 initial protons per bunch, even for a shot-to-shot fluctuation of $\pm 30\%$ (see figure 6.1, top right). However, in the case of a higher N_0 per bunch of 3×10^9 , the dosimetric deviations were more pronounced, especially for the $\pm 30\%$ fluctuations (see figure 6.1, bottom right). Therefore, in the case of high N_0 per bunch, only a fluctuation of $\pm 10\%$ might be acceptable (this is because more protons per bunch, less bunches would be needed to deliver the fractional dose). This study presented

crucial limits for the development of the future laser systems and LAP beams on the basis of clinical parameters. Even though up to $\pm 10\%$ shot-to-shot fluctuations would be tolerable clinically, laser systems must strive for better stability. Also, as mentioned in the treatment planning study in section 5.3.5, it was found that with the assumed initial RPA like proton spectrum and with the improved transport efficiency the output LAP bunches have up to 2 orders of magnitude higher proton number per LAP bunch than necessary for a dose of 2 Gy per fraction even when applying beams with 2 cm spot-sizes. This sets the priority for future development in laser proton acceleration, i.e. reducing the number of protons per bunch while improving the stability of the beam. In addition it provides a cushion for small losses in transport efficiency from including additional equipment like beam and dose monitors in the gantry system.

The above mentioned 3D TPS study on beam fluctuation only assumed the fluctuation in the total number of protons per bunch, this would be the first type of fluctuation presented in the section 5.2.9. There can be more types of fluctuations in LAP beams, for example in the shape of the spectrum or shift in the peak energy etc. The fluctuations also would depend on the type of laser-proton acceleration, for example TNSA or RPA, which result in different output beam spectra. The influence of fluctuations on treatment plans needs extensive studies, perhaps, after advances in LAP-CERR and after demonstration of clinically relevant LAP bunches with experimentally verified energy spectrum and pulse-to-pulse fluctuations.

The quality of treatment plans and treatment delivery time present a critical challenge for the commercial success of laser-driven PT systems. If future laser systems are still limited to 10 Hz repetition rates, then laser-driven PT could mostly provide treatment options for patients with small tumours and patients which qualify for hypo-fractionation². Another, option could be radio-surgery where a high dose rate is delivered to very small volumes. Hypo-fractionation and radio-surgery regimes could benefit from the fact that LAP bunches contain a large number of protons and if focused tightly to small regions could provide large amount of dose in relatively short treatment time. However, both of these regimes would require better beam stability, as they would require lower number of LAP bunches than standard fractionation which might not statistically cancel out beam fluctuations.

Nevertheless, it has been shown that LAP beams with the advanced gantry design with ELPIS beam delivery system can compete with the conventional PT systems on the basis of clinically deliverable quality treatment plans. An article by Vanderstraeten et al. (Vanderstraeten et al., 2014) discussed in detail the cost of setting up and the economic sustainability of hadron therapy machines which are currently available commercially. The article discussed proton only, carbon only and combined carbon and proton therapy facilities. However, only conventional proton beam facilities are discussed here and a rough comparison is extended towards a possible future LAP beam therapy facility. A conventional PT facility can be set up for around 51 million Euros as an initial investment which

²Standard treatment fractions usually deliver a dose of 2 Gy per fraction, however, in some cases a higher dose, of about 5 Gy, is used. This is called hypo-fractions and is mostly utilized to achieve higher biological effect to treat small volume metastasis.

would include building infrastructure with imaging and planning equipment, where proton beam equipment (accelerator and single gantry) would cost around 25 million Euros.

The new high-power laser system and associated pulsed gantry must compete with this price to compete in the commercial market. The conventional PT gantry (see figures 2.2 and 2.3) essentially forms a conical layout and can take about 300 m³ of volumetric space to revolve. Whereas, the pulsed gantry presented here for LAP sources would make a cylindrical form (see figure 5.13) and may take around 60 m³ of volumetric space in the building. This would reduce the requirement of space by about 4 – 5 times, for each gantry. Also, it is worthwhile to mention that abandoning the iron-core not only elevates the field strength but also makes pulsed magnets much lighter in weight. For example, the 50° pulsed prototype sector magnet with about 8 T field strength is about 60 times lighter than a 50° 2 T iron-core magnet. This in turn would make lighter gantries possible with less constraints on the associated supporting structures and building. For these reasons, the demands on the building infrastructure and footprint of a laser-driven PT facility could be lowered. However, the size of the laser systems might take up several tens square metre of space (Limpert et al., 2011), whereas on the other hand, the actual size of the conventional cyclotrons are being reduced to about 3 m in diameter and 1.6 m in height (Schillo, 2014). This size difference might be compensated by the fact that in a laser-driven system the need for long, heavy magnetic transferlines can be eliminated and along with the compact pulsed gantry system could reduce the overall size. This means a facility based on a single laser accelerator with multiple gantries would benefit the most from the space saving.

However, a crucial limit would come from the necessary treatment delivery time which is limited essentially by the low repetition rate of high-power laser systems (of about 10 Hz). As described in the reference (Vanderstraeten et al., 2014), a conventional PT system would require about 20 min treatment time for each patient, in which 18 min would be dedicated to the patient setup and only 2 min for beam-ON time³. However, one treatment plan per fraction via intensity modulated laser-driven PT system would require 6 – 8 min of irradiation time, i.e. beam-ON time. Even if an average irradiation time of 8 min is considered⁴, then a total treatment time of 26 min would be required for laser-driven systems (as the patient set up time is fixed due to the quality issues). This means one high-power laser system can accommodate two or at maximum three gantries. The current commercial vendors of conventional PT systems give the option of multiple gantries with single conventional accelerator, however, recently a surge in demand for single room (one accelerator and one gantry) has been seen (Friesel and Antaya, 2009; Mevion Medical Systems, 2017; Ion Beam Applications (IBA), 2017; Particle Therapy Co-Operative Group, 2016), which is mainly due to the associated high investment costs. If two gantries per laser system are used in a laser-driven PT facility, then it is possible to setup a patient in one room while irradiating one in the other, to utilize the maximum possible beam-ON

³The 2 min beam-ON time is a conservative number and modern multi-field and IMPT irradiation schemes may require longer irradiation times, where the increase of time depends upon tumour size, number of fields, the rotation speeds of the gantry systems etc.

⁴In a clinical environment, a range of tumours with small to large sizes would be treated. A longer average of 8 min of irradiation time is used here for the sake of conservative discussion.

time provided by the laser system. This could reduce the patient waiting time compared with single room conventional PT systems. The pulsed gantry size reduction could allow to accommodate two gantries instead of one conventional gantry in the same hospital space. With the possible increase in patient throughput, the equipment and staff costs per treatment costs must then be less expensive than the available single room conventional systems.

Another crucial issue with LAP beam applications is the generation of debris from the laser-target and the generation of secondary radiation from beam capture and energy selection systems. The debris being the by-product of the laser-driven acceleration process (described in section 2.4.3) contaminates the clean laser-target assembly and would require frequent maintenance. This would demand for the need of stable, inexpensive, reliable and clean laser-targets which would generate minimum debris, such as cryogenic hydrogen jets (Obst et al., 2017). This requires research and development of such laser-targets, which can achieve higher proton energies via either existing or new laser-driven acceleration mechanisms.

Furthermore, the need to select protons from the accelerated bunch (which contains electrons and other ions) and then to select only a small portion of the proton energy spectrum per bunch for dose application, will produce a large number of secondary radiation. The quantity and type of secondary radiation will depend upon the type of acceleration mechanism and the generated LAP energy spectrum. It is important to study the generation and protection of secondary radiations, which is crucial not just for the protection of patient and hospital staff but also to study the protection and activation of the beamline elements. Recently, a radiation protection study was initiated for this purpose which is still going on. The gantry design presented here could accommodate beam dumps and radiation protection shielding around the beamline and patient area. However, the results from this radiation protection study will predict and determine the feasibility of laser-driven beam for PT applications.

One option to make the laser-driven PT systems more attractive could be to deliver more than one type of ions via laser acceleration. Heavier ions, like helium ions, are gaining interests in the medical community because of their potential dosimetric and radiobiological benefits over proton beams (Fuchs et al., 2015; Mairani et al., 2016). ${}^4\text{He}^{2+}$ with energies of about 800 – 1000 MeV (i.e. about 200 – 250 MeV per nucleon) can provide doses to deep seated tumours. It has been shown theoretically that He beams with these energies can also be generated with the next generation PW laser systems (Bulanov et al., 2015). The increased mass of these ions would demand a laser power of about 3 PW, this would increase the demand on laser and laser-targets. However, if such laser-driven He beams become available in the future then they can also be utilized for radiation therapy applications. This means that to keep the size of the gantry for He beams (with magnetic rigidity of up to 4.5 Tm) same as the advanced clinical gantry design presented (for protons with magnetic rigidity of up to 2.43 Tm), the magnetic fields strengths need to be increased. For example, the magnetic field strength in the sector magnets used for the advanced gantry is about 10 T and for He beams for the same curvature about 15 T field strength would be required. This increase is possible to achieve or (if not)

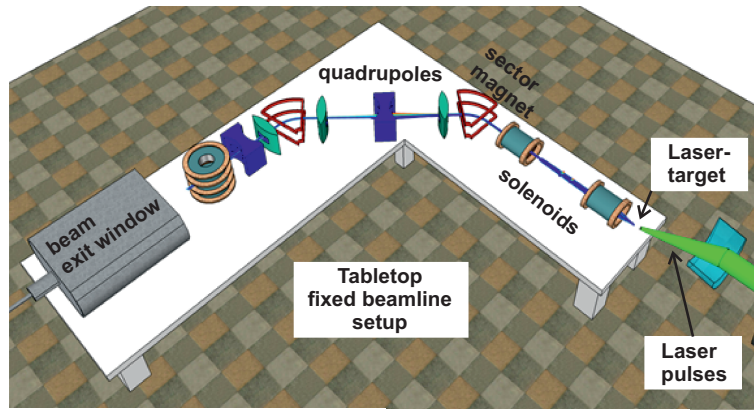


Figure 6.2: A possible intermediate pulsed beamline setup. This can incorporate beamline concepts, such as capture and collimation, energy selection and beam scanning, from the advanced gantry solution, and can filter and transport LAP bunches to an experimental site through the beam exit window. This fixed beamline solution can be utilized for radio-biological experiments in future.

the size of the gantry could be increased by a few percent. Nevertheless, the gantry with ELPIS beam delivery system would be able to deliver advanced treatment options with He beams as well. It could be possible, by changing the laser-target assembly and laser pulse parameters, to deliver an option of two type of particle beams by the same equipment. This may provide an advantage for the laser-driven therapy systems, as cyclotron based systems can not provide two types of beams, and to have two beam options much larger synchrotron accelerators are required.

The presented clinical gantry design would require only three types of pulsed magnets for practical realization, namely solenoids, dipoles and quadrupoles. The design, construction and characterization of the pulsed magnets is under way, as explained in section 3.3. A first prototype pulsed beamline section has been successfully tested at HZDR with a 10 MeV proton beam from the tandetron accelerator (see section 5.4). The main purpose of this experiment was to establish pulse powering of more than one pulsed magnet, synchronizing traversing beam bunches with pulsing of magnets and characterizing the beamline section. This proof-of-principle experiment provided the basic controls and confidence to use this type of high-field magnets for complete beamlines. Also, the first prototype pulsed quadrupole has been designed and manufactured, and is ready to be tested. Furthermore, it is planned to conduct experiments in the near future, which would include beam shaping and scanning via quadrupoles. These experiments would show the feasibility and complexity of these new beam shaping and scanning techniques. The next steps would include individual pulsed magnets and beamline characterization with higher proton energies with stable beam parameters, such as stable conventional beams available at the University Proton Therapy Dresden, Germany (UPTD). Furthermore, pulsed magnets, which can generate and withstand higher magnetic field strengths and have cooling mechanisms, are in the design and manufacturing stages. Up until now experiments were conducted with the pulsed magnets at low repetition rates, i.e. less than 1 Hz. The development of a new energy efficient 10 Hz pulse generator system is also underway. This will allow to take a step further towards the practical realization of

10 Hz beamline systems.

The success of pulsed gantry systems depends on the future development, characterization and economical feasibility of individual pulsed magnets with demanded magnetic field strengths and pulsing systems. Another option could be to develop a hybrid magnetic system for the gantries, consisting of pulsed and superconducting magnets. The recent development in the superconducting magnets for ion beam therapy systems (Syresin and Morozov, 2016; Iwata et al., 2017) could also be used for LAP beams. This would present different challenges like the effect of quick rise and fall of magnetic fields in pulsed magnets on the superconducting magnetic systems. Nevertheless, such hybrid system can also provide compact, economical gantry solutions.

The clinical application of LAP beams for cancer treatment would be the ultimate goal in the future. The main hurdle towards laser-driven PT is a laser accelerator providing beams of therapeutic quality, i.e. therapeutic energies, optimal intensities, stability, reliability and low maintenance. Despite the recent advances in the field of laser systems, clinical application of laser-driven PT might not be available in the next decade. However, the necessary concepts must be developed in parallel. For example, besides the development and characterization of pulsed magnets and beamlines it is necessary to develop a platform for experiments, such as radio-biological experiments, characterization of beam monitors and dosimeters for intense beams. A pulsed beamline which could cater available, and LAP beams with intermediate energies up to 100 – 150 MeV, could provide such a platform. This intermediate pulsed beamline (see figure 6.2) could incorporate the beamline functionalities developed for the advanced clinical gantry, such as two-step capture and collimation, energy selection, beam control and beam scanning. Furthermore, this beamline can be attached to the existing laser-target chamber, without the need to design special laser-target chambers as suggested for the clinical gantry solutions. The already manufactured pulsed magnets and existing power supplies can be readily used for this intermediate beamline. This will give a platform and user facility for testing and characterizing new equipment, radio-biological effects, new dose models etc., and thus, can be used to establish laser-driven proton beam therapy.

Chapter 7

Summary

Motivation: Radiotherapy is an important modality in cancer treatment commonly using photon beams from compact electron linear accelerators. However, due to the inverse depth dose profile with maximum dose deposition at the end of their path (Bragg peak), proton beams allow a dose escalation within the target volume and reduction in surrounding normal tissue. Up to 20% of all radiotherapy patients could benefit from proton therapy (PT). Conventional accelerators are utilized to obtain proton beams with therapeutic energies of 70 – 250 MeV. These beams are then transported to the patient via magnetic transferlines and a rotatable beamline, called gantry, which are large and bulky. PT requires huge capex, limiting it to only a few big centres worldwide treating much less than 1% of radiotherapy patients. The new particle acceleration by ultra-intense laser pulses occurs on micrometer scales, potentially enabling more compact PT facilities and increasing their widespread. These laser-accelerated proton (LAP) bunches have been observed recently with energies of up to 90 MeV and scaling models predict LAP with therapeutic energies with the next generation petawatt laser systems.

Challenges: Intense pulses with maximum 10 Hz repetition rate, broad energy spectrum, large divergence and short duration characterize LAP beams. In contrast, conventional accelerators generate mono-energetic, narrow, quasi-continuous beams. A new multi-functional gantry is needed for LAP beams with a capture and collimation system to control initial divergence, an energy selection system (ESS) to filter variable energy widths and a large acceptance beam shaping and scanning system. An advanced magnetic technology is also required for a compact and light gantry design. Furthermore, new dose deposition models and treatment planning systems (TPS) are needed for high quality, efficient dose delivery.

Materials and Methods: In conventional dose modelling, mono-energetic beams with decreasing energies are superimposed to deliver uniform spread-out Bragg peak (SOBP). The low repetition rate of LAP pulses puts a critical constraint on treatment time and it is highly inefficient to utilize conventional dose models. It is imperative to utilize unique LAP beam properties to reduce total treatment times. A new 1D Broad Energy Assorted depth dose Deposition (BEAD) model was developed using computational software package Python and Monte-Carlo simulation package Geant4. It could deliver similar SOBP by

superimposing several LAP pulses with variable broad energy widths. The BEAD model sets the primary criteria for the gantry, i.e. to filter and transport pulses with up to 20 times larger energy widths than conventional beams for efficient dose delivery.

Air-core pulsed magnets can reach up to 6 times higher peak magnetic fields than conventional iron-core magnets and the pulsed nature of laser-driven sources allowed their use to reduce the size and weight of the gantry. An isocentric gantry was designed with integrated laser-target assembly, beam capture and collimation, variable ESS and large acceptance achromatic beam transport. The computational software package Mathematica was utilized to calculate beam optics formalism and then General particle tracer (GPT) simulation code was employed to verify the calculated beamline with realistic magnetic fields and beam properties. An advanced clinical gantry was designed later with a novel active beam shaping and scanning system, called ELPIS. The filtered beam outputs via the advanced gantry simulations were implemented in an advanced 3D TPS, called LAP-CERR. A LAP beam gantry and TPS were brought together for the first time, and clinical feasibility was studied for the advanced gantry via tumour conformal dose calculations on real patient data.

Furthermore, for realization of pulsed gantry systems, a first pulsed beamline section consisting of prototypes of a capturing solenoid and a sector magnet was designed and tested at tandem accelerator with 10 MeV pulsed proton beams. A first air-core pulsed quadrupole was also designed.

Results: The preliminary gantry design showed the prospect of compact pulsed magnetic systems, and would require three types of pulsed magnets namely solenoids, dipoles and quadrupoles. It showed for the first time the possibility to filter and transport selectable broad-energetic LAP beams, and these beams can generate uniform 1D SOBP in water phantom as per BEAD model. Although it provided a limited output beam control, these results sparked the development and testing of new pulsed high-field magnets.

An advanced gantry with the new ELPIS system was then designed and simulated. Simulated results show that achromatic beams with actively selectable beam sizes in the range of 1 – 20 cm diameter with selectable energy widths ranging from 19 – 3% can be delivered via the advanced gantry. ELPIS can also scan these large beams to a $20 \times 10 \text{ cm}^2$ irradiation field. This gantry is about 2.5 m in height and about 3.5 m in length, which is about 4 times smaller in volume than the conventional PT gantries. The clinical feasibility study on a head and neck tumour patient shows that these filtered beams can deliver state-of-the-art 3D treatment plans. The treatment times by using a larger fraction of the initial energy spectrum and integrating an active intensity modulation scheme in the gantry can be reduced to about 8 min for large sized tumours.

Experimental characterization of a prototype pulsed beamline section was performed successfully and the synchronization of proton pulse with peak magnetic field in the individual magnets was established. This showed the practical applicability and feasibility of pulsed beamlines. The newly designed pulsed quadrupole with three times higher field gradients than iron-core quadrupoles is already manufactured and will be tested in near future.

Conclusion: The main hurdle towards laser-driven PT is a laser accelerator providing beams of therapeutic quality, i.e. energy, intensity, stability, reliability. Nevertheless, the presented advanced clinical gantry design presents a complete beam transport solution for future laser-driven sources and shows the prospect and limitations of a compact laser-driven PT facility. Further development in the LAP-CERR is needed as it has the potential to utilize advanced beam controls from the ELPIS system and optimize doses on the basis of advanced dose schemes, like partial volume irradiation, to bring treatment times further down. To realize the gantry concept, further research, development and testing in higher field and higher (up to 10 Hz) repetition rate pulsed magnets to cater therapeutic proton beams is crucial.

Zusammenfassung

Motivation: Die Strahlentherapie ist eine wichtige Therapieform der Krebsbehandlung, die am häufigsten mit kompakten Elektronenlinearbeschleunigern erzeugte Photonenstrahlen verwendet. Protonenstrahlen erlauben jedoch aufgrund des inversen Tiefendosisprofils mit maximaler Dosis (Bragg-Peak) am Ende ihres Weges eine Dosismaximierung innerhalb des Zielvolumens bei gleichzeitiger Reduktion der Dosis im umgebenden Normalgewebe. Bis zu 20% aller Strahlentherapiepatienten könnten von der Protonentherapie (PT) profitieren. Bisher werden herkömmliche Beschleuniger verwendet, um die Protonenstrahlen mit therapeutischen Energien von 70 – 250 MeV zu erzeugen. Diese Strahlen werden dann mittels Magnete, die auch auf einer rotierbaren Einheit, einer sogenannten Gantry, montiert sein können, zu dem Patienten geführt. Protonentherapie (PT) sind somit groß und voluminös und sehr kostenintensiv. Deshalb sind PT nur auf wenige große Zentren beschränkt und weltweit werden weniger als 1% der Strahlentherapiepatienten mit Protonenstrahlen behandelt. Die neuartige Teilchenbeschleunigung durch ultra-intensive Laserimpulse benötigt zur Beschleunigung nur wenige Mikrometer, was möglicherweise kompaktere PT-Einrichtungen ermöglicht und deren Verbreitung erhöhen könnte. Es wurden bereits Laser beschleunigten Protonen (LAP) mit Energien von bis zu 90 MeV nachgewiesen und Skalierungsmodelle sagen LAP mit therapeutischen Energien für die nächste Generation von Petawatt-Lasersystemen voraus.

Herausforderungen: LAP-Strahlen sind gekennzeichnet durch intensive Pulse mit einer maximalen Wiederholrate von 10 Hz, einem breiten Energiespektrum, großer Divergenz und kurzer Dauer. Im Gegensatz dazu erzeugen herkömmliche Beschleuniger monoenergetische, schmale, quasi kontinuierliche Strahlen. Deshalb wird für LAP-Strahlen eine neue multifunktionale Gantry mit einem Fokussier- und Kollimationssystem zur Steuerung der anfänglichen Divergenz, einem Energieselektionssystem (ESS) zum Filtern variabler Energiebreiten und einem Strahlformungs- und Abtastsystem mit großer Akzeptanz benötigt. Für ein kompaktes Gantry-Design ist auch eine unkonventionelle Magnettechnologie erforderlich. Darüber hinaus werden für eine effiziente Dosisapplikation mit hoher Tumorkonformität neue Strategien und Behandlungsplanungssysteme (TPS) benötigt.

Material und Methoden: Bei der konventionellen Dosisapplikation werden viele von den monoenergetischen Photonenstrahlen überlagert, um einen homogenen, ausgedehnten Bragg Peak (SOBP) zu erzeugen. Die niedrige Repetitionsrate von LAP-Pulsen setzt jedoch eine kritische Einschränkung für die Behandlungszeit, und es ist sehr ineffizient, diese herkömmliche Strategie zu verwenden. Es ist daher zwingend notwendig, die einzigartigen Eigenschaften der LAP zu verwenden, um die Gesamtbehandlungszeiten zu reduzieren. Ein neues 1D-Modell zur Erzeugung der Tiefendosis (BEAD) wurde mit dem Softwarepaket Python und dem Monte-Carlo-Simulationspaket Geant4 entwickelt. Es erzeugt ähnliche SOBP, indem mehrere LAP-Pulse mit variablen und relativ großen En-

ergiebreiten überlagert werden. Das BEAD-Modell legt das Hauptkriterium für die Gantry fest, d. h. für eine effiziente Dosisapplikation müssen Strahlpulse mit bis zu 20 mal größeren Energiebreiten als bei konventionellen Anlagen gefiltert und geführt werden.

Gepulste Magnete mit Luftkern können bis zu 6-mal höhere Magnetfelder als herkömmliche Magnete mit Eisenkern erreichen. Die gepulste Natur von lasergetriebenen Quellen erlaubt die Verwendung solcher Magnete, um die Größe und das Gewicht der Gantry zu reduzieren. Eine isozentrische Gantry mit integrierter Laser-Target-Anordnung, Strahlfokussierung und -kollimation, variablem ESS und achromatischen Strahltransport mit großer Akzeptanz konstruiert. Das Softwarepaket Mathematica wurde verwendet, um die Strahloptik zu berechnen, und dann wurde weiter General Particle Tracer (GPT) verwendet, um die berechnete Strahlführung mit realistischen Magnetfeldern und Strahleigenschaften zu verifizieren. Darauf folgend wurde eine zweite Gantry mit einem neuartigen aktiven Strahlformungs- und Abtastsystem, genannt ELPIS, für den späteren klinischen Einsatz entwickelt. Die mit der Simulation bestimmten Strahleigenschaften am Ausgang der zweiten Gantry wurden in einem eigens entwickelten 3D-TPS, dem sogenannten LAP-CERR, implementiert. Somit wurde erstmalig auch eine LAP-Gantry und ein TPS zusammengeführt und die klinische Machbarkeit wurde für die zweite Gantry mittels tumorkonformer Dosisberechnungen an realen Patientendaten untersucht.

Weiterhin wurde zur Realisierung von gepulsten Gantry-Systemen ein erstes System aus gepulsten Magneten, bestehend aus einem Solenoids und einem Sektormagneten, am Tandembeschleuniger aufgebaut mit einem 10 MeV gepulsten Protonenstrahlen getestet. Auch ein erster gepulster Quadrupol mit Luftkern wurde entwickelt.

Ergebnisse: Das vorläufige Design zeigt die Machbarkeit einer kompakten Gantry und würde drei Arten von gepulsten Magneten erfordern, nämlich Solenoide, Dipole und Quadrupole. Es zeigt auch die Möglichkeit, LAP-Strahlen mit variabler Energie und Energiebreite zu filtern und zu führen. Diese Strahlen können einen 1D-SOBP im Wasserphantom gemäß dem BEAD-Modell erzeugen. Obwohl es eine nur begrenzte Kontrolle des Strahls am Ausgang zur Verfügung stellt, lösten diese Ergebnisse die Entwicklung und das Testen von neuen gepulsten Hochfeldmagneten aus.

Die zweite Gantry mit dem neuen ELPIS-System wurde dann entworfen und simuliert. Die Ergebnisse der Simulation zeigen, dass achromatische Strahlen mit aktiv wählbaren Strahlgrößen im Bereich von 1 – 20 cm Durchmesser mit wählbaren Energiebreiten von 3 – 19% geliefert werden können. ELPIS kann diese Strahlen auch zu einem $20 \times 10 \text{ cm}^2$ Bestrahlungsfeld durch Scannen zusammensetzen. Diese Gantry ist etwa 2,5 m hoch und etwa 3,5 m lang, was etwa 4-mal kleiner ist als die Gantries bei herkömmlichen PT-Portalen. Die Studie mit dem TPS an einem Kopf-Hals-Tumorpatienten zeigt, dass mit diesen Strahlen die Anforderungen an 3D-Behandlungspläne nach dem Stand der Technik erfüllt werden können. Unter Verwendung eines größeren Anteils des anfänglichen Energiespektrums und der Integration einer aktiven Intensitätsmodulation können die Behandlungszeiten für großdimensionierte Tumore auf etwa 8 Minuten reduziert werden.

Die experimentelle Charakterisierung eines Systems gepulster Magnete wurde erfolgreich durchgeführt und auch der Protonenpuls mit dem Magnetfeld synchronisiert. Dies

zeigte die praktische Anwendbarkeit und Machbarkeit gepulster Strahlführungen. Der neu konzipierte, gepulste Quadrupol mit dreifach höheren Feldgradienten als konventionelle Quadrupole mit Eisenkern wird bereits hergestellt und in naher Zukunft getestet.

Schlussfolgerung: Die Haupthürde hin zu lasergetriebenem PT ist ein Laserbeschleuniger, der Strahlen von therapeutischer Qualität liefert, d. h. Energie, Intensität, Stabilität, Zuverlässigkeit. Das vorgestellte, zweite Gantry-Design stellt jedoch eine vollständige Strahltransportlösung für den klinischen Einsatz von zukünftigen lasergetriebenen Quellen dar und zeigt Möglichkeiten und Grenzen einer kompakten PT-Einrichtung. Die Weiterentwicklung des LAP-CERR ist erforderlich, um die verbesserte Strahlkontrolle aus dem ELPIS-System zu verwenden und die Dosis auch auf der Grundlage neuer Bestrahlungstechniken wie Teilvolumenbestrahlung zu optimieren und um die Behandlungszeiten weiter zu senken. Um das Gantry-Konzept zu realisieren, ist weitere Forschung, Entwicklung und Test mit höheren Feldstärken und höhere Pulswiederholrate (bis zu 10 Hz) von entscheidender Bedeutung, um therapeutische Protonenstrahlen zu erzeugen.

Bibliography

Agostinelli S, Allison J, Amako K, Apostolakis J, Araujo H, Arce P, Asai M, Axen D, Banerjee S, Barrand G, Behner F, Bellagamba L, Boudreau J, Broglia L, Brunengo A, Burkhardt H, Chauvie S, Chuma J, Chytrcek R, Cooperman G, Cosmo G, Degt-yarenko P, Dell'Acqua A, Depaola G, Dietrich D, Enami R, Feliciello A, Ferguson C, Fesefeldt H, Folger G, Foppiano F, Forti A, Garelli S, Giani S, Giannitrapani R, Gibin D, Cadenas JJG, Gonzz I, Abril GG, Greeniaus G, Greiner W, Grichine V, Grossheim A, Guatelli S, Gumplinger P, Hamatsu R, Hashimoto K, Hasui H, Heikki-nen A, Howard A, Ivanchenko V, Johnson A, Jones FW, Kallenbach J, Kanaya N, Kawabata M, Kawabata Y, Kawaguti M, Kelner S, Kent P, Kimura A, Kodama T, Kok-oulin R, Kossov M, Kurashige H, Lamanna E, Lamp, Lara V, Lefebure V, Lei F, Liendl M, Lockman W, Longo F, Magni S, Maire M, Medernach E, Minamimoto K, de Fre-itas PM, Morita Y, Murakami K, Nagamatu M, Nartallo R, Nieminen P, Nishimura T, Ohtsubo K, Okamura M, O'Neale S, Oohata Y, Paech K, Perl J, Pfeiffer A, Pia MG, Ranjard F, Rybin A, Sadilov S, Salvo ED, Santin G, Sasaki T, Savvas N, Sawada Y, Scherer S, Sei S, Sirotenko V, Smith D, Starkov N, Stoecker H, Sulkimo J, Taka-hata M, Tanaka S, Tcherniaev E, Tehrani ES, Tropeano M, Truscott P, Uno H, Ur-ban L, Urban P, Verderi M, Walkden A, Wander W, Weber H, Wellisch JP, Wenaus T, Williams DC, Wright D, Yamada T, Yoshida H, and Zschesche D. 2003. Geant4 - a simulation toolkit. Nucl Instrum Methods Phys Res , Sect A, 506(3):250 – 303. URL <http://www.sciencedirect.com/science/article/pii/S0168900203013688>.

Allison J, Amako K, Apostolakis J, Araujo H, Dubois PA, Asai M, Barrand G, Capra R, Chauvie S, Chytrcek R, Cirrone GAP, Cooperman G, Cosmo G, Cuttone G, Daquino GG, Donszelmann M, Dressel M, Folger G, Foppiano F, Generowicz J, Grichine V, Guatelli S, Gumplinger P, Heikkinen A, Hrivnacova I, Howard A, Incerti S, Ivanchenko V, Johnson T, Jones F, Koi T, Kokoulin R, Kossov M, Kurashige H, Lara V, Larsson S, Lei F, Link O, Longo F, Maire M, Mantero A, Mascialino B, McLaren I, Lorenzo PM, Minamimoto K, Murakami K, Nieminen P, Pandola L, Parlati S, Peralta L, Perl J, Pfeiffer A, Pia MG, Ribon A, Rodrigues P, Russo G, Sadilov S, Santin G, Sasaki T, Smith D, Starkov N, Tanaka S, Tcherniaev E, Tome B, Trindade A, Truscott P, Urban L, Verderi M, Walkden A, Wellisch JP, Williams DC, Wright D, and Yoshida H. 2006. Geant4 developments and applications. IEEE Trans Nucl Sci, 53(1):270–278. URL <http://ieeexplore.ieee.org/stamp/stamp.jsp?tp=&arnumber=1610988&isnumber=33833>.

Antoine S, Autin B, Beeckman W, Collot J, Conjat M, Forest F, Fourrier J, Froidefond E,

- Lancelot J, Mandrillon J, Mandrillon P, M F, Mori Y, Neuvisse D, Ohmori C, Pasternak J, and Planche T. 2009. Principle design of a protontherapy, rapid-cycling, variable energy spiral FFAG. *Nucl Instrum Methods Phys Res , Sect A*, 602(2):293 – 305. URL <https://doi.org/10.1016/j.nima.2009.01.025>.
- Baron MH, Pommier P, Favrel V, Truc G, Balosso J, and Rochat J. 2004. A “one-day survey ”: as a reliable estimation of the potential recruitment for proton- and carbon-ion therapy in France. *Radiother Oncol*, 73:15–17. URL <http://www.ncbi.nlm.nih.gov/pubmed/15974560>.
- Borghesi M. 2014. Laser-driven ion acceleration: State of the art and emerging mechanisms. *Nucl Instrum Methods Phys Res, Sect A*, 740:6 – 9. URL <https://doi.org/10.1016/j.nima.2013.11.098>.
- Bortfeld T. 1997. An analytical approximation of the Bragg curve for therapeutic proton beams. *Med Phys*, 24(12):2024–2033. URL <https://aapm.onlinelibrary.wiley.com/doi/pdf/10.1118/1.598116>.
- Brüchner K, Beyreuther E, Baumann M, Krause M, Oppelt M, and Pawelke J. 2014. Establishment of a small animal tumour model for in vivo studies with low energy laser accelerated particles. *Radiat Oncol*, 9(1):1–9. URL <http://dx.doi.org/10.1186/1748-717X-9-57>.
- Bulanov SS, Esarey E, Schroeder CB, Leemans WP, Bulanov SV, Margarone D, Korn G, and Haberer T. 2015. Helium-3 and Helium-4 acceleration by high power laser pulses for hadron therapy. *arXiv:150503921*. URL <https://arxiv.org/abs/1505.03921v1>.
- Bulanov SV, Esirkepov TZ, Khoroshkov VS, Kuznetsov AV, and Pegoraro F. 2002. Oncological hadrontherapy with laser ion accelerators. *Phys Lett A*, 299:240–247. URL [https://doi.org/10.1016/S0375-9601\(02\)00521-2](https://doi.org/10.1016/S0375-9601(02)00521-2).
- Bulanov SV and Khoroshkov VS. 2002. Feasibility of using laser ion accelerators in proton therapy. *Plasma Phys Rep*, 28(5):453456. URL <https://aip.scitation.org/doi/abs/10.1063/1.1843524>.
- Burris-Mog T. 2012. Capture and transport of laser accelerated protons by pulsed magnetic fields: advancements toward laser-based proton therapy. University of Nevada, Reno, USA, Dissertation.
- Burris-Mog T, Harres K, Nürnberg F, Busold S, Bussmann M, Deppert O, Hoffmeister G, Joost M, Sobiella M, Tauschwitz A, Zielbauer B, Bagnoud V, Hermannsdörfer T, Roth M, and Cowan TE. 2011. Laser accelerated protons captured and transported by a pulse power solenoid. *Phys Rev ST Accel Beams*, 14:121301. URL <https://link.aps.org/doi/10.1103/PhysRevSTAB.14.121301>.
- Busold S, Almomani A, Bagnoud V, Barth W, Bedacht S, Blažević A, Boine-Frankenheim O, Brabetz C, Burris-Mog T, Cowan T, Deppert O, Droba M, Eickhoff H, Eisenbarth U, Harres K, Hoffmeister G, Hofmann I, Jaeckel O, Jaeger R, Joost M, Kraft S, Kroll

- F, Kaluza M, Kester O, Lecz Z, Merz T, Nürnberg F, Al-Omari H, Orzhekhovskaya A, Paulus G, Polz J, Ratzinger U, Roth M, Schaumann G, Schmidt P, Schramm U, Schreiber G, Schumacher D, Stoeckler T, Tauschwitz A, Vinzenz W, Wagner F, Yaramyshev S, and Zielbauer B. 2014a. Shaping laser accelerated ions for future applications - The LIGHT collaboration. *Nucl Instrum Methods Phys Res , Sect A*, 740(0):94 – 98. URL <https://doi.org/10.1016/j.nima.2013.10.025>.
- Busold S, Schumacher D, Brabetz C, Jahn D, Kroll F, Deppert O, Schramm U, Cowan TE, Blažević A, Bagnoud V, and Roth M. 2015. Towards highest peak intensities for ultra-short MeV-range ion bunches. *Sci Rep*, 5(12459). URL <http://dx.doi.org/10.1038/srep12459>.
- Busold S, Schumacher D, Deppert O, Brabetz C, Frydrych S, Kroll F, Joost M, Al-Omari H, Blažević A, Zielbauer B, Hofmann I, Bagnoud V, Cowan TE, and Roth M. 2013. Focusing and transport of high-intensity multi-MeV proton bunches from a compact laser-driven source. *Phys Rev ST Accel Beams*, 16:101302. URL <http://link.aps.org/doi/10.1103/PhysRevSTAB.16.101302>.
- Busold S, Schumacher D, Deppert O, Brabetz C, Kroll F, Blažević A, Bagnoud V, and Roth M. 2014b. Commissioning of a compact laser-based proton beam line for high intensity bunches around 10 MeV. *Phys Rev ST Accel Beams*, 17:031302. URL <http://link.aps.org/doi/10.1103/PhysRevSTAB.17.031302>.
- Bychenkov VY, Rozmus W, Maksimchuk A, Umstadter D, and Capjack CE. 2001. Fast ignitor concept with light ions. *Plasma Phys Rep*, 27(12):1017–1020. URL <https://doi.org/10.1134/1.1426135>.
- Caporaso G, Akana G, Anaya R, Blackfield D, Carroll J, Chen YJ, Cook E, Falabella S, Guethlein G, Harris J, Hawkins S, Hickman B, Holmes C, Horner A, Nelson S, Paul A, Poole B, Rhodes M, Richardson R, Sampayan S, Sanders D, Sullivan J, Wang L, Watson J, Weir J, Pearson D, and Slenes K. 2010. Status of the dielectric wall accelerator. In *Particle accelerator. Proceedings, 23rd Conference, PAC'09, Vancouver, Canada, May 4-8, 2009, TH3GAI02*. URL <http://accelconf.web.cern.ch/AccelConf/PAC2009/papers/th3gai02.pdf>.
- Caporaso G, Sampayan S, Chen Y, Harris J, Hawkins S, Holmes C, Krogh M, Nelson S, Nunnally W, Paul A, Poole B, Rhodes M, Sanders D, Selenes K, Sullivan J, Wang L, and Watson J. 2007. Compact accelerator concept for proton therapy. *Nucl Instrum Methods Phys Res B*, 261(1-2 SPEC. ISS.):777–781. URL <https://doi.org/10.1016/j.nimb.2007.04.187>.
- Chen YJ, Caporaso GJ, Guethlein G, Sampayan S, Akana G, Anaya R, Blackfield D, Cook E, Falabella S, Gower E, Harris J, Hawkins S, Hickman B, Holmes C, Horner A, Nelson S, Paul A, Pearson D, Poole B, Richardson R, Sanders D, Stanley J, Sullivan J, Wang L, Watson J, and Weir J. 2009. Compact dielectric wall accelerator development for intensity modulated proton therapy and homeland security applications. In *10th*

- International Conference on Applications of Nuclear Techniques, Crete, Greece. URL https://inis.iaea.org/search/search.aspx?orig_q=RN:41025193.
- Chubar O, Elleaume P, and Chavanne J. 1998. A 3D magnetostatics computer code for insertion devices. *J Synchrotron Rad*, 5:481–484. URL <http://ieeexplore.ieee.org/stamp/stamp.jsp?tp=&arnumber=753258&isnumber=16177>.
- Cirrone GAP, Carpinelli M, Cuttone G, Gammino S, Jia SB, Korn G, Maggiore M, Manti L, Margarone D, Prokupek J, Renis M, Romano F, Schillaci F, Tomasello B, Torrisi L, Tramontana A, and Velyhan A. 2013. ELIMED, future hadrontherapy applications of laser-accelerated beams. *Nucl Instrum Methods Phys Res , Sect A*, 730(Supplement C):174 – 177. URL <http://www.sciencedirect.com/science/article/pii/S0168900213006517>.
- Clarke RJ, Ledingham KWD, McKenna P, Robson L, McCanny T, Neely D, Lundh O, Lindau F, Wahlstrm CG, Simpson PT, and Zepf M. 2006a. Detection of short lived radioisotopes as a fast diagnostic for intense laser-solid interactions. *Appl Phys Lett*, 89(14):141117. URL <http://dx.doi.org/10.1063/1.2358940>.
- Clarke RJ, Neely D, Edwards RD, Wright PNM, Ledingham KWD, Heathcote R, McKenna P, Danson CN, Brummitt PA, Collier JL, Hatton PE, Hawkes SJ, Hernandez-Gomez C, Holligan P, Hutchinson MHR, Kidd AK, Lester WJ, Neville DR, Norreys PA, Pepler DA, Winstone TB, Wyatt RWW, and Wyborn BE. 2006b. Radiological characterisation of photon radiation from ultra-high-intensity laserplasma and nuclear interactions. *J Radiol Prot*, 26(3):277. URL <http://stacks.iop.org/0952-4746/26/i=3/a=002>.
- COMSOL. 2017. COMSOL Multiphysics Finite Element Analysis Software (formerly FEM-LAB). [Updated: 01.06.2018]. URL <https://www.comsol.com/comsol-multiphysics>.
- Cowan TE, Fuchs J, Ruhl H, Kemp A, Audebert P, Roth M, Stephans R, Barton I, Blazevic A, Brambrink E, Cobble J, Fernández J, Gauthier JC, Geissel M, Hegelich M, Kaae J, Karsch S, Sage GPL, Letzring S, Manclossi M, Meyroneinc S, Newkirk A, Pépin H, and Renard-LeGalloudec N. 2004. Ultralow emittance, multi-MeV proton beams from a laser virtual-cathode plasma accelerator. *Phys Rev Lett*, 92(20):204801–4. URL <https://link.aps.org/doi/10.1103/PhysRevLett.92.204801>.
- Cozzi L, Fogliata A, Lomax A, and Bolsi A. 2001. A treatment planning comparison of 3D conformal therapy, intensity modulated photon therapy and proton therapy for treatment of advanced head and neck tumours. *Radiother Oncol*, 61:287–297. URL [https://doi.org/10.1016/S0167-8140\(01\)00403-0](https://doi.org/10.1016/S0167-8140(01)00403-0).
- Crandall KR and Rusthoi DP. 1997. TRACE 3-D Documentation, third edition. Los Alamos National Laboratory, Los Alamos, New Mexico, USA. URL <http://laacg.lanl.gov/laacg/services/traceman.pdf>.
- Daido H, Nishiuchi M, and Pirozhkov AS. 2012. Review of laser-driven ion sources and their applications. *Rep Prog Phys*, 75:056401. URL <http://stacks.iop.org/0034-4885/75/i=5/a=056401>.

- Danson C, Hillier D, Hopps N, and Neely D. 2015. Petawatt class lasers worldwide. *High Power Laser Sci Eng*, 3:e3. URL http://journals.cambridge.org/article_S2095471914000528.
- Doria D, Kakolee KF, Kar S, Litt SK, Fiorini F, Ahmed H, Green S, Jeynes JCG, Kavanagh J, Kirby D, Kirkby KJ, Lewis CL, Merchant MJ, Nersisyan G, Prasad R, Prise KM, Schettino G, Zepf M, and Borghesi M. 2012. Biological effectiveness on live cells of laser driven protons at dose rates exceeding 10^9 Gy/s. In *AIP Advances*, volume 2. AIP. URL <http://link.aip.org/link/?ADV/2/011209/1>.
- Dunne M. 2006. A high-power laser fusion facility for Europe. *Nat Phys*, 2. URL <http://dx.doi.org/10.1038/nphys208>.
- Durante M and Loeffler JS. 2010. Charged particles in radiation oncology. *Nat Rev Clin Oncol*, 7:37–43. URL <http://dx.doi.org/10.1038/nrclinonc.2009.183>.
- Eickhoff H, Weinrich U, and Alonso J. 2011. Design criteria for medical accelerators. In: Linz U (Ed) *Ion beam therapy - fundamentals, technology, clinical applications*. Springer-Verlag, Berlin, Germany, 325-343.
- Eliasson B, Liu CS, Shao X, Sagdeev RZ, and Shukla PK. 2009. Laser acceleration of monoenergetic protons via a double layer emerging from an ultra-thin foil. *New J Phys*, 11(7):073006. URL <http://stacks.iop.org/1367-2630/11/i=7/a=073006>.
- Esirkepov T, Borghesi M, Bulanov SV, Mourou G, and Tajima T. 2004. Highly efficient relativistic-ion generation in the laser-piston regime. *Phys Rev Lett*, 92(17):175003. URL <http://link.aps.org/doi/10.1103/PhysRevLett.92.175003>.
- Fan J, Luo W, Fourkal E, Lin T, Li J, Veltchev I, and Ma CM. 2007. Shielding design for a laser-accelerated proton therapy system. *Phys Med Biol*, 52:3913–3930. URL http://iopscience.iop.org/0031-9155/52/13/017/pdf/0031-9155_52_13_017.pdf.
- Fiuza F, Stockem A, Boella E, Fonseca RA, Silva LO, Haberberger D, Tochitsky S, Gong C, Mori WB, and Joshi C. 2012. Laser-driven shock acceleration of monoenergetic ion beams. *Phys Rev Lett*, 109:215001. URL <https://link.aps.org/doi/10.1103/PhysRevLett.109.215001>.
- Flanz J. 2012. Particle beam scanning. In: Paganetti H (Ed) *Proton therapy physics*. Taylor and Francis Group, USA, 157-189.
- Fourkal E, Li JS, Ding M, Tajima T, and Ma CM. 2003. Particle selection for laser-accelerated proton therapy feasibility study. *Med Phys*, 30(7):1660–1670. URL <https://doi.org/10.1118/1.1586268>.
- Friesel DL and Antaya TA. 2009. Medical Cyclotrons. *Rev Accel Sci Technol*, 02(01):133–156. URL <http://www.worldscientific.com/doi/abs/10.1142/S1793626809000272>.

- Fuchs H, Alber M, Schreiner T, and Georg D. 2015. Implementation of spot scanning dose optimization and dose calculation for helium ions in Hyperion. *Med Phys*, 42(9):5157–5166. URL <http://dx.doi.org/10.1118/1.4927789>.
- Garcia S, Chatain D, and Perin JP. 2014. Continuous production of a thin ribbon of solid hydrogen. *Laser Part Beams*, 32:569–575. URL http://journals.cambridge.org/article_S0263034614000524.
- Garonna A, Amaldi U, Bonomi R, Campo D, Degiovanni A, Garlasché M, Mondino I, Rizzoglio V, and Andrés SV. 2010. Cyclinac medical accelerators using pulsed C^{6+}/H_2^+ ion sources. *J Instrum*, 5(09):C09004. URL <http://stacks.iop.org/1748-0221/5/i=09/a=C09004>.
- Geer S and Loos M. 2013. General Particle Tracer (GPT), User Manual ver 3.01. URL www.pulsar.nl.
- Goitein M, Lomax AJ, and Pedroni ES. 2002. Treating cancer with protons. *Phys Today*, 55(9):45–50. URL <https://doi.org/10.1063/1.1522215>.
- Gottschalk B. 2012. Physics of proton interactions in matter. In: Paganetti H (Ed) *Proton therapy physics*. Taylor and Francis Group, USA, 19-59.
- Haberberger D, Tochitsky S, Fiuza F, Gong C, Fonseca RA, Silva LO, Mori WB, and Joshi C. 2012. Collisionless shocks in laser-produced plasma generate monoenergetic high-energy proton beams. *Nat Phys*, 8:95–99. URL <http://dx.doi.org/10.1038/nphys2130>.
- Hand L and Panofsky W. 1959. Magnetic quadrupole with rectangular aperture. *Rev Sci Instrum*, 30(10):927–930. URL <https://doi.org/10.1063/1.1716386>.
- Harres K, Alber I, Tauschwitz A, Bagnoud V, Daido H, Günther M, Nürnberg F, Otten A, Schollmeier M, Schütrumpf J, Tampo M, and Roth M. 2010. Beam collimation and transport of quasineutral laser-accelerated protons by a solenoid field. *Phys Plasmas*, 17(2):023107. URL http://pop.aip.org/resource/1/phpaen/v17/i2/p023107_s1.
- Hatchett SP, Brown CG, Cowan TE, Henry EA, Johnson JS, Key MH, Koch JA, Langdon AB, Lasinski BF, Lee RW, Mackinnon AJ, Pennington DM, Perry MD, Phillips TW, Roth M, Sangster TC, Singh MS, Snavely RA, Stoyer MA, Wilks SC, and Yasuike K. 2000. Electron, photon, and ion beams from the relativistic interaction of Petawatt laser pulses with solid targets. *Phys Plasmas*, 7(5):2076–2082. URL <http://dx.doi.org/10.1063/1.874030>.
- Henig A. 2010. Advanced approaches to high intensity laser-driven ion acceleration. Fakultät für Physik, Ludwig Maximilians Universität München, Germany, Dissertation.
- Henig A, Steinke S, Schnürer M, Sokollik T, Hörlein R, Kiefer D, Jung D, Schreiber J, Hegelich BM, Yan XQ, Meyer-ter-Vehn J, Tajima T, Nickles PV, Sandner W, and Habs D. 2009. Radiation-pressure acceleration of ion beams driven by circularly polarized

- laser pulses. *Phys Rev Lett*, 103:245003. URL <http://link.aps.org/doi/10.1103/PhysRevLett.103.245003>.
- Herlach F. 1999. Pulsed Magnets. *Rep Prog Phys*, 62:859–920. URL <http://iopscience.iop.org/article/10.1088/0034-4885/62/6/201/pdf>.
- Hofmann I, Meyer-ter-Vehn J, Yan X, and Al-Omari H. 2012a. Chromatic energy filter and characterization of laser-accelerated proton beams for particle therapy. *Nucl Instrum Methods Phys Res A*, 681:44–54. URL <https://doi.org/10.1016/j.nima.2012.04.022>.
- Hofmann I, Meyer-ter-Vehn J, Yan X, Orzhekhovskaya A, and Yaramyshev S. 2011. Collection and focusing of laser accelerated ion beams for therapy applications. *Phys Rev ST Accel Beams*, 14:031304. URL <https://link.aps.org/doi/10.1103/PhysRevSTAB.14.031304>.
- Hofmann KM. 2015. Feasibility and optimization of compact laser-driven beam lines for proton therapy: a treatment planning study. Fakultät für Physik, Technische Universität München, Germany, Dissertation.
- Hofmann KM, Masood U, Pawelke J, and Wilkens JJ. 2015. A treatment planning study to assess the feasibility of laser-driven proton therapy using a compact gantry design. *Med Phys*, 42(9):5120–5129. URL <https://doi.org/10.1118/1.4927717>.
- Hofmann KM, Schell S, and Wilkens JJ. 2012b. Laser-driven beam lines for delivering intensity modulated radiation therapy with particle beams. *J Biophotonics*, 5(11-12):903–911. URL <https://doi.org/10.1002/jbio.201200078>.
- Humphries S. 1986. Principles of charged particle acceleration. John Wiley and Sons, USA.
- Ion Beam Applications (IBA). 2017. Proteus ONE proton therapy system. [Updated: 01.05.2018]. URL <https://iba-worldwide.com/proton-therapy/proton-therapy-solutions/proteus-one>.
- Iwata Y, Fujimoto T, Matsuba S, Fujita T, Sato S, Furukawa T, Hara Y, Mizushima K, Saraya Y, Tansho R, Saotome N, Shirai T, and Noda K. 2017. Recent progress of a superconducting rotating-gantry for carbon-ion radiotherapy. *Nucl Instrum Methods Phys Res , Sect B*, 406:338 – 342. ISSN 0168-583X. URL <https://doi.org/10.1016/j.nimb.2016.10.040>. Proceedings of the 12th European Conference on Accelerators in Applied Research and Technology (ECAART12).
- Jung D. 2012. Ion acceleration from relativistic laser nano-target interaction. Fakultät für Physik, Ludwig Maximilians Universität München, Germany. Dissertation.
- Karsch L, Beyreuther E, Enghardt W, Gotz M, Masood U, Schramm U, Zeil K, and Pawelke J. 2017. Towards ion beam therapy based on laser plasma accelerators. *Acta Oncol*, 56(11):1359–1366. URL <https://doi.org/10.1080/0284186X.2017.1355111>.

- Karsch L and Pawelke J. 2014. Theoretical investigation of the saturation correction for ionization chambers irradiated with pulsed beams of arbitrary pulse length. *Z Med Phys*, 3:201–10. URL <https://doi.org/10.1016/j.zemedi.2013.10.007>.
- Karsch L, Richter C, and Pawelke J. 2011. Experimental investigation of the collection efficiency of a PTW Roos ionization chamber irradiated with pulsed beams at high pulse dose with different pulse lengths. *Z Med Phys*, 21(1):4. URL <https://doi.org/10.1016/j.zemedi.2010.10.008>.
- Kiriyama H, Kando M, Pirozhkov AS, Kishimoto M, Kon A, Nishiuchi M, Sakaki H, Ogura K, Kanasaki M, Tanaka H, Fukuda Y, Mori M, Mashiba Y, Asakawa MR, Sagisaka A, Koga J, Esirekepov TZ, Hayashi Y, Kotaki H, Miyasaka Y, Sekiguchi K, Bulanov SV, and Kondo K. 2016. The current status of the J-KAREN laser upgrade. In 2016 Conference on Lasers and Electro-Optics (CLEO), 1–2. URL <https://ieeexplore.ieee.org/stamp/stamp.jsp?tp=&arnumber=7788565>.
- Klimo O, Psikal J, Limpouch J, and Tikhonchuk VT. 2008. Monoenergetic ion beams from ultrathin foils irradiated by ultrahigh-contrast circularly polarized laser pulses. *Phys Rev ST Accel Beams*, 11:031301. URL <https://link.aps.org/doi/10.1103/PhysRevSTAB.11.031301>.
- Kluge T, Cowan TE, Debus A, Schramm U, Zeil K, and Bussmann M. 2011. Electron temperature scaling in laser interaction with solids. *Phys Rev Lett*, 107(20):205003. URL <http://link.aps.org/doi/10.1103/PhysRevLett.107.205003>.
- Kluge T, Enghardt W, Kraft SD, Schramm U, Zeil K, Cowan TE, and Bussmann M. 2010. Enhanced laser ion acceleration from mass-limited foils. *Phys Plasmas*, 17(12):123103. URL <https://doi.org/10.1063/1.3519512>.
- Kraft SD, Richter C, Zeil K, Baumann M, Beyreuther E, Bock S, Bussmann M, Cowan TE, Dammene Y, Enghardt W, Helbig U, Karsch L, Kluge T, Laschinsky L, Lessmann E, Metzkes J, Naumburger D, Sauerbrey R, Schürer M, Sobiella M, Woithe J, Schramm U, and Pawelke J. 2010. Dose-dependent biological damage of tumour cells by laser-accelerated proton beams. *New J Phys*, 12:085003. URL <http://iopscience.iop.org/article/10.1088/1367-2630/12/8/085003/pdf>.
- Kroll F, Pawelke J, and Karsch L. 2013. Preliminary investigations on the determination of three-dimensional dose distributions using scintillator blocks and optical tomography. *Med Phys*, 40(8):082104. URL <https://doi.org/10.1118/1.4813898>.
- Krushelnick K, Clark EL, Allott R, Beg FN, Danson CN, Machacek A, Malka V, Najmudin Z, Neely D, Norreys PA, Salvati MR, Santala MIK, Tatarakis M, Watts I, Zepf M, and Dangor AE. 2000. Ultrahigh-intensity laser-produced plasmas as a compact heavy ion injection source. *IEEE Trans Plasma Sci*, 28:1110–1155. URL <http://www.scopus.com/inward/record.url?scp=33747272929&partnerID=8YFLogxK>.
- Kumar V. 2009. Understanding the focusing of charged particle beams in a solenoid magnetic field. *Am J Phys*, 77(8):737–741. doi:<http://dx.doi.org/10.1119/>

- 1.3129242. URL <http://scitation.aip.org/content/aapt/journal/ajp/77/8/10.1119/1.3129242>.
- Ledingham KWD and Galster W. 2010. Laser-driven particle and photon beams and some applications. *New J Phys*, 12:045005. URL <http://stacks.iop.org/1367-2630/12/i=4/a=045005>.
- Ledingham KWD, McKenna P, McCanny T, Shimizu S, Yang JM, Robson L, Zweit J, Gillies JM, Bailey J, Chimon GN, Clarke RJ, Neely D, Norreys PA, Collier JL, Singhal RP, Wei MS, Mangles SPD, Nilson P, Krushelnick K, and Zepf M. 2004. High power laser production of short-lived isotopes for positron emission tomography. *J Phys D: Appl Phys*, 37(16):2341. URL <http://stacks.iop.org/0022-3727/37/i=16/a=019>.
- Ledingham KWD, McKenna P, and Singhal RP. 2003. Applications for nuclear phenomena generated by ultra-intense lasers. *Science*, 300(5622):1107–1111. URL <http://science.sciencemag.org/content/300/5622/1107>.
- Levin WP, Kooy H, Loeffler JS, and DeLaney TF. 2005. Proton beam therapy. *Br J Cancer*, 93:849854. URL <http://dx.doi.org/10.1038/sj.bjc.6602754>.
- Limpert J, Nillson J, Rand D, Fan TY, Babzien M, Bayramian A, and Dawson J. 2011. Laser applications for future high-energy and high-intensity accelerators. In: Leemans W, Chou W, Uesaka M (Issue Eds) *Beam dynamics newsletter No. 56*. International Committee for Future Accelerators (ICFA), 13-87. URL http://icfa-usa.jlab.org/archive/newsletter/icfa_bd_nl_56.pdf.
- Linz U and Alonso J. 2007. What will it take for laser driven proton accelerators to be applied to tumor therapy? *Phys Rev ST Accel Beams*, 10:094801. URL <https://link.aps.org/doi/10.1103/PhysRevSTAB.10.094801>.
- Linz U and Alonso J. 2016. Laser-driven ion accelerators for tumor therapy revisited. *Phys Rev Accel Beams*, 19:124802. URL <https://link.aps.org/doi/10.1103/PhysRevAccelBeams.19.124802>.
- Lomax AJ, Bortfeld T, Goitein G, Debus J, Dykstra C, Tercier PA, Coucke PA, and Mirimanoff RO. 1999. A treatment planning inter-comparison of proton and intensity modulated photon radiotherapy. *Radiother Oncol*, 51(3):257 – 271. URL [https://doi.org/10.1016/S0167-8140\(99\)00036-5](https://doi.org/10.1016/S0167-8140(99)00036-5).
- Lomax NJ and Scheib SG. 2003. Quantifying the degree of conformity in radiosurgery treatment planning. *Int J Radiat Oncol Biol Phys*, 55(5):1409–1419. URL [http://dx.doi.org/10.1016/s0360-3016\(02\)04599-6](http://dx.doi.org/10.1016/s0360-3016(02)04599-6).
- Luo W, Fourkal E, Li J, and Ma CM. 2005. Particle selection and beam collimation system for laser-accelerated proton beam therapy. *Med Phys*, 32(3):794–806. URL <https://doi.org/10.1118/1.1861772>.

- Ma CM, Velchev I, Fourkal E, Li JS, Luo W, Fan J, Lin T, and Pollack A. 2006. Development of a laser-driven proton accelerator for cancer therapy. *Laser Phys*, 16(4):639–646. URL <https://doi.org/10.1134/S1054660X06040165>.
- Macchi A, Veghini S, Liseykina TV, and Pegoraro F. 2010. Radiation pressure acceleration of ultrathin foils. *New J Phys*, 12(4):045013. URL <http://stacks.iop.org/1367-2630/12/i=4/a=045013>.
- Macchi A, Veghini S, and Pegoraro F. 2009. “Light Sail” acceleration reexamined. *Phys Rev Lett*, 103:085003. URL <https://link.aps.org/doi/10.1103/PhysRevLett.103.085003>.
- Mairani A, Dokic I, Magro G, Tessonnier T, Kamp F, Carlson DJ, Ciocca M, Cerutti F, Sala PR, Ferrari A, Bhlen TT, Ji O, Parodi K, Debus J, Abdollahi A, and Haberer T. 2016. Biologically optimized helium ion plans: calculation approach and its in vitro validation. *Phys Med Biol*, 61(11):4283. URL <http://stacks.iop.org/0031-9155/61/i=11/a=4283>.
- Malka V, Faure J, Gauduel YA, Lefebvre E, Rousse A, and Phuoc KT. 2008. Principles and applications of compact laser-plasma accelerators. *Nat Phys*, 4:447–453. URL <http://dx.doi.org/10.1038/nphys966>.
- Malka V, Fritzler S, Grillon G, Chambaret JP, Antonetti A, Hulin D, Lefebvre E, D’Humières E, Ferrand R, Albaret C, and Meyroneinc S. 2004. Practicability of protontherapy using compact laser systems. *Med Phys*, 31(6):1587. URL <https://doi.org/10.1118/1.1747751>.
- Masood U, Bussmann M, Cowan T, Enghardt W, Karsch L, Kroll F, Schramm U, and Pawelke J. 2014. A compact solution for ion beam therapy with laser accelerated protons. *Appl Phys B*, 117(1):41–52. URL <http://dx.doi.org/10.1007/s00340-014-5796-z>.
- Masood U, Cowan TE, Enghardt W, Hofmann KM, Karsch L, Kroll F, Schramm U, Wilkens JJ, and Pawelke J. 2017a. A light-weight compact proton gantry design with a novel dose delivery system for broad-energetic laser-accelerated beams. *Phys Med Biol*, 62(13):5531–5555. URL <http://stacks.iop.org/0031-9155/62/i=13/a=5531>.
- Masood U, Karsch L, Pawelke J, and Kroll F. 2017b. Einrichtung zum Abrastern mit aufgeweiteten Teilchenstrahlen. Patent Appl. No. DE 10 2016 225 798.6.
- Mayer R, Mock U, Jäger R, Pötter R, Vutuc C, Eiter H, Krugmann K, Hammer J, Hirn B, Hawliczek R, Knocke-Abulesz TH, Lukas P, Nechville E, Pakisch B, Papauschek M, Raunik W, Rhomberg W, Sabitzer H, Schratter-Sehn A, Sedlmayer F, Wedrich I, and Auberger T. 2004. Epidemiological aspects of hadron therapy: a prospective nationwide study of the Austrian project MedAustron and the Austrian Society of Radiooncology (OEGRO). *Radiother Oncol*, 73:24–28. URL [https://doi.org/10.1016/S0167-8140\(04\)80008-2](https://doi.org/10.1016/S0167-8140(04)80008-2).

- Meer D and Psoroulas S. 2015. Gantries and dose delivery systems. *Mod Phys Lett A*, 30(17):1540021. URL <http://adsabs.harvard.edu/abs/2015MPLA...3040021M>.
- Metzkes J, Cowan TE, Karsch L, Kraft SD, Pawelke J, Richter C, Richter T, Zeil K, and Schramm U. 2011. Preparation of laser-accelerated proton beams for radiobiological applications. *Nucl Instrum Methods Phys Res A*, 653(1):172–175. URL <https://doi.org/10.1016/j.nima.2010.12.065>.
- Metzkes J, Karsch L, Kraft SD, Pawelke J, Richter C, Schürer M, Sobiella M, Stiller N, Zeil K, and Schramm U. 2012. A scintillator-based online detector for the angularly resolved measurement of laser-accelerated proton spectra. *Rev Sci Instrum*, 83:123301. URL <https://doi.org/10.1063/1.4768672>.
- Metzkes J, Zeil K, Kraft SD, Karsch L, Sobiella M, Rehwald M, Obst L, Schlenvoigt HP, and Schramm U. 2016. An online, energy-resolving beam profile detector for laser-driven proton beams. *Rev Sci Instrum*, 87(8):083310. URL <https://doi.org/10.1063/1.4961576>.
- Mevion Medical Systems. 2017. MEVION S250 Proton Therapy System. [Updated: 01.05.2018]. URL <http://www.mevion.com/products/mevion-s250-proton-therapy-system>.
- Mevion Medical Systems. 2018. MEVION S250i Proton Therapy System with HyperScan. [Updated: 01.05.2018]. URL <http://www.mevion.com/products/mevion-s250i-hyperscan-adaptive-aperturetm>.
- Misu T, Iwata Y, Sugiura A, Hojo S, Miyahara N, Kanazawa M, Murakami T, and Yamada S. 2004. Design study of compact medical fixed-field alternating-gradient accelerators. *Phys Rev Spec Top Accel Beams*, 7:094701–12. URL <https://link.aps.org/doi/10.1103/PhysRevSTAB.7.094701>.
- Mora P. 2003. Plasma expansion into a vacuum. *Phys Rev Lett*, 90:185002. URL <https://link.aps.org/doi/10.1103/PhysRevLett.90.185002>.
- Moteabbed M, Yock TI, and Paganetti H. 2014. The risk of radiation-induced second cancers in the high to medium dose region: a comparison between passive and scanned proton therapy, IMRT and VMAT for pediatric patients with brain tumors. *Phys Med Biol*, 59(12):2883. URL <http://stacks.iop.org/0031-9155/59/i=12/a=2883>.
- Nguyen V. 2008. Pummeling cancer with protons. [Updated: 01.01.2018]. URL <http://www.biofusiondesign.com/2008/11/16/pummeling-cancer-with-protons-2/>.
- Obst L, Göde S, Rehwald M, Brack FE, Branco J, Bock S, Bussmann M, Cowan TE, Curry CB, Fiuza F, Gauthier M, Gebhardt R, Helbig U, Huebl A, Hübner U, Irman A, Kazak L, Kim JB, Kluge T, Kraft S, Loeser M, Metzkes J, Mishra R, Rödel C, Schlenvoigt HP, Siebold M, Tiggesbäumker J, Wolter S, Ziegler T, Schramm U, Glenzer SH, and Zeil K. 2017. Efficient laser-driven proton acceleration from cylindrical and planar cryogenic hydrogen jets. *Sci Rep*, 7(1):10248. URL <https://doi.org/10.1038/s41598-017-10589-3>.

- Oppelt M, Baumann M, Bergmann R, Beyreuther E, Brchner K, Hartmann J, Karsch L, Krause M, Laschinsky L, Leann E, Nicolai M, Reuter M, Richter C, Srt A, Schnell M, Schrer M, Woithe J, Kaluza M, and Pawelke J. 2015. Comparison study of in vivo dose response to laser-driven versus conventional electron beam. *Radiat Environ Biophys*. URL <https://doi.org/10.1007/s00411-014-0582-1>.
- Owen H, Lomax A, and Jolly S. 2016. Current and future accelerator technologies for charged particle therapy. *Nucl Instrum Meth A*, 809:96–104. URL <https://doi.org/10.1016/j.nima.2015.08.038>.
- Paganetti H. 2012. Proton therapy: history and rationale. In: Paganetti H (Ed) *Proton therapy physics*. Taylor and Francis Group, USA, 1-18.
- Paganetti H. 2014. Relative biological effectiveness (RBE) values for proton beam therapy. Variations as a function of biological endpoint, dose, and linear energy transfer. *Phys Med Biol*, 59(22):R419. URL <http://stacks.iop.org/0031-9155/59/i=22/a=R419>.
- Paganetti H, Athar BS, Moteabbed M, Adams JA, Schneider U, and Yock TI. 2012. Assessment of radiation-induced second cancer risks in proton therapy and IMRT for organs inside the primary radiation field. *Phys Med Biol*, 57(19):6047. URL <http://stacks.iop.org/0031-9155/57/i=19/a=6047>.
- Particle Therapy Co-Operative Group. 2016. Particle therapy facilities in operation. [Updated: 29.07.2017]. URL <http://www.ptcog.ch/index.php/facilities-in-operation>.
- Peach KJ, Aslaninejad M, Barlow RJ, Beard CD, Bliss N, Cobb JH, Easton MJ, Edgecock TR, Fenning R, Gardner ISK, Hill MA, Owen HL, Johnstone CJ, Jones B, Jones T, Kelliher DJ, Khan A, Machida S, McIntosh PA, Pattalwar S, Pasternak J, Pozimski J, Prior CR, Rochford J, Rogers CT, Seviour R, Sheehy SL, Smith SL, Strachan J, Tygier S, Vojnovic B, Wilson P, Witte H, and Yokoi T. 2013. Conceptual design of a nonscaling fixed field alternating gradient accelerator for protons and carbon ions for charged particle therapy. *Phys Rev ST Accel Beams*, 16(34):030101. URL <http://link.aps.org/doi/10.1103/PhysRevSTAB.16.030101>.
- Pulsar Physics. 2014. General Particle Tracer (GPT) beam tracking code (ver 3.01). [Updated: 01.06.2014]. URL <http://www.pulsar.nl/gpt/index.html>.
- Python Software Foundation. 2015. Python programming language (ver. 2.7.8). [Updated: 01.07.2017]. URL <https://www.python.org/>.
- Reiser M. 2008. *Theory and design of charged particle beams*, second edition. WILEY-VCH Verlag GmbH & Co. KGaA, Weinheim, Germany.
- Richter C, Karsch L, Dammene Y, Kraft SD, Metzkes J, Schramm U, Schürer M, Sobiella M, Weber A, Zeil K, and Pawelke J. 2011. A dosimetric system for quantitative cell

- irradiation experiments with laser-accelerated protons. *Phys Med Biol*, 56:1529–1543. URL <http://stacks.iop.org/0031-9155/56/i=6/a=002>.
- Roth M, Cowan TE, Key MH, Hatchett SP, Brown C, Fountain W, Johnson J, Pennington DM, Snavely RA, Wilks SC, Yasuike K, Ruhl H, Pegoraro F, Bulanov SV, Campbell EM, Perry MD, and Powell H. 2001. Fast ignition by intense laser-accelerated proton beams. *Phys Rev Lett*, 86:436–439. URL <https://link.aps.org/doi/10.1103/PhysRevLett.86.436>.
- Schardt D, Elsässer T, and Schulz-Ertner D. 2010. Heavy-ion tumor therapy: Physical and radiobiological benefits. *Rev Mod Phys*, 82:383–425. URL <https://link.aps.org/doi/10.1103/RevModPhys.82.383>.
- Schell S. 2011. Dose delivery and treatment planning methods for efficient radiation therapy with laser-driven particle beams. Technische Universität München, Germany, Dissertation.
- Schell S and Wilkens JJ. 2010. Advanced treatment planning methods for efficient radiation therapy with laser accelerated proton and ion beams. *Med Phys*, 37(10):5330–5340. URL <https://doi.org/10.1118/1.3491406>.
- Schillaci F, Anzalone A, Cirrone GAP, Carpinelli M, Cuttone G, Cutroneo M, Martinis CD, Giove D, Korn G, Maggiore M, Manti L, Margarone D, Musumarra A, Perozziello FM, Petrovic I, Pisciotta P, Renis M, Ristic-Fira A, Romano F, Romano FP, Schettino G, Scuderi V, Torrisi L, Tramontana A, and Tudisco S. 2014. ELIMED, MEDical and multidisciplinary applications at ELI-Beamlines. *J Phys Conf Ser*, 508(1):012010. URL <http://stacks.iop.org/1742-6596/508/i=1/a=012010>.
- Schillo M. 2014. Global industrial development of accelerators for charged particle therapy. Proceedings of IPAC2014, 19121916. URL <http://jacow.org/IPAC2014/papers/weib01.pdf>.
- Schippers M. 2012. Proton accelerators. In: Paganetti H (Ed) Proton therapy physics. Taylor and Francis Group, USA, 61-102.
- Schramm U, Bussmann M, Irman A, Siebold M, Zeil K, Albach D, Bernert C, Bock S, Brack F, Branco J, Couperus J, Cowan T, Debus A, Eisenmann C, Garten M, Gebhardt R, Grams S, Helbig U, Huebl A, Kluge T, Khler A, Krr J, Kraft S, Kroll F, Kuntzsch M, Lehnert U, Loeser M, Metzkes J, Michel P, Obst L, Pausch R, Rehwald M, Sauerbrey R, Schlenvoigt H, Steiniger K, and Zarini O. 2017. First results with the novel petawatt laser acceleration facility in Dresden. *J Phys Conf Ser*, 874(1):012028. URL <http://stacks.iop.org/1742-6596/874/i=1/a=012028>.
- Schreiber J, Bell F, Grüner F, Schramm U, Geissler M, Schnürer M, Ter-Avetisyan S, Hegelich BM, Cobble J, Brambrink E, Fuchs J, Audebert P, and Habs D. 2006. Analytical model for ion acceleration by high-intensity laser pulses. *Phys Rev Lett*, 97(4):045005. URL <http://link.aps.org/doi/10.1103/PhysRevLett.97.045005>.

- Schreiber J, Bolton PR, and Parodi K. 2016. Invited Review Article: Hands-on laser-driven ion acceleration: A primer for laser-driven source development and potential applications. *Rev Sci Instrum*, 87(7):071101. URL <http://scitation.aip.org/content/aip/journal/rsi/87/7/10.1063/1.4959198>.
- Schuerer M, Karsch L, Pawelke J, Zschetzsche J, and Kroll F. 2016. Elektromagnet zur Fuehrung von Teilchenstrahlen zur Strahlentherapie. Patent No. DE 10 2015 200 213 A1.
- Schürer M, Baumann M, Beyreuther E, Brüchner K, Enghardt W, Kaluza M, Karsch L, Laschinsky L, Lessmann E, Nicolai M, Oppelt M, Reuter M, Richter C, Sävert A, Schnell M, Woithe J, and Pawelke J. 2012. Irradiation system for pre-clinical studies with laser accelerated electrons. *Biomed Tech*, 57:62–65. URL <https://doi.org/10.1515/bmt-2012-4244>.
- Schürer M, Hermannsdoerfer T, Karsch L, Kroll F, Masood U, and Pawelke J. 2015. Advanced short-pulsed high-field electromagnetic dipoles for laser-based proton therapy. *Biomedical Engineering / Biomedizinische Technik*, 60(Suppl.1):284. doi:10.1515/bmt-2014-5011.
- Schwoerer H, Pfotenhauer S, Jäckel O, Amthor KU, Liesfeld B, Ziegler W, Sauerbrey R, Ledingham KWD, and Esirkepov T. 2005. Laser-plasma acceleration of quasi-monoenergetic protons from microstructured targets. *Nature*, 439:445–448. URL <http://dx.doi.org/10.1038/nature04492>.
- Scuderi V, Jia SB, Carpinelli M, Cirrone G, Cuttone G, Korn G, Licciardello T, Maggiore M, Margarone D, Pisciotta P, Romano F, Schillaci F, Stancampiano C, and Tramontana A. 2014. Development of an energy selector system for laser-driven proton beam applications. *Nucl Instrum Methods Phys Res, Sect A*, 740(Supplement C):87 – 93. URL <https://doi.org/10.1016/j.nima.2013.10.037>.
- Siebold M. 2013. Development of the diode pumped Petawatt Laser System PEnELOPE. Online. URL <http://www.hzdr.de/db/Cms?pNid=2098>.
- Siebold M, Loeser M, Harzendorf G, Nehring H, Tsybin I, Roeser F, Albach D, and Schramm U. 2014. High-energy diode-pumped D2O-cooled multi-slab Yb:YAG and Yb:QX-glass lasers. *Opt Lett*, 3611. URL <http://dx.doi.org/10.1364/OL.39.003611>.
- Slopsema R. 2012. Beam delivery using passive scattering. In: Paganetti H (Ed) *Proton therapy physics*. Taylor and Francis Group, USA, 125-156.
- Smith A, Gillin M, Bues M, Zhu XR, Suzuki K, Mohan R, Woo S, Lee A, Komaki R, and Cox J. 2009. The M. D. Anderson proton therapy system. *Med Phys*, 36(9):4068–4083. URL <https://doi.org/10.1118/1.3187229>.
- Snively RA, Key MH, Hatchett SP, Cowan TE, Roth M, Phillips TW, Stoyer MA, Henry EA, Sangster TC, Singh MS, Wilks SC, MacKinnon A, Offenberger A, Pennington

- DM, Yauike K, Langdon AB, Lasinski BF, Perry MD, and Campbell EM. 2000. Intense high-energy proton beams from petawatt-laser irradiation of solids. *Phys Rev Lett*, 85(14):2945–2948. URL <https://link.aps.org/doi/10.1103/PhysRevLett.85.2945>.
- Snuverink J. 2018. Object Oriented Parallel Accelerator Library (OPAL). [Updated: 01.06.2018]. URL <https://gitlab.psi.ch/OPAL/src/wikis/home>.
- Syresin EM and Morozov NA. 2016. Simulations of a superconducting ion gantry. *Phys Part Nucl Lett*, 13(6):760–764. ISSN 1531-8567. URL <https://doi.org/10.1134/S1547477116060091>.
- Tramontana A, Anzalone A, Candiano G, Carpinelli M, Cirrone GAP, Cuttone G, Korn G, Licciardello T, Maggiore M, Manti L, Margarone D, Musumarra A, Perozziello F, Pisciotta P, Raffaele L, Romano F, Romano FP, Stancampiano C, Schillaci F, Scuderi V, Torrisi L, and Tudisco S. 2014. Medical research and multidisciplinary applications with laser-accelerated beams: the ELIMED network at ELI-Beamlines. *J Instrum*, 9(04):C04026. URL <http://stacks.iop.org/1748-0221/9/i=04/a=C04026>.
- Trbojevic D, Parker B, Keil E, and Sessler AM. 2007. Carbon/proton therapy: A novel gantry design. *Phys Rev ST Accel Beams*, 10:053503. URL <http://link.aps.org/doi/10.1103/PhysRevSTAB.10.053503>.
- Umstadter D. 2000. Photonuclear physics: Laser light splits atom. *Nature*, 404. URL <http://dx.doi.org/10.1038/35005202>.
- Vanderstraeten B, Verstraete J, Croock RD, Neve WD, and Lievens Y. 2014. In search of the economic sustainability of hadron therapy: the real cost of setting up and operating a hadron facility. *Int J Radiat Oncol Biol Phys*, 89(1):152 – 160. URL <https://doi.org/10.1016/j.ijrobp.2014.01.039>.
- Wagner F, Deppert O, Brabetz C, Fiala P, Kleinschmidt A, Poth P, Schanz VA, Tebartz A, Zielbauer B, Roth M, Stöhlker T, and Bagnoud V. 2016. Maximum proton energy above 85 MeV from the relativistic interaction of laser pulses with micrometer thick CH₂ targets. *Phys Rev Lett*, 116:205002. URL <http://link.aps.org/doi/10.1103/PhysRevLett.116.205002>.
- Wettengel S. 2014. Untersuchung und vergleich von topologien zur erzeugung hoher gepulster magnetfelder für eine medizinische anwendung. Institut Für Elektrotechnik und Informationstechnik, Technische Universität Dresden, Germany, Diplomarbeit.
- Wiedemann H. 2007. Particle accelerator physics. Springer-Verlag Berlin Heidelberg New York.
- Wilson RR. 1946. Radiobiological use of fast protons. *Radiology*, 47:487–91. URL <https://doi.org/10.1148/47.5.487>.
- Wolfram Research Inc. 2015. Wolfram Mathematics ver. 10. [Updated: 01.07.2017]. URL <http://www.wolfram.com/mathematica/?source=nav>.

- Yan XQ, Wu HC, Sheng ZM, Chen JE, and Meyer-ter-Vehn J. 2009. Self-Organizing GeV, Nanocoulomb, Collimated Proton Beam from Laser Foil Interaction at $7 \times 10^{21} \text{ W/cm}^2$. *Phys Rev Lett*, 103(4):135001. URL <http://link.aps.org/doi/10.1103/PhysRevLett.103.135001>.
- Yogo A, Maeda T, Hori T, Sakaki H, Ogura K, Nishiuchi M, Sagisaka A, Kiriya H, Okada H, Kanazawa S, Shimomura T, Nakai Y, Tanoue M, Sasao F, Bolton PR, Murakami M, Nomura T, Kawanishi S, and Kondo K. 2011. Measurement of relative biological effectiveness of protons in human cancer cells using a laser-driven quasimonoenergetic proton beamline. *Appl Phys Lett*, 98(5):053701. URL <https://doi.org/10.1063/1.3551623>.
- Yong S, Kun Z, Chao C, Jun-Gao Z, Yuan-Rong L, Zhi-Yu G, Jia-Er C, and Xue-Qing Y. 2014. Preliminary design of a laser accelerator beam line. *Chin Phys C*, 38(11):117011. URL <http://stacks.iop.org/1674-1137/38/i=11/a=117011>.
- Zeil K. 2013. Efficient laser-driven proton acceleration in the ultra-short pulse regime. Fakultät Mathematik und Naturwissenschaften der Technischen Universität Dresden, Germany, Dissertation.
- Zeil K, Bussmann M, Beyreuther E, Burris-Mog T, Cowan TE, Enghardt W, Karsch L, Kraft SD, Laschinsky L, Metzkes J, Naumburger D, Oppelt M, Richter C, Sauerbrey R, Schürer M, Schramm U, and Pawelke J. 2012. Dose-controlled irradiation of cancer cells with laser-accelerated proton pulses. *Appl Phys B*, 110(4):437–444. URL <http://dx.doi.org/10.1007/s00340-012-5275-3>.
- Zeil K, Kraft SD, Bock S, Bussmann M, Cowan TE, Kluge T, Metzkes J, Richter T, Sauerbrey R, and Schramm U. 2010. The scaling of proton energies in ultrashort pulse laser plasma acceleration. *New J Phys*, 12:045015. URL <http://stacks.iop.org/1367-2630/12/i=4/a=045015>.
- Zeil K, Metzkes J, Kluge T, Bussmann M, Cowan TE, Kraft SD, Sauerbrey R, Schmidt B, Zier M, and Schramm U. 2014. Robust energy enhancement of ultrashort pulse laser accelerated protons from reduced mass targets. *Plasma Phys Controlled Fusion*, 56(8):084004. URL <http://stacks.iop.org/0741-3335/56/i=8/a=084004>.
- Zhao T, Sun B, Grantham K, Rankine L, Cai B, Goddu S, Santanam L, Knutson N, Zhang T, Reilly M, Bottani B, Bradley J, Mutic S, and Klein E. 2016. Commissioning and initial experience with the first clinical gantry-mounted proton therapy system. *J Appl Clin Med Phys*, 17(2). URL <https://doi.org/10.1120/jacmp.v17i2.5868>.
- Zhuo HB, Chen ZL, Yu W, Sheng ZM, Yu MY, Jin Z, and Kodama R. 2010. Quasimonoenergetic proton bunch generation by dual-peaked electrostatic-field acceleration in foils irradiated by an intense linearly polarized laser. *Phys Rev Lett*, 105:065003. URL <http://link.aps.org/doi/10.1103/PhysRevLett.105.065003>.
- Ziegler JF. 2015. SRIM–Stopping and Range of Ions in Matter [Updated: 01.06.2015]. URL <http://www.srim.org/>.

Acknowledgements

I would like to extend my deepest gratitude towards Prof. W Enghardt for giving me the opportunity to join his team as a PhD student. I am profoundly grateful for his constructive supervision, insurmountable patience, incontestable positive attitude and continuous encouragement. I am indebted to J Pawelke for his never-ending support, kindness, immense patience and providing an excellent and friendly work environment as the group leader. I want to thank him for being there for me on every level and having confidence in me till the end. I also like to thank Prof. U Schramm for providing an excellent scientific support and exemplary work environment at HZDR. This has been a remarkable professional and tremendous personal journey for me.

I would like to thank L Karsch for his in-depth scientific guidance throughout, especially in the beginning. Also, I would like to thank F Kroll for scientific discussions, experimental support and being a great work companion. My sincere thanks to U Lehnert and T Burris-Mog for thorough discussions and tutorials in accelerator physics and their guidance in setting up simulations. In connection with my PhD work, I had the chance to collaborate with Prof. JJ Wilkens and KM Hofmann from Technical University Munich, Germany. I like to thank them for the excellent collaboration and rewarding work. It has been an absolute pleasure working with them. Aside from my PhD work, I had the great opportunity to do a research project at Paul Scherrer Institute (PSI), Switzerland, which was funded by the federal government of Germany. It was an excellent experience and I would like to thank Prof. AJ Lomax, D Meer, S Psoroulas, A Adelmann, M Egloff and V Rizzoglio for their scientific contributions and experimental support. It enhanced my capabilities and perspective.

I also like to mention and thank K Zeil, T Kluge, J Metzkes and S Kraft for the in-depth scientific explanations and discussions in the subject of laser acceleration. I also like to show my special appreciation to Prof. TE Cowan and M Bussmann for their critical scientific conversations, motivation and exuberant hallway debates. I like to thank M Gotz specially for proof reading my thesis, and for his constructive criticism. I also like to present my sincere appreciation to M Schürer, M Sobiella, T Herrmannsdörfer, E Beyreuther, B Lutz, M Oppelt, M Priegnitz, S Schöne, R Perrin, A Khalek, F Fiedler, K Stützer, C Golnik, C Richter and A Müller for their scientific assistance and providing comfortable work place. I also like to acknowledge the support crew at Tandem accelerator, high-field workshop and the IT department at HZDR for their much needed technical support and smooth operations.

I like to extend my gratitude towards Prof. P Michael who has been kind enough to

analyze my work. I like to thank the institutions, OncoRay and HZDR, for providing great opportunities to nurture professional needs like expert lectures, training courses, journal clubs and seminars.

I like to thank my family and close friends to make life gentle and fun, and for their support during this long journey. At the end, I would like to extend my sincere and deepest gratitude to E Tzavaras who endured my struggles, and provided never-ending support, comfort and stability in my life.

I would like to acknowledge and thank the financial support for this work provided by the German Ministry of Education and Research (BMBF), grant numbers 03ZIK445, 03Z1N511 and 03Z1O511.

**Technische Universität Dresden
Medizinische Fakultät Carl Gustav Carus
Promotionsordnung vom 24. Juli 2011**

Erklärungen zur Eröffnung des Promotionsverfahrens

1. Hiermit versichere ich, dass ich die vorliegende Arbeit ohne unzulässige Hilfe Dritter und ohne Benutzung anderer als der angegebenen Hilfsmittel angefertigt habe; die aus fremden Quellen direkt oder indirekt übernommenen Gedanken sind als solche kenntlich gemacht.
2. Bei der Auswahl und Auswertung des Materials sowie bei der Herstellung des Manuskripts habe ich Unterstützungsleistungen von folgenden Personen erhalten:
Prof. Dr. W Enghardt, Dr. J Pawelke, Dr. L Karsch, Hr. F Kroll, Prof. Dr. JJ Wilkens and Dr. KM Hofmann
3. Weitere Personen waren an der geistigen Herstellung der vorliegenden Arbeit nicht beteiligt. Insbesondere habe ich nicht die Hilfe eines kommerziellen Promotionsberaters in Anspruch genommen. Dritte haben von mir weder unmittelbar noch mittelbar geldwerte Leistungen für Arbeiten erhalten, die im Zusammenhang mit dem Inhalt der vorgelegten Dissertation stehen.
4. Die Arbeit wurde bisher weder im Inland noch im Ausland in gleicher oder ähnlicher Form einer anderen Prüfungsbehörde vorgelegt.
5. Die Inhalte dieser Dissertation wurden in folgender Form veröffentlicht:
 - Masood U, Cowan TE, Enghardt W, Hofmann KM, Karsch L, Kroll F, Schramm U, Wilkens JJ, Pawelke J. 2017. A light-weight compact proton gantry design with a novel dose delivery system for broad-energetic laser-accelerated beams. Phys Med Biol 62 (13):55315555. URL: <http://stacks.iop.org/0031-9155/62/i=13/a=5531>
 - Masood U, Karsch L, Pawelke J, Kroll F. 2016. Patent:Einrichtung zum Abrastern mit aufgeweiteten Teilchenstrahlen. Patent Appl. No. DE 10 2016 225 798.6
 - Masood U, Bussmann M, Cowan T, Enghardt W, Karsch L, Kroll F, Schramm U, Pawelke J. 2014. A compact solution for ion beam therapy with laser accelerated protons. Appl Phys B 117 (1):4152. URL: <https://doi.org/10.1007/s00340-014-5796-z>
 - Karsch L, Beyreuther E, Enghardt W, Gotz M, Masood U, Schramm U, Zeil K, Pawelke J. 2017. Towards ion beam therapy based on laser plasma accelerators. Acta Oncol, 56(11):13591366. URL: <https://doi.org/10.1080/0284186X.2017.1355111>.

- Hofmann KM, Masood U, Pawelke J, Wilkens JJ. 2015. A treatment planning study to assess the feasibility of laser-driven proton therapy using a compact gantry design. Med Phys 42 (9):51205129. DOI: 10.1118/1.4927717

6. Ich bestätige, dass es keine zurückliegenden erfolglosen Promotionsverfahren gab.
7. Ich bestätige, dass ich die Promotionsordnung der Medizinischen Fakultät der Technischen Universität Dresden anerkenne.
8. Ich habe die Zitierrichtlinien für Dissertationen an der Medizinischen Fakultät der Technischen Universität Dresden zur Kenntnis genommen und befolgt.

Dresden, 13. September 2018

Anlage 2

Hiermit bestätige ich die Einhaltung der folgenden aktuellen gesetzlichen Vorgaben im Rahmen meiner Dissertation

(Nicht angekreuzte Punkte sind für meine Dissertation nicht relevant.)

- ☐ das zustimmende Votum der Ethikkommission bei Klinischen Studien, epidemiologischen Untersuchungen mit Personenbezug oder Sachverhalten, die das Medizinproduktegesetz betreffen
- ☐ die Einhaltung der Bestimmungen des Tierschutzgesetzes
- ☐ die Einhaltung des Gentechnikgesetzes
- ☒ die Einhaltung von Datenschutzbestimmungen der Medizinischen Fakultät und des Universitätsklinikums Carl Gustav Carus.

Dresden, 13. September 2018

